NMR SPECTROSCOPY OF SILVER AND ARSENIC CONTAINING SOLIDS

A Thesis

Presented to

The Faculty of Graduate Studies

of

The University of Guelph

by

XIAOLONG LIU

In partial fulfilment of requirements

for the degree of

Doctor of Philosophy

April, 2008

Your file Votre référence
ISBN: 978-0-494-42571-8
Our file Notre référence
ISBN: 978-0-494-42571-8

ABSTRACT

NMR SPECTROSCOPY OF SILVER AND ARSENIC CONTAINING SOLIDS

Xiaolong (Bruce) Liu

University of Guelph, 2008

Supervisor

Dr. Glenn H. Penner

Using high resolution CP/MAS NMR techniques, a series of organosilver compounds has been systematically studied by solid state ^{109}Ag and ^{13}C NMR spectroscopy. The chemical shift tensors obtained from the slow CP/MAS ^{109}Ag and ^{13}C NMR spectra have provided valuable structural information, most of which is in good agreement with the available crystal structure data.

Computational studies have been carried out on a series of silver compounds. The slope between ^{109}Ag experimental chemical shifts and calculated chemical shieldings at B3LYP/DGDZVP level is -1.1, which is very close to the theoretically ideal value of -1 and is good enough to be used to predict isotropic chemical shifts.

Deuterium NMR spectra lineshapes and spin lattice relaxation times were used to investigate the molecular dynamics of the benzene silver perchlorate complex. Deuterium NMR spectra indicate that the benzene ring is rapidly reorienting about its 6-fold axis. Activation energies obtained from fitting the T_1 curve as a function of temperature were 23.9 ± 0.5 kJ/mol; simulations of the spectral lineshapes gave 23.2 ± 1.0 kJ/mol. T_1 measurements showed a phase transition at 303 (±3) K. In order to compare the ^{109}Ag and ^{13}C CP/MAS spectra to the low temperature phase,

the solid state ^{109}Ag and ^{13}C NMR spectra were obtained at 320 K. The ^{109}Ag chemical shift tensor values differ significantly between the two phases, where those for ^{13}C show very little change.

NMR measurements of chemical shifts and nuclear quadrupolar coupling constants (χ) of Arsenic and Iodine nuclei have been performed on Me_4AsI and Me_4NI. ^{75}As χ value of 12.38 ± 0.30MHz has been obtained for Me_4AsI. Moreover, ^{127}I χ values of Me_4AsI and Me_4NI were 62.0 ± 0.5 and 23.6 ± 0.2 MHz, respectively. The indirect spin-spin coupling constant ^1J (^{13}C-^{75}As) was obtained as 20 ± 2 Hz for Me_4AsI. This represents the first reported measurement of a ^{13}C-^{75}As J-coupling value.

ACKNOWLEDGEMENTS

I would first and foremost like to thank my supervisor, *Professor Glenn H. Penner*, for his valuable advice and supervision during the past three years. Special acknowledgements go to *Professor Mark D. Baker, Professor Michael K. Denk and Professor William P. Power* of the GWC^2 for their participation and helpful suggestions as my Ph.D committee members. *Professor Yining Huang* of the University of Western Ontario is gratefully acknowledged for his kindness in consenting to be the external examiner for my Ph.D defense.

I am especially thankful to *Dr. Jun Gu and Ms. Valerie Robertson* of the NMR Center for their kindness and technical support in operating the spectrometer. I would also like to extend my gratitude to *Professors Marcal Schlaf, Kathryn E. Preuss and William W. L. Tam* for permission to use their dry boxes. I am thankful to *Professor Nick P. C. Westwood* for his help in quantum chemical calculation. A special thanks to *Peng Liu* for his help with the computational aspect of this work, as well as Kyle Wu for his help with my sample preparation.

My very sincere thanks are also due to our colleagues in the Penner's group, including Renee Webber and Liang Li. Their companionship and collaboration have made my Ph.D study a wonderful learning experience.

Finally, I would like to thank my dearest wife, Fengdan Wang, for her support and encouragement.

LIST OF ABBREVIATIONS AND SYMBOLS USED

ADF	Amsterdam Density Functional
α, β, γ	Euler angles
1D	One dimensional
2D	Two dimensional
B_0	External magnetic field
B_1	Radio-frequency (r.f.) field
B_{eff}	Effective field
CP	Cross polarization
CP/MAS	Cross polarization/magic angle spinning
CPMG	Carr-Purcell Meiboom-Gill pulse sequence
CS	Chemical shift
CSA	Chemical shift anisotropy
CSD	Cambridge structure database
δ	Chemical shift
d	Residual dipolar coupling constant
D_1	Relaxation delay
DAS	Dynamic-Angle spinning
ΔJ	Anisotropic indirect spin-spin coupling constant
DFT	Density functional theory
DGDZVP	Density Gaussian double-zeta-split-valence plus polarization basis set
E_a	Arrhenius Activation energy

ECP	Effective core potential
EFG	Electronic field gradient
η	Asymmetry parameters for the chemical shift interaction
η_Q	Asymmetry parameter for the nuclear quadrupole interaction
FID	Free induction delay
FT	Fourier transformation
γ	Magnetogyric ratio
GIAO	Gauge-invariant atomic orbitals
GTO	Gaussian-type orbital
$\hat{H}$	Hamiltonian operator
HF	Hartree-Fock
HPDEC	High power decoupling
H_{CS}	Chemical shift interaction Hamiltonian
H_{dd}	Dipole-dipole coupling Hamiltonian
H_Q	Quadrupolar coupling Hamiltonian
H_{SC}	Indirect coupling interaction Hamiltonian
H_z	Zeeman interaction Hamiltonian
I	Eigenvalue of the angular spin momentum
IGLO	Individual gauge for localized orbitals
J_{ij}	Coulomb integral in MO theory
k	Motional rate
K_{ij}	Exchange integral in MO theory
J_{iso}	Isotropic indirect spin-spin coupling constant

$J(\omega)$	Power spectral density function
κ	Skew
χ	Nuclear quadrupolar coupling constant
Λ	Transverse relaxation matrix
μ	Magnetic dipole moment
Lanl2DZ	Los Alamos ECP plus double-zeta basis set
LORG	Localized orbitals-local origin`
MAS	Magic angle spinning
MO	Molecular orbital
MP2	Møller-Plesset second-order perturbation theory
NMR	Nuclear magnetic resonance
NQR	Nuclear quadrupolar resonance
NS	Number of scans
Ω	Span of the chemical shift anisotropy
ω_0	Larmor frequency
ω_r	Angular rotation frequency
PAS	Principal axis system
Ψ	Eigenfunction corresponding to eigenvalue of $\hat{H}$
ppm	Parts per million
QCC	Quadrupolar coupling constant
QCPMG	Quadrupolar Carr-Purcell Meiboom-Gill pulse sequence
σ	Magnetic shielding
σ^d	Diamagnetic contribution to σ

σ^p	Paramagnetic contribution to σ
R_{DD}	Direct dipolar coupling constant
r_{IS}	Internuclear distance of two coupled nuclei
S/N	Signal-to-noise ratio
SSB	Spinning side bands
STO	Slater-type orbital
T	Temperature
T_1	Spin-lattice relaxation time
T_2	Spin-spin relaxation time
τ_c	Correlation time
τ_∞	Infinite correlation time
ν_R	MAS spinning rate
VT	Variable temperature
XRD	X-ray diffraction
Z	Number of molecules per unit cell

TABLE OF CONTENTS

LIST OF TABLES

LIST OF FIGURES

INTRODUCTION

Chapter I

Introduction to Solid State Nuclear Magnetic Resonance Spectroscopy

1.1 Introduction to NMR

Nuclear magnetic resonance (NMR) in the bulk condensed phase was reported for the first time in 1946 by Bloch et al. [1] and by Purcell et al. [2]. The development of pulsed Fourier transform NMR spectroscopy by Ernst and Anderson [3] prompted the widespread application of NMR spectroscopy. Currently, NMR spectroscopy is one of the most powerful techniques to investigate molecular structure. In addition, NMR spectroscopy is a powerful technique for investigating time-dependent chemical phenomena, including reaction kinetics and intramolecular dynamics.

Solid-state NMR can provide useful information on the number of molecules in the crystallographic asymmetric unit and on the site symmetry of the molecule in the crystal lattice to assist in the refinement of powder XRD data. It also can be used to measure internuclear distances directly, and often with great accuracy. For amorphous and disordered solids, such as inorganic glasses and organic polymers, solid state NMR can provide invaluable structural information which cannot be obtained by any other technique. Solution and solid-state NMR are both excellent methods of determining chemical composition. NMR offers numerous ways to study dynamic aspects over a large range of characteristic motional rates. Thus it is desirable to exploit this technique for studying structure and dynamics of solid materials.

However, due to the presence of spatially dependent anisotropic interactions, the spectral resolution of solid state NMR spectra is orders of magnitude lower than that of high-resolution NMR in liquids. Important advances were achieved in the 1970s by combining high-speed mechanical rotation of the sample with ingenious manipulation of the nuclear

spins such as multiple-pulse irradiation, high-power homo- and heteronuclear decoupling, and cross polarization [4].

1.2 Basic Theory of NMR

1.2.1 Nuclear Spin

Nuclear spin is one of the nuclear fundamental properties, which can be described by a spin angular momentum. The spin angular momentum is quantized, with a magnitude, $|I|$, that can be specified in terms of a quantum number, I, by:

$$|I| = \hbar[I(I+1)]^{1/2} \tag{1.1}$$

where $\hbar$ is the modified Plank's constant and equal to h/2π. A nucleus with a non-zero nuclear spin number generates a magnetic moment, μ:

$$\vec{\mu} = \gamma\hbar\vec{I} \tag{1.2}$$

where γ is the magnetogyric ratio, a constant which is used to measure the strength of the nuclear magnetic moment. Both angular momentum and the magnetic moment are vector quantities, they have both magnitude and direction. A positive magnetogyric ratio, γ, indicates that the vector directions of the magnetic moment and angular momentum are parallel to each other; on the other hand, a negative value implies that the directions are anti-parallel.

1.2.2 Zeeman Interaction (H_Z)

In an NMR spectrometer, the static external magnetic field is directed by convention along the z-axis of the laboratory coordinate system.

Since both nuclear spin angular momentum I and the nuclear magnetic moment μ are quantized vectors, when placed in an external static magnetic field (B_0), their observable components in the z direction, taken to be the direction along B_0, is given by

$$I_z = \hbar m \tag{1.3}$$

$$\mu_z = \gamma I_z \tag{1.4}$$

where m is another magnetic quantum number. The allowed values of m_I are:

$$m = I, I-1, I-2 \ldots -I$$

There are (2I+1) possible values of m_I.

In the presence of an external magnetic field (B_0), the spin states of the nucleus have energies given by

$$\mathrm{E} = -\mu \cdot \mathrm{B}_0 \tag{1.5}$$

The static external magnetic field is directed by convention along the z-axis of the laboratory coordinate system. For this geometry, equation 1.5 reduces to

$$\mathrm{E}_m = -\gamma I_z \mathrm{B}_0 = -m\hbar\gamma \mathrm{B}_0 \tag{1.6}$$

in which B_0 is the static magnetic field strength. In the presence of a static magnetic field, the projections of the angular momentum of the nuclei onto the z-axis of the laboratory frame results in (2I+1) equally spaced energy levels, which are known as the Zeeman levels.

At equilibrium, the different energy states are unequally populated because lower energy orientations of the magnetic dipole vector are more probable. The relative population of a state is given by the Boltzmann distribution,

$$\frac{N_m}{N} = \exp\left(\frac{-E_m}{k_B T}\right) \Big/ \sum_{m=-I}^{I} \exp\left(\frac{-E_m}{k_B T}\right) \tag{1.7}$$

In which N_m is the number of nuclei in the mth state and N is the total number of spins, T is the absolute temperature, and k_B is the Boltzmann constant. Substituting equation 1.6 into equation 1.7, then the new equation can be expressed as:

$$\frac{N_m}{N} = \exp\left(\frac{m\hbar\gamma B_0}{k_B T}\right) \Big/ \sum_{m=-I}^{I} \exp\left(\frac{m\hbar\gamma B_0}{k_B T}\right) \tag{1.8}$$

Because at ambient temperature $m\hbar\gamma B_0 / k_B T \ll 1$, this exponential function can be expanded to first order using a Taylor series:

$$\begin{aligned} \frac{N_m}{N} &\approx \left(1 + \frac{m\hbar\gamma B_0}{k_B T}\right) \Big/ \sum_{m=-I}^{I} \left(1 + \frac{m\hbar\gamma B_0}{k_B T}\right) \\ &\approx \frac{1}{2I+1}\left(1 + \frac{m\hbar\gamma B_0}{k_B T}\right) \end{aligned} \tag{1.9}$$

Note that the populations of the states depend both on the nucleus type through γ and on the applied field strength B_0.

The bulk magnetic moment, **M**, of a macroscopic sample is given by the vector sum of the corresponding quantities for individual nuclei, μ and I. At thermal equilibrium, the transverse components (e.g., the x- and y-components) of μ and I for different nuclei in the sample are uncorrelated and sum to zero. The small population differences between energy levels give rise to a bulk magnetization of the sample parallel (longitudinal) to the static

magnetic field, $\mathbf{M} = M_0\mathrm{k}$, in which k is the unit vector in the z-direction. Using above equations, M_0 is given by:

$$\begin{aligned} M_0 &= \gamma\hbar \sum_{m=-I}^{I} mN_m \\ &= N\gamma\hbar \sum_{m=-I}^{I} m\exp(m\gamma\hbar B_0/k_BT) \Big/ \sum_{m=-I}^{I} \exp(m\gamma\hbar B_0/k_BT) \\ &\approx N\gamma\hbar \sum_{m=-I}^{I} m(1+m\gamma\hbar B_0/k_BT) \Big/ \sum_{m=-I}^{I} (1+m\gamma\hbar B_0/k_BT) \\ &\approx \left[N\gamma^2\hbar^2 B_0/k_BT(2I+1)\right] \sum_{m=-I}^{I} m^2 \\ &\approx N\gamma^2\hbar^2 B_0 I(I+1)/3k_BT \end{aligned} \qquad (1.10)$$

Transitions between Zeeman levels can be stimulated by applied electromagnetic radiation. The selection rule governing magnetic dipole transitions is $\Delta m = \pm 1$. Thus, the photon energy, ΔE, required to excite a transition between the m and m+1 Zeeman states is

$$\Delta \mathrm{E} = |\hbar\gamma \mathrm{B}_0| \qquad (1.11)$$

According to the Bohr condition, the frequency of the required electromagnetic radiation is given by

$$\omega_0 = \Delta \mathrm{E}/\hbar = |\gamma \mathrm{B}_0| \qquad (1.12)$$

or

$$\nu_0 = \omega/2\pi = |\gamma/2\pi| \mathrm{B}_0 \qquad (1.13)$$

This frequency is known as the *Larmor frequency* of the nucleus.

1.2.3 Chemical Shift Interaction ($\mathbf{H_{CS}}$)

A general feature of NMR spectroscopy is that the observed resonance frequencies depend on the local environments of individual nuclei and differ slightly from the

frequencies predicted by equation 1.12 and 1.13 for a "bare" nucleus. The differences in resonance frequencies are referred to as chemical shifts and offer the possibility of distinguishing between otherwise identical nuclei in different chemical environments.

The phenomenon of the chemical shift arises because motions of electrons induced by the external magnetic field generate secondary magnetic fields. The net magnetic field at the location of a specific nucleus depends upon the static magnetic field and local secondary fields. The effect of the secondary fields is called nuclear magnetic shielding and can augment or diminish the effect of the external magnetic field. In general, the electronic charge distribution in a molecule is anisotropic and the effects of shielding on a particular nucleus are described by the nuclear shielding tensor, represented by 3 x 3 matrix.

$$\hat{\sigma} = \begin{bmatrix} \sigma_{xx} & \sigma_{xy} & \sigma_{xz} \\ \sigma_{yx} & \sigma_{yy} & \sigma_{yz} \\ \sigma_{zx} & \sigma_{zy} & \sigma_{zz} \end{bmatrix} \xrightarrow{diagonalization} \begin{bmatrix} \sigma_{11} & 0 & 0 \\ 0 & \sigma_{22} & 0 \\ 0 & 0 & \sigma_{33} \end{bmatrix} \qquad (1.14)$$

In the principal coordinate system of the shielding tensor, the matrix representing the tensor is diagonal, with principal components σ_{11}, σ_{22}, and σ_{33}.

In isotropic liquid solution, collisions lead to rapid reorientation of the molecule and consequently, of the shielding tensor. Under these circumstances, the effects of shielding on a particular nucleus can be given by:

$$\sigma_{iso} = (\sigma_{11} + \sigma_{22} + \sigma_{33})/3 \qquad (1.15)$$

where σ_{iso} is the average, isotropic, shielding constant for the nucleus.

Chemical shielding is an absolute value relative to a "bare" nucleus; chemical shift is usually used because it is a value relative to a more convenient reference signal. The chemical shift δ can be expressed by:

$$\delta = 10^6(\nu - \nu_{ref})/\nu_{ref} \approx 10^6(\sigma_{ref} - \sigma) \qquad (1.16)$$

The chemical shift usually has a small value in units of 10^{-6}, or ppm, which is independent of the applied magnetic field B_0. Depending on the local symmetry at the nucleus, the magnitude of the chemical shift will vary as a function of the orientation of the molecule with respect to the external magnetic field. This orientation dependence of the chemical shift is referred to as chemical shift anisotropy (CSA). In its principal axis system, the chemical shift tensor is fully expressed by the three diagonal elements δ_{11}, δ_{22} and δ_{33} ($\delta_{11} \geq \delta_{22} \geq \delta_{33}$). The isotropic chemical shift is described in terms of the three principal components:

$$\delta_{iso} = (\delta_{11} + \delta_{22} + \delta_{33})/3 \qquad (1.17)$$

Chemical shift anisotropies can be measured directly from simple one-dimensional NMR spectra of powder samples by observing the powder patterns in the spectra. If the powder patterns from inequivalent nuclear sites are resolved, it is still possible to extract the anisotropic shielding parameters from a one-dimensional spectrum via spectral simulation. For spin-1/2 nuclei, CP/MAS methods can provide chemical anisotropic parameters. For spins >1/2, quadrupolar-coupling effects tend to dominate spectra and render the observation of shielding effects difficult.

Span (Ω) and skew (κ), are often used to describe the orientational dependence of the chemical shift tensor at a nucleus in the magnetic field. The definition of Ω and κ are:

$$\Omega = \delta_{11} - \delta_{33} \qquad (1.18)$$

and

$$\kappa = \frac{3(\delta_{22} - \delta_{iso})}{\Omega} \qquad (1.19)$$

The anisotropic chemical shifts are illustrated schematically in Figure 1.1. In the case of the non-axial symmetric molecular structure, Figure 1.1 (b), each of the three principal elements of the chemical shift components possesses a unique value, i.e. δ_{11}, δ_{22}, δ_{33}. When the molecular structure has axial symmetric property (C_n, $n \geq 3$), Figure 1.1 (a) (c), two of the

principal elements are identical. In addition, in the case of spherical symmetry the three chemical shift components are equal and one single narrow peak is observed.

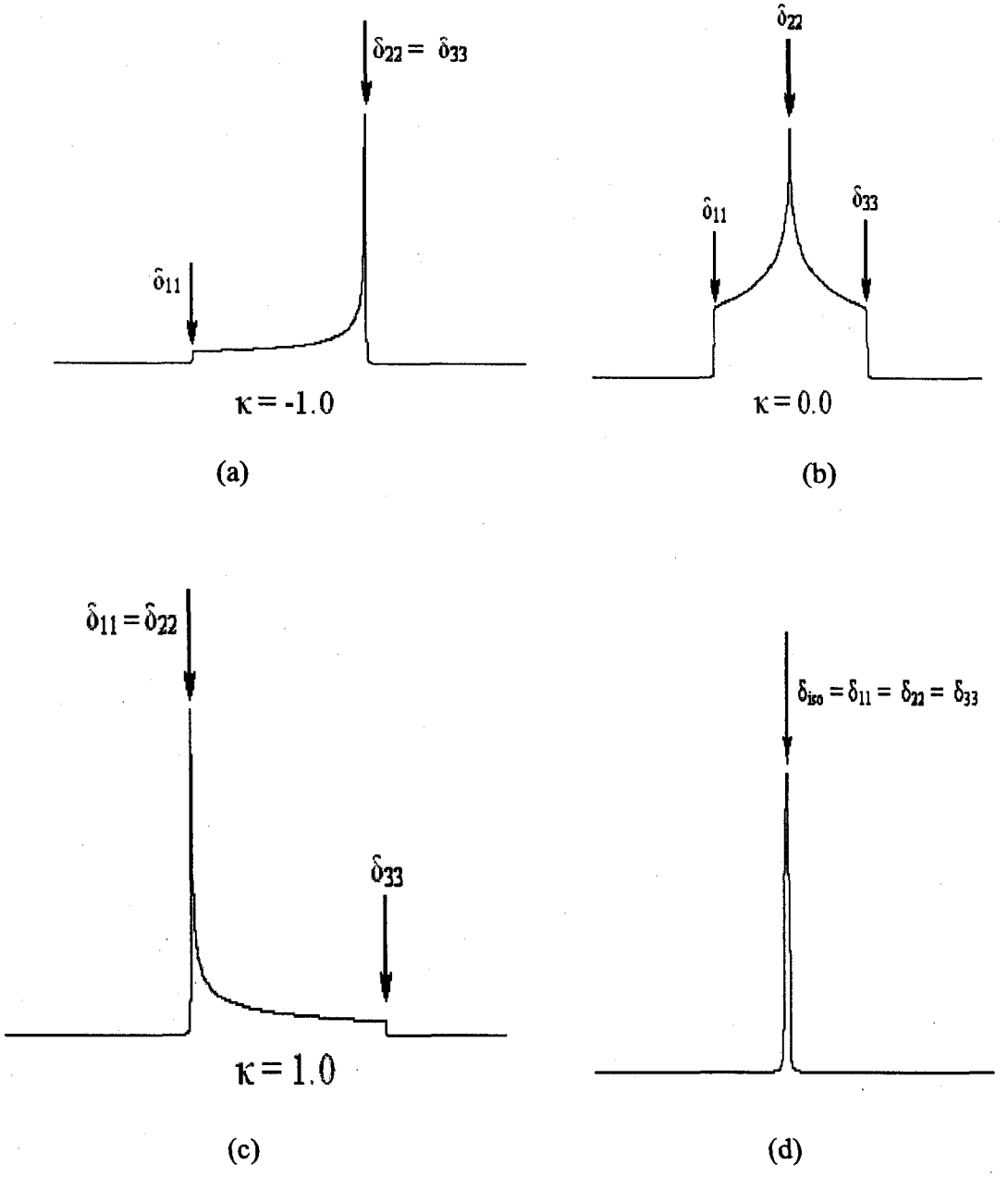

Figure 1.1 Typical powder pattern lineshapes display the character of chemical shift components and different skews.

1.2.4 Dipole-Dipole Coupling (H_{dd})

Dipole-dipole or dipolar coupling is the interaction of magnetic moments, directly through space. In solution, the dipole-dipole interaction is averaged to zero by rapid and random molecular tumbling. But in solids this interaction can be a major cause of linebroadening.

The Hamiltonian for dipolar coupling between two spins I and S in angular frequency units (rad s^{-1}) is [5]:

$$\hat{H}_{dd} = \left(\frac{\mu_0}{4\pi}\right)\gamma_I\gamma_S\hbar\left(\frac{\hat{I}\cdot\hat{S}}{r^3} - 3\left(\frac{\left(\hat{I}\cdot\vec{r}\right)\left(\hat{S}\cdot\vec{r}\right)}{r^5}\right)\right) \tag{1.20}$$

Expressing this equation in spherical polar coordinates, and expanding the scalar products, equation 1.22 can be rewritten as the "Dipolar Alphabet":

$$\hat{H}_{dd} = \left(\frac{\mu_0}{4\pi}\right)\frac{\gamma_I\gamma_S\hbar}{r^3}\left(A+B+C+D+E+F\right) \tag{1.21}$$

where

$$A = \hat{I}_z\cdot\hat{S}_z\left(1-3\cos^2\theta\right) \tag{1.22}$$

$$B = \frac{1}{4}\left[\hat{I}_+\hat{S}_- + \hat{I}_-\hat{S}_+\right]\left(3\cos^2\theta - 1\right) \tag{1.23}$$

$$C = \frac{3}{2}\left[\hat{I}_z\hat{S}_+ + \hat{I}_+\hat{S}_z\right]\sin\theta\cos\theta e^{-i\phi} \tag{1.24}$$

$$D = \frac{3}{2}\left[\hat{I}_z\hat{S}_- + \hat{I}_-\hat{S}_z\right]\sin\theta\cos\theta e^{+i\phi} \tag{1.25}$$

$$E = \frac{3}{4}\left[\hat{I}_+\hat{S}_+\right]\sin^2\theta e^{-2i\phi} \tag{1.26}$$

$$F = \frac{3}{4}\left[\hat{I}_-\hat{S}_-\right]\sin^2\theta e^{+2i\phi} \tag{1.27}$$

where $\hat{I}_-$, $\hat{S}_-$ and $\hat{I}_+$, $\hat{S}_+$ are the lowering and raising operators respectively acting on spins I and S, r is the internuclear distance of the I and S, θ is the angle between the I-S internuclear vector and the magnetic field direction, ϕ is a polar angle which is defined in the following Figure 1.2.

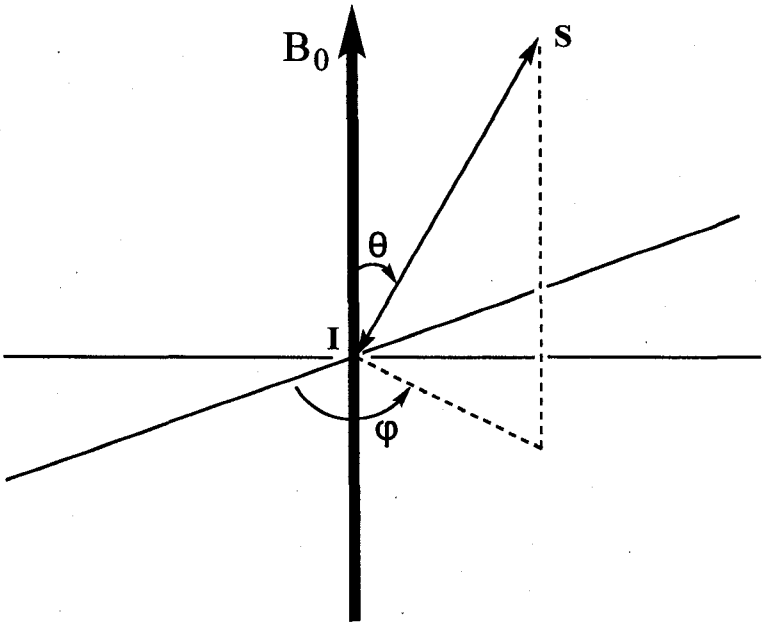

Figure 1.2 Orientation of dipole-dipole interaction in the PAS of the magnetic field.

1.2.5 Indirect Coupling Interaction (H_{SC})

High resolution NMR spectra of liquids reveal fine structure due to interactions between the nuclei. Ramsey and Purcell suggested that the interaction is mediated by the electrons forming the chemical bonds between the nuclei [6]. This interaction is known as spin-spin coupling or indirect coupling. The strength of the interaction is measured by the indirect coupling constant, $^nJ_{ab}$, in which n designates the number of covalent bonds separating the two nuclei, a and b. The Hamiltonian describing the spin-coupling interaction is:

$$\hat{H}_J = \hat{I}_a \cdot \hat{J}_{ab} \cdot \hat{I}_b \qquad (1.28)$$

Where $\hat{I}_a$ and $\hat{I}_b$ are the nuclear spins for the coupled nuclei and $\hat{J}_{ab}$ is the indirect spin-spin coupling tensor. The symmetric part of the spin-spin tensor can be separated into three terms, J_{11}, J_{22} and J_{33} in its principal axis system. Indirect coupling modifies the energy levels of the system, and the NMR spectrum is modified correspondingly. In solution NMR, we just see the isotropic value J_{iso}:

$$J_{iso} = \frac{1}{3}(J_{11} + J_{22} + J_{33}) \qquad (1.29)$$

The spin-coupling interaction is independent of field strength, with its values usually much smaller than those for the other interactions. In contrast to dipolar coupling, which is an interaction through space, indirect coupling is a through-bond interaction. In principle, one can measure both the anisotropy and asymmetry of J tensor in solid state NMR study. In practice, it is difficult to separate the dipolar coupling and indirect coupling interactions via experiment. The effective dipolar coupling constant, R_{eff}, is usually obtained.

$$R_{eff} = R - \Delta J/3 \qquad (1.30)$$

where $\Delta J = J_{\parallel} - J_{\perp}$, assuming that J is axially symmetric, with $J_{\parallel}$ designating the componet oriented along the internuclear vector and $J_{\perp}$ is the component which is perpendicular to the internuclear vector. Literature on the experimental and computational measurement of J by solid state NMR methods has been covered by several reviews [7, 8].

1.2.6 Quadrupolar Coupling (H_Q)

Quadrupolar nuclei are those nuclei with $I > 1/2$. The quadrupolar Hamiltonian, in the case where the interaction with the applied field B_0 outweighs the quadrupolar term, can be written in tensorial form as:

$$\hat{H}_Q = \frac{eQ}{6I(2I-1)\hbar}\hat{I}\cdot\vec{V}\cdot\hat{I} \qquad (1.31)$$

The electric field gradient is described by the tensor eq, and the electric field gradient tensor is traceless. Two parameters, the quadrupole coupling constant, QCC or χ, and the asymmetry parameter, η_Q, are defined from the principal values of the electric field gradient tensor in its principal axis frame, i.e. eq_{xx}, eq_{yy}, eq_{zz}:

$$\chi = \frac{e^2 q_{zz} Q}{h} \qquad (1.32)$$

$$\eta_Q = \frac{|eq_{xx}| - |eq_{yy}|}{|eq_{zz}|} \qquad (1.33)$$

where $|eq_{zz}| \geq |eq_{xx}| \geq |eq_{yy}|$ and $eq_{xx} + eq_{yy} + eq_{zz} = 0$.

Under static conditions the quadrupolar Hamiltonian can be expressed to first order perturbation theory in the applied field B_0 as [9]

$$\hat{H}_Q = \frac{3\chi h}{8I(2I-1)}\left(3\cos^2\theta - 1 + \frac{1}{2}\eta_Q \sin^2\theta\cos 2\varphi\right)\left(3\hat{I}_z^2 - \hat{I}^2\right) \qquad (1.34)$$

where θ and φ are the polar angles defining the orientation of the applied field B_0 in the principal axis frame of the electric field gradient tensor. This equation is suitable when the Larmor frequency is much larger than the quadrupole coupling constant. Figure 1.3 shows the orientation of B_0 in the PAS of the EFG tensor.

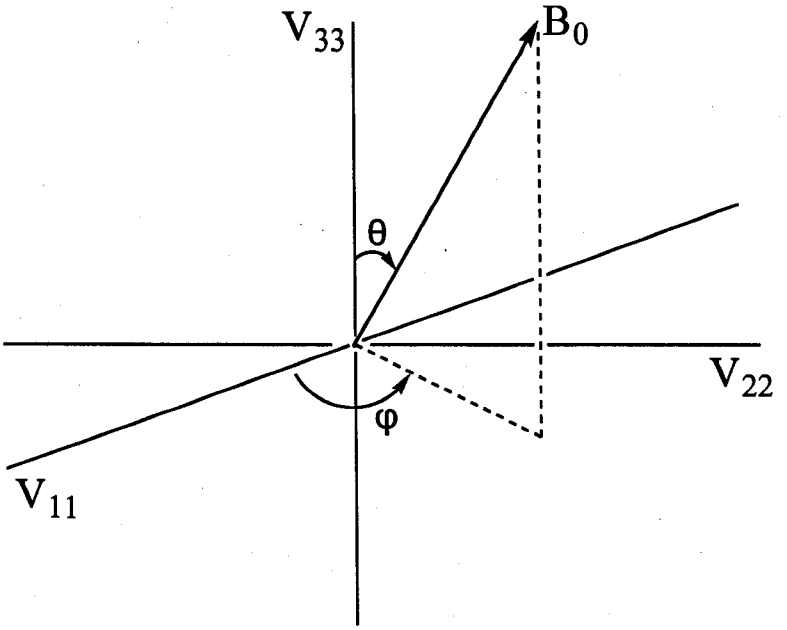

Figure 1.3 Orientation of B_0 in the PAS of the EFG tensor.

If the Zeeman interaction is the dominant term in the Hamiltonian for the spin system, the approximate energies of the spin system are found by using perturbation theory. The first- and second-order energy corrections to the energies of the Zeeman levels from quadrupole coupling by using perturbation theory are [9, 10]:

$$E_m^{(1)} = \frac{e^2qQ}{4I(2I-1)}\left(I(I+1)-3m^2\right)\left[\frac{1}{2}\left(3\cos^2\theta-1\right)+\eta_Q\cos 2\varphi\sin^2\theta\right] \qquad (1.35)$$

and

$$\begin{aligned} E_m^{(2)} = &-\left(\frac{e^2qQ}{4I(2I-1)}\right)^2\frac{m}{\omega_0}\left\{-\frac{1}{5}\left(I(I+1)-3m^2\right)\left(3+\eta_Q^2\right)\right. \\ &+\frac{1}{28}\left(8I(I+1)-12m^2-3\right)\left[\left(\eta_Q^2-3\right)\left(3\cos^2\theta-1\right)+6\eta_Q\sin^2\theta\cos 2\varphi\right] \\ &+\frac{1}{8}\left(18I(I+1)-34m^2-5\right)\left[\frac{1}{140}\left(18+\eta_Q^2\right)\left(35\cos^4\theta-30\cos^2\theta+3\right)\right. \\ &\left.\left.+\frac{3}{7}\eta_Q\sin^2\theta\left(7\cos^2\theta-1\right)\cos 2\phi+\frac{1}{4}\eta_Q^2\sin^4\theta\cos 4\varphi\right]\right\} \end{aligned} \qquad (1.36)$$

where m denotes the magnetic quantum number associated with the particular Zeeman level.

The second-order term depends inversely on the Larmor frequency; thus the value of this term decreases with increasing field strength. In other word, as B_0 is increased, this central transition lineshape which is affected by the second-order energy correction becomes narrower.

The central transition of half-integer quadrupolar nuclei is not broadened to first-order by quadrupole coupling. However, for large χ the satellite transitions are broadened by the first-order quadrupole coupling interaction. This first order broadening factor makes the satellite transitions largely unobservable in NMR experiments, because they are too far off resonance. The lack of first-order broadening on the central transition makes it significantly easier to observe than the satellites.

Mostly, interpretation of solid state NMR spectra of quadrupolar nuclei relies upon the high-field approximation, where the Larmor frequency is much greater than the quadrupolar frequency. Most reported quadrupolar coupling constants obtained with high-field solid state NMR techniques on diamagnetic solids are consistent with the high-field approximation [11].

The simulated powder spectra for a spin = 3/2 nucleus with QCC = 0.4 MHz, and different η_Q are shown in Figure 1. 4. This Figure shows both central transition and satellite transitions.

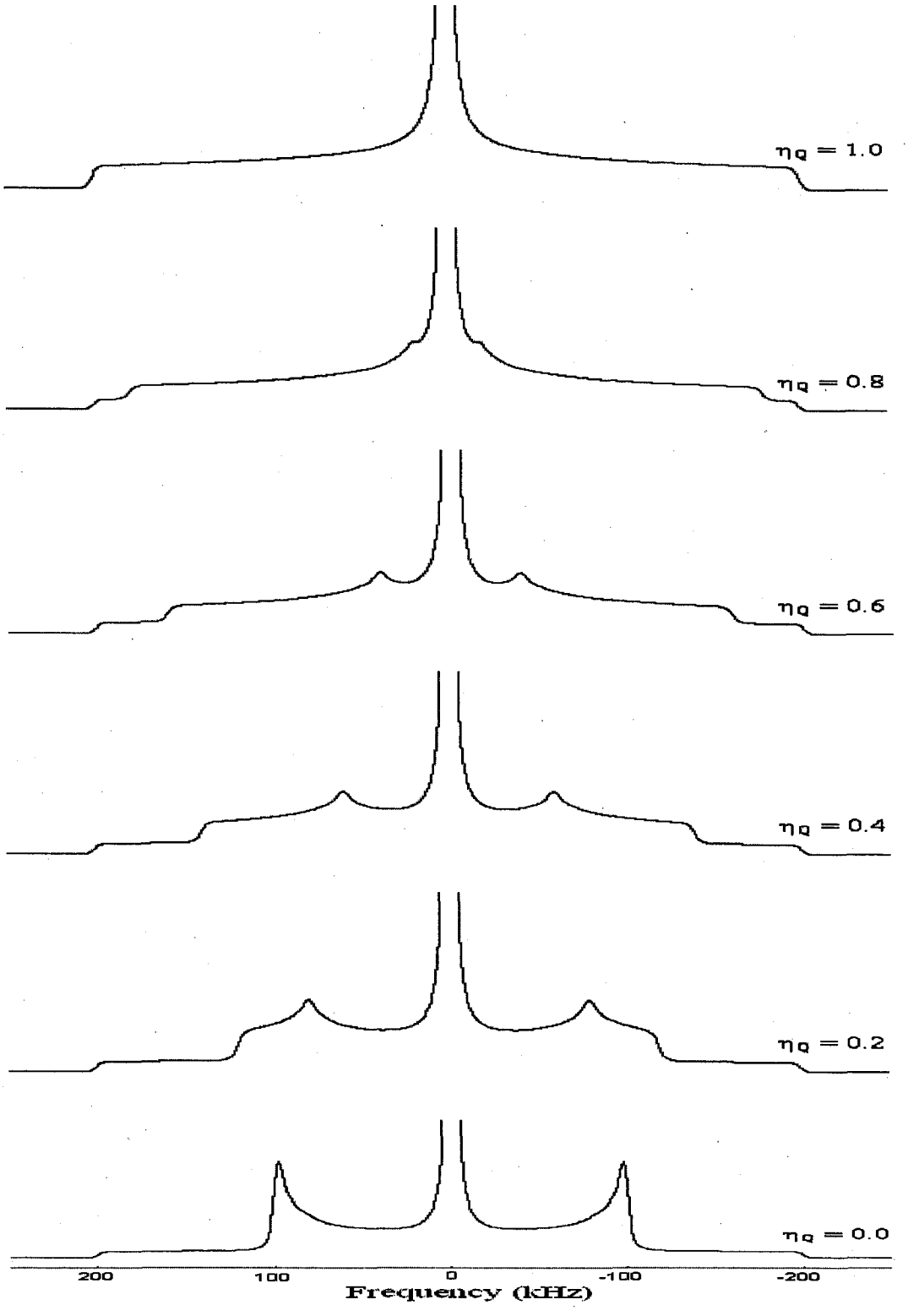

Figure 1.4 Simulated static solid state NMR spectra for I = 3/2 nuclei with QCC = 0.4 MHz and different values of η_Q. The central transition which is a simple isotropic Lorentzian line in these examples has been truncated in order to show the less intense satellite transition.

1.3 Essential Techniques for NMR of Spin-1/2 Nuclei

1.3.1 Magic Angle Spinning (MAS)

Magic-angle spinning (MAS) is used to remove both chemical shift anisotropy and heteronuclear dipolar coupling interactions which contribute to the large line-broadening in solid state NMR spectra. This technique, independently recognized by Lowe [12] and Andrew [13], is now used routinely for obtaining high-resolution NMR spectra in solids.

If the sample is spun about an axis inclined at an angle θ_R to the applied field (see Figure 1.5), then θ, the angle describing the orientation of the interaction tensor fixed in a molecule within the sample, varies with time as the molecule rotates with the sample. The average of $(3\cos^2\theta\text{-}1)$ in these circumstances can be shown to be

$$\left\langle 3\cos^2\theta - 1\right\rangle = \frac{1}{2}\left(3\cos^2\theta_R - 1\right)\left(3\cos^2\beta - 1\right) \qquad (1.37)$$

The angle β is between the principal z-axis of the shielding tensor and the spinning axis; θ_R is the angle between the applied field and the spinning axis; θ is the angle between the principal z-axis of the interaction tensor and the applied field B_0. If θ_R is set to 54.74°, then $\left\langle 3\cos^2\theta - 1\right\rangle = 0$. Therefore, provided that the spinning rate is fast enough, the interaction anisotropy averages to zero. See Figure 1.5.

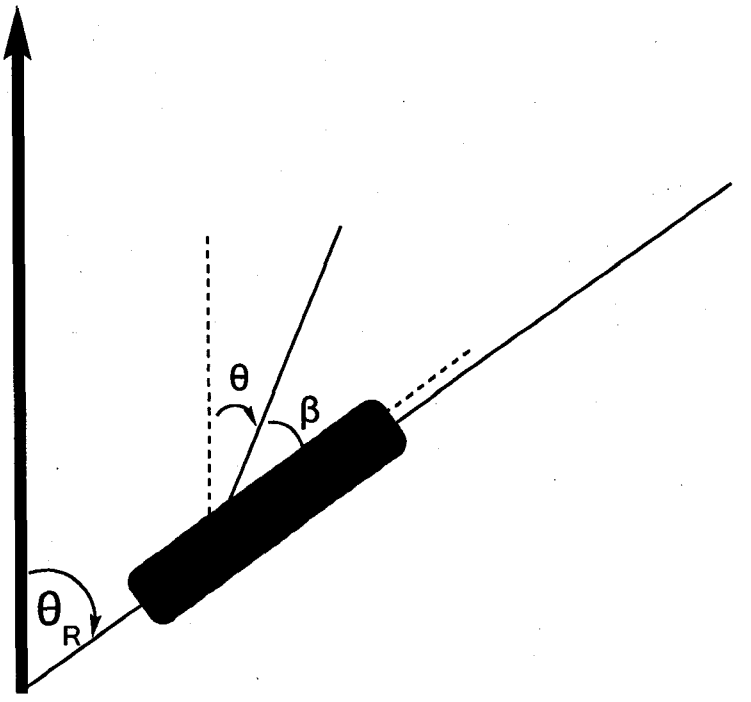

Figure 1.5 Schematic of the magic angle spinning experiment.

In order for magic-angle spinning to reduce a powder pattern to a single line at the isotropic chemical shift, the rate of the sample spinning must be fast in comparison to the anisotropy of the interaction being modulated. 'Fast' in this context means approximately a factor of at least three times greater than the anisotropy.

Slower spinning produces a set of spinning sidebands in addition to the line at the isotropic chemical shift. The spinning sidebands are sharp lines, set at the spinning frequency apart and radiate out from the line at the isotropic chemical shift. Spinning sidebands are very useful because they contain information on the anisotropic interaction of the nucleus.

Sharp chemical-shift sidebands occur because the chemical-shift Hamiltonian commutes with itself at different orientations so that the chemical-shift anisotropy is averaged out after each full rotor period [14]. As a result, the anisotropic component of the time signal is periodic with the rotor period t_r, and spectral intensity appears at the 'harmonics'

$n\cdot(2\pi/ t_r) = n\cdot\omega_r$. One good example of spinning sidebands is shown in Figure 1.6.

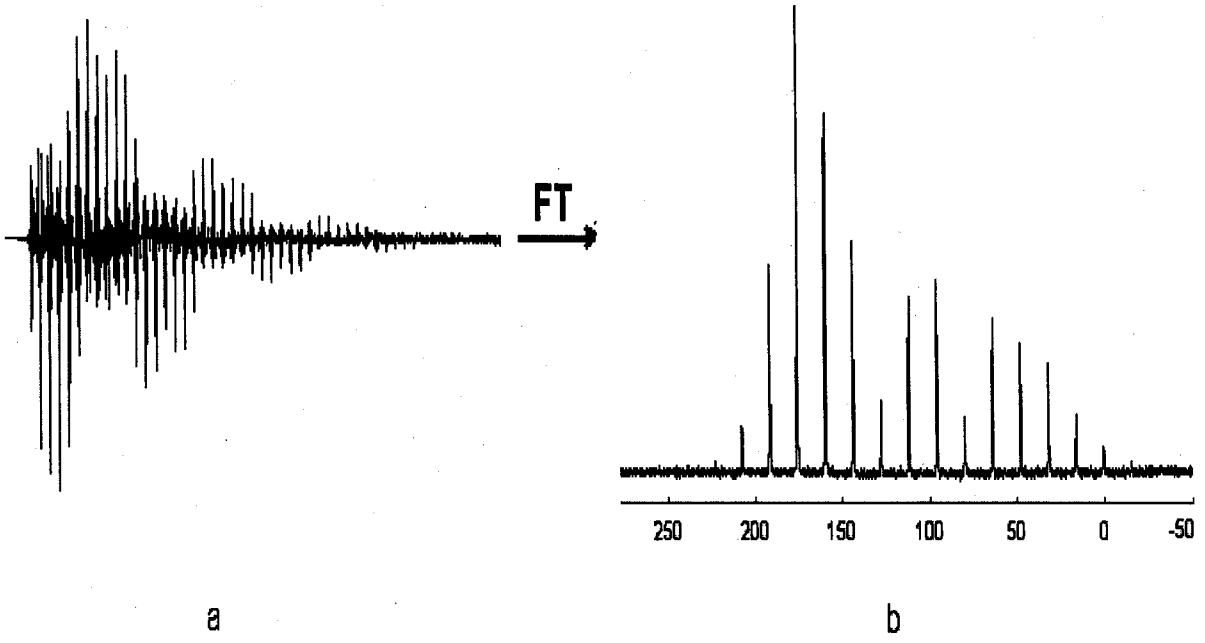

Figure 1.6 ^{13}C Magic angle spinning FID and spectrum of $C_6H_6\cdot AgClO4$. (a) Time domain signal with rotational echoes at multiples of t_R . (b) Corresponding spectrum with spinning sidebands at multiples of $\nu_R = 1/ t_R = 2000$ Hz.

In principle, MAS can remove the effects of first-order quadrupolar linebroadening completely. In practice, this would require spinning rates that are much faster than the quadrupolar powder pattern width. Such spinning speeds are unlikely to be achievable for most cases. For example at achievable spinning speeds, a typical ^2H powder pattern (QCC = 180 kHz) breaks into a series of sharp spinning sidebands.

MAS can narrow the central transition lineshape of half-integer quadrupolar nuclei; however, complete removal of the anisotropic quadrupolar effects by this technique is not possible. Equation 1.36 clearly shows that the second order perturbation of quadrupolar Hamiltonian is not averaged to zero when θ is at the magic angle. Figure 1.7 shows the effect of MAS on central transitions of half-integer spins for different asymmetry parameters.

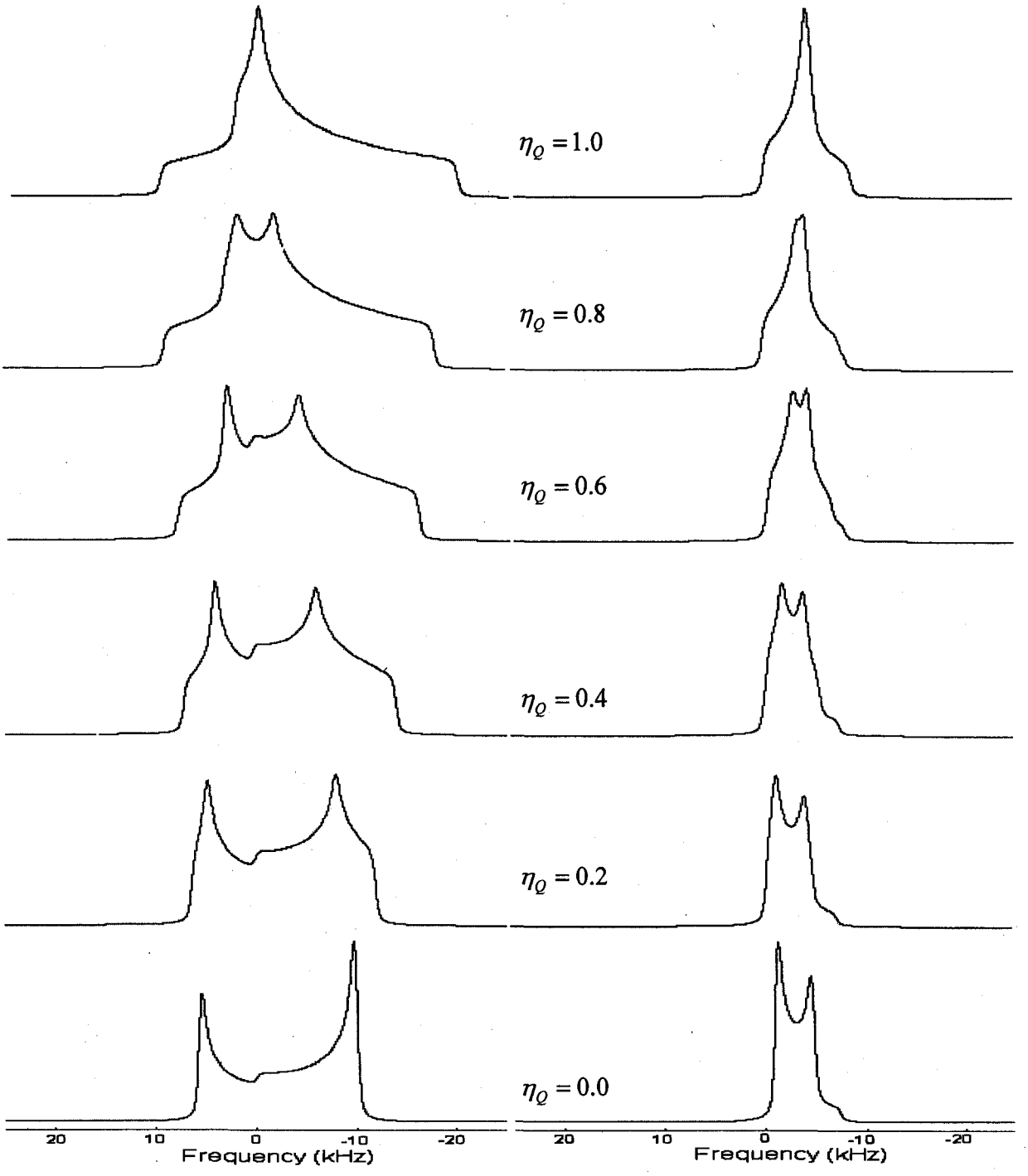

Figure 1.7 Static (left) and MAS (right) spectra show the effects of magic-angle spinning on the central lineshape for a half-integer quadrupolar nucleus (spin = 3/2, QCC = 3.2 MHz, ν_0 = 85.636 MHz).

1.3.2 High Power Decoupling (HPDEC)

High power decoupling consists of applying a continuous irradiation of very high power (100-1000 watts) at the resonance frequency of nucleus (or nuclei) to be decoupled (usually proton).

This technique is often used in combination with MAS, allowing one to obtain high resolution spectra. An improved technique on standard continue-wave (CW) decoupling is known as two-pulse phase-modulated (TPPM) [15] decoupling, which improves both the resolution and sensitivity of the dilute-spin spectrum. This pulse sequence consists of a series of pulses of alternating phase.

Furthermore, the decoupling efficiency is improved by incorporating the TPPM scheme into a supercycle called SPARC-16, which is an abbreviation for small phase angle rapid cycling with 16 steps. This method is called SPINAL-64 [16], an acronym for small phase incremental alternation, with 64 steps. SPINAL-64 was used for high power decoupling in this work.

1.3.3 Cross Polarization (CP)

Although heteronuclear dipolar coupling can be a drawback, as it can prevent one from obtaining a high resolution NMR spectrum, it can also be an advantage. The dipolar interaction can be manipulated to provide an enhancement in signal-to-noise via the polarization transfer technique.

In such an experiment, the polarization of abundant nuclei, I, can be transferred to dilute nuclei, X, during a contact time (Figure 1.8).

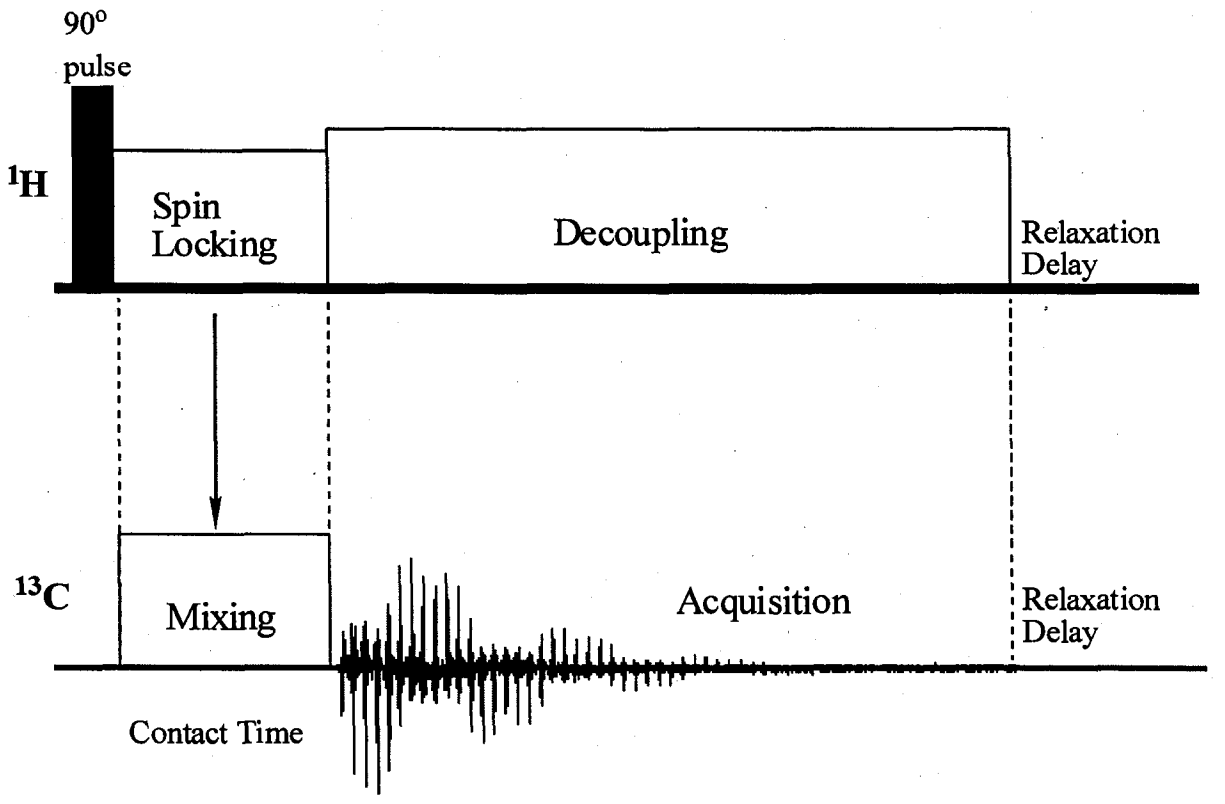

Figure 1.8 The Cross-polarization pulse sequence.

The amplitudes of the two contact pulses in the cross-polarization experiment have to be carefully set so as to achieve the Hartmann-Hahn matching condition [4]:

$$\gamma_I B_{1I} = \gamma_X B_{1X} \qquad (1.38)$$

The cross-polarization technique has a twofold advantage: First, it enhances the signal-to-noise ratio by a theoretical factor of γ_I/γ_X, greatly improving the sensitivity of the dilute nuclei. Secondly, the experimental delay time is determined by T_{1I}, which means that with CP one can obtain a multiscan spectrum in the time it takes to obtain a single pulse spectrum without CP, and thus greatly improves the signal-to-noise in a given time (T_{1I} is usually much less than the T_{1X}).

The combination of cross-polarization, MAS and high power decoupling is the routine technique for solid state high resolution NMR of dilute nuclei. This experiment is known as the CP/MAS experiment.

1.3.4 The Spin-echo

In solid state NMR, rapidly decaying magnetization arising from chemical shift anisotropy, dipolar coupling, quadrupolar coupling, etc., can cause the loss of a significant part of the FID due to a finite probe dead time. This problem is overcome by use of the Hahn-echo pulse sequence [17] for lines broadened by chemical shift anisotropy or heteronuclear dipole-dipole coupling:

$$90^{o}_{x} - \tau - 180^{o}_{y} - \tau - acquire$$

and the solid or quadrupole-echo pulse sequence [18] (Figure 1.9):

$$90^{o}_{x} - \tau_1 - 90^{o}_{y} - \tau_2 - acquire$$

for lines broadened by quadrupole coupling or homonuclear dipole-dipole coupling.

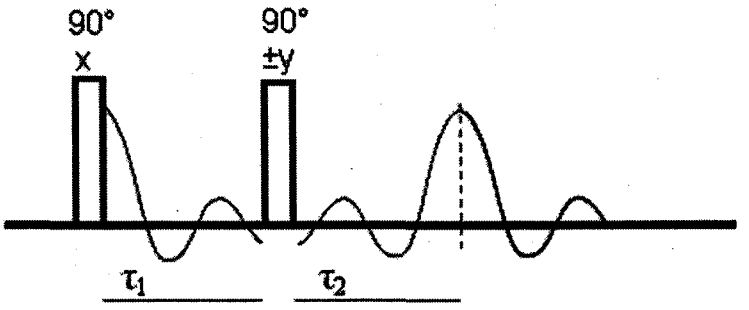

Figure1.9 Solid-echo pulse sequence.

Using the quadrupolar echo pulse sequences, acquisition of the FID signal begins at time τ_2 after the last pulse, and hence, no signal is lost due to a dead time delay. Therefore the

distortion due to dead time is avoided. It is very important to know that two potentially important sources of spectral distortion are possible in quadrupolar echo experiments [19]. Firstly, transverse relaxation occurring in the time, τ, between the pulses should be negligible; otherwise short transverse relaxation time causes the spectral distortion. Secondly, the phase of second pulse can not be adjusted to compensate the errors introduced by different chemical shifts during the evolution time. But this distortion can be avoided by interleaving 180° pulses in the sequence at appropriate times [20].

Chapter 1: References

[1] F. Bloch, W. M. Hansen, M. Packard, *Phy. Rev.*, 69 (1946) 127.

[2] E. M. Purcell, H. C. Torrey, R. V. Pound, *Phys. Rev.*, 69 (1946) 37.

[3] R. R. Ernst, W. A. Anderson, *Rev. Sci. Instrum.*, 37 (1966) 93.

[4] S. R. Hartmann, and E. L. Hahn, *Phys. Rev.*, 128 (1962) 2042.

[5] M. J. Duer, " *Solid-State NMR Spectroscopy- principles and applications*", (2002), Blackwell Science Ltd., Oxford, England.

[6] N. F. Ramsey, E. M. Purcell, *Phys. Rev.*, 85 (1952) 143.

[7] W. P. Power, R. E. Wasylishen, *Anuu. Rep. Nucl. Magn. Reson. Spectrosc.*, 23 (1991) 1.

[8] J. Vaara, J. Jokisaari, R. E. Wasylishen and D. L. Bryce, *Progress in NMR Spectroscopy*, 41 (2002) 233.

[9] A. Abragam, "*The Principles of Nuclear Magnetism*", Clarendon Press, Oxford (1983), Ch. VII. [10] M. H. Cohen and F. Reif, *Solid-State Physics*, 5 (1957) 321.

[10] C. P. Slichter, "*Principles of Magnetic Resonance*", Springer-Verlag, Berlin (1990).

[11] D. L. Bryce, and G. D. Sward, *Magn. Reson. Chem.*, 44 (2006) 409.

[12] I. J. Lowe, *Phys. Rev. Lett.*, 2 (1959) 285.

[13] E. R. Andrew, A. Bradbury, and R. G. Eades, *Nature*, 182 (1958) 1659.

[14] M. M. Maricq, J. S. Waugh, *J. Chem. Phys.*, 70 (1979) 3300.

[15] A. E. Bennett, C. M. Rienstra, M. Auger, K. V. Lakshmi, and R. G. Griffin, *J. Chem. Phys.*, 103 (1995) 6951.

[16] Y. Yu, and B. M. Fung, *J. Magn. Reson.*, 130 (1998) 317.

[17] E. L. Hahn, *Phys. Rev.*, 80 (1950) 580.

[18] J. H. Davis, K. R. Jeffrey, M. Bloom, M. I. Valic, and T. P. Higgs, *Chem. Phys. Lett.*, 42 (1976) 390.

[19] G. L. Hoatson, R. L. Vold, *Solid State NMR III, Organic Matter*, Springer-Verlag, (1994) 1.

[20] G. L. Haotson, K. J. Hewitt, *Mol. Phys.*, 40 (1980) 1153.

Chapter II

Brief Review of Solid State ^{109}Ag NMR Spectroscopy

2. 1 Introduction to Low- γ Nuclei

A convenient definition of "low-γ" is taken from the frequency ranges of magic-angle spinning (MAS) NMR probes provided by the major manufacturers. Standard MAS NMR probes normally tune down to the resonance frequency of ^{15}N. Low-γ nuclei are therefore taken as those that resonate at frequencies below that of ^{15}N. The lower end is truncated at, or above a resonant frequency about 5-10 MHz, since most commercial spectrometers will not operate below this frequency. The nuclei that satisfy this definition, along with some of their relevant properties, are listed in Table 2. 1.

Table 2. 1 NMR properties of some low-γ nuclei [1]

Isotope	spin	Natural abundance (A) (%)	ν_0 at 11.7 T	Relative receptivity[b]	Quadrupole moment (fm^2)[7]	Quadrupole broadening factor[c]
^{57}Fe	1/2	2.19	16.19	4.2×10^{-3}		
^{89}Y	1/2	100	24.585	0.696		
^{103}Rh	1/2	100	15.862	0.180		
^{107}Ag	1/2	51.82	20.239	0.197		
^{109}Ag	1/2	48.18	23.268	0.279		
^{169}Tm	1/2	100	41.35	3.216		
^{183}W	1/2	14.40	20.809	0.061		
^{14}N	1	99.63	36.14	2.841	2.02	N.A.
^{25}Mg	5/2	10.13	30.63	0.397	19.94	8.60
^{33}S	3/2	0.76	38.405	0.040	-6.78	3.30
^{35}Cl	3/2	75.53	49.045	8.091	-8.17	3.75
^{37}Cl	3/2	24.47	40.825	1.514	-6.44	2.80
^{39}K	3/2	93.10	23.36	1.079	6.01	4.27
^{43}Ca	7/2	0.14	33.69	9.1×10^{-3}	-4.08	0.139
^{47}Ti	5/2	7.28	28.23	0.224	29	19.73
^{49}Ti	7/2	5.51	28.24	0.225	24	5.74
^{53}Cr	3/2	9.55	28.255	0.196	-15	21.9
^{61}Ni	3/2	1.19	44.745	0.092	16.2	16.18
^{67}Zn	5/2	4.11	31.34	0.173	15.0	4.76
^{73}Ge	9/2	7.76	17.49	0.095	-17.3	2.62
^{83}Kr	9/2	11.55	19.3	0.188	25.3	5.08
^{85}Rb	5/2	72.15	48.425	11.177	27.4	10.27
^{87}Sr	9/2	7.02	21.745	0.164	33.5	7.91
^{91}Zr	5/2	11.23	46.649	1.549	-20.6	6.02
^{95}Mo	5/2	15.72	32.71	0.751	-2.2	0.98
^{97}Mo	5/2	9.46	33.395	0.481	25.5	12.88
^{99}Ru	5/2	12.72	23.07	0.213	7.9	1.80
^{101}Ru	5/2	17.07	25.855	0.402	45.7	53.75
^{105}Pd	5/2	22.23	23.00	0.368	66.0	125.5
^{131}Xe	3/2	21.18	41.225	1.350	-12.0	9.62
^{135}Ba	3/2	6.59	49.92	0.746	16.0	14.12
^{177}Hf	7/2	18.50	20.21	0.278	336	1566
^{189}Os	3/2	16.10	39.18	0.880	85.6	513.3
^{201}Hg	3/2	13.22	33.225	0.441	38.6	122.9

Isotopes are listed according to atomic number.

[a] Adapted from reference 1, table 1.

[b] Relative receptivity: the receptivity given by $\gamma^3 AI(I+1)$ relative to ^{13}C adjusted for quadrupolar nuclei by the fractional contribution of the central transition.

[c] Quadrupole broadening factor: the second-order quadrupolar broadening of the central transition which is proportional to $\frac{\chi^2(I(I+1)-\frac{3}{4})^2}{\gamma(2I(2I-1))^2}$ and has been normalized to ^{27}Al.

How does γ affect the NMR spectrum? First, at a fixed field the net magnetization of the sample contributed from the fraction of nuclei is proportional to γ, according to Boltzmann distribution. Second, the net magnetization is proportional to this fraction multiplied by the magnetic moment, which is also proportional to γ. These two conclusions can be directly obtained from the equations in section 1.2.2. Thirdly, the NMR signal is proportional to γ, according to Faraday's law of electromagnetic induction by the rate of procession of this total magnetization in the NMR coil. Hence the intrinsic sensitivity per spin is proportional to γ^3, and thus when γ is low the sensitivity is low.

For half integer spin quadrupolar nuclei, the satellite transitions experience first-order broadening, but the central (1/2, -1/2) transition only experiences quadrupolar broadening to second order. The second-order broadening is inversely proportional to ν_0, which means that in the high-field limit ($\nu_Q \ll \nu_0$) the central transition is much narrower than the satellite transitions. Because this broadening scales inversely with the Larmor frequency (ν_0), lower frequency spectra have broader powder patterns when compared to higher frequency spectra, which adds to the problems of sensitivity. Common ways of circumventing such difficulties include running NMR experiments at ultrahigh magnetic field strengths, at very low temperatures, employing isotopic labeling and /or choosing special pulse sequences.

Firstly, ultrahigh magnetic field strengths can narrow the broadening of the central transition and increase the sensitivity. Secondly, low temperatures can increase the population difference for energy levels determined by the Boltzmann distribution, hence enhance the S/N ratio. The noise generated by the coil which is proportional to the square root of temperature, therefore low temperatures can decrease the noise, in other words, increase the S/N ratio. Thirdly, employing isotopic labeling can also increase net

magnetization of the sample if natural abundance is low. Finally, choosing special pulse sequences such as QCPMG can enhance the signal intensity.

When the relaxation needs to be taken into account the situation is even worse. Although the relaxation strongly depends on the various interactions experienced by the nucleus, all other things being equal, smaller magnetic moments usually lead to less efficient relaxation for low-γ spin-1/2 nuclei, e.g., low- γ values yield small dipolar coupling interactions, greatly lengthening the experimental time needed to acquire an adequate signal-to-noise (S/N).

Low- γ values yield small dipolar coupling interactions, and thus, in cross polarization experiments the X-channel of the spectrometer and probe must sustain rather high power levels and very long contact times in order to match the CP condition with reasonably short 90° pulses.

2.2 Experimental Approaches for Low- γ Nuclei

One of the key factors in making low-γ nuclei more accessible is improving their sensitivity. The most direct way is by the application of ever higher magnetic fields. The basic sensitivity increases as $B_0^{7/4}$ for spin-1/2 nuclei. The situation is even better for non-integer spin quadrupole nuclei because of the additional narrowing of the second-order quadrupole broadening so that the sensitivity of the experiment increases as $B_0^{11/4}$ [2].

The most common experiment in FT NMR is the application of a single pulse followed by acquisition of the free induction decay (FID) [3]. This is certainly the most direct way of performing an FT NMR experiment; but there are many potential pitfalls. Those are

particularly relevant to low-γ nuclei relative to effects that corrupt the start of the FID. These effects can be divided into two groups, viz. dead time and probe ringing.

Deadtime refers generally to all effects that result in the spectrometer being unable to accurately record the NMR signal. It is usual to split these effects into those from the probe [4] and those from other electronic parts of the spectrometer (e.g., filters). The probe deadtime can be readily understood: voltage associated with the nominally square pulse envelope of the B_1 field cannot drop instantaneously to zero at its end because of the time constant of the probe circuit. The strength of the rotating B_1 field is [5, 6]

$$B_1 \cong 3\left(P Q / V \nu_0\right)^{1/2} \cong 3.7\left(P T_R / V\right)^{1/2} \tag{2.1}$$

where P is the transmitter power , Q is the quality factor, ν_0 is the Larmor frequency, V is the volume of the coil, and T_R is the ringdown time of the coil which is included in dead time. The Q and T_R are given by:

$$Q = 2\pi\nu_0 L / R \tag{2.2}$$

$$T_R \propto Q / \nu_0 \tag{2.3}$$

where L is the coil inductance, and R is the coil resistance. The ringdown time becomes worse at lower frequencies, because a low ν_0 usually implies a long T_R. Long ringdown times and thereby long dead time may cause significant problems in the observing lower frequency nuclei.

Ringing is often used as an all-embracing term that describes effects that induce a voltage in the coil that is not an NMR signal. One source can be attributed to electromagnetic effects of the pulse interacting with the surroundings (e.g., the probe body) so that either mechanical and/or reradiation effects occur. An obvious source of mechanical ringing is the

force exerted on the wire in the very high magnetic field as the time-varying current of the pulse is present. This can cause acousto-mechanical effects in the coil that continue for some time after the pulse turned off and produces a short lived pseudo-FID.

Both of these effects can be reduced by careful probe design, such as the coil orientation, and construction of the probe body. Much research has gone into reducing these effects and has been reviewed by Gerothanassis, [7] where extensive referencing of the primary literature is given.

A common way to overcome deadtime/ringing problems for quadrupolar nuclei is to form a signal with an effective time zero point outside the deadtime, i.e. an echo. There are a multitude of methods for forming echoes [8, 9]. The rotation produced by the second pulse in the two –pulse echo experiments is not critical. In practice, the best choice is the second pulse of twice the length of the first, with the actual length being a trade-off between sensitivity and uniformity of the irradiation. Thus, for low-γ nuclei the use of short pulses that correspond to significant pulse angles, so as to produce significant sensitivity, means that a high power transmitter is necessary. There is also a trade-off in the size of coil, with smaller coils producing higher B_1 fields, and hence better lineshapes from the shorter pulses that can consequently be applied. However, there is a loss of sensitivity because of the smaller sample. In recording echoes there is an important practical consideration- applying the echo moves the effective $t = 0$ position for the FID outside the region where it is corrupted. To prevent phasing problems from re-emerging, the data sampling rate used should be sufficient to allow this point to be accurately defined. If T_2 is sufficiently short that an echo time can be used that the whole echo (both before and after the maximum) to be accurately recorded without an unacceptably large loss of intensity, there is no need to

accurately define the new t=0 position. Fourier transformation of the whole echo (which effectively amounts to integration between $\pm\infty$) followed by magnitude calculation removes phasing errors, producing a pure absorption lineshape with the signal-to-noise $\sqrt{2}$ times larger than that obtained by transforming from the echo maximum.

The principle of most pulse sequences is that signal and artifacts show differing coherence with the pulse, so that, with a suitable combination of pulses and phase cycling, artifacts cancel. Piezoelectronic properties of the sample can also produce ringing effects. Often, changing the physical state of the sample, e.g., going from a single crystal or a coarse powder to a fine powder, can help considerably. Again, echo experiments are usually used and the detailed calculation of echo formation to cancel out piezoelectric effects has been presented. [10]

The most common solid state NMR approach is magic angle spinning (MAS). For higher-γ nuclei the trend in recent years has been to employ ever faster spinning by using smaller diameter rotors. This is especially true for quadrupolar nuclei. As noted above, the second-order quadrupolar broadening is usually worse for nuclei with smaller magnetic moments, so that fast spinning would seem attractive. However, the ability to narrow a wider range of lines by spinning faster is usually more than outweighed by the reduction in S/N from using a smaller sample, so that a compromise often needs to be reached. Since dead time/ringing effects can be significant at the lower frequencies used, it is usual to acquire the MAS FID using an echo. The echo spacing is then set to an integral multiple of the period of the MAS rotation. There are of course many other solid state NMR approaches that have been developed, especially for quadrupolar nuclei, and there is no reason in principle why these cannot be used for low-γ nuclei.

Cross-polarization (CP) is a very important technique to improve the NMR sensitivity of low-γ nuclei. First, the cross-polarization method can transfer magnetization from abundant nuclei (usually ^{1}H) to low-γ nuclei, yields a more intense NMR signal. The potential enhancement of the signal is proportional to the ratio γ_H/γ_X. Second, the recycle time of the experiment is governed by the relaxation time of the abundant nucleus (^{1}H), which is usually shorter than that of the observed nucleus, which means that the rapid signal accumulation due to shorter recycling time increases the S/N ratio in a given time. In addition, MAS and heteronuclear decoupling increase the signal intensities by suppressing the line broadening due to dipolar couplings and chemical shift anisotropies. Therefore a combination of CP, MAS and heteronuclear decoupling methods is an excellent way to obtain high quality NMR spectra of low-γ nuclei.

There is also an important hardware consideration in that, to achieve CP, the Hartmann-Hahn match condition $\gamma_H B_{1H} = \gamma_X B_{1X}$ must be met. As B_1 is the RF field generated by the pulse at the respective Larmor frequencies for the two nuclei, this means that the power on the X-side has to be high for low-γ nuclei. This puts significant strain on the probe and the preamplifier electronics. The first examples of ^{109}Ag CP/MAS spectroscopy were reported by Merwin and Sebald [11].

The quadrupolar Carr-Purcell Meiboom-Gill (QCPMG) sequence [12] was used as a means to enhance the S/N ratio in the NMR experiment of half-integer quadrupolar nuclei. A combination of CP and spikelet echo pulse sequences (QCPMG) method can effectively enhance the sensitivity. This method is very useful for samples with long spin-lattice relaxation times, unusual spinning speed-dependent CP behavior, low natural abundance, low –γ value, or a combination of these factors. The following discussion is about the advantages

of the CP/CPMG method. First, the CP method can effectively shorten the recycling time which means that the recycling time is not determined by the long spin-lattice relaxation of the low –γ nuclei. Second, the QCPMG or CPMG experiment is very useful for obtaining high S/N spectra of stationary samples. If the samples are difficult to spin, damaged by spinning, or undergo structure and/ or phase changes as a result of small temperature variation. The QCPMG or CPMG experiment is a good choice to circumvent those troubles. Because high spinning speed can attenuate the magnetization transfer in CP experiment, which can be a serious problem in CP/MAS experiments, the combination of CP method with CPMG sequence can be a good substitute tool to the NMR study of low γ spin-1/2 nuclei. Thirdly, the CPMG sequence can effectively enhance the sensitivities; hence this technique is advantageous to obtain the spectra of the nuclei with low natural abundance or low γ value or a combination of these two factors.

2.3 Solid State NMR Studies of Silver-109

Solid-state NMR studies of silver would be helpful in understanding areas from fast ion conducting glasses to organometallic complexes of biological significance. All naturally occurring silver is found in two isotopes, ^{107}Ag and ^{109}Ag. Both of these isotopes also happen to be magnetically active. Due to a factor of 1.4 higher receptivity of ^{109}Ag over ^{107}Ag, ^{109}Ag is the favored isotope for the NMR spectroscopist. Unless otherwise noted, all references to silver NMR are to the ^{109}Ag isotope. In keeping with being a heavy metal, silver shows a significant chemical shift range (~1000 ppm) making it a sensitive probe of chemical inequivalence.

In materials where T_1 is long and there are protons available from magnetization transfer, CP is advantageous. A characteristic of most silver CP experiments is the long contact times typically used, ranging from 10 to over 100 ms. To date it appears that all CP has been performed using 7 mm or larger MAS rotors with spinning speeds typically in the range 2-5 kHz. Another problem with CP/MAS of low-γ nuclei is the reduction in signal as the rate of sample spinning is increased. This is due to the interference that occurs between the sample spinning and the dipolar mediated cross polarization, which is particularly acute at higher spinning rates [13]. Fig. 4 shows the ^{109}Ag signal intensity for a sample of $AgSO_3CH_3$ as a function of spinning rate.

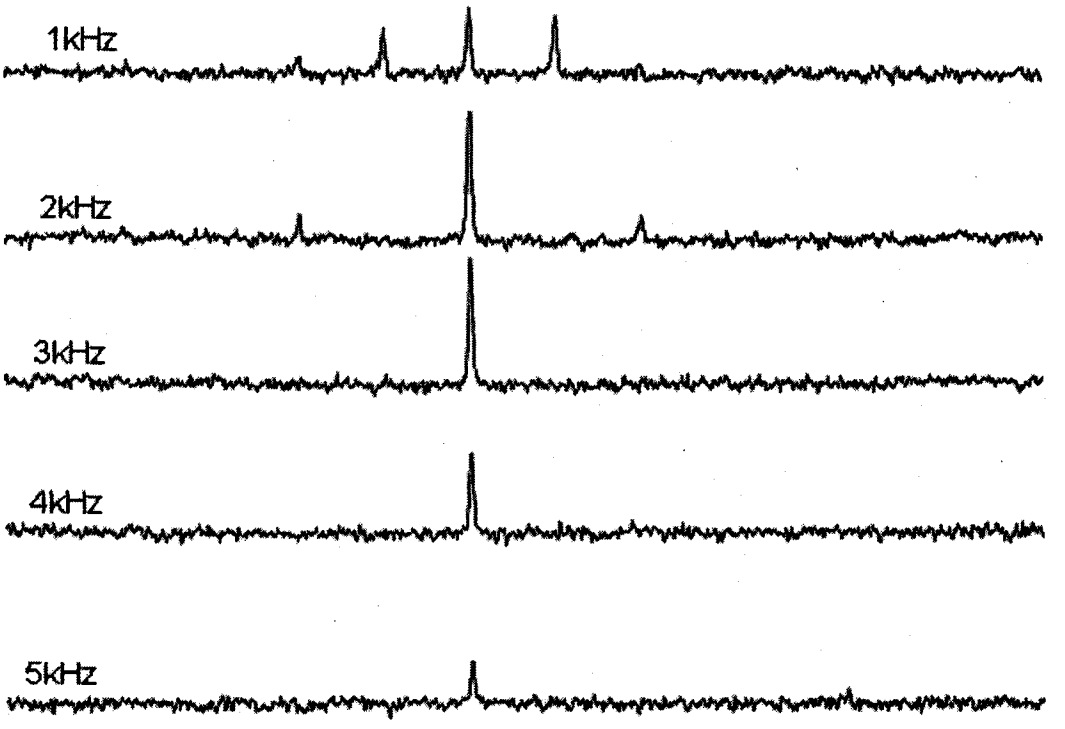

Figure 2.1 ^{109}Ag CP/MAS spectrum of $AgCH_3SO_3$ (8 scans) at 23.3 MHz and sample rotation rate at 1 kHz, 2 kHz, 3 kHz, 4 kHz and 5 kHz. With permission from the authors

For samples such as $AgSO_3CH_3$ where the span of the chemical shift tensor is relatively small, slow spinning is not a problem. However, system with large spans present a dilemma in that fast MAS concentrates the signal into the center band but also reduces the efficiency of the cross polarization.

The most recent review of solid state ^{109}Ag NMR study was written in 2006 by Penner and Liu [14]. In that review, almost all of reported solid state ^{109}Ag NMR studies before 2006 were summarized. Schurko and his co-workers showed that the CP/CPMG method can also be used to obtain high intensity ^{109}Ag spectra in their article [15].

Chapter 2: References

[1] M. E. Smith, E. R. H. van Eck, *Progr. NMR Spectrosc.*, 34 (1999) 159.

[2] R. K. Harris, "*Nuclear Magnetic Resonance Spectroscopy*", Longman, Harlow, (1986).

[3] K. Schmidt-Rohr, and H. W. Spiess, "*Multidimentional Solid-State NMR and Polymer*", (1994), Academic Press Limited, San Diego, CA, USA.

[4] E. Fukushima, S. B. W. Roeder, *J. Magn. Reson.*, 333 (1979) 199.

[5] W. G. Clark and J. A. McNeil, *Rev. Sci. Instrum.*, 44 (1973) 844.

[6] E. Fukushima and S. B. W. Roeder, "*Experimental Pulse NMR-A nuts and bolts approach* ", Addison-Wesley Publishing Company, Inc. (1981).

[7] P. I. Gerothanassis, *Prog. NMR Spectrosc.*, 19 (1987) 267.

[8] E. L. Hahn, *Phys. Rev.*, 80 (1950) 580.

[9] J. H. Davis, K. R. Jeffrey, M. Bloom, M. I. Valic, and T. P. Higgs, *Chem. Phys. Lett.*, 42 (1976) 390.

[10] P. P. Man, *Solid State NMR*, 1 (1992) 149.

[11] L. H. Merwin, and A. Sebald, *J. Magn. Reson.*, 97 (1992) 628.

[12] F. H. Larsen, H. J. Jakobson, P. D. Ellis, and N. C. Nielsen, *J. Phys. Chem.* A, 101 (1997) 8597.

[13] E. O. Stejskal, J. Schaefer, *J. Magn. Reson.*, 28 (1977) 105.

[14] G. H. Penner and X. Liu, *Progr. NMR Spectrosc.*, 49 (2006) 151.

[15] I. Hung, A. J. Rossini, and R. W. Schurko, *J. Phys. Chem.* A, 108 (2004) 7112.

Chapter III

Relaxation Time and Lineshape Analysis of ^{2}H NMR Spectra

3.1 Introduction

The general theory of quadrupolar nuclei is discussed in the section 1.2.7. In the case of ^{2}H, the high-field approximation, e.g. the Zeeman interaction is much bigger than the quadrupolar interaction, is valid. The energy shifts due to the quadrupolar interaction for the single nucleus with an axial symmetric electronic field gradient may be obtained from perturbation theory as:

$$E_m = \frac{1}{8}\left(\frac{e^2qQ}{h}\right)\left(2-3m^2\right)\left(3\cos^2\theta - 1\right) \qquad (3.1)$$

where θ is the angle between the largest principal component of the electronic field gradient tensor and the magnetic field, m is equal to -1, 0, or 1. The energy level diagram for the combined Zeeman and quadrupolar interaction for a spin = 1 nucleus is given in Figure 3.1.

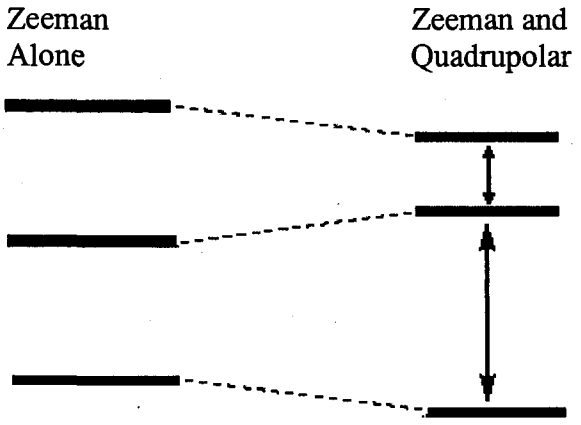

Figure 3.1 Schematic representations of the energy levels of a spin = 1 nucleus resulting from the Zeeman interaction and the Zeeman and quadrupolar interaction in a magnetic field.

The allowed transitions are $\Delta m = \pm 1$ and the spectrum for a spin 1 nucleus with an axially symmetric electric field gradient consists of a doublet with a peak separation given by:

$$\Delta\nu = \frac{3}{4}\left(\frac{e^2qQ}{h}\right)\left(3\cos^2\theta - 1\right) \qquad (3.2)$$

where $\Delta\nu$ is the separation in frequency units.

For a polycrystalline material, equation 3.2 must be averaged over all possible crystal orientations, yielding a spectrum like that shown in Figure 3.2.

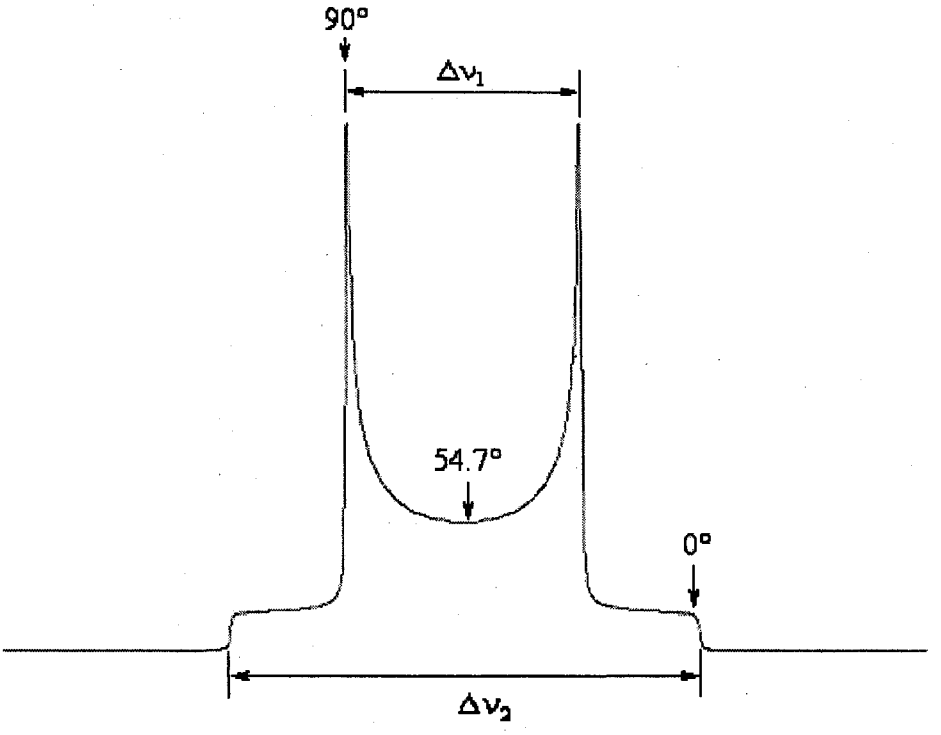

Figure 3.2 Schematic representation of the powder pattern resulting from the sum of the contributions from the random orientations of a spin 1 nucleus with respect to the magnetic field in a polycrystalline sample.

For a rigid deuteron, the separation of the central doublet $\Delta\nu_1$ is (3.3) and that of the outermost shoulders $\Delta\nu_2$ is (3.4)

$$\Delta\nu_1 = \frac{3}{4}\left(\frac{e^2qQ}{h}\right) = \frac{3}{4}\chi_{rigid} \qquad (3.3)$$

$$\Delta\nu_2 = \frac{3}{2}\left(\frac{e^2qQ}{h}\right) = \frac{3}{2}\chi_{rigid} \qquad (3.4)$$

Relaxation rates and ^2H powder line-shapes are affected by any molecular motion. If the timescale for the molecular reorientation is of the order of the quadrupolar interaction or greater, the observed frequencies will be partially averaged and the resulting lineshape can be analyzed to determine the rate and mode of motion for a given motional model. This analysis can be used to distinguish between a fast continuous diffusion and a discrete jumping motion.

If one considers a molecular solid, any reorientational motion of a molecule in the solid is governed by the intermolecular potential that exists in that solid. Deuterium NMR spectroscopy is an excellent technique for studying the dynamics of molecules (or parts of molecules) in solids. Both the deuterium lineshape and the spin-lattice relaxation time are very sensitive to the rate and type of motion that the molecule undergoes. Moreover, molecules can be selectively deuterated and deuteration is relatively inexpensive (compared to ^{13}C and ^{15}N enrichment).

3.2 Powder Lineshape Analysis

Molecular reorientations usually have strong effects on the powder lineshape when the motional rate exceeds the width of the powder spectrum. In the case of exchange of the X-^2H bond between three or more equivalent sites the separation $\Delta\nu_1$ is given by:

$$\Delta\nu_{ave.} = \left(\frac{3e^2qQ}{4h}\right) \times \frac{\left(3\cos^2\alpha - 1\right)}{2} = \frac{3}{8}\chi_{rigid}\left(3\cos^2\alpha - 1\right) \qquad (3.5)$$

where $\Delta\nu_{ave.}$ is the doublet separation in frequency units, and α is the angle between the principal axis of the electronic field gradient tensor (assumed to be along the X-^{2}H bond vector) and the axis of rotation.

When the rate of molecular motion is of the same order of magnitude as χ, the ^{2}H NMR lineshape becomes very sensitive to the exchange rate. Simulations for these motions and the resulting spectra give the rate constants, which, when plotted against the inverse temperature yields Arrhenius activation energies, E_a, for the motion [1].

3.3 ^{2}H Powder Pattern Spectra Obtained Using the Quadrupole Echo Method

The width of ^{2}H powder patterns for static samples necessitates the use of the echo techniques to record undistorted powder patterns, rather than simple pulse-acquire experiments. The receiver deadtime which must be left after a pulse means that the initial part of the FID in a pulse-acquire experiment is not recorded. This lost data constitutes a significant part of the total FID for broad powder patterns, which have correspondingly short FIDs and lead to severely distorted frequency spectra on Fourier transformation. ^{2}H powder patterns are generally recorded with a quadrupole echo, or solid echo, pulse sequence: $90_x^0 - \tau_1 - 90_y^0 - \tau_2 - acquire$ [2]. The delays τ_1 and τ_2 are approximately equal, but, in practice, τ_1 and τ_2 are adjusted so that the data acquisition begins exactly at the echo maximum.

Assuming that the quadrupolar interaction is dominant, ^{2}H powder pattern should be symmetric about its isotropic chemical shift. Experimentally, however, ^{2}H powder patterns often appear distinctly asymmetric due to a variety of factors which should each be attended

to as far as possible before the final spectrum is recorded. Firstly, finite pulse widths do not give uniform excitation over the whole powder pattern. In order to get symmetric excitation about the isotropic chemical shift of the ^2H powder patterns, it is necessary that the centre of the powder pattern be on resonance. If it is not, it is unlikely that a symmetric powder pattern can ever be recorded. Secondly, the NMR probe response may not be symmetric. This particular feature is governed by the probe electronics and can be altered to some extent on most modern probeheads. Once the ^2H powder pattern has been set on resonance, the probe response can be examined. If the powder pattern is unsymmetric at this point in the experiment setup, it is probably the fault of the probe response. The matching and tuning should be adjusted in small steps until a symmetric ^2H powder pattern is obtained.

When recording ^2H powder patterns with a quadrupole echo pulse sequence to study molecular motion, it is often useful to record powder patterns for several different echo delay times, τ_1. The variation in echo intensity with τ_1 is determined by the transverse relaxation rate. It is the anisotropic T_2 arising from molecular motion which causes the distortion of the ^2H powder lineshapes. The variation in echo intensity with τ_1, in combination with the ^2H powder lineshapes (also as a function of τ_1), thus gives useful information on the rate and geometry of the molecular motional process.

3.4 Relaxation Time Studies

3.4.1 Semi-classical Description of Relaxation

The Bloch theory assumes that the components of M decay to M_0 exponentially, but the components of M_0 parallel and perpendicular to B_0 (i.e. M_z, $M_{x,y}$) have different time constants T_1 and T_2 with the z axis chosen along B_0 [3].

$$\frac{d}{dt}M_z = (M_0 - M_z)/T_1 \tag{3.6}$$

$$\frac{d}{dt}M_x = -M_x/T_2 \tag{3.7}$$

$$\frac{d}{dt}M_y = -M_y/T_2 \tag{3.8}$$

where T_1 is the longitudinal or "spin-lattice" relaxation time, and T_2 is the transverse or "spin-spin" relaxation time.

A group of spin $I \neq 0$ nuclei placed in a magnetic field would distribute themselves between the different spin states according to the Boltzmann relation. As a result, the population difference gives rise to a magnetization M_0. According to Curie's law the magnitude of nuclear magnetization is:

$$M_0 = \frac{N\gamma^2 I(I+1)}{3kT} B_0 \tag{3.9}$$

where N is the number of spins which cause the magnetization, I is the spin number and γ the gyromagnetic ratio. The process of growth towards the equilibrium magnetization given by Curie's Law is defined as spin-lattice relaxation and this process is exponential as equation 3.6 described.

The rate at which magnetization builds up in a static field depends on the mechanisms available for the spins to transfer energy to the surroundings. In order to undergo a transfer, the nucleus needs to see fields fluctuating at its Larmor frequency. For spin > ½ the interaction between an EFG with a nuclear quadrupolar moment of the nucleus is the major source of the relaxation.

3.4.2 T_1 Relaxation Time Study of ^2H

In analyzing relaxation data, the dominant nuclear spin interaction effecting relaxation must be known and it must exceed the effects of other interactions by at least an order of magnitude, otherwise the data becomes extremely complex to interpret. The dominant relaxation mechanism of ^2H nuclei is nearly always the quadrupolar interaction.

All relaxation processes can ultimately be described as some linear combination of spectral density functions, $J(\omega)$, and can be viewed as being proportional to the probability of finding a component of the motion at a given frequency, ω. Only when a suitable component exists at the spin Larmor frequency can longitudinal relaxation occur. The calculation of the exact spectral density for any real molecular motion has never been solved. The basic difficulty is that the molecular motions are extremely complicated.

The typical form of the spectral density function is:

$$J(\omega)=\frac{2\tau_c}{1+\omega^2\tau_c^2} \qquad (3.10)$$

where τ_c is a characteristic of the relaxation known as the correlation time for the particular motion involved. The relationship between $J(\omega)$ and ω is shown in Figure 3.3.

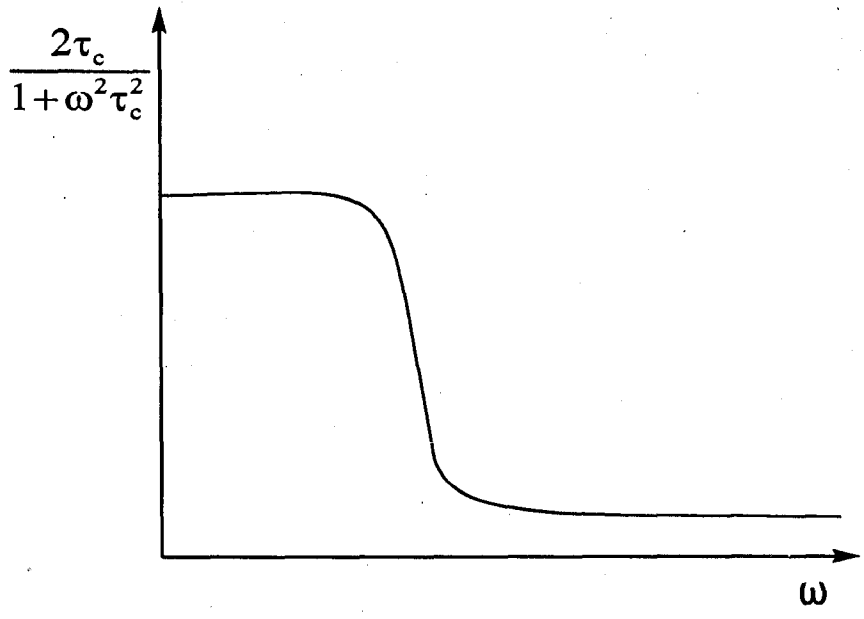

Figure 3.3 The function J(ω) changes with the increasing value ω.

The typical form of the spectral density function has following characteristics. In a particular system and for a given τ_c, the spectral density is a constant at small ω and falls off as $1/\omega^2$ at large ω as shown in Figure 3.3. For a thermally activated process the correlation time is proportional to $\exp(E_a/RT)$ as shown in equation 3.11.

$$\tau_c = \tau_\infty e^{-\frac{Ea}{RT}} \tag{3.11}$$

For deuterium, the T_1 can be expressed as [4]:

$$T_1^{-1} = R \cong T_{1Q}^{-1} = K\left(\frac{\tau_c}{1+\omega_0^2\tau_c^2} + \frac{4\tau_c}{1+4\omega_0^2\tau_c^2}\right) \tag{3.12}$$

where K is a constant that depends on the magnitude of the quadrupolar interaction, the angle θ that the C-^{2}H bond makes with the rotational axis and the type of reorientational motion.

A plot of $ln T_1$ versus the inverse temperature can be fitted to the above two equations simultaneously to give K, E_a, τ_∞ and χ, this plot can be fitted using the Bloembergen, Purcell and Pound (BPP) theory [5]. Figure 3.4 shows a typical $\ln T_1$ versus 1/T curve.

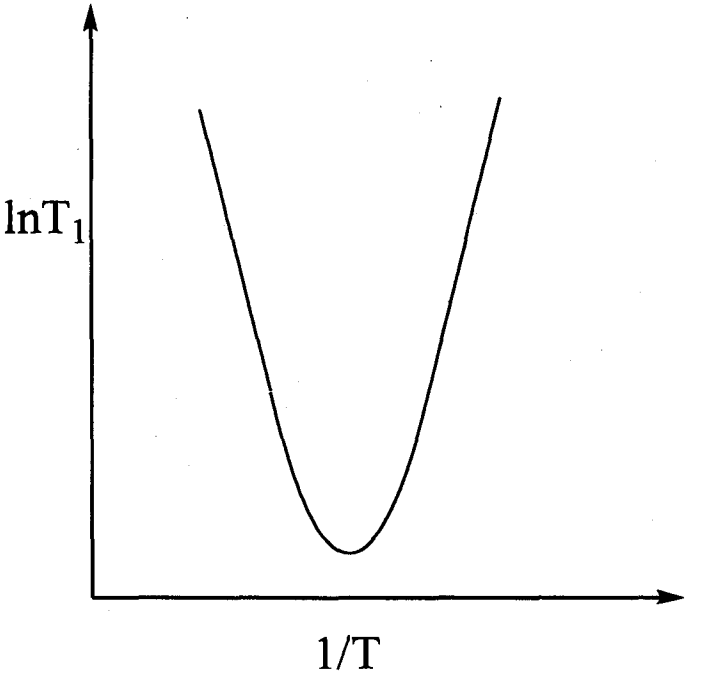

Figure 3.4 This curve shows the $\ln T_1$ varying with 1/T.

When $\omega_0^2\tau_c^2 \ll 1$, equation 3.12 can be re-written as:

$$T_1^{-1} = 5K\tau_c = 5K\tau_\infty e^{\frac{E_a}{RT}} = K'e^{\frac{E_a}{RT}} \qquad (3.13)$$

and the slope of a plot of $\ln T_1$ versus the inverse temperature can be used to obtain the activation energy E_a. Therefore, even if the achievable sample temperatures are such that a T_1 minimum can not be reached, it is still possible to obtain the activation energy for the molecular reorientation.

3.4.3 Measurement of T_1 by the Inversion Recovery Method

The pulse sequence is [180°-τ-90°(FID)-T_d]$_n$, where a delay time T_d, should allow for complete relaxation ($T_d > 5T_1$), this delay must used in order for the Bolzmann populations to be re-established between 180° pulses. The accumulated FID is Fourier transformed, and the evolution period τ is varied. The natural logarithm of the peak height or area, S, for each peak may be plotted against τ, and thus T_1 is found according to the following equation:

$$\ln[S(\infty) - S(t)] = \ln 2 + \ln S(\infty) - \tau/T_1 \qquad (3.14)$$

At short recovery times τ the signal will appear negative. With increasing τ, the signal will become more and more positive until full recovery is obtained.

3.5 ^{2}H Relaxation Time and Lineshape Analysis of Benzene

For benzene, rapid six-fold reorientation partially averages the electric field gradient tensor, whose C_6 symmetry axis is perpendicular to the benzene plane, resulting in an axially symmetric lineshape, with an effective asymmetry parameter, η_Q (eff.) = 0.

The magnitude of the deuterium quadrupolar coupling constant is directly proportional to the largest component of the electric field gradient, eq_{zz}, around the deuterium nucleus and is sensitive to the X-^{2}H bond length (where X=B, C, N,....) and to the electrostatic nature of the X nucleus. Quadrupolar coupling constants for aromatic deuterons are around 180 kHz [6].

Rotational motion of the benzene ring in its crystalline state can be studied through the measurement of the ^{2}H spin-lattice relaxation times (T_1) and the ^{2}H lineshapes. From an

NMR spin-lattice relaxation (T_1) study of ^2H the energy required for reorientation of the benzene ring can be obtained. The reorientation rates can be obtained from the lineshape analysis of the NMR spectrum of ^2H. The in-plane reorientation of benzene in the pure solid, in numerous complexes and inclusion compounds has been studied by several techniques. This is a summarized in a table in the discussion section of this thesis.

Chapter 3: References

[1] M.S. Grenfield, A. D. Ronemus, R. L. Vold, R. R. Vold, P. D. Ellis, T. R. Raidy, *J. Magn. Reson.*, 72 (1987) 89.

[2] J. H. Davis, K. R. Jeffrey, M. Bloom, M. I. Valic, and T. P. Higgs, *Chem. Phys. Lett.*, 42 (1976) 390.

[3] F. Bloch, *Phys. Rev.*,70 (1946) 460.

[4] A. Abragam, "*The Principles of Nuclear Magnetism*", Oxford University Press, Oxford, (1961).

[5] N. Bloembergen, E. M. Purcell and R. V. Pound, *Phys. Rev.*, 73 (1948) 679.

[6] N. Chandrakumar, "*NMR – Basic Principles and Progress*", Edited by P. Diehl, E. Fluck, H. Gűnther, R. Kosfeld and J. Seelig, (1996).

Chapter IV

Quantum Chemical Calculations of NMR Parameters

4.1 Basic Theory of Computational NMR Parameters

4.1.1 Shieldings as Second Derivatives of the Energy

The chemical shielding observed in NMR spectroscopy is an electronic effect, and therefore can be treated by quantum chemical calculations. The applied (external) magnetic field B_{ext} induces an electronic current j, which according to the Biot-Savart law [1] generates an additional, induced magnetic field. The nucleus experiences an effective field given by the sum of the applied external and induced fields:

$$\vec{B}_{eff} = \vec{B}_{ext} + \vec{B}_{ind} \tag{4.1}$$

The induced field B_{ind} is proportional to the applied field

$$\vec{B}_{ind} = -\sigma \cdot \vec{B}_{ext} \tag{4.2}$$

Here σ is chemical shielding tensor. In molecules the electron distribution is not spherically symmetric, so the chemical shielding is a tensor.

For the splitting of the nuclear spin energy levels in the presence of an external magnetic field, we obtain:

$$\Delta E = -\mu B_{eff} = -\gamma \hbar m_J B_{eff} = -\gamma \hbar m_J (1-\sigma) B_{ext} = -\mu (1-\sigma) B_{ext} \tag{4.3}$$

The shielding σ appears in a term bilinear in the external magnetic field B_{ext} and the nuclear magnetic moment m_J of interest. This means that the shielding tensor is a second-order property and thus can be obtained via the corresponding sum-over-states expressions of second-order perturbation theory (which was demonstrated by Ramsay [2]) or via the corresponding second derivative of the electronic energy [3]. The derivative approach is more convenient for most quantum chemical calculations, which can be expressed as:

$$\sigma_{ij} = \left(\frac{d^2 E_{electronic}}{d\mathrm{B}_i dm_{Jj}} \right)_{\mathrm{B},m_J=0} \tag{4.4}$$

4.1.2 Ramsey's Theory of Shielding in Molecules

Ramsey developed a quantum-mechanical method for calculating chemical shielding tensors in which both the interaction with the external magnetic field B_0 and the interaction with a local magnetic field B_{ind} due to the magnetic dipole moment are treated as perturbations of the energy of the electron system.

For all calculations of molecular properties, it is essential to first specify the corresponding perturbed Hamiltonian. While this is a rather straightforward task for most properties, some difficulties arise in case of the magnetic field.

In the presence of an external magnetic field, the momentum operator p in the electronic Hamiltonian

$$\hat{\mathrm{H}} = \frac{\vec{p}^2}{2m} + \vec{V}(r) \tag{4.5}$$

where m is the mass of the electron. Equation 4.5 needs to be replaced by its mechanical counterpart

$$\vec{p} \rightarrow \pi = \vec{p} + \frac{e}{c}\vec{A}(r) \tag{4.6}$$

In Eq. 4.6, e denotes the elementary charge, c the speed of light, and $\vec{A}$ the vector potential describing the external magnetic field.

The magnetic field is uniquely determined via

$$\vec{\mathrm{B}}_{ext} = \nabla \times \vec{A} \tag{4.7}$$

from the vector potential $\vec{A}$.

Carrying out the substitution given by Eq.4.6, one obtains the Hamiltonian for an electron in an external magnetic field

$$\hat{\mathrm{H}} = \frac{\left(\vec{p} - \frac{e}{c}\vec{A}\right)^2}{2m} + \vec{V}(r) \tag{4.8}$$

It is sufficient to consider static magnetic fields which are adequately described by the vector potential

$$\vec{A} = \frac{1}{2} B_{ext} \times \vec{r} + r^{-3}(\mu \times \vec{r}) \tag{4.9}$$

As the vector potential satisfies the Coulomb gauge condition

$$\nabla \cdot \vec{\mathrm{A}} = 0 \tag{4.10}$$

Eq.4.8 can be rewritten as

$$\hat{\mathrm{H}} = \frac{\vec{p}^2}{2m} + \frac{e}{mc}\vec{\mathrm{A}} \cdot \vec{p} + \frac{e^2}{2mc^2}\vec{\mathrm{A}}^2 + \vec{V}(r) \tag{4.11}$$

Insertion of the explicit form of the vector potential Eq.4.9 and $p = -i\hbar\nabla$ into Eq. 4.11 then yields the Hamiltonian

$$\hat{\mathrm{H}} = -\frac{\hbar^2}{2m}\nabla^2 - \frac{ie\hbar}{2mc}\vec{\mathrm{A}} \cdot \nabla + \frac{e^2}{8mc^2}\vec{\mathrm{A}}^2 + \vec{V}(r) \tag{4.12}$$

This equation can be rewritten as:

$$\hat{\mathrm{H}} = \hat{\mathrm{H}}_0 + \hat{\mathrm{H}}_1 + \hat{\mathrm{H}}_2 \tag{4.13}$$

where

$$\hat{\mathrm{H}}_0 = -\frac{\hbar^2}{2m}\vec{\nabla}^2 + \vec{V}(r) \tag{4.14}$$

$$\hat{\mathrm{H}}_1 = -\frac{ie\hbar}{2mc}\vec{\mathrm{A}} \cdot \nabla \tag{4.15}$$

$$\hat{H}_2 = \frac{e^2}{8mc^2}\vec{A}^2 \tag{4.16}$$

The eigenfunctions of $\hat{H}_0$ are just the eigenfunctions of the electron system in the absence of magnetic fields. $\hat{H}_1$ and $\hat{H}_2$ can be treated as perturbation terms.

$$\vec{A}\cdot\nabla = \left(\frac{1}{2}\vec{B}_{ext} + \vec{\mu}r^{-3}\right)\left(x\frac{\partial}{\partial y} - y\frac{\partial}{\partial x}\right) \tag{4.17}$$

and

$$\vec{A}^2 = \left(\frac{1}{2}\vec{B}_{ext} + \vec{\mu}r^{-3}\right)^2\left(x^2+y^2\right) = \left[\frac{1}{4}\vec{B}_{ext}^2 + \vec{\mu}\vec{B}_{ext}r^{-3} + \vec{\mu}r^{-6}\right]\left(x^2+y^2\right) \tag{4.18}$$

In equation 4.17 and 4.18, both B_{ext} and μ are along the z direction of the applied magnetic field. According to perturbation theory, the energy of this electronic system in an external magnetic field can be calculated using the perturbed wave functions. The ground-state perturbed energy, to second order, of the electron system is

$$\Delta E = \left\langle \psi_0 \middle| \hat{H}_1 + \hat{H}_2 \middle| \psi_0 \right\rangle - \sum_{n\neq 0} \frac{\left\langle \psi_0 \middle| \hat{H}_1 + \hat{H}_2 \middle| \psi_n \right\rangle \left\langle \psi_n \middle| \hat{H}_1 + \hat{H}_2 \middle| \psi_0 \right\rangle}{E_n - E_0} \tag{4.19}$$

where ψ_0 is the unperturbed ground state of the system and ψ_n is one of the excited states. According to equation 4.3, ΔE is linear in both μ and B_{ext}. From equation 4.15 and 4.17 it will be seen that $\hat{H}_1$ contributes no terms to the first-order perturbed energy because both equations contain no cross terms in μ and B_{ext}. On the other hand, according to equation 4.18 the operator appears twice so that the coefficients are squared and then $\hat{H}_2$ makes no or trivial contribution to the second-order perturbed energy. Therefore Equation 4.17 can be expanded and the cross terms are isolated in μB_{ext},

$$\Delta E = \left\{ \begin{array}{l} \dfrac{e^2}{2mc^2}\left(\psi_0\left|\dfrac{x^2+y^2}{r^3}\right|\psi_0\right) + \\ \dfrac{e^2\hbar^2}{2m^2c^2}(E_n - E_0)^{-1}\left(\begin{array}{l}\left(\psi_0\left|x\dfrac{\partial}{\partial y} - y\dfrac{\partial}{\partial x}\right|\psi_n\right)\left(\psi_n\left|r^{-3}\times\left(x\dfrac{\partial}{\partial y} - y\dfrac{\partial}{\partial x}\right)\right|\psi_0\right) + \\ \left(\psi_0\left|r^{-3}\times\left(x\dfrac{\partial}{\partial y} - y\dfrac{\partial}{\partial x}\right)\right|\psi_n\right)\left(\psi_n\left|x\dfrac{\partial}{\partial y} - y\dfrac{\partial}{\partial x}\right|\psi_0\right)\end{array}\right) \end{array} \right\} \mu B_{ext}$$

$$+ [\text{non } \mu B_{ext} \text{ terms}] \qquad (4.20)$$

The first term in curly bracket in equation 4.20 is the diamagnetic part of the shielding tensor in Ramsey's formula, the second term is the paramagnetic part of the shielding tensor in Ramsey's formula [2].

It is easier to obtain the first and second derivative of the Hamiltonian than that of the energy. And thus the following expressions are the first and second derivative of the Hamiltonian with respect to B_i

$$\frac{\partial H}{\partial B_i} = -\frac{ie\hbar}{2mc}(\vec{r}\times\nabla)_i \qquad (4.21)$$

$$\frac{\partial^2 H}{\partial B_i \partial B_j} = \frac{e^2}{4mc^2}\left[(\vec{r}\cdot\vec{r})\delta_{ij} - r_i r_j\right] \qquad (4.22)$$

Considering in addition the vector potential, A, due to the magnetic moments

$$A = \frac{m_J \times (\vec{r} - \vec{R}_o)}{|\vec{r} - \vec{R}_o|^3} \qquad (4.23)$$

and $\vec{R}_o$ as an arbitrary parameter called gauge origin, the corresponding derivative of $\hat{H}$ with respect to m_J is given by

$$\frac{\partial H}{\partial m_{Jj}} = -\frac{ie\hbar}{mc}\frac{\left[(\vec{r} - \vec{R}_o)\times\nabla\right]_j}{|\vec{r} - \vec{R}_o|^3} \qquad (4.24)$$

For the mixed derivative with respect to B_i and m_j the following expression is obtained

$$\frac{\partial^2 H}{\partial \mathrm{B}_i \partial m_{jj}} = \frac{e^2}{2mc} \frac{\vec{r} \cdot (\vec{r} - \vec{R}_o)\delta_{ij} - \vec{r}_j (\vec{r} - \vec{R}_o)_i}{|\vec{r} - \vec{R}_o|^3} \tag{4.25}$$

This equation shows that the derivative of Hamiltonian depends on the choice of the gauge origin $\vec{R}_o$.

4.1.3 Gauge-Origin Dependence in the Calculation of Magnetic Properties

The problem of gauge-invariance (or gauge-origin independence) in the calculation of magnetic properties arises because of the use of the vector potential $\vec{A}$ for the description of the magnetic interactions in the Hamiltonian. While A uniquely defines the magnetic field via Eq. 4.9, there is no unique choice of $\vec{A}$ to a given magnetic field B_{ext}. The reason is the $\vec{\nabla}$ operator in Eq.4.9 which allows adding the gradient of an arbitrary scalar function to $\vec{A}$ without changing the corresponding magnetic field. For a static homogeneous field, the vector potential can be chosen in the general form

$$\vec{\mathrm{A}} = \frac{1}{2} \vec{\mathrm{B}}_{ext} \times (\vec{r} - \vec{R}_o) \tag{4.26}$$

with $\vec{R}_o$ as an arbitrary parameter, the so-called gauge origin.

Basic physical laws require that values for observable quantities must be independent of the chosen gauge or gauge-origin. This statement is known as the principle of gauge-invariance (gauge independence). It is an obvious statement, as Hamiltonians differing only in $\vec{R}_o$ describe the same physical system with the same physical properties. There are a variety of approaches for overcoming the gauge problem. On the one hand, a common gauge origin may be employed (generally the origin of the molecular coordinate system) and

sufficiently large basis sets are applied to approach the Hartree-Fock limit so that the gauge dependence is minimized. On the other hand, some alternative approaches are significantly better than the common origin approach.

Ditchfield [4] introduced the idea of employing atomic orbitals of the calculation which carry a complex gauge factor referred to the position of the nucleus where the particular orbital is centered. These orbitals, which are called London orbitals [5], form the basis for his gauge-including atomic orbital (GIAO) approach. Wolinsky, Hinton, and Pulay [6] have produced an efficient implementation of this theory, which has expanded its applicability significantly.

Kutzelnigg and Schindler [7, 8] introduced the individual gauge for localized orbitals coupled Hartree-Fock (IGLO) approach so that the complex gauge factors are contained in and refer to the centroid of localized molecular orbitals. In this theory the complex gauge factors enter only in the form of developments leading to the working equations and do not introduce the extra bookkeeping required in the GIAO approach.

Hansen and Bouman [9, 10] have designed a local origin variant of the coupled Hartree-Fock method (LORG) in which the random phase approximation is applied. In this theory, gauge independent orbitals are not introduced explicitly, by expanding angular momentum terms relative to a local origin for each orbital and using properties of the random phase approximation they arrive at shielding expressions that contain no reference to an overall gauge origin.

The GIAO, IGLO, and LORG methods are basically equivalent in terms in terms of their calculation ability. Because GIAO method is more efficient in the convergence of the

chemical shielding value as a function of basis set size [6], the GIAO method is especially illustrated in the following section.

4.1.4 The GIAO Method

The GIAO method [4-6] consists of choosing local gauge origins for atomic orbitals $|\varphi_\mu\rangle$. This means in particular that the corresponding nucleus at which the atomic orbital is centered is chosen as the "natural" gauge origin.

Within the concept of local gauge origins, the GIAO ansatz is based on the following gauge transformation

$$\vec{A} \rightarrow \vec{A} - \vec{\nabla}\Lambda_\mu(\vec{r}) \tag{4.27}$$

And the gauge factor is given by:

$$\Lambda_\mu(\vec{r}) = \frac{ie}{2c\hbar}\left[(\vec{R}_\mu - \vec{R}_o)\times \vec{\mathrm{B}}_{ext}\right]\cdot \vec{r} \tag{4.28}$$

where $\vec{R}_o$ as the original gauge origin in the Hamiltonian and $\vec{R}_\mu$ is the center of the basis function $|\chi_\mu\rangle$. Consider the equation of the gauge transformation, the calculation of the magnetic properties are now carried out with the following perturbation-dependent basis function

$$|\varphi_\mu(\vec{\mathrm{B}}_{ext})\rangle = \exp\left(-\frac{ie}{2c\hbar}(\vec{\mathrm{B}}_{ext}\times(\vec{R}_\mu - \vec{R}_o))\cdot\vec{r}\right)|\varphi_\mu(0)\rangle \tag{4.29}$$

instead of the usual field-independent functions $|\varphi_\mu(0)\rangle$. The field-dependent basis functions of Eq. 4.25 have been termed as gauge-including atomic orbitals or London orbitals.

In the GIAO method, the gauge-origin problem is solved by fixing the gauge in an optimal way. This first provides unique results and second ensures fast basis set convergence, as for each AO the corresponding optimal gauge is used.

The use of perturbation-dependent basis functions ensures proper behavior of the wavefunction in the presence of the magnetic field. Gauge-origin independent results are obtained, as these basis functions are especially tailored to the chosen gauge. Fast basis set convergence is achieved, because the GIAOs are constructed in such a manner that they provide exact first-order solutions in the presence of the magnetic field provided the corresponding AO is the correct zeroth-order solution [11].

4.2 Ab initio Calculations of NMR Magnetic Shieldings

In the ab initio calculation of chemical shielding, the effect of electronic currents producing internal fields is a very small one and can be treated by perturbation theory. Because of the smallness of the effect, very accurate wavefunctions are needed. This means that whatever level theory is used, large basis sets are needed.

In this section brief general information about these methods is shown and followed with the relative NMR calculation comments.

4.2.1 Hartree-Fock Method

In Hartree-Fock theory [12-17], one is interested in finding a set of spin orbitals $\{\chi_a\}$ such that the single determinant formed from these spin orbitals is the best possible energetic

approximation to the ground state of the n-electron system described by an electronic Hamiltonian. The Fock operator is used to replace the electronic Hamiltonian.

$$\hat{F}_i(x_i) = \hat{h}_i(x_i) + \sum_j \left[2\hat{J}_j(x_i) - \hat{K}_j(x_i)\right] \tag{4.30}$$

where $\hat{h}_i(x_i)$ is a one-electron operator:

$$\hat{h}_i(x_i) = -\frac{\nabla_i^2}{2} - \sum_A^N \frac{Z_A}{r_{iA}} \tag{4.31}$$

$\hat{J}_j(x_i)$ and $\hat{K}_j(x_i)$ are the Coulomb and exchange operators, respectively. The physical meaning of the Coulomb interaction between pairs of orbitals is that the Coulomb integral $J_{1,2} = \int |\phi_1(r)| \frac{e^2}{|r-r'|} |\phi_2(r')|^2 \, dr dr'$ represents the Coulomb repulsion energy of two charge densities, $|\phi_1|^2$ and $|\phi_2|^2$, integrated over all locations r and r' of the two electrons.

The exchange integral $K_{1,2} = \int \phi_1(r)\phi_2(r') \frac{e^2}{|r-r'|} \phi_2(r)\phi_1(r') dr dr'$ can be thought of as the Coulomb repulsion between two electrons whose coordinates r and r' are both distributed throughout the "overlap region" $\phi_1\phi_2$.

With the development of computer techniques, the ability to carry out Hartree-Fock calculations with fairly large basis sets has allowed one to approach sufficiently close to the Hartree-Fock limit in magnetic shielding calculations. But Hartree-Fock theory is an approximation, which means that the Hartree-Fock limit in calculations can be achieved, but does not mean that a good result is obtained. Electron correlation appears to be particularly important for shielding in systems involving lone pairs and multiple-bonds, and where nearly degenerate or low-lying excited states are present. In the next section shielding calculations

including electron correlation by way of many-body Møller-Plesset perturbation theory in the GIAO method are discussed.

4.2.2 The MP2 Method

Møller-Plesset perturbation theory [18-20] is a systematic procedure for finding the correlation energy beyond the Hartree-Fock approximation. In this approach, the total electronic Hamiltonian of an n-electron system is partitioned into two parts:

$$\hat{H} = \hat{H}_0 + \lambda \hat{V} \tag{4.32}$$

where $\hat{H}_0$ represents an unperturbed Hamiltonian, λ a dimensionless parameter, and $\hat{V}$ the perturbation term.

In the majority of cases, Hartree-Fock theory yields quite good results for investigating shielding calculation problems. However, there are those cases involving lone pairs and multiple bonds where lack of correlation in the Hartree-Fock approach causes severe error and where post-Hartree-Fock (e.g., MP2) approaches are needed. However, the high computational cost of the MP2 method limits its application.

4.3 Density Functional Theory (DFT)

Another approach to ab initio calculations is density functional theory (DFT), whose origins are to be found in the early work of Hohenberg, Kohn, and Sham in the mid 1960s [21, 22]. The basis for density functional theory (DFT) is that the ground state electronic energy is determined completely by the electron density ρ (r). The "intuitive" proof of why the density completely defines the system is due to E. B. Wilson [23], who argued that:

(i) The integral of the density defines the number of electrons.

(ii) The cusps in the density define the position of the nuclei.

(iii) The heights of the cusps define the corresponding nuclear charges.

The goal of DFT methods is to design functionals connecting the electron density with energy [24-28]. The success of modern DFT methods is based on the suggestion by Kohn and Sham in 1965 that the electron kinetic energy should be calculated from an auxiliary set of orbitals used for representing the electron density [22].

Kohn and Sham (KS) introduced a set of KS orbitals obeying the following equation:

$$\left\{-\frac{\hbar^2}{2m}\nabla^2 + V(r) + \frac{e^2}{2}\int\frac{\rho(r')}{|r-r'|}dr' + U_{XC}(r)\right\}\phi_j = \varepsilon_j\phi_j \qquad (4.33)$$

where the so-called exchange-correlation potential $U_{XC}(r) = \delta E_{XC}[\rho]/\delta\rho(r)$ could be obtained by functional differentiation if the exchange-correlation energy functional $E_{XC}[\rho]$ were known. KS also showed that the KS orbitals $\{\phi_j\}$ could be used to compute the density ρ by adding up the orbital densities multiplied by orbital occupancies n_j:

$$\rho(r) = \sum_j n_j|\phi_j(r)|^2 \qquad (4.34)$$

here $n_j = 0, 1, 2$ is the occupation number of the orbital ϕ_j in the state being studied. Now the kinetic energy should be calculated as

$$T = \sum_j n_j\langle\phi_j(r)|-\frac{\hbar^2}{2m}\nabla^2|\phi_j(r)\rangle \qquad (4.35)$$

The difference between various DFT methods is the choice of the functional form for the exchange-correlation energy.

DFT methods are effective alternatives to the conventional ab initio methods because electron-correlation is implicitly included via the exchange-correlation functional. Within DFT, the calculation of NMR shielding constants is particularly attractive because there is no

explicit dependence on the exchange-correlation integrand. The shielding calculation equations simply depend on the Kohn-Sham orbitals and eigenvalues. Compared with Hartree-Fock theory, DFT theory needs less computational resources (computer hardware and calculation time), and therefore is more favorable for the calculations of larger chemical or biological systems.

4.4 Basis Sets and the Gauge-Origin Problem

The need to accurately describe the magnetic-field perturbations means the NMR shielding calculations are ultimately very sensitive to the quality of the basis set and gauge-origin method employed.

The main disadvantage of popular basis sets in use today for NMR shielding calculation is that they are energy-optimized and therefore concentrate on optimizing the basis functions associated with the inner-shell electrons since they account for the majority of the total energy [29]. The calculated diamagnetic shielding term for a particular nucleus under investigation remains almost invariant to changes in its molecular electronic environment, because this term is dominated by contributions from the inner-shell electrons. Therefore, from a basis set perspective, the accurate determination of the shielding constant requires large, flexible basis sets that are capable of describing the valence and virtual orbitals that affect the paramagnetic shielding term.

In all-electron NMR calculations contracted Gaussian-type orbitals (CGTOs) are the most widely used basis sets, which describe the core atomic orbitals with a particular contraction scheme and include two or three valence functions for each valence atomic

orbital. Slater-type orbitals (STOs) have also been utilized but to a lesser extent. In heavy-atom systems involving a large number of electrons, the computational effort can be reduced by representing the inner shells by effective core potentials (ECPs). In ECP methods, only the valence electrons are treated in the all electron calculations. The magnitude of the absolute shieldings calculated using ECPs are significantly underestimated. This discrepancy arises from the incorrect behavior of the molecular orbitals derived from ECPs at distances close the nucleus which causes the paramagnetic term to be significantly underestimated.

Variation in basis sets quality can lead to very different NMR shielding results. In general, larger basis sets produce better quality results.

The accuracy of the NMR shielding calculations also depends upon the choice of gauge-origin. The Gauge-Including Atomic Orbital (GIAO) method is the most widely used in the calculations of magnetic properties. In the section 4.1.4 a detailed description of GIAO method has been shown.

4.5 Relativistic Effects in the Calculations of Heavy-atom Shieldings

The presence of large correlation effects and low-lying excited states in the first-row (3d) transition metal complexes are a result of strong repulsive interactions between the compact 3d orbitals and the ligand orbitals. As a result, these transition metals have very wide shielding ranges (10^3-10^4 ppm) and chemical shifts are very sensitive to ligand types which are associated with these nuclei. Therefore, it is a severe challenge to predict the metal NMR shielding and chemical shifts in the first-row transition metal complexes. For the

second- (4d) and third-row (5d) transition metal complexes these effects become less severe due to reduced metal-ligand interaction [29].

The scarcity of reliable absolute shielding scales and gas phase data for these nuclei means that calculated chemical shifts are compared to solution or solid state experimental NMR data. Thus, the presence of intermolecular crystal or solvent effects may affect the comparison between theoretical shieldings with experiment chemical shifts. However, in the case of the metal shieldings such effects have been shown to be small [30- 32].

The high velocities associated with the core electrons in heavy nuclei contribute significant relativistic effects to the heavy atom (or neighboring light atom) NMR shielding parameters. The magnitude of the relativistic effects increases down the periodic table, and by the sixth period (i.e. third-row transition metals) inclusion of these effects in the calculations becomes mandatory [33]. Thus, the effects of Einstein's special relativity must be considered in their theoretical description.

In recent years there has been increased interest in the role of relativistic effects on NMR shielding calculations in heavy atom systems. Relativistic effects can influence NMR shieldings in one of two ways: either indirectly, by affecting molecular structure, i.e., through contraction in the bond length; or directly, by affecting the electronic structure at a fixed geometry. These effects do not necessarily reinforce each other [34, 35]. In general, relativistic effects contract the inner core s- and p-orbitals producing larger diamagnetic shielding terms, these effects tend to cancel out in relative chemical shift calculations. For the valence orbitals, the s- and p-orbitals become more contracted, and as a consequence the d- and f-orbitals are more effectively screened from the nucleus, and thus expand. As a result, the changes in the relativistic effects can have a significant impact on the NMR shieldings.

For heavy atom systems, the lack of accurate absolute shielding scales means that chemical shifts rather than absolute shieldings are more commonly used which tend to attenuate the relativistic effects [36], due to the inherent scaling to a common reference.

There are a number of different methodologies available for carrying out relativistic computations in a variationally stable manner. Each of them requires the implementation of a specific set of perturbation operators for the purpose of NMR calculations. It is very important to keep the method internally consistent in order to avoid singularities, variational collapse, and meaningless results.

Two-component methods which are classified to include the important effects of spin-orbit coupling can be more efficient and have been applied to a large range of transition-metal complexes. If spin-orbit coupling is neglected in a two-component Hamiltonian, the approach turns into a one-component method-scalar relativistic approach.

Presently, for transition-metal systems the most frequently applied two-component relativistic DFT NMR method is based on the zeroth-order regular approximation (ZORA) [37-40]. Nuclear shieldings have been successfully computed based on the second-order Douglas-Kroll-Hess (DKH2) transformed Hamiltonian [41-44].

Besides these direct relativistic methods, the relativistic effects on a heavy atom's valence shell can also be incorporated in an otherwise nonrelativistic computation by employing effective core potentials (ECPs) for the heavy atom.

Chapter 4: References

[1] L. D. Landau, E. M. "*Lifschitz, Lehrbuch der Theoretischen Physik*", Bd. II, Akademie Verlag, Berlin, (1981).

[2] N. F. Ramsay, *Phys. Rev.*, 78 (1950) 699.

[3] J. Gauss, "*Modern Methods and Algorithms of quantum Chemistry*", edited by J. Grotendorst (John von Neumann Institute for Computing, Julich, (2000).

[4] R. Ditchfield, *Mol. Phys.*, 27 (1974) 789.

[5] F. London, *J. Phys. Radium*, 8 (1937) 397.

[6] K. Wolinski, J. F. Hinton, P. Pulay, *J. Am. Chem. Soc.*, 112 (1990) 8251.

[7] W. Kutzelnigg, *Israel J. Chem.*, 19 (1980) 193.

[8] M. Schindler, and W. Kutzelnigg, *J. Chem. Phys.*, 76 (1982) 1919.

[9] A. E. Hansen, and T. D. Bouman, *J. Chem. Phys.*, 82 (1985) 5035.

[10] T. D. Bouman, and A. E. Hansen, *Chem. Phys. Lett.*, 149 (1988) 510.

[11] P. Pulay, J. F. Hinton, K. Wolinski, "*Nuclear Magnetic Shielding and Molecular Structure*", J. A. Tossell, Ed., Kluwer, Dordrecht, (1993).

[12] D. R. Hartree, *Proc. Cam. Phil. Soc.*, 24 (1928) 89.

[13] D. R. Hartree, *Proc. Cam. Phil. Soc.*, 24 (1928) 111.

[14] D. R. Hartree, *Proc. Cam. Phil. Soc.*, 24 (1928) 426.

[15] V. Fock, *Z. Physik.*, 61 (1930) 126.

[16] J. C. Slater, *Phys. Rev.*, 34 (1929) 1293.

[17] J. C. Slater, *Phys. Rev.*, 35 (1930) 509.

[18] C. Møller and M. S. Plesset, *Phys. Rev.*, 46 (1934) 618.

[19] G. Hetzer, P. Pulay, and H.-J. Werner, *Chem. Phys. Lett.*, 290 (1998) 143.

[20] M. Schütz, G. Hetzer and H.-J. Werner, *J. Chem. Phys.*, 111 (1999) 5691.

[21] P. Hohenberg and W. Kohn, *Phys. Rev.*, 136 (1964) B864

[22] W. Kohn and L. J. Sham, *Phys. Rev.*, 140 (1965) A1133.

[23] P.O. Löwdin, *Int. J. Quant. Chem.*, S19 (1986) 19.

[24] R. G. Parr, W. Yang, "*Density Functional Theory*", Oxford University Press, 1989.

[25] L. J. Bartolotti, K. Flurchick, *Rev. Comp. Chem.*, 7 (1996) 187.

[26] A. St-Amant, *Rev. Comp. Chem.*, 7 (1996) 217; T. Ziegler, *Chem. Rev.*, 91 (1991) 651.

[27] E. J. Baerends, O.V. Gritsenko, *J. Phys. Chem.*, 101 (1997) 5383.

[28] W. Kohn, M. C. Holthausen, "*A Chemist's Guide to Density Functional Theory*", Wiley-VCH, 2000.

[29] P. J. Wilson, *Annu. Reports on NMR Spectroscopy*, 49 (2003) 118.

[30] D. R. Eaton, R. J. Buist. and B. G. Sayer, *Can. J. Chem.*, 65 (1987) 1332.

[31] M. Kaupp, V. G. Malkin, O. L. Malkina, and D. R. Salahub, *J. Am. Chem. Soc.*, 117 (1995) 1851.

[32] P. Zhou, S. C. F. Au-Yeung, and X. P. Xu, *J. Am. Chem. Soc.*, 121(1999) 1030.

[33] M. Buhl, M. Kaupp, O. L. Malkina and V.G. Malkin, *J. Comput. Chem.*, 20 (1999) 91.

[34] G. Schreckenbach, and T. Ziegler,*Int. J. Quantum. Chem.*, 61 (1997) 899.

[35] M. Kaupp, and O. L. Malkina, *J. Chem.Phys.*, 108 (1998) 3648.

[36] M. Bulh, G. Hopp, W. von Philipsborn, M. –H. Prosenc, U. Rief, and H.-H. Brintzinger, *Organometallics*, 15 (1996) 778.

[37] Wolff S.K., Ziegler T., van Lenthe E., Baerends E.J., *J. Chem. Phys.*, 110 (1999) 7689.

[38] Bouten R., Baerends E.J., van Lenthe E., Visscher L., Schreckenbach G., Ziegler, T.,

J. Chem. Phys., 104 (2000) 5600.

[39] Autschbach J., Ziegler T., *J. Chem. Phys.*, 113 (2000) 936.

[40] Autschbach J., Ziegler T., *J. Chem. Phys.*, 113 (2000) 9410.

[41] Fukuda R., Hada M., Nakatsuji H., *J. Chem. Phys.*, 118 (2003) 1015.

[42] Fukuda R., Hada M., Nakatsuji H., *J. Chem. Phys.*, 118 (2003) 1027.

[43] Fukui H., Baba T., *J. Chem. Phys.*, 117 (2002) 7836.

[44] Baba T., Fukui H., *Mol. Phys.*, 100 (2002) 623.

EXPERIMENTAL

Chapter V

Experimental Details

5.1 Synthesis of Organosilver Complexes

Since most silver compounds investigated in this work are both light and air (water) sensitive, all the syntheses were carefully conducted in the dark and protected by nitrogen. For solid-state NMR experiments, most samples were ground into fine powders and carefully packed into rotors under argon in a dry box. All silver salts ($AgClO_4$, $AgCO_2CF_3$ and $AgSO_3CF_3$) were purchased from Alfa Aesar, Johnson Matthey Company. NHC silver complexes were synthesized by the research group of Prof. Michael Organ of the chemistry department at York University. The other chemicals were purchased from Aldrich.

5.1.1 Silver Arene Derivatives

Crystals of the Ag (I) complexes with liquid arene derivatives were obtained by dissolving anhydrous silver salts in the corresponding arene compounds and then allowing the solvent to evaporate slowly by blowing nitrogen gas over the solution [1-5].

5.1.2 Silver Hexamethylbenzene Complexes

Crystals of the Ag (I) complexes with hexamethylbenzene derivatives were obtained by dissolving anhydrous silver salts and hexamethylbenzene (in a 1:1 mole ratio) in toluene and then allowing the toluene to evaporate slowly by blowing nitrogen gas over the solution.

5.2 NMR Parameters

Most NMR experiments presented in this work were performed on a Bruker AV-500 Ultra Shielded NMR spectrometer (B_0 = 11.75 T) in the NMR Center of University of Guelph. A Bruker low frequency 7 mm HX CP/MAS probe was used for most of our MAS and CP/MAS silver NMR experiments.

For ^{1}H-^{13}C cross-polarization MAS, static ^{2}H, ^{75}As and ^{127}I experiments, samples were packed into 4mm o.d. zirconia rotors and experiments were conducted using a 4mm HFX probe.

Some NMR experiments were performed on a Bruker AV-900 Ultra Shielded NMR spectrometer (B_0 = 21.15 T), which is located at National Ultrahigh-field NMR Facility for Solids in Ottawa, Canada.

Silver NMR experiments were set up with the standard, silver methylsulfate, using a 90° pulse of 10 μs. A contact time of 40ms was employed in the cross-polarization pulse sequence, with 10 s recycle delay. ^{109}Ag chemical shifts were referenced to an infinitely dilute solution of $AgNO_3$ (δ_{iso}= 0 ppm) using silver methylsulfate as a secondary standard (δ_{iso} = 34.96 ppm). Powder samples were placed in a 7 mm zirconium rotor with Kel-F cap.

Air and moisture sensitive samples were packed in an argon dry glovebox and the 7mm zirconia rotors were sealed using an airtight Teflon cap.

^{13}C resonances were referenced to tetramethylsilane (δ_{iso} = 0 ppm) using glycine as a secondary standard (δ_{iso} = 176.01 ppm for the carboxylate resonance).

^{2}H NMR experiments were set up with the standard, dimethyl sulfone $(CD_3)_2SO_2$, using a 90° pulse of 3μs. ^{2}H chemical shifts were referenced to tetramethylsilane (δ_{iso} = 0 ppm) using dimethyl sulfone as a secondary standard (δ_{iso} = 2.77 ppm).

The reference frequency and liquid state 90° pulse length of ^{75}As were obtained from solid $NaAsF_6$, which possesses nearly perfect octahedral symmetry at the arsenic site and yields an NMR resonance dominated by scalar couplings, δ (saturated $NaAsF_6$) = 0 ppm. The solid state 90° pulse length of ^{75}As is half of the liquid state 90° pulse length (Solid state 90° pulse length = Solution 90° pulse length/(I+1/2)).

A solid state sample of KI was used for RF power calibration and for ^{127}I chemical shift referencing, δ (solid KI) = 0 ppm.

Static ^{2}H NMR spectra were obtained using the solid echo pulse sequence [6]:

Recycle delay--$(90^o)_x$-τ_1--$(90^o)_y$--τ_2—acqu

5.3 The Temperature Calibration for Various-Temperature Experiments of HFX Probe

Low temperatures for ^{2}H solid echo experiments were achieved by passing dry nitrogen gas (from a high-pressure nitrogen tank) through a heat exchanger immersed in a liquid nitrogen dewar. A Bruker BVT-2000 unit was used for temperature control, and temperatures were stable to ±1 K. All temperatures were calibrated according to the method described by the Bruker Instruments' VT-calibration manual [7] as detailed below. At least 30 minutes was allowed to pass before beginning the experiments, to allow the samples to reach thermal equilibrium.

When a variable temperature (VT) NMR experiment is performed, the displayed temperature is not necessarily the actual sample temperature. When the actual temperature needs be known with a high degree of accuracy it is important to calibrate the sample temperature relative to the temperature displayed by the VT unit.

The common method to perform this calibration is to observe the chemical shift separation between the OH resonances and CH_n resonances in either methanol or ethylene glycol. Generally methanol is used for low-temperature calibration, and ethyl glycol is used above ambient temperature. The temperature dependence of this shift has been well studied, and a variety of conversion methods have been reported to enable the determination of the "true" sample temperature.

We used 100% methanol, as a calibration sample. The following equation was used to obtain the actual sample temperature:

$$T = -23.832\Delta^2 - 29.46\Delta + 403.0 \qquad (5.1)$$

where Δ is the ^1H chemical shift difference (ppm) between CH_3 and OH peaks of CH_3OH [7]. The ^1H chemical shift differences and calibrated temperatures were tabulated in the Table 5.1.

Table 5.1 The static various-temperature experiment data of the HFX probe using methanol as calibration sample.

Δ-The ^1H chemical shift difference (ppm) between CH_3 and OH peaks (error = 0.02 ppm)	Thermocouple Temperature	Calibrated Temperature (Using equation 7.5) (error = 2 K)
1.6	294.4	294.7
1.8	270	269.2
2.0	250	248.0
2.2	230	227.8
2.3	210	205.2
2.4	200	194.1
2.5	190	184.8

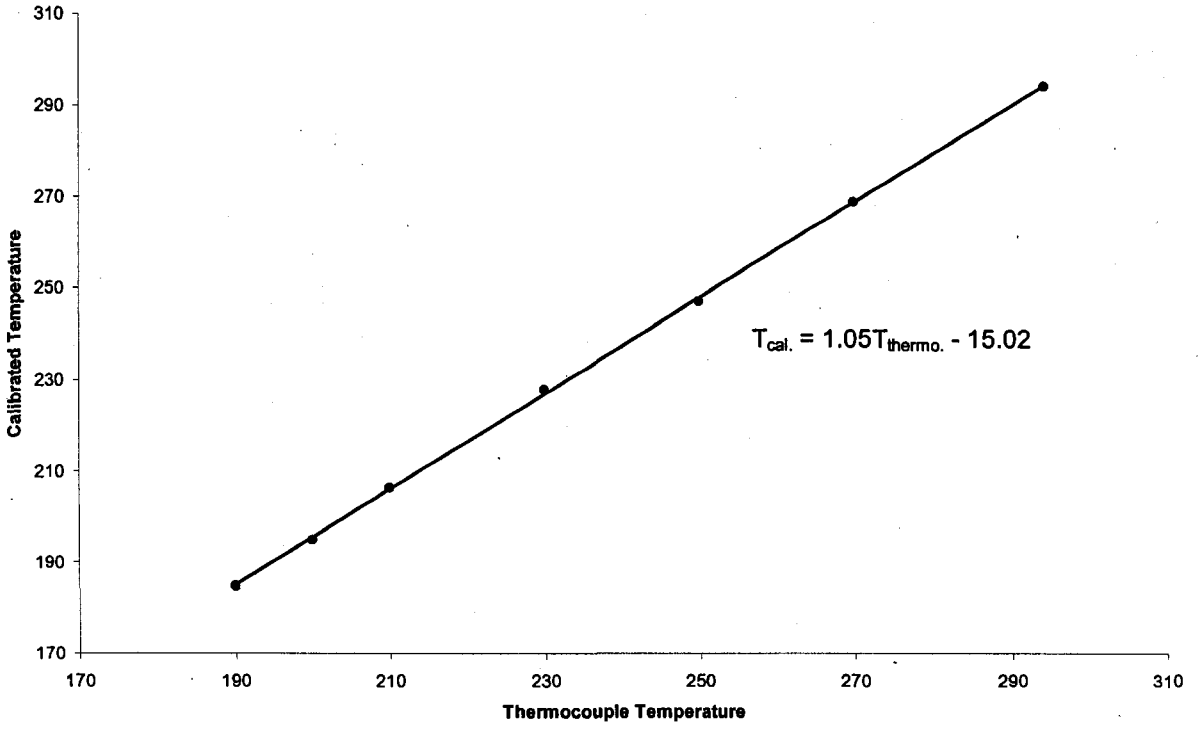

Figure 5.1 The calibrated Temperature versus the thermocouple temperature.

Using the equation derived from the plot of thermocouple temperatures versus calibration temperatures, the calibrated temperatures of samples can be obtained.

5.4 NMR Spectra Simulation

All the NMR spectra were edited with WINNMR program, a program used to process XWINNMR data. All NMR parameters, including C_Q, η_Q, δ_{iso}, Ω, κ and J were determined by analytical simulations of the NMR spectra using the WSolids program package, which was kindly provided by the research group of Prof. R. E. Wasylishen of the University of Alberta [8].

5.5 Computational Methods

5.5.1 Gaussian Calculations

Ab initio calculations were performed using the Gaussian-03 C.02 [9] package on a Pentium IV dual-channel DDR PC. Three methods were used: HF [10-15], B3LYP [16-18] and MP2 [19-21]. DGDZVP [22, 23] was the basis set of choice throughout the study. DGDZVP is an all electron basis set.

Geometry optimizations were performed on the selected molecules in the section 6.3.1, and the resulting structures were used to calculate chemical shift tensors.

Non-optimized structures in sections 6.3.2 and 6.3.3 were obtained from the Cambridge Crystallographic Database.

London's gauge-invariant atomic orbitals (GIAO) method [24-28] was employed for all computations of chemical shielding. With this method absolute chemical shielding values, relative to the bare nucleus, were obtained.

5.5.2 ADF Calculations

DFT calculations were performed using ADF (trial version) [29] on a Pentium IV dual-channel DDR PC. The double-zeta Slater type basis set was used.

When X-ray diffraction structures were available, chemical shielding parameters and quadrupolar coupling constants were calculated directly using the X-ray coordinates. ^{1}H positions are also from X-ray diffraction structures.

Otherwise, all atoms' geometry optimizations were carried out, and the resulting structures were used to calculate the chemical anisotropic parameters and quadrupolar parameters.

5.6 Other Softwares

Simulation programs such as MXQET [30] and WSolids [8] were used to simulate lineshapes best matched with those of the experimental spectra. ^2H T_1 vs temperature curve for the low temperature phase of benzene silver perchlorate was fitted using the BPP program [31], which utilizes a non-linear least square (Levenberg-Marquardt) method, to obtain the parameters k, E_a and τ_∞.

Chapter 5: References

[1] G. W. Hunt, T. C. Lee, E. L. Amma, *Inorg. Nucl. Chem. Lett.*, 10 (1974) 909.

[2] R. E. Rundle, J. H. Goring, *J. Am. Chem. Soc.*, 72 (1950) 5337.

[3] H. G. Smith, R. E. Rundle, *J. Am. Chem. Soc.*, 80 (1958) 5075.

[4] R. K. McMullan, T. F. Koetzle, C. J. Fritchie Jr., *Acta Cryst.*, B53 (1997) 645.

[5] R. W. Turner, E. L. Amma, *J. Am. Chem. Soc.*, 88 (1966), 3243.

[6] J. H. Davis, K. R. Jeffrey, M. Bloom, M. I. Valic, and T. P. Higgs, *Chem. Phys. Lett.*, 42 (1976) 390.

[7] *Bruker* instruments, Inc. *VT-Calibration manual.*

[8] K. Eichele, R. E. Wasylishen, *Wsolids NMR Simulation Package*, Version 1.17.24, University of Tübingen, Tübingen, Germany, (2001).

[9] M. J. Frisch, G. W. Trucks, H. B. Schlegel, G. E. Scuseria, M. A. Robb, J. R. Cheeseman, J. A. Montgomery, Jr., T. Vreven, K. N. Kudin, J. C. Burant, J. M. Millam, S. S. Iyengar, J. Tomasi, V. Barone, B. Mennucci, M. Cossi, G. Scalmani, N. Rega, G. A. Petersson, H. Nakatsuji, M. Hada, M. Ehara, K. Toyota, R. Fukuda, J. Hasegawa, M. Ishida, T. Nakajima, Y. Honda, O. Kitao, H. Nakai, M. Klene, X. Li, J. E. Knox, H. P. Hratchian, J. B. Cross, C. Adamo, J. Jaramillo, R. Gomperts, R. E. Stratmann, O. Yazyev, A. J. Austin, R. Cammi, C. Pomelli, J. W. Ochterski, P. Y. Ayala, K. Morokuma, G. A. Voth, P. Salvador, J. J. Dannenberg, V. G. Zakrzewski, S. Dapprich, A. D. Daniels, M. C. Strain, O. Farkas, D. K. Malick, A. D. Rabuck, K. Raghavachari, J. B. Foresman, J. V. Ortiz, Q. Cui, A. G. Baboul, S. Clifford, J. Cioslowski, B. B. Stefanov, G. Liu, A. Liashenko, P. Piskorz, I. Komaromi, R. L. Martin, D. J. Fox, T. Keith, M. A. Al-Laham, C. Y. Peng, A. Nanayakkara, M.

Challacombe, P. M. W. Gill, B. Johnson, W. Chen, M. W. Wong, C. Gonzalez, and J. A. Pople, Gaussian, Inc., Pittsburgh PA, (2003).

[10] D. R. Hartree, *Proc. Cam. Phil. Soc.*, 24 (1928) 89.

[11] D. R. Hartree, *Proc. Cam. Phil. Soc.*, 24 (1928) 111.

[12] D. R. Hartree, *Proc. Cam. Phil. Soc.*, 24 (1928) 426.

[13] V. Fock, *Z. Physik.*, 61 (1930) 126.

[14] J. C. Slater, *Phys. Rev.*, 34 (1929) 1293.

[15] J. C. Slater, *Phys. Rev.*, 35 (1930) 509.

[16] A. D. Becke, *J. Chem. Phys.*, 98 (1993) 5648.

[17] S. H. Vosko, L. Wilk, and M. Nusair, *Can. J. Phys.*, 58 (1980) 1200.

[18] C. Lee, W. Wang, and R. G. Parr, *Phys. Rev.* B, 37 (1988) 785.

[19] C. Møller and M. S. Plesset, *Phys. Rev.*, 46 (1934) 618.

[20] G. Hetzer, P. Pulay, and H.-J. Werner, *Chem. Phys. Lett.*, 290 (1998) 143.

[21] M. Schütz, G. Hetzer and H.-J. Werner, *J. Chem. Phys.*, 111 (1999) 5691.

[22] N. Godbout, D. R. Salahub, J. Andzelm, and E. Wimmer, *Can. J. Chem.*, 70 (1992) 560.

[23] C. Sosa, J. Andzelm, E. C. Elkin, E. Wimmer, K. D. Dobbs, and D. A. Dixon, *J. Phys. Chem.*, 96 (1992) 6630.

[24] F. London, *J. Phys. Radium*, 8 (1937) 397.

[25] R. McWeeny, *Phys. Rev.*, 126 (1962) 1028.

[26] R. Ditchfield, *Mol. Phys.*, 27 (1974) 789.

[27] J. L. Dodds, R. McWeeny, and A. J. Sadlej, *Mol. Phys.*, 41 (1980) 1419.

[28] K. Wolinski, J. F. Hilton, and P. Puley, *J. Am. Chem. Soc.*, 112 (1990) 8251.

[29] Amsterdam Density Functional program (ADF trial version 2006.01); Division of Theoretical Chemistry, Vrije University, De Boelelaan 1083, 1081 HV Amsterdam, The Netherlands; http://www.scm.com.

[30] M. S. Greenfield, A. D. Ronemus, R. L. Vold, R. R. Vold, P. D. Ellis, and T. E. Raidy, *J. Magn. Reson.*, 72 (1987) 89.

[31] BPP software, created by Stephen Daleman, Department of Chemistry, *University of Guelph*, Guelph, ON, Canada.

RESULTS AND DISCUSSION

OBJECTIVES

1. Objectives of Solid State NMR and Quantum Chemical Calculation Studies of Silver Containing Compounds:

i) To measure the ^{109}Ag chemical shift tensor components, (δ_{11}, δ_{22} and δ_{33}), in a series of NHC silver complexes.

ii) To measure the ^{109}Ag and ^{13}C chemical shift tensor components, (δ_{11}, δ_{22} and δ_{33}), in a series of silver-aromatic complexes.

iii) A comparison of the spectra to what is expected from known crystal structures.

iv) To use the experimental results to make predictions about the crystal structures.

v) To investigate the use of quantum chemical calculations in predicting silver chemical shifts.

2. Objectives of Deuterium Lineshape and T_1 Studies of Deuterated-Benzene Silver Perchlorate Complexes

i) To investigate the ring dynamics in silver-benzene complexes.

ii) A comparison with known activation energies for other benzene complexes.

3. Objectives of Solid State NMR Study of An Arsenic Containing Compound

i) To obtain the solid state ^{75}As NMR parameters from the central transition spectra in some arsenic-containing compounds in which the arsenic sites have high symmetric characters.

ii) A comparison of the ^{127}I quadrupolar coupling constants of Me_4AsI and Me_4NI to what is expected from known crystal structures.

iii) To investigate the effects of quadrupolar nuclei (^{75}As) on NMR spectra of spin = ½ (^{13}C).

iv) To investigate the dynamics of the Me_4As^+ cation in solid Me_4AsI.

Chapter VI

Solid State MAS NMR and Quantum Chemical Studies of Silver Complexes

6. 1 N-Heterocyclic Carbene Silver Complexes

N-heterocyclic carbene (NHC) silver complexes have been reported recently to behave as efficient catalysts in transesterification reactions [1], and they are the most popular complexes used for NHC transfer [2, 3]. Their common use as transfer agents is due to their straightforward synthesis, usually circumventing the need for free NHC isolation, and the relative stability of the Ag-NHC complexes in air and light [2, 4].

NHCs have been very important ligands for metal catalyzed Suzuki and Negishi coupling reactions [5, 6, 7]. The importance of these compounds is in part due to their ability to bind to a wide variety of metals in a fashion akin to the previously popular phosphine-based ligands.

NHCs are depicted in Figure 6.1.1. The stability of an NHC is largely due to the π-donation from the p orbitals of the carbene. NHCs have been found to be excellent σ-donors to metals which were believed the principle binding mode. Back-donation from the metal to the ligand was believed to be "negligible". However, recent theoretical and structural evidence has suggested that π-back-donation plays a larger role than previously thought. The degree of back-donation is dependent upon the metal of interest.

Several theoretical studies have been done involving N- Heterocyclic carbene complexes of Group 11 metals [8, 9, 10]. An analysis of the bonding revealed the population of the relevant orbitals in the group 11 NHC complexes. This analysis is consistent with the bonding orbitals of the Ag(I) being a hybridization of the filled d_{z^2} orbital and empty s orbital [8]. This is rationalized as Coulombic repulsion from the lone pair of the NHC forcing the d_{z^2} and s orbitals to hybridize.

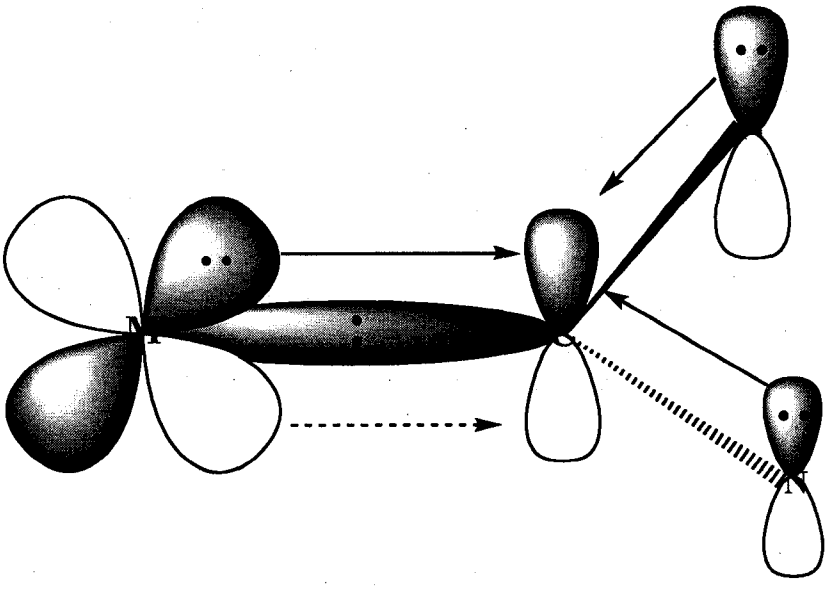

Figure 6.1.1 Orbital diagram of a N-heterocyclic carbene.

Analyses of NHC carbenes of both silver NHC halide and silver N-heterocyclic biscarbenes by Ziegler and Rauk's energy decomposition schemes suggested that the bonds are mostly electrostatic in nature, with orbital interactions making a smaller concentration [9]. The stabilization energy from the orbital interactions using this method was found to be approximately 70% coming from σ interactions and 30% from π interactions. The calculated π interactions suggested a fairly high degree of π-back-donation for the silver NHC systems. However, π-back-donation for other similar silver carbene systems was found to be approximately half that of the previous value [10].

The π-donation of the nitrogen atoms to the empty p orbital is due to the carbene increasing the amount of electron density by drawing electron density from the lone pairs of the adjacent nitrogen atoms. Structural evidence also supports this theoretical view by comparison of the carbene-nitrogen bond distances of the complex vs. the free carbene [11, 12].

The structure characterization of NHC complexes of silver has led to very complex bonding motifs in the solid state, especially in complexes with halide anions. They can be divided into two main areas, mono-NHC (one NHC per ligand) and multi-NHC (more than one NHC per ligand) complexes, mono-NHC complexes being the most prominent in this thesis.

A series of N-heterocyclic carbene NHC-AgCl complexes [NHC = SIMes, Imes, IPr, SIpr, IEt, Ity, and SIPrFL] were synthesized by the research group of Michael G. Organ of the Chemistry Department in York University. The compounds were synthesized through reaction of the imidazolium chloride salts with Ag_2O or by direct metalation of the corresponding imidazol-2-ylidene carbene in the presence of AgCl [13]. ^{109}Ag solid state NMR spectra of this series of silver NHC complexes were obtained in this work.

6.1.1 Solid State ^{109}Ag NMR Spectra of Silver NHC Complexes

6.1.1.1 SIPr-AgCl (1,3-bis(2,6-diisopropylphenyl)imidazolidin-2-ylidene silver(I) chloride)

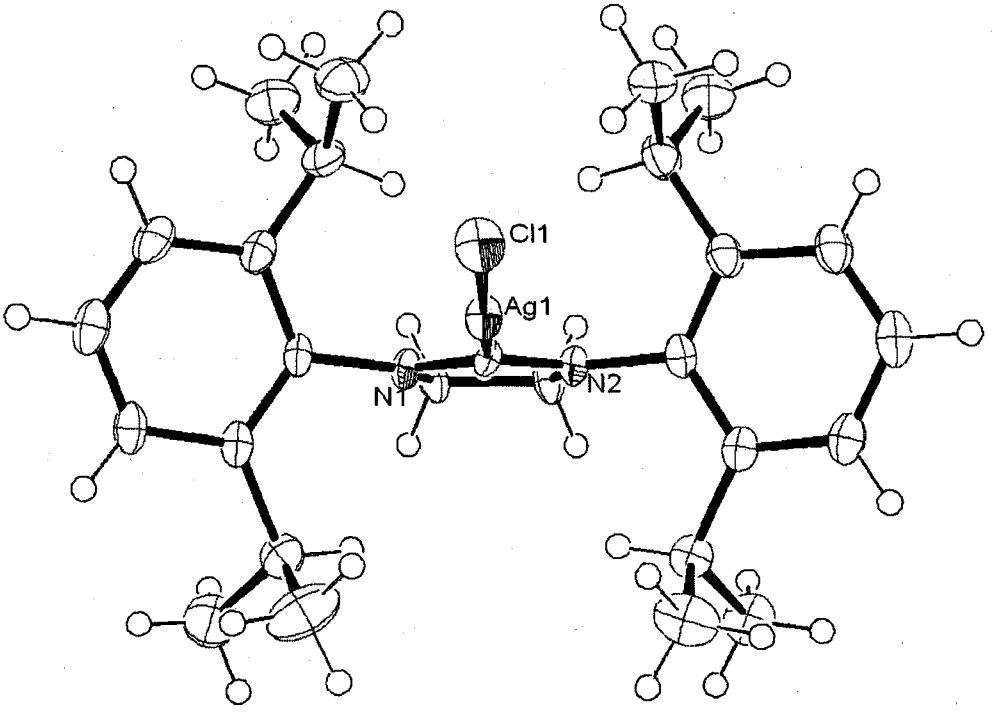

Figure 6.1.2 An ORTEP-III drawing of SIPr-AgCl (1,3-bis(2,6-diisopropylphenyl) imidazolidin-2-ylidene silver(I) chloride) [13].

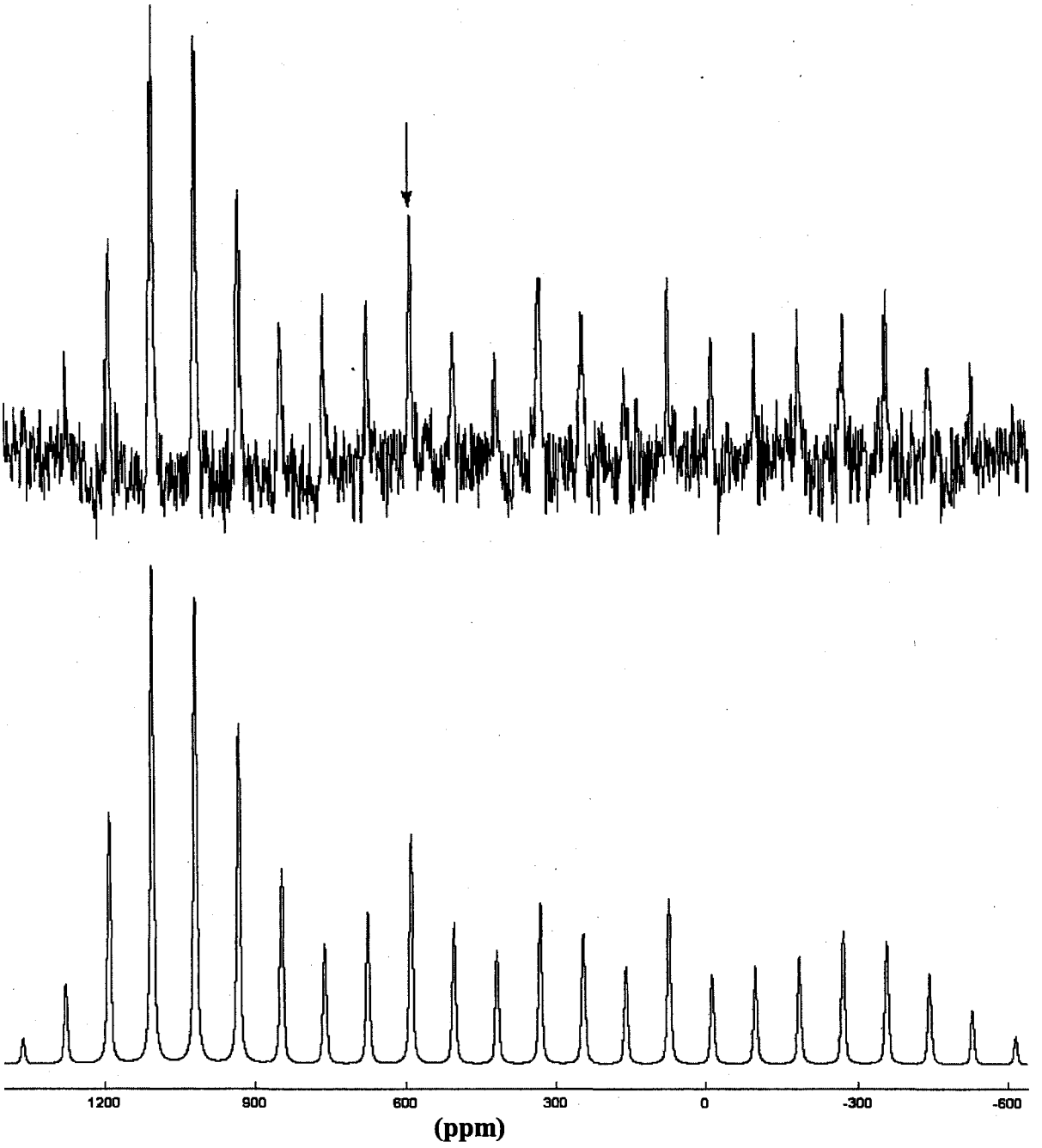

Figure 6.1.3 Experimental (top) and simulated (bottom) ^{109}Ag CP/MAS NMR spectra of SIPr-AgCl(1,3-bis(2,6-diisopropylphenyl)imidazolidin-2-ylidene silver(I) chloride): $\nu_R = 2$ kHz; NS = 8000. The arrow indicates the isotropic chemical shift.

Table 6.1.1 Solid state ^{109}Ag NMR parameters of SIPr-AgCl obtained from the simulation of the experimental spectrum.

δ_{11}	δ_{22}	δ_{33}	δ_{iso}	Ω	κ
1230 (38)	1136 (36)	-600 (28)	588.7 (7)	1830 (50)	0.88 (0.04)

6.1.1.2 IPr-AgCl (1,3-bis(2,6-diisopropylphenyl)imidazol-2-ylidene silver(I)chloride)

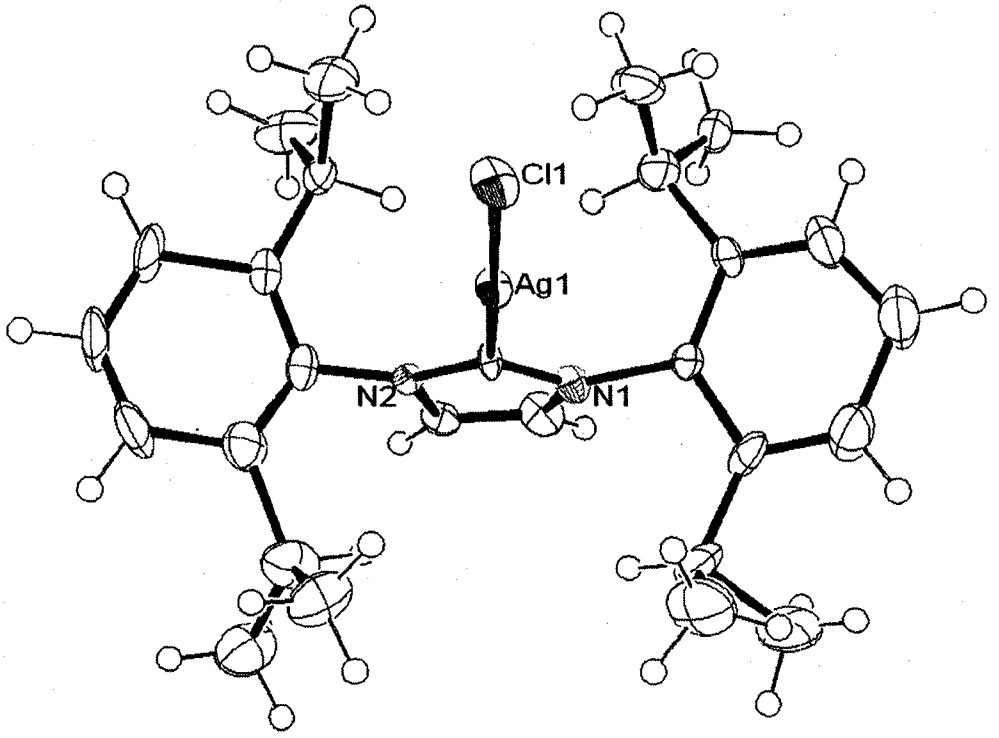

Figure 6.1.4 An ORTEP-III drawing of IPr-AgCl (1,3-bis(2,6-diisopropylphenyl) imidazol-2-ylidene silver(I) chloride) [13].

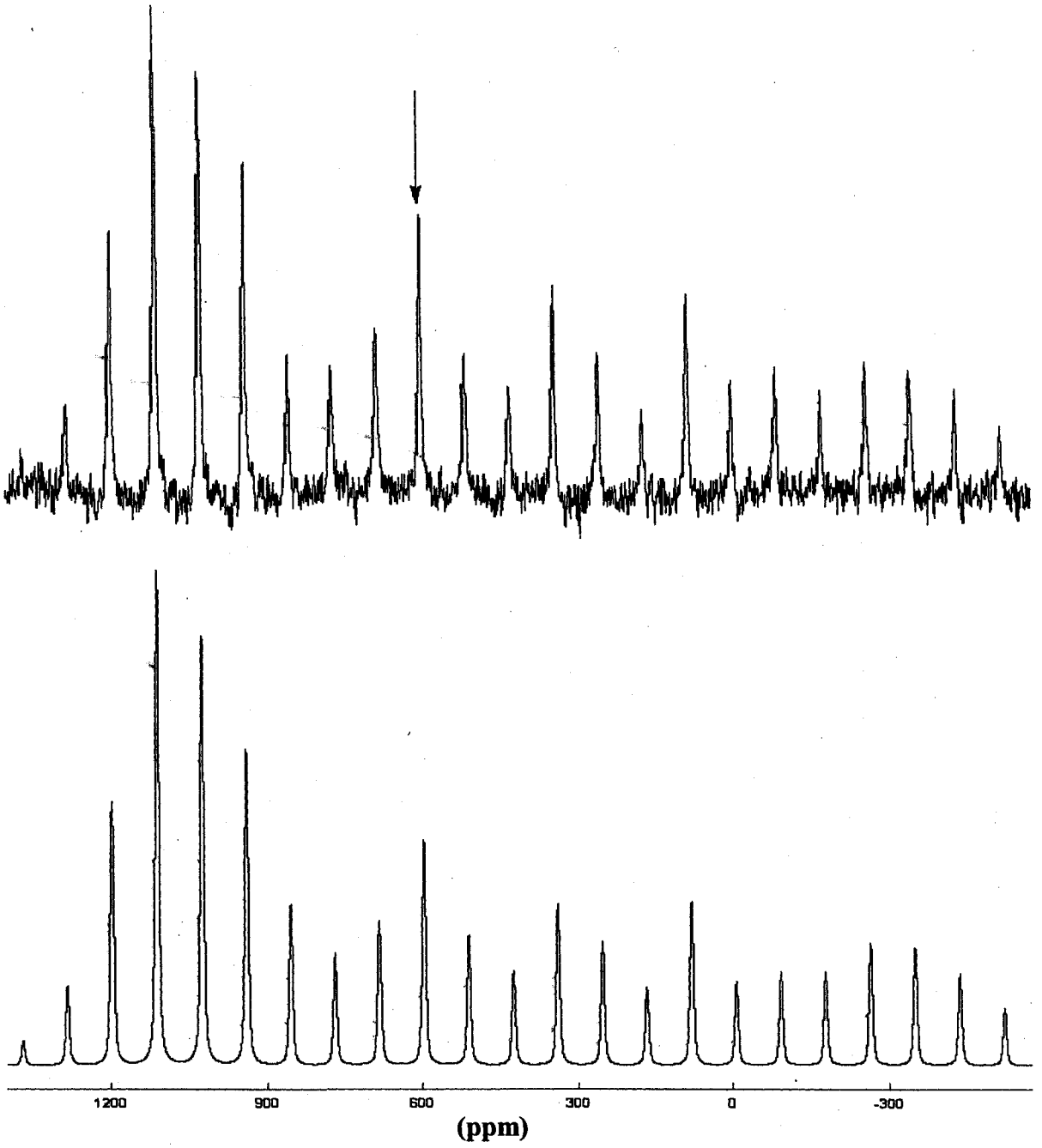

Figure 6.1.5 Experimental (top) and simulated (bottom)^{109}Ag CP/MAS NMR spectra of IPr-AgCl(1,3-bis(2,6-diisopropylphenyl)imidazol-2-ylidene silver(I) chloride): ν_R = 2 kHz, NS = 10000. The arrow indicates the isotropic chemical shift.

Table 6.1.2 Solid state ^{109}Ag NMR parameters of IPr-AgCl obtained from the simulation of the experimental spectrum.

δ_{11}	δ_{22}	δ_{33}	δ_{iso}	Ω	κ
1210 (44)	1188 (50)	-612 (36)	595.3 (6)	1822 (50)	0.96 (0.04)

6.1.1.3 IMes-Ag-IMes (Bis(1,3-bis(2,6-diisopropylphenyl)imidazol-2-ylidene) silver(I))

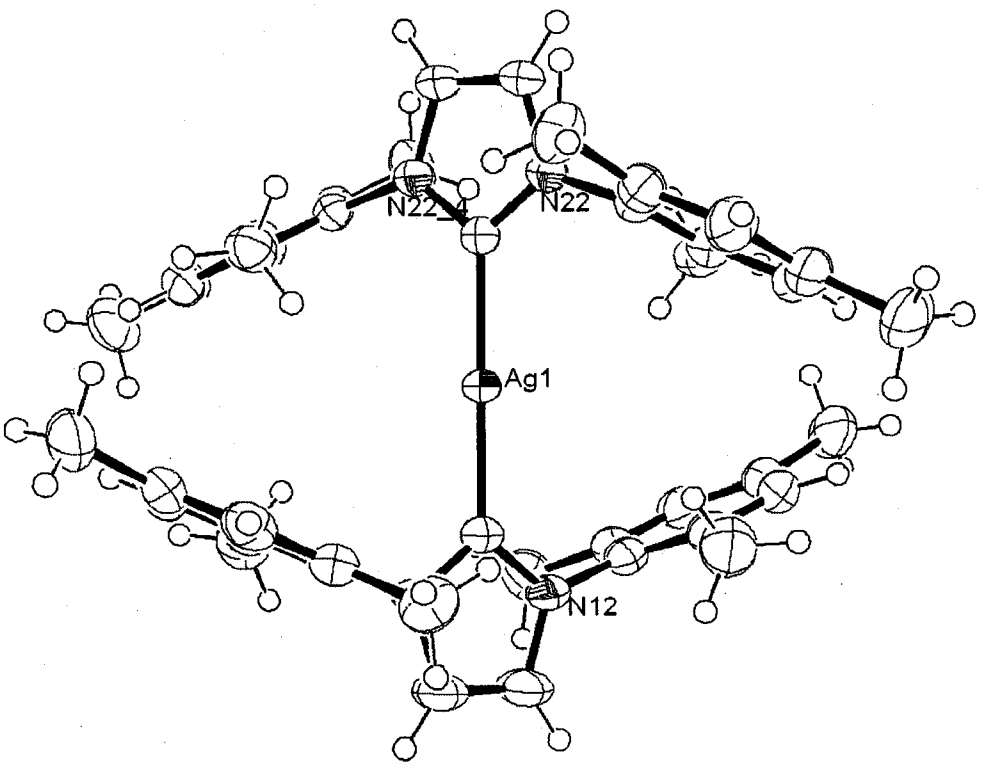

Figure 6.1.6 An ORTEP-III drawing of IMes-Ag-IMes (Bis(1,3-bis(2,4,6 trimethylphenyl)imidazol-2-ylidene) silver(I)) [13].

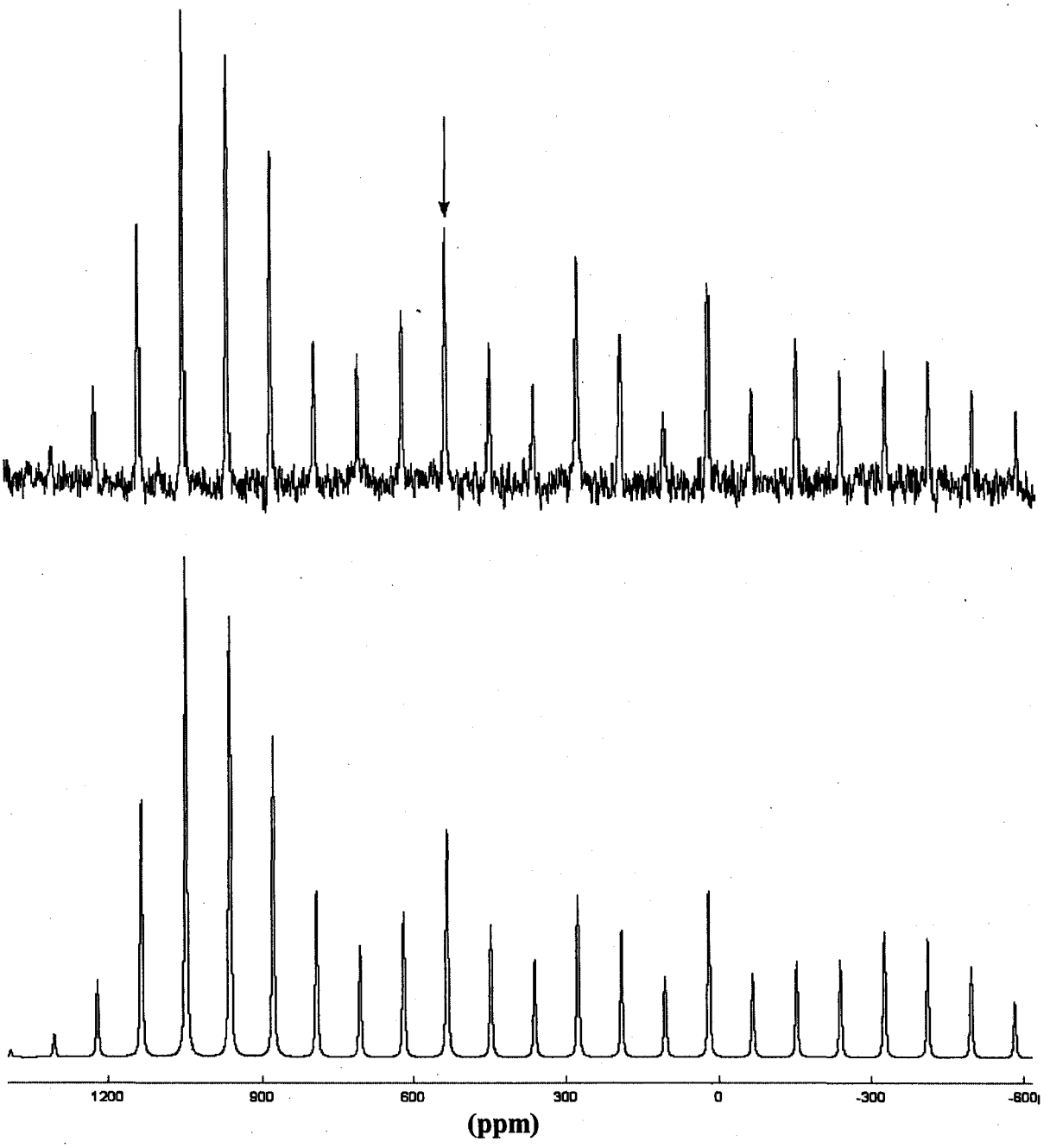

Figure 6.1.7 Experimental (top) and simulated (bottom) ^{109}Ag CP/MAS NMR spectra of IMes-Ag-IMes (Bis(1,3-bis(2,4,6-trimethylphenyl)imidazol-2-ylidene) silver(I)): $\nu_R = 2$ kHz; NS = 10000. The arrow indicates the isotropic chemical shift.

Table 6.1.3 Solid state ^{109}Ag NMR parameters of IMes-Ag-IMes obtained from the simulation of the experimental spectrum.

δ_{11}	δ_{22}	δ_{33}	δ_{iso}	Ω	κ
1140 (54)	1130 (56)	-668 (42)	534 (5)	1808 (60)	0.96 (0.04)

6.1.1.4 SIMes-AgCl ((1,3-bis(2,6-diisopropylphenyl)imidazolidin-2-ylidene) silver(I)) chloride

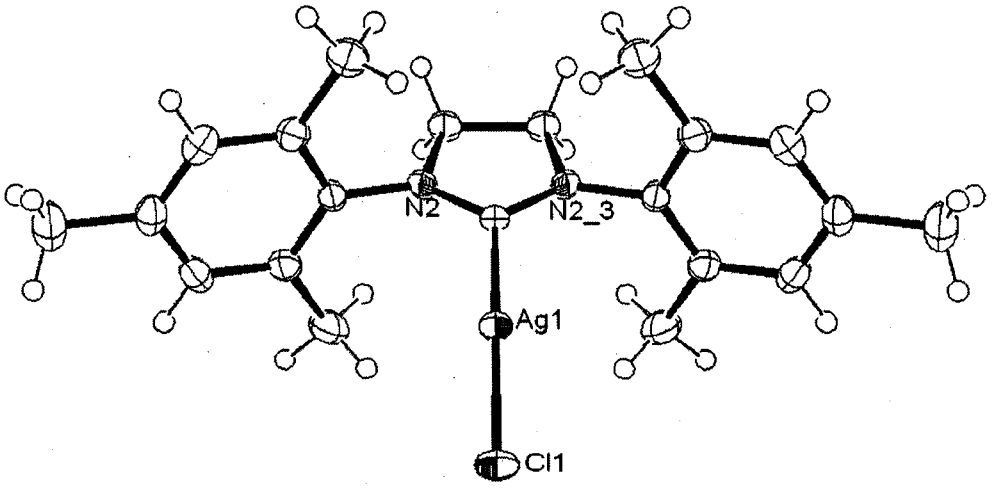

Figure 6.1.8 An ORTEP-III drawing of SIMes-AgCl (1,3-bis(2,4,6-trimethylphenyl) imidazolidin-2-ylidene silver(I) chloride) [13].

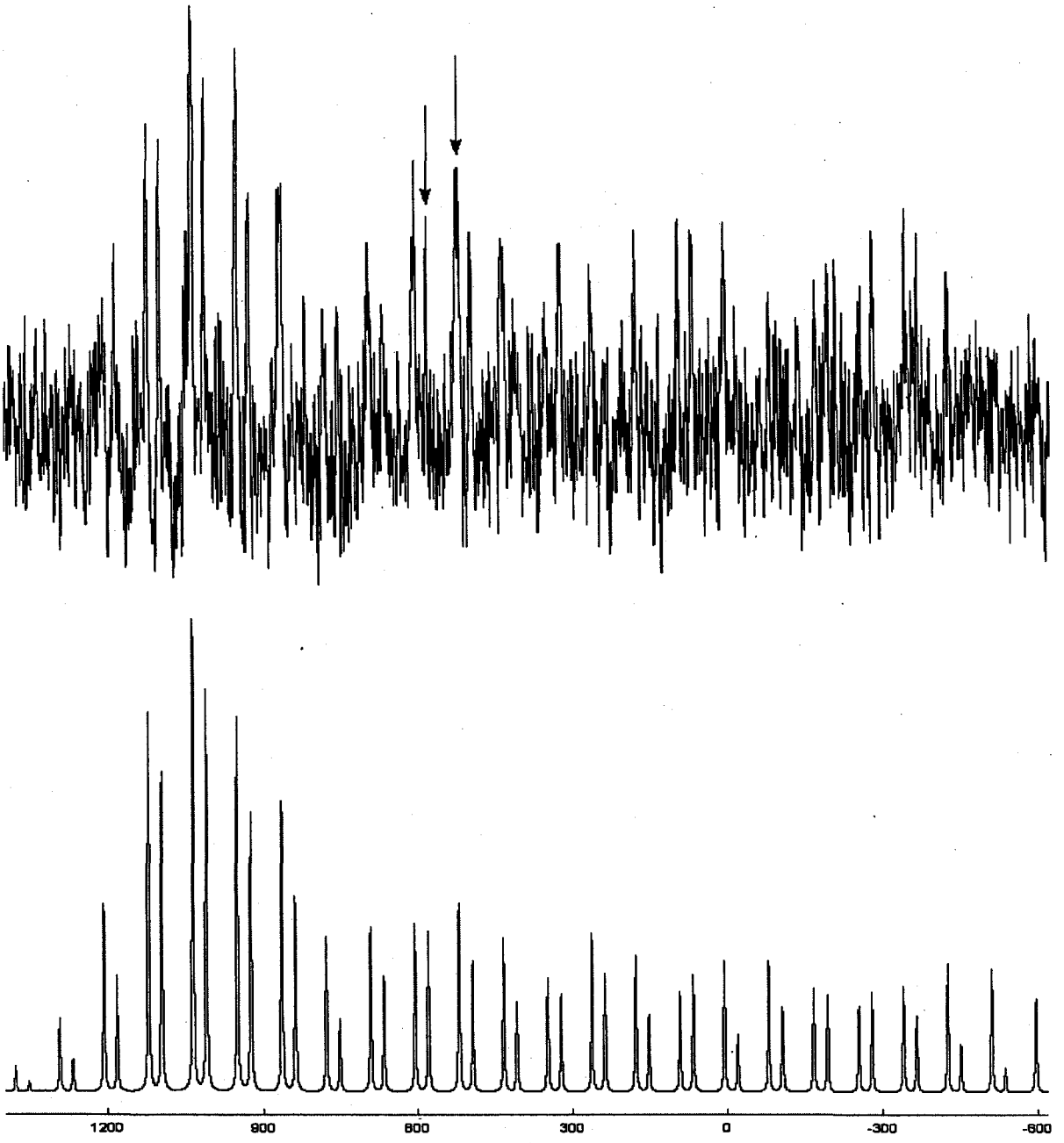

Figure 6.1.9 Experimental (top) and simulated (bottom) ^{109}Ag CP/MAS NMR spectra of SIMes-AgCl. ν_R = 2 kHz; NS = 10000 and an intensity ratio of 1:1. The arrows indicate the isotropic chemical shifts.

Table 6.1.4 Solid state ^{109}Ag NMR parameters of SIMes-AgCl obtained from the simulation of the experimental spectrum.

δ_{11}	δ_{22}	δ_{33}	δ_{iso}	Ω	κ
1220 (68)	1060 (64)	-720 (48)	520 (6)	1940 (100)	0.81 (0.08)
1140 (60)	1140 (60)	-540 (48)	580 (6)	1680 (120)	0.95 (0.05)

6.1.1.5 IEt-AgCl (1,3-bis(2,6-diethylphenyl)imidazol-2-ylidene silver(I)chloride)

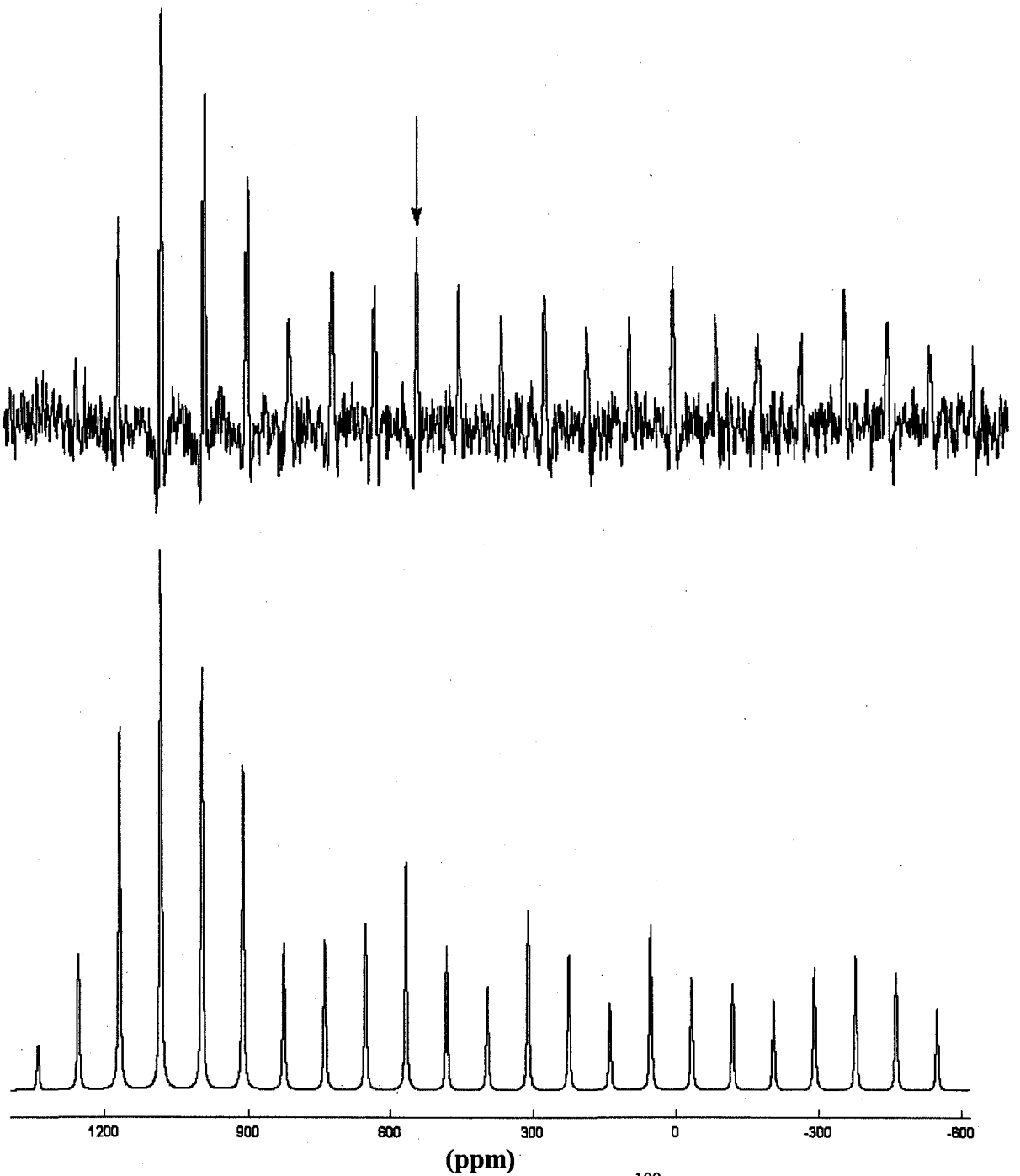

Figure 6.1.10 Experimental (top) and simulated (bottom) ^{109}Ag CP/MAS NMR spectra of IEt-AgCl: ν_R = 2 kHz; NS = 10000. The arrow indicates the isotropic chemical shift.

Table 6.1.5 Solid state ^{109}Ag NMR parameters of IEt-AgCl obtained from the simulation of the experimental spectrum.

δ_{11}	δ_{22}	δ_{33}	δ_{iso}	Ω	κ
1218 (45)	1158 (42)	-672 (38)	568 (5)	1890 (52)	0.94 (0.06)

6.1.1.6 Ity-AgCl

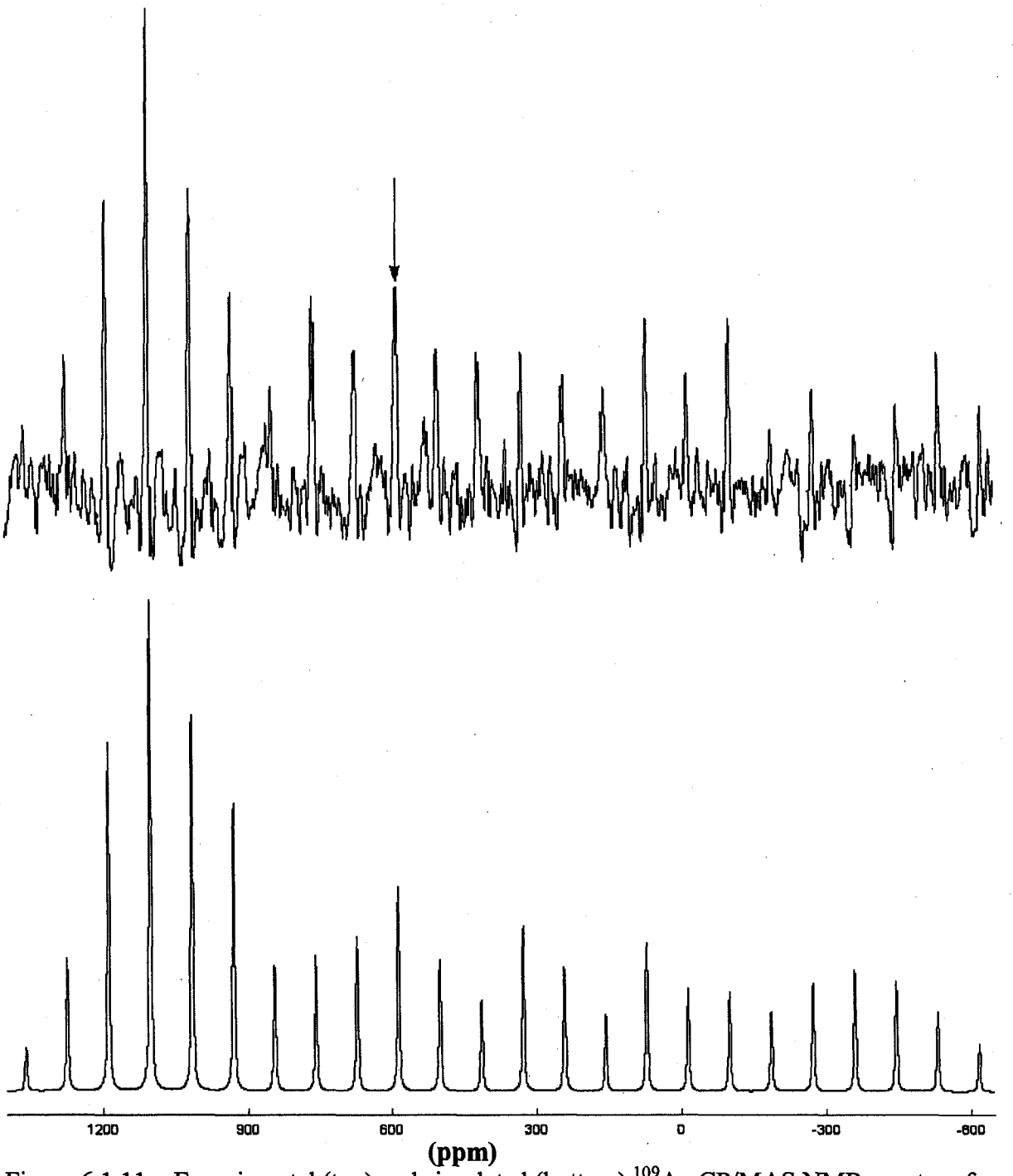

Figure 6.1.11 Experimental (top) and simulated (bottom) ^{109}Ag CP/MAS NMR spectra of Ity-AgCl: ν_R = 2 kHz; NS = 10000. The arrow indicates the isotropic chemical shift.

Table 6.1.6 Solid state ^{109}Ag NMR parameters of Ity-AgCl obtained from the simulation of the experimental spectrum.

δ_{11}	δ_{22}	δ_{33}	δ_{iso}	Ω	κ
1268 (44)	1162 (42)	-680 (34)	583.3 (6)	1980 (50)	0.88 (0.08)

6.1.1.7 SIPrFL-AgCl

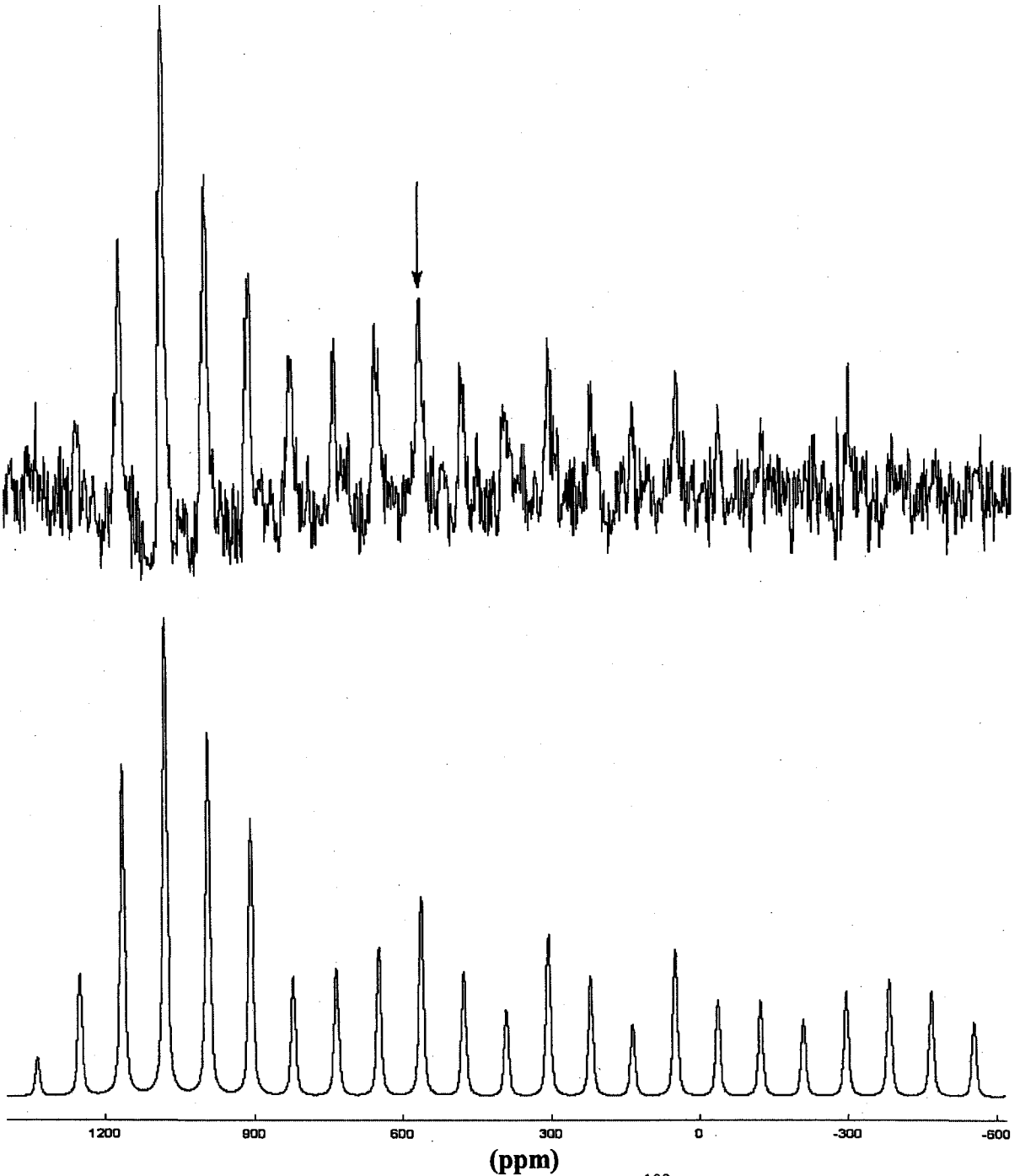

Figure 6.1.12 Experimental (top) and simulated (bottom) ^{109}Ag CP/MAS NMR spectra of SIPrFL-AgCl: ν_R = 2 kHz; NS = 10000. The arrow indicates the isotropic chemical shift.

Table 6.1.7 Solid state ^{109}Ag NMR parameters of SIPrFL-AgCl obtained from the simulation of the experimental spectrum.

δ_{11}	δ_{22}	δ_{33}	δ_{iso}	Ω	κ
1240 (58)	1150 (52)	-700 (48)	563.3 (8)	1940 (90)	0.90 (0.09)

6.1.2 Discussion of the ^{109}Ag Solid State NMR Study of Various Silver NHC Complexes

Although the solid state structure of silver NHCs, revealed by X-ray diffraction studies, gives an abundance of structural information (Table 6.1.8 shows structural parameters of some silver NHC complexes), the solid state NMR study of these complexes provides insight into the nuances of NHC-Ag bonding (Table 6.1.9 organized all of our NHC complexes' solid state NMR parameters).

Table 6.1.8 Structural parameters of some silver NHC complexes.

Compound	Lattice point group	Space group	Symmetry elements
SIPr-AgCl	Monoclinic (Z=8)	$P2_1/n$	2-fold screw axis, inversion center, glide plane
IPr-AgCl	Monoclinic (Z=2)	$P2_1$	2-fold screw axis
IMes-Ag-IMes	Monoclinic (Z=8)	Pbcn	2-fold screw axis, 2-fold rotation axis, inversion centers, glide plane
SIMes-AgCl	Monoclinic (Z=2)	$Cmc2_1$	2-fold screw axis, glide plane, mirror plane, centering vector

From the crystal structure we know that IMes is a multi-NHC complex - the complex of silver with noncoordinating anions exists as biscarbene salts with the cationic silver bound by two carbene moieties and the noncoordinating anion balancing out the charge (C_2-Ag) and the others are mono-NHC complexes - the bonding motifs of these complexes have been characterized by coordinating halide directly bonding silver (C-Ag-X). The short distances between Ag and C/Cl indicate the significant covalent bonding.

The crystalline form of SIPr-AgCl is in the monoclinic space group $P2_1/n$ [13] with Z=8. The structure also shows that the Ag cations are related by inversion centers and thus chemically and magnetically equivalent. This is in accordance with the ^{109}Ag CP/MAS NMR spectrum, which consists of one pattern of spinning sidebands.

IPr-AgCl crystallizes in the monoclinic space group $P2_1$ with Z=2 [13]. The structure also shows that the Ag cations are not magnetically equivalent. But this is not in agreement with the ^{109}Ag CP/MAS NMR spectrum, which consists of one pattern of spinning sidebands. However, one can not rule out the possibility that the two inequivalent silver nuclei happen to have nearly the same chemical shift.

The crystalline form of IMes-Ag-IMes is monoclinic and belongs to the space group Pbcn with Z=8 [13]. The structure also shows that the Ag cations are related by inversion centers and thus chemically and magnetically equivalent. This is in accordance with the ^{109}Ag CP/MAS NMR spectrum, which consists of one pattern of spinning sidebands.

Solid SIMes-AgCl exists in the monoclinic space group $Cmc2_1$ with two magnetically inequivalent Ag atoms in the crystallographic asymmetric unit (no inversion center relating the Ag atoms) [13]. This structure implies that one should see two signals in the ^{109}Ag CP/MAS NMR spectrum. Two patterns of spinning sidebands illustrate this. The same molecular structure also indicates that the structure difference between the two inequivalent silver atoms is small. The close isotropic chemical shifts are consistent with this observation.

Table 6.1.9 The solid state NMR parameters of some silver NHC complexes.

Compound	δ_{11}	δ_{22}	δ_{33}	δ_{iso}	Ω	κ
SIPr-AgCl	1230 (38)	1136 (36)	-600 (28)	588.7 (7)	1830 (50)	0.88 (0.04)
IPr-AgCl	1210 (44)	1188 (50)	-612 (36)	595.3 (6)	1822 (50)	0.96 (0.04)
IMes-Ag-IMes	1140 (54)	1130 (56)	-668 (42)	534 (5)	1808 (60)	0.96 (0.04)
SIMes-AgCl	1220 (68)	1060 (64)	-720 (48)	520 (6)	1940 (100)	0.81 (0.08)
	1140 (60)	1140 (60)	-540 (48)	580 (6)	1680 (120)	0.95 (0.05)
Iet-AgCl	1218 (45)	1158 (42)	-672 (38)	568 (5)	1890 (52)	0.94 (0.06)
Ity	1268 (44)	1162 (42)	-680 (34)	583.3 (6)	1980 (50)	0.88 (0.08)
SIPrFL	1240 (58)	1150 (52)	-700 (48)	563.3 (8)	1940 (90)	0.90 (0.09)

The κ values of these silver NHC complexes are close to 1, which indicates that the ^{109}Ag shielding is nearly axially symmetric. This is as expected from the near linear C-Ag-Cl/C geometry in all of the NHC complexes studied here. This linear symmetry at silver sites has been shown in section 6.1.

The solid state ^{109}Ag CP/MAS NMR spectra of Iet-AgCl, Ity and SIPrFL show a single pattern of spinning sidebands, therefore one type of Ag atom exists in each of these three complexes. The span (Ω) for all of the complexes are relatively large (1680 – 1980 ppm), indicating a large anisotropy in the ^{109}Ag chemical shift. This is consistent with most other compounds where silver is in a linear arrangement.

Chapter 6-1: References

[1] A.C. Sentman, C. Szilárd, R. M. Waymouth, J. L. Hedrick, *J. Org. Chem.*, 70 (2005) 2391.

[2] H. M. Wang, I.J.B. Lin, *Organometallics*, 17 (1998) 972.

[3] I. J. B. Lin, C. S. Vasam, *Comm. Inorg. Chem.*, 25 (2004) 75.

[4] M. V. Baker, D. H. Brown, R. A. Haque, B. W. Skelton, A. H. White, *J. Chem. Soc.*, DaltonTrans., (2004) 3756.

[5] C. J. O'Brien, E. A. B. Kantchev, G. A. Chass, N. Hadei, A. C. Hopkinson, M. G. Organ, D. H. Setiadi, T. Tang, and D. Fang, *Tetrahedron*, 61 (2005) 9723.

[6] J. C. Garrison, and W. J. Youngs, *Chem. Rev.*, 105 (2005) 3978.

[7] A. Fürstner, *Angew Chem. Int. Ed.*, 39 (2000) 3031.

[8] C. Boehme, G. Frenking, *Organometallics*, 17 (1998) 5801.

[9] D. Nemcsok, K. Wichmann, G. Frenking, *Organometallics*, 23 (2004) 3640.

[10] X. Hu, I. Castro-Rodriguez, K. Olsen, K. Meyer, *Organometallics*, 23 (2004) 3640.

[11] A. J. Arduengo, III, R. L. Harlow, M. Kline, *J. Am. Chem. Soc.*, 113 (1991) 361.

[12] A. J. Arduengo, III, H. V. R. Dias, J. C. Calabrese, F. Davidson, *Organometallics*, 12 (1993) 3405.

[13] P. de Frémont, N. M. Scott, E. D. Stevens, T. Ramnial, O. C. Lightbody, C. L. B. Macdonald, J. A.C. Clyburne, C. D. Abernethy, S. P. Nolan, *Organometallic*, 24 (2005) 6301.

6.2 Solid State NMR Study of Some Silver-arene Complexes

Complexes of benzene with Ag (I) have been extensively studied since the very beginning of modern day transition metal arene chemistry [1]. Crystal structures of several complexes of the form $AgX\text{-}C_6H_6$ are known, with stoichiometric ratios of 2:1 (X= CF_3CO_2 [2]), 1:1 (X=ClO_4 [3, 4, 5], X= $AlCl_4$ [6], X= $N(SO_2F)_2$ [7], and X=CF_3SO_3 [8, 9]), 1:2 (X= $CB_{11}H_{11}F$ [10], X=$CB_9H_8F_2$ [11]) and 1:3 (X=BF_4 [12]), depending on the nature of the anion. The coordination mode of the arene to the Ag (I) is also variable, between η^1 and η^2, with benzene acting as a terminal or bridging ligand.

The silver cation behaves as both an electron acceptor and an electron back-donor. The silver accepts electrons from the aromatic ring, and back-donates electrons to a π^* orbital of the ring. The best overlap is achieved when the silver is positioned midway between two carbons of the aromatic ring.

6.2.1. Solid State ^{109}Ag and ^{13}C NMR Spectra of Some Silver-Arene Complexes

6.2.1.1 Benzene Silver Perchlorate Complexes

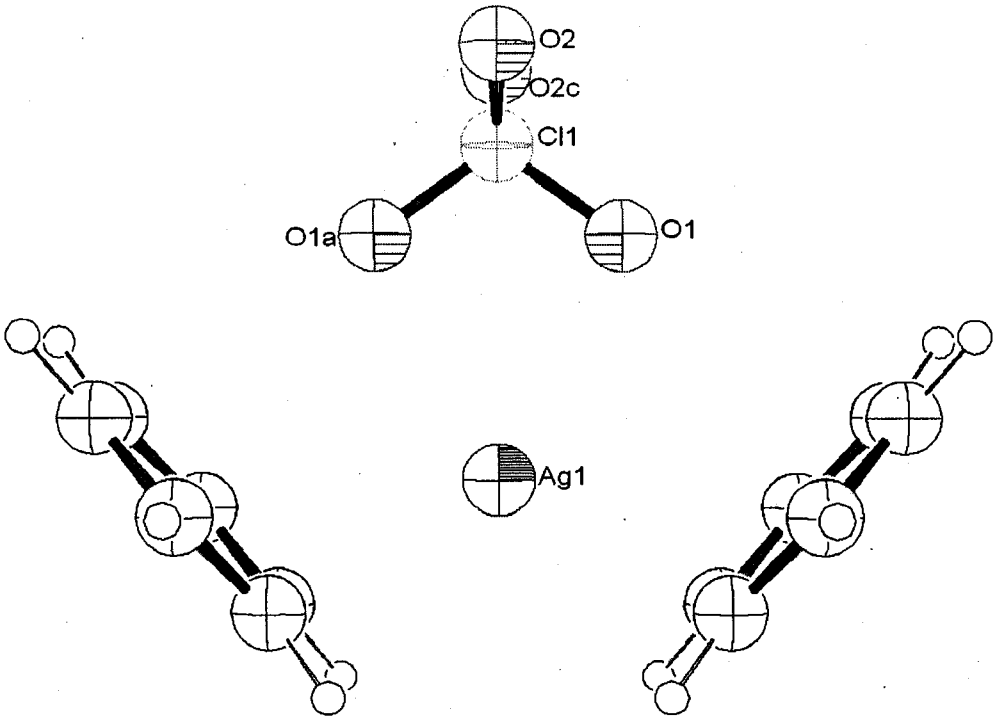

Figure 6.2.1 An ORTEP-III drawing of benzene silver perchlorate complexes ($C_6H_6 \cdot AgClO_4$) [5]

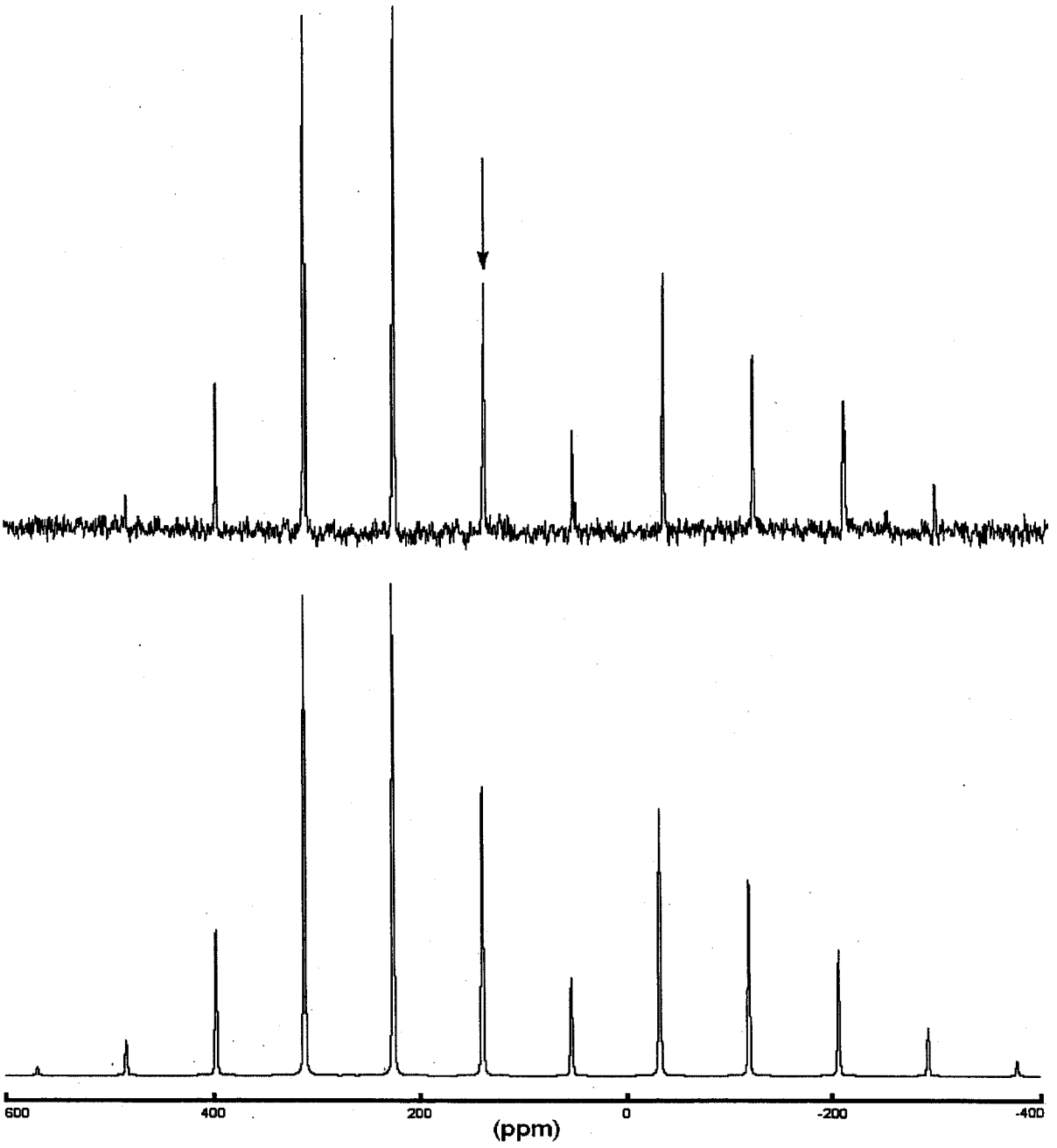

Figure 6.2.2 Experimental (top) and simulated (bottom) solid state ^{109}Ag CP/MAS NMR spectra of $C_6H_6 \cdot AgClO_4$. $\nu_R = 2$ kHz, NS = 4000. The arrow indicates the isotropic chemical shift.

Table 6.2.1 Solid state ^{109}Ag NMR parameters of $C_6H_6 \cdot AgClO_4$ obtained from the simulation of the experimental spectrum.

δ_{11}	δ_{22}	δ_{33}	δ_{iso}	Ω	κ
418 (8)	292 (8)	-292 (6)	139 (2)	710 (12)	0.64 (0.02)

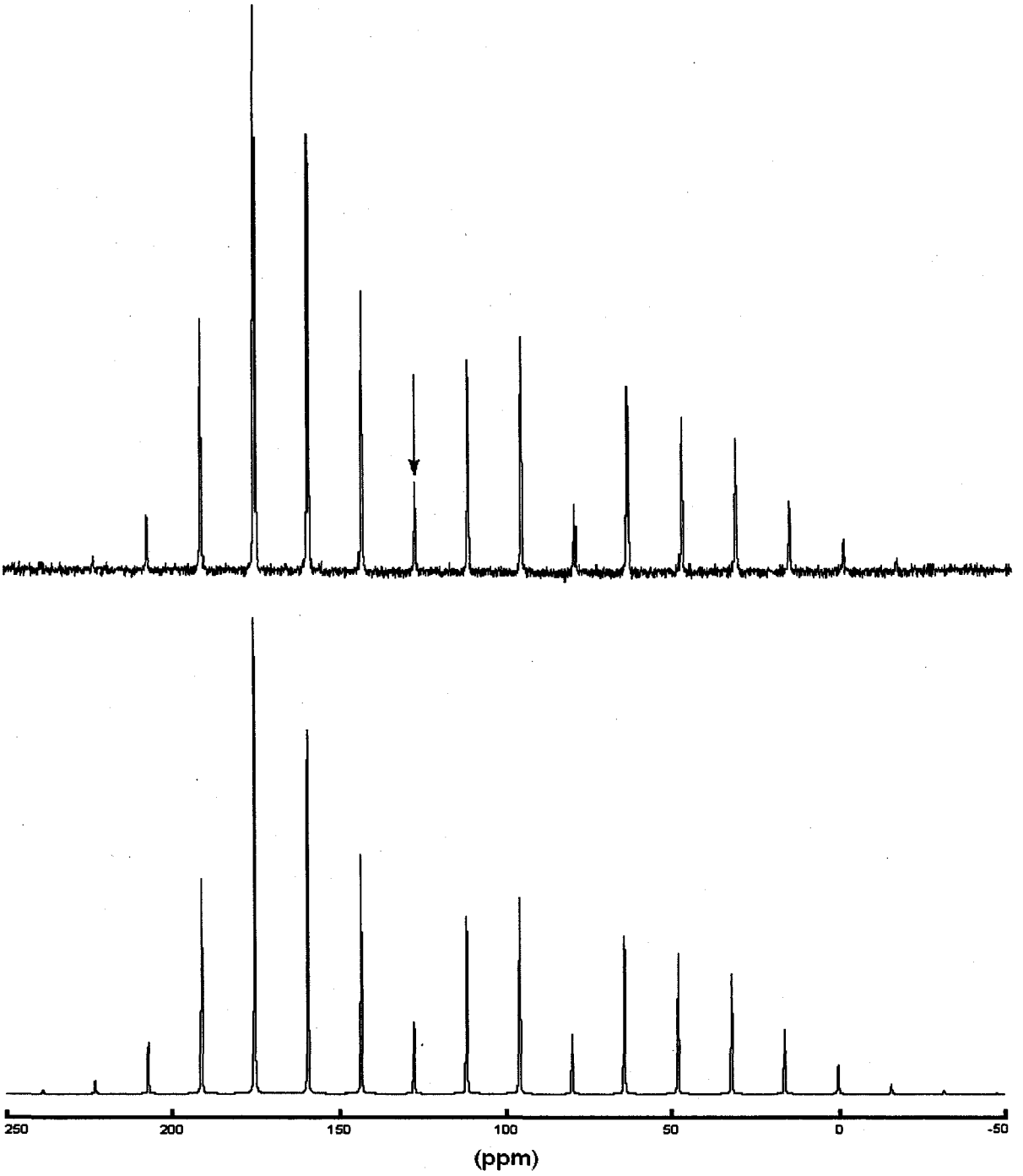

Figure 6.2.3 Experimental (top) and simulated (bottom) solid state ^{13}C CP/MAS NMR spectra of $C_6H_6 \cdot AgClO_4$: $\nu_R = 2$ kHz, NS = 400. The arrow indicates the isotropic chemical shift.

Table 6.2.2 Solid state ^{13}C NMR parameters of $C_6H_6 \cdot AgClO_4$ obtained from the simulation of the experimental spectrum.

δ_{11}	δ_{22}	δ_{33}	δ_{iso}	Ω	κ
196 (6)	184 (4)	3 (6)	128 (1)	193 (10)	0.87 (0.04)

6.2.1.2 Benzene Silver Trifluoroacetate ($C_6H_6 \cdot AgCF_3CO_2$)

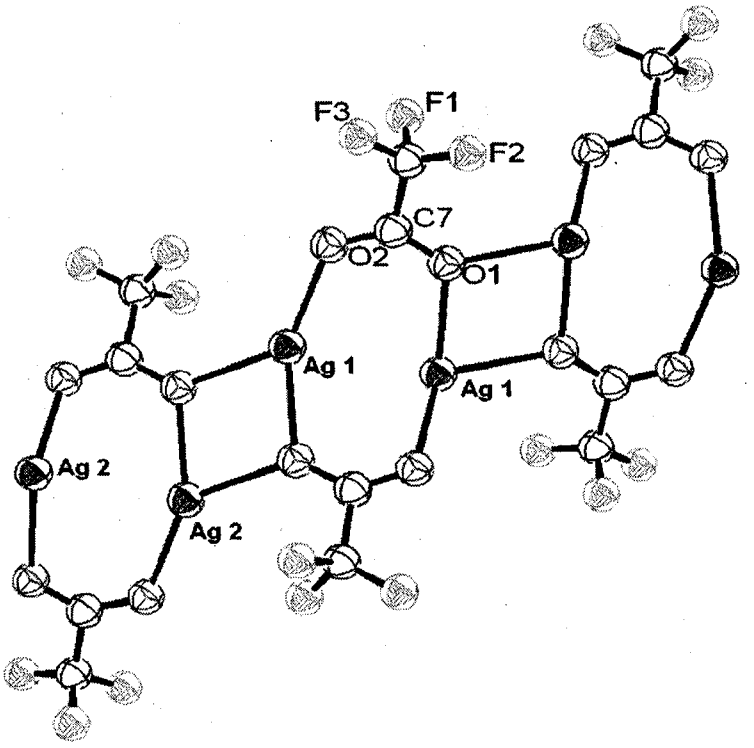

Figure 6.2.4 One of the parallel chains of Ag atoms is defined by only Ag(2) and the other by Ag(1), both running horizontal in this view. Ag(1) is bound to benzene (not shown) and three oxygen atoms, Ag(2) is bound only three oxygen atoms [2].

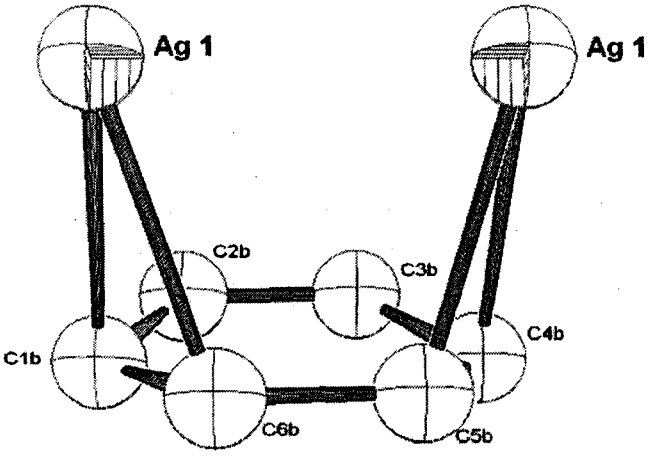

Figure 6.2.5 The structure of benzene bonding to Ag(1) in solid $C_6H_6 \cdot AgCF_3CO_2$ [2].

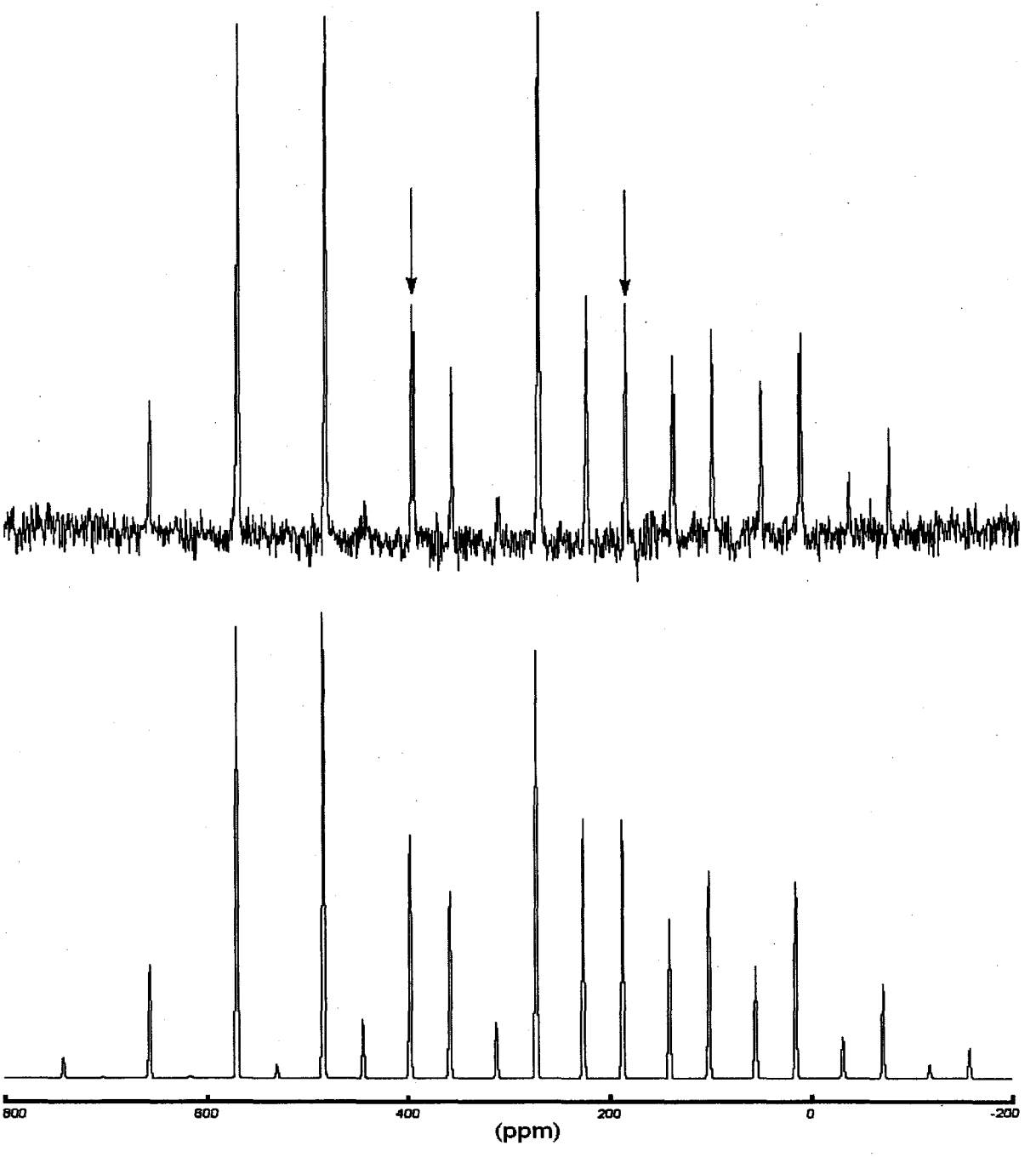

Figure 6.2.6 Experimental (top) and simulated (bottom) solid state ^{109}Ag CP/MAS NMR spectra of benzene silver trifluoroacetate ($C_6H_6 \cdot AgCF_3CO_2$). $\nu_R = 2$ kHz, NS = 5339, the total intensity ratio is 1:1. The arrows indicate the isotropic chemical shifts.

Table 6.2.3 Solid state ^{109}Ag NMR parameters of $C_6H_6 \cdot AgCF_3CO_2$ obtained from the simulation of the experimental spectrum.

δ_{11}	δ_{22}	δ_{33}	δ_{iso}	Ω	κ
630 (16)	596 (14)	-32 (11)	398 (2)	662 (22)	0.89 (0.03)
440 (16)	250 (14)	-130 (11)	187 (2)	570 (22)	0.33 (0.03)

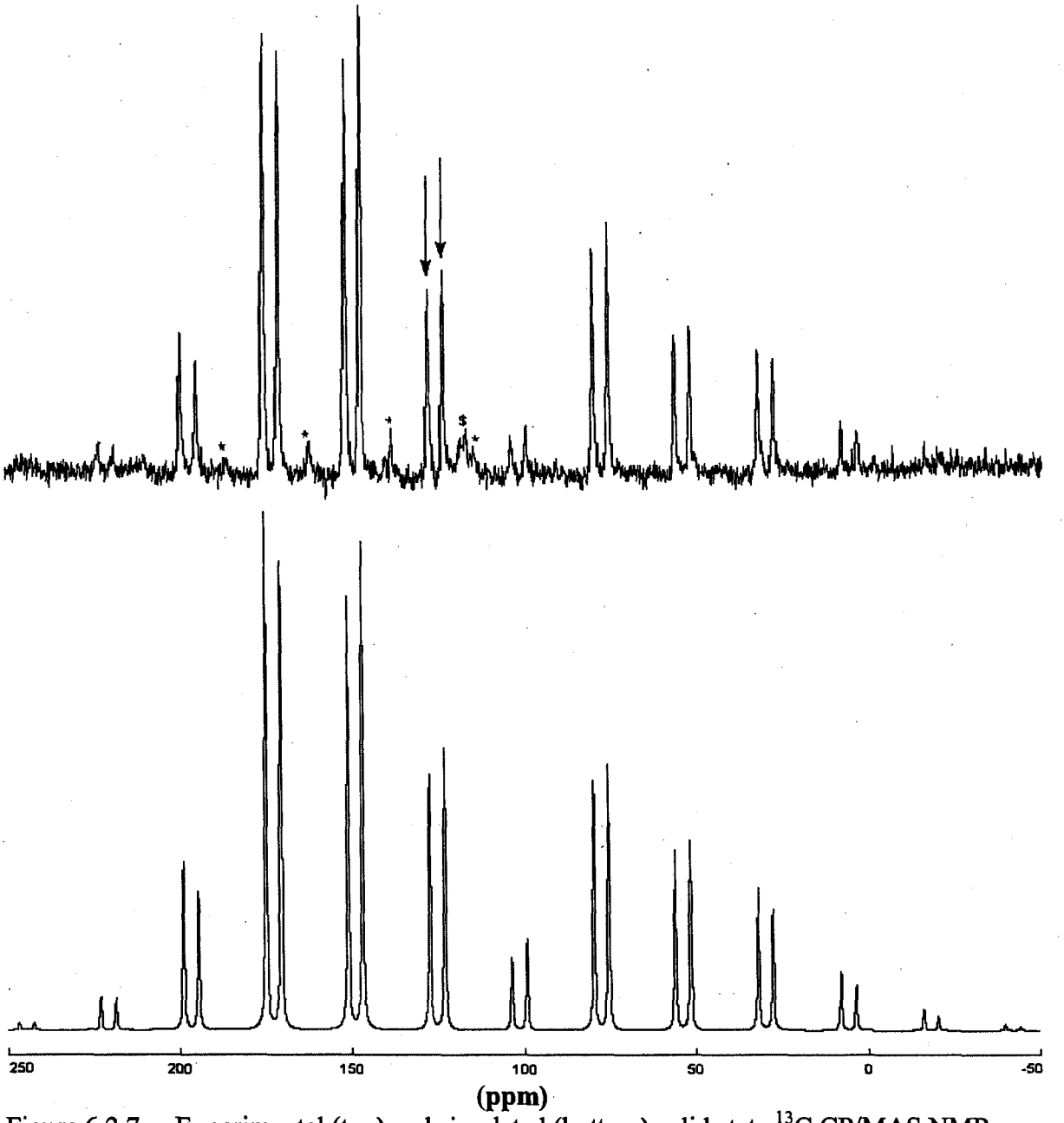

Figure 6.2.7 Experimental (top) and simulated (bottom) solid state ^{13}C CP/MAS NMR spectra of benzene silver trifluoroacetate ($C_6H_6 \cdot AgCF_3CO_2$). ν_R = 3 kHz, NS = 800, the intensity ratio is 1:1. The asterisks (*) indicate the ^{13}C spinning sidebands of CO_2 group in $CF_3CO_2^-$. The dollar ($) indicates ^{13}C peak of CF_3 group in $CF_3CO_2^-$. The arrows indicate the isotropic chemical shifts.

Table 6.2.4 Solid state ^{13}C NMR parameters of $C_6H_6 \cdot AgCF_3CO_2$ obtained from the simulation of the experimental spectrum.

δ_{11}	δ_{22}	δ_{33}	δ_{iso}	Ω	κ
202 (6)	180 (4)	0 (6)	127 (1)	202 (10)	0.78 (0.04)
199 (6)	166 (4)	4 (6)	123 (1)	195 (10)	0.66 (0.04)

6.2.1.3 Benzene Silver Triflate ($C_6H_6 \cdot AgCF_3SO_3$)

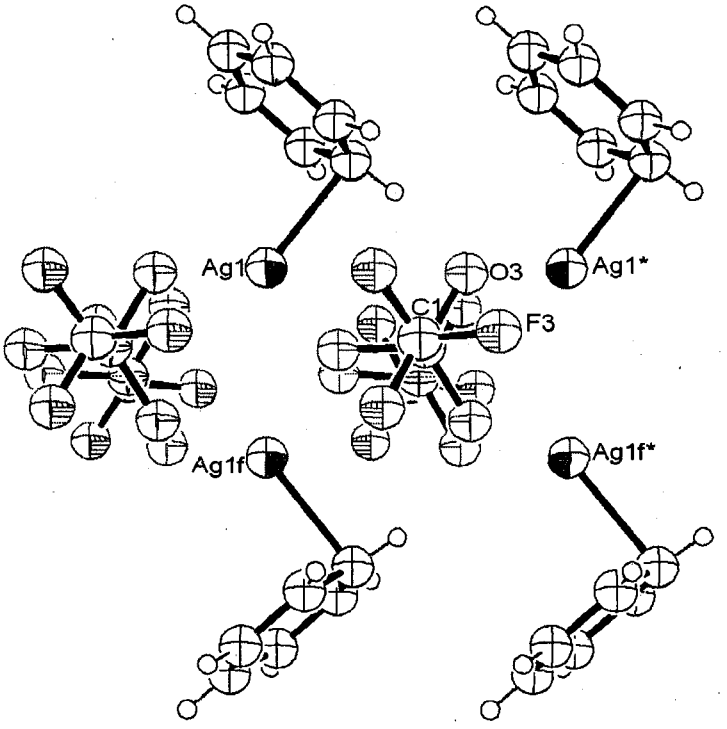

Figure 6.2.8-A An ORTEP-III drawing of the benzene silver triflate complex ($C_6H_6 \cdot AgSO_3CF_3$) [9].

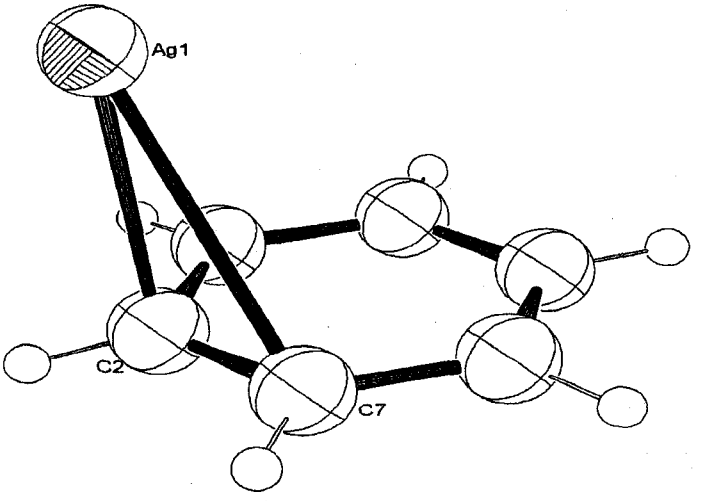

Figure 6.2.8-B An ORTEP-III drawing of the bond connection between silver and benzene in the benzene silver triflate complexes ($C_6H_6 \cdot AgSO_3CF_3$) [9].

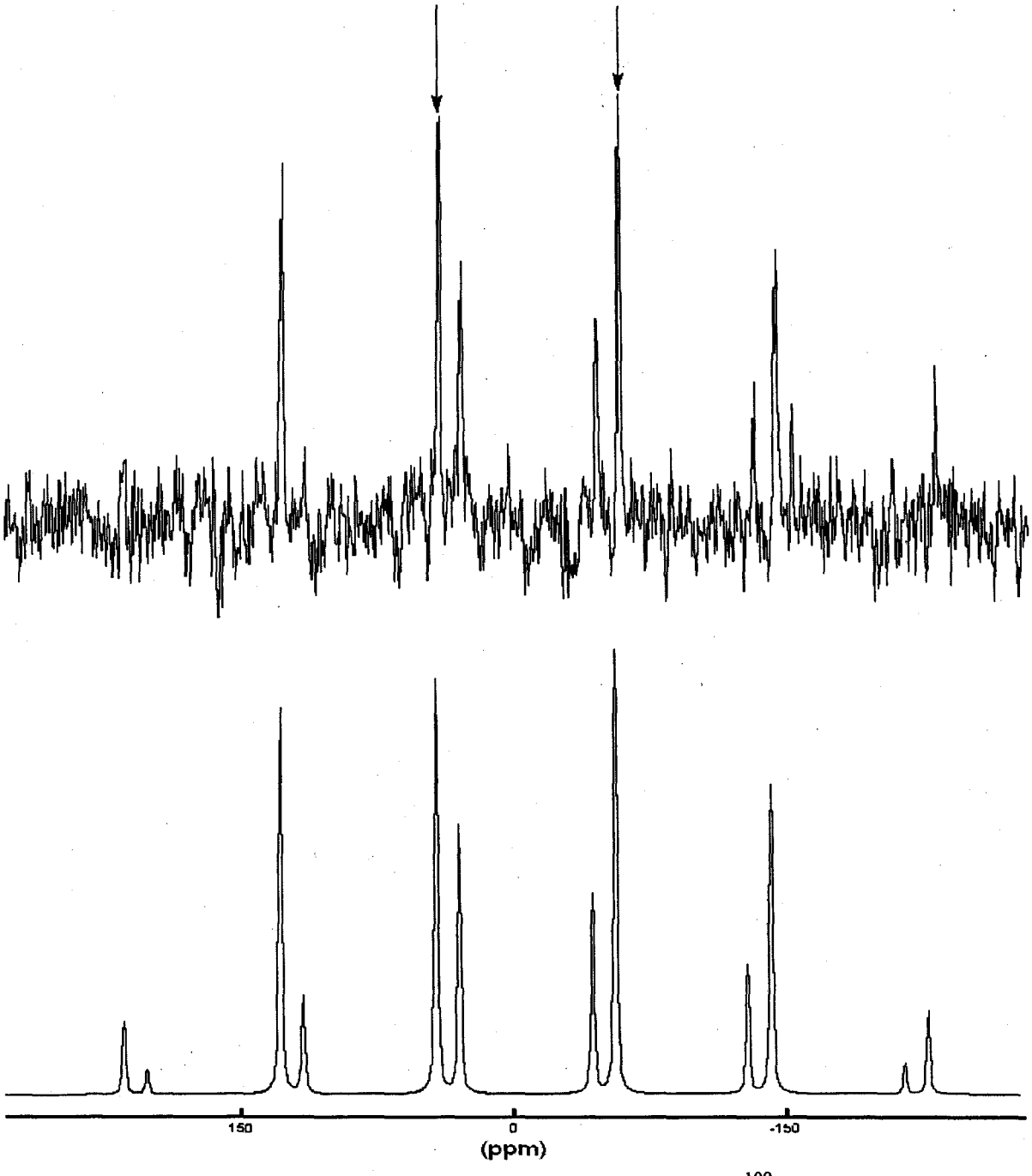

Figure 6.2.9 Experimental (top) and simulated (bottom) solid state ^{109}Ag CP/MAS NMR spectra of benzene silver triflate ($C_6H_6 \cdot AgCF_3SO_3$). ν_R = 2 kHz, NS = 7595, the total intensity ratio is 1:1. The arrows indicate the isotropic chemical shifts.

Table 6.2.5 Solid state ^{109}Ag NMR parameters of $C_6H_6 \cdot AgCF_3SO_3$ obtained from the simulation of the experimental spectrum.

δ_{11}	δ_{22}	δ_{33}	δ_{iso}	Ω	κ
210 (18)	106 (12)	-190 (8)	42 (2)	400 (24)	0.48 (0.04)
150 (18)	-70 (12)	-250 (8)	-57 (2)	400 (24)	-0.10 (0.04)

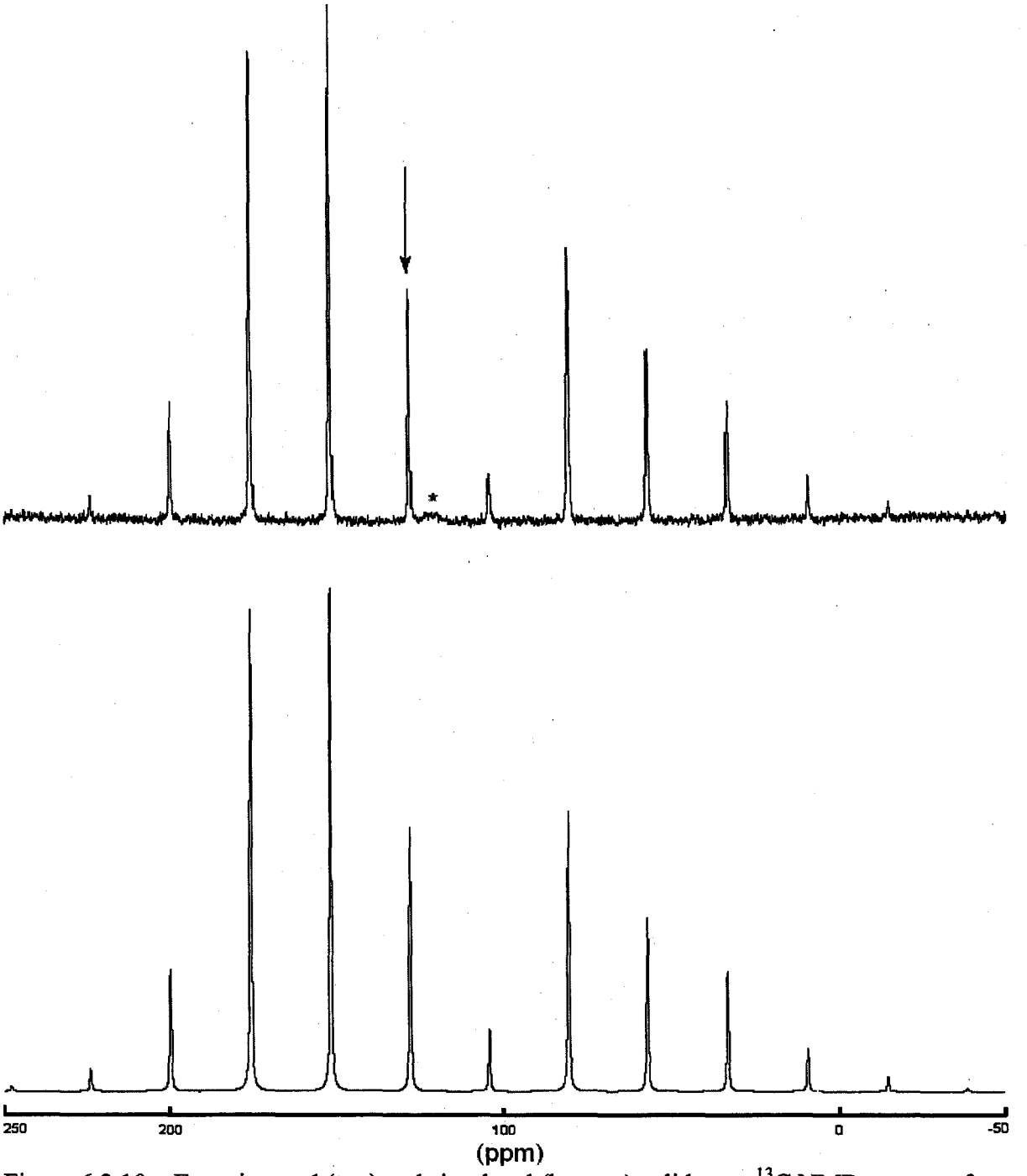

Figure 6.2.10 Experimental (top) and simulated (bottom) solid state ^{13}C NMR spectra of benzene silver triflate ($C_6H_6 \cdot AgCF_3SO_3$). ν_R = 3 kHz, NS = 800. The asterisks (*) indicates the ^{13}C peak of CF_3 group in $CF_3SO_3^-$. The arrow indicates the isotropic chemical shift.

Table 6.2.6 Solid state ^{13}C NMR parameters of $C_6H_6 \cdot AgCF_3SO_3$ obtained from the simulation of the experimental spectrum.

δ_{11}	δ_{22}	δ_{33}	δ_{iso}	Ω	κ
194.6 (3)	181.6 (3)	9.6 (2)	128.6 (1)	185 (4)	0.86 (0.03)

6.2.1.4 Para-xylene Silver Perchlorate

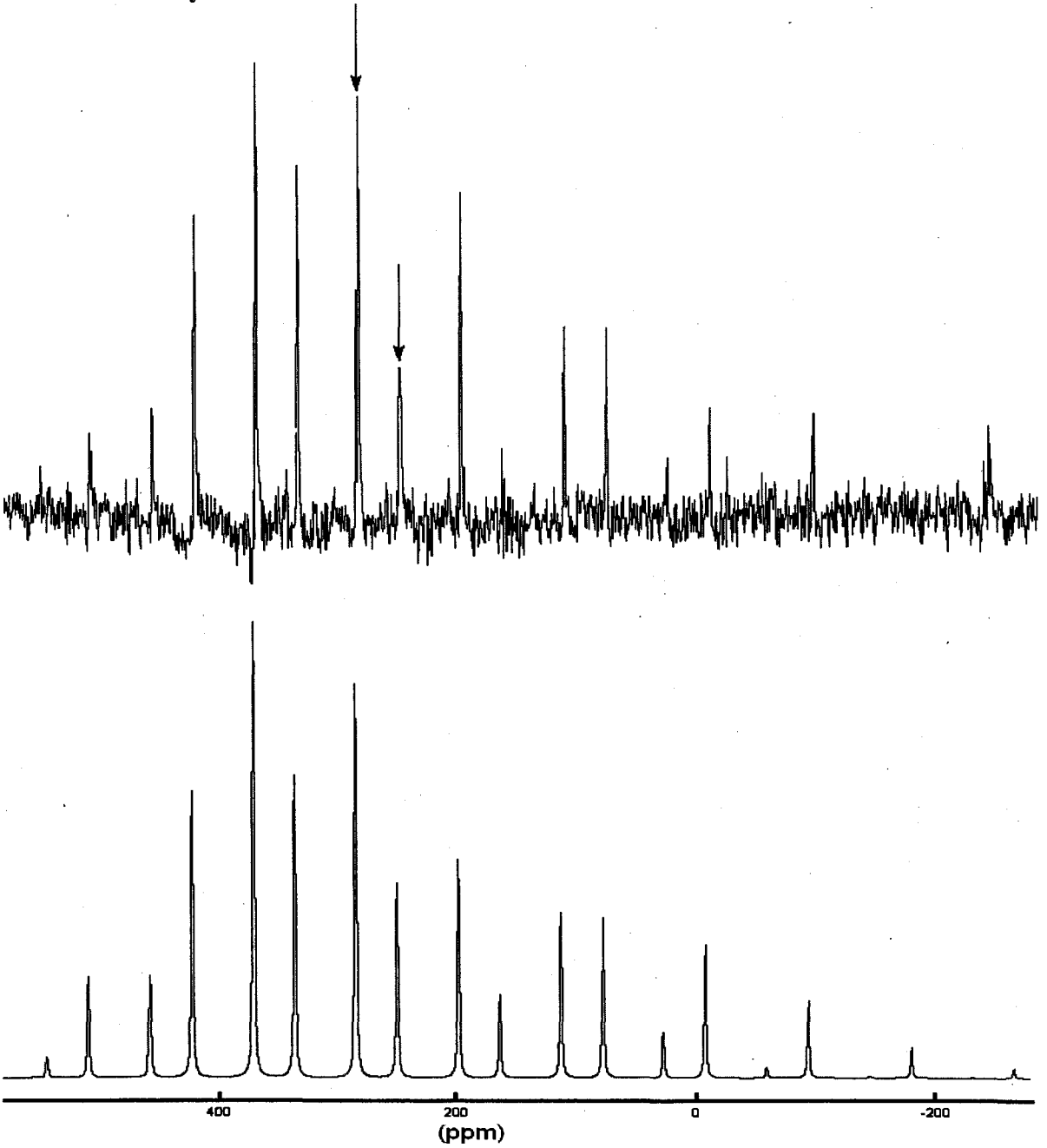

Figure 6.2.11 Experimental (top) and simulated (bottom) solid state ^{109}Ag CP/MAS NMR spectra of para-xylene silver perchlorate. ν_R = 2 kHz, NS = 5733, and a total intensity ratio of 1:1. The arrows indicate the isotropic chemical shifts.

Table 6.2.7 Solid state ^{109}Ag NMR parameters of para-xylene silver perchlorate obtained from the simulation of the experimental spectrum.

δ_{11}	δ_{22}	δ_{33}	δ_{iso}	Ω	κ
552 (14)	376 (12)	-178 (8)	250 (2)	730 (24)	0.51 (0.04)
468 (14)	354 (12)	32 (8)	285 (2)	436 (24)	0.47 (0.04)

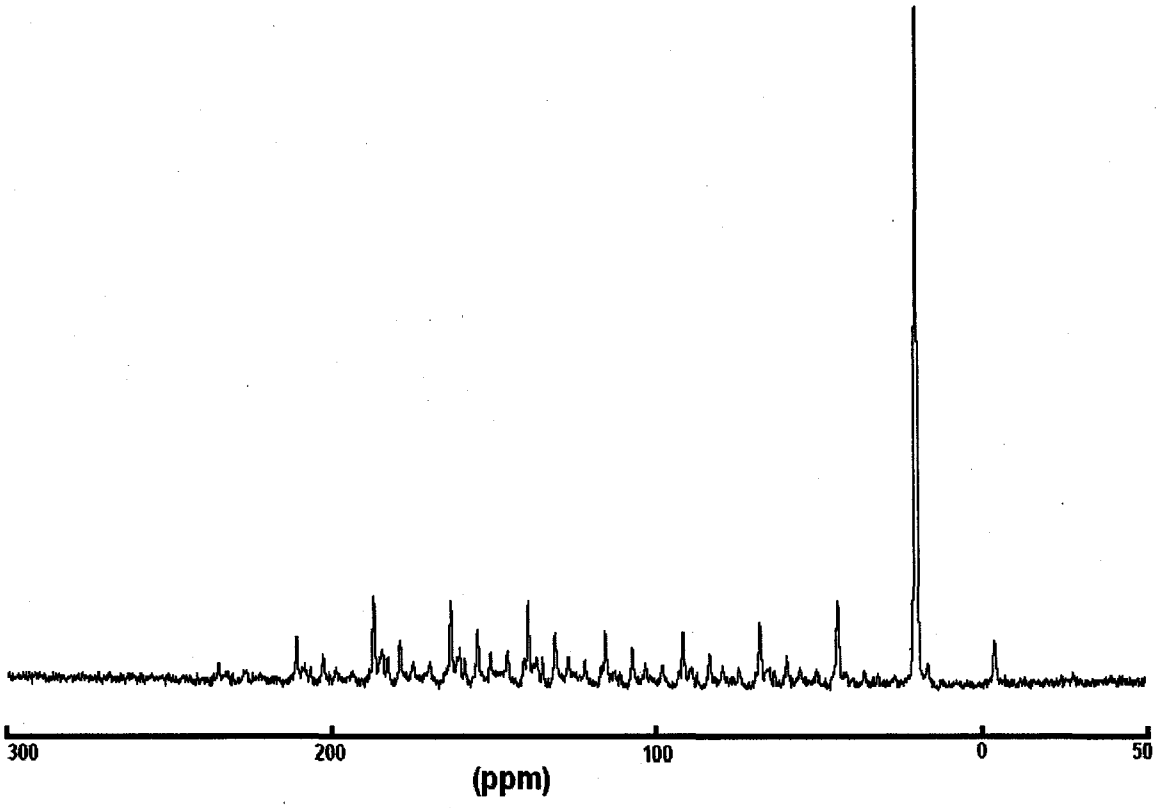

Figure 6.2.12 Experimental solid state ^{13}C NMR spectra of para-xylene silver perchlorate, $\nu_R = 3$ kHz, NS = 7054.

The ^{13}C isotropic chemical shifts of phenyl ring and methyl groups of para-xylene silver perchlorate obtained from CP/MAS NMR experimental spectrum are 141 ± 0.8, 139.5 ± 0.8, 138 ± 0.8, 137 ± 0.8, 135 ± 0.8, 131.5 ± 0.8, 127 ± 0.8, 122 ± 0.8 ppm and 20 ± 1.0 ppm respectively.

6.2.1.5 Mesitylene Silver Triflate

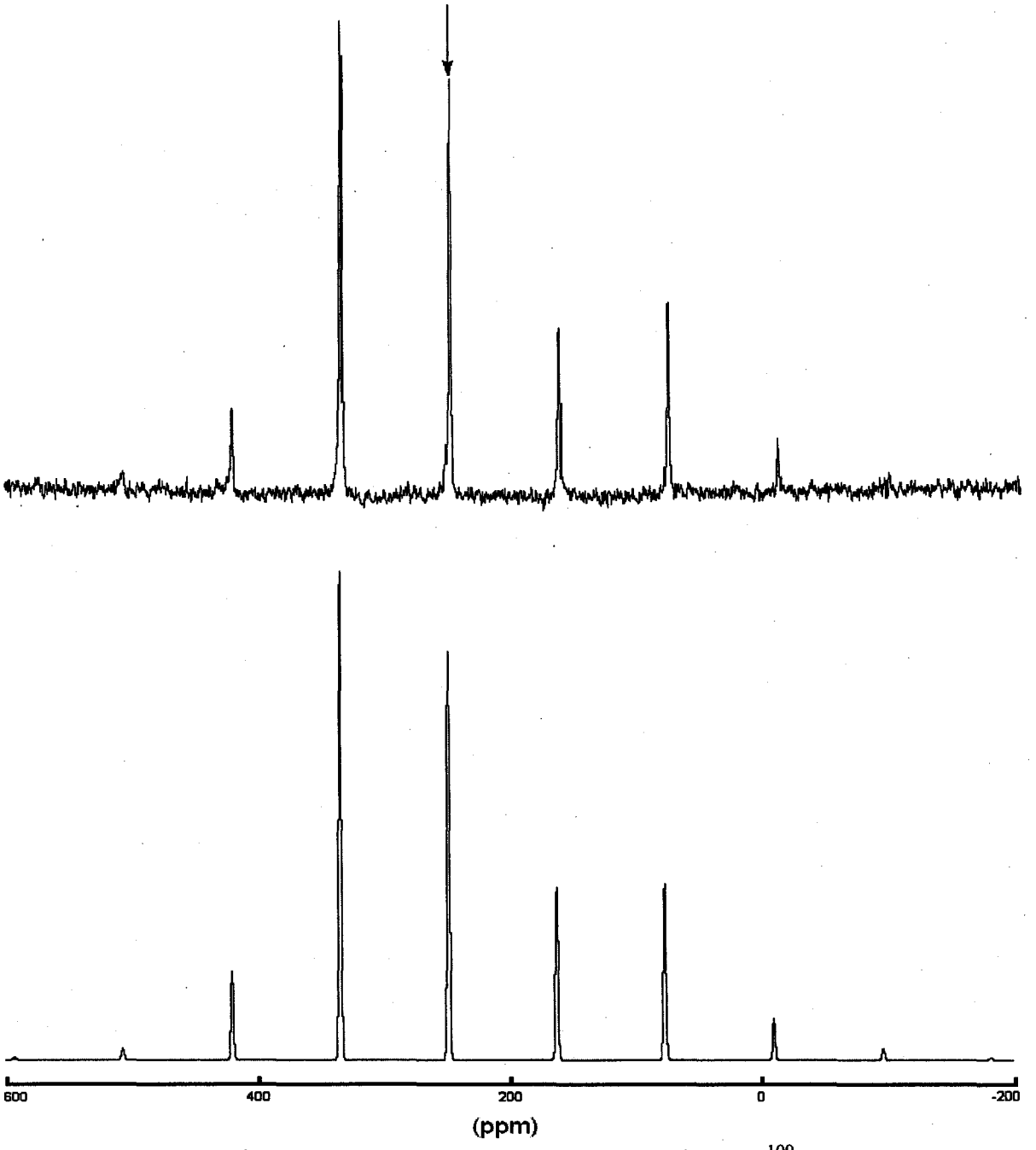

Figure 6.2.13 Experimental (top) and simulated (bottom) solid state ^{109}Ag CP/MAS NMR spectra of mesitylene silver triflate, $\nu_R = 2$ kHz, NS = 2106. The arrow indicates the isotropic chemical shift.

Table 6.2.8 Solid state ^{109}Ag NMR parameters of mesitylene silver triflate obtained from the simulation of the experimental spectrum.

δ_{11}	δ_{22}	δ_{33}	δ_{iso}	Ω	κ
374 (18)	374 (18)	-3 (12)	248 (2)	378 (28)	0.95 (0.04)

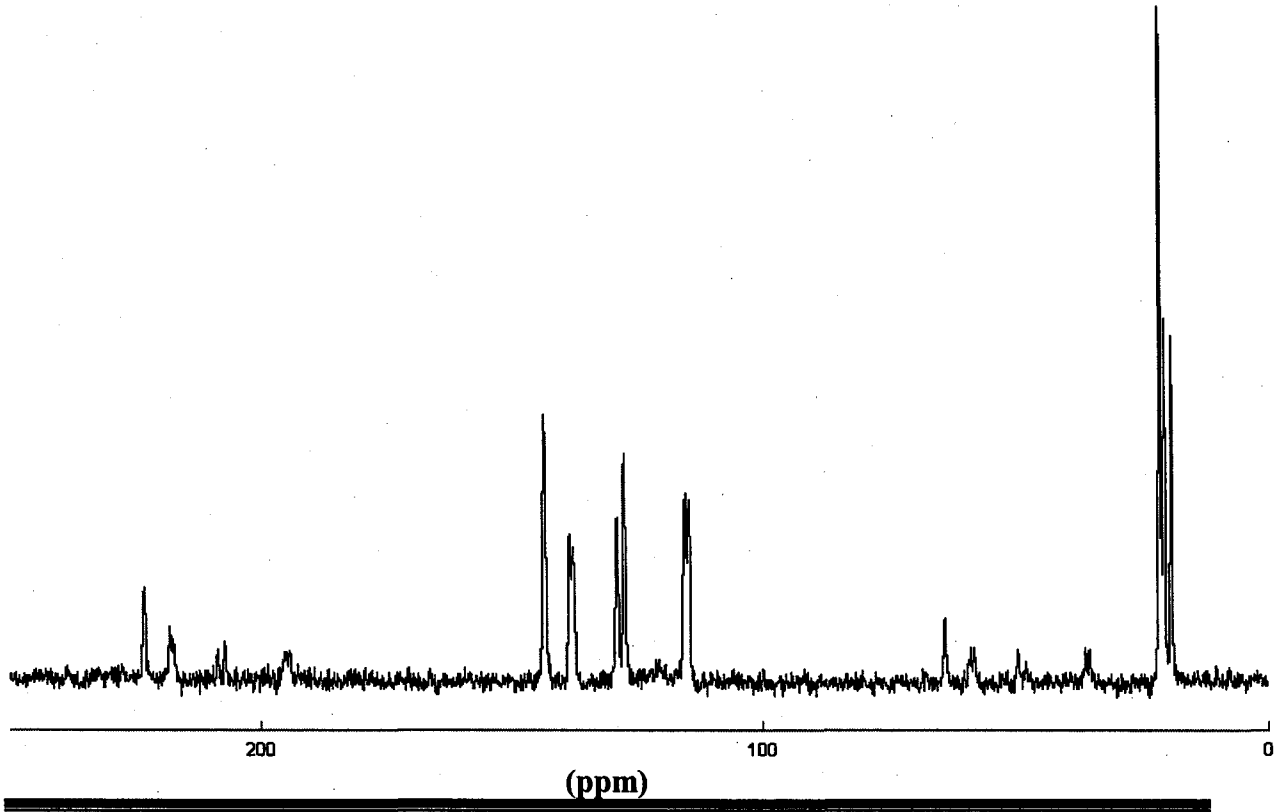

Figure 6.2.14 Experimental solid state ^{13}C NMR spectra of mesitylene silver triflate, υ_R = 5 kHz, NS = 9424. The asterisks (*) indicates the ^{13}C peak of CF_3 group in $CF_3SO_3^-$.

The ^{13}C isotropic chemical shifts of phenyl ring and methyl groups of mesitylene silver triflate obtained from CP/MAS NMR experimental spectrum are 144 ± 0.8, 139 ± 0.8, 138 ± 0.8, 129 ± 0.8, 128 ± 0.8, 116 ± 0.8, 115 ± 0.8 ppm and 21.4 ± 0.4, 20.5 ± 0.4, 19.2 ± 0.4 ppm respectively.

6.2.1.6 Hexamethylbenzene Silver Trifluoroacetate

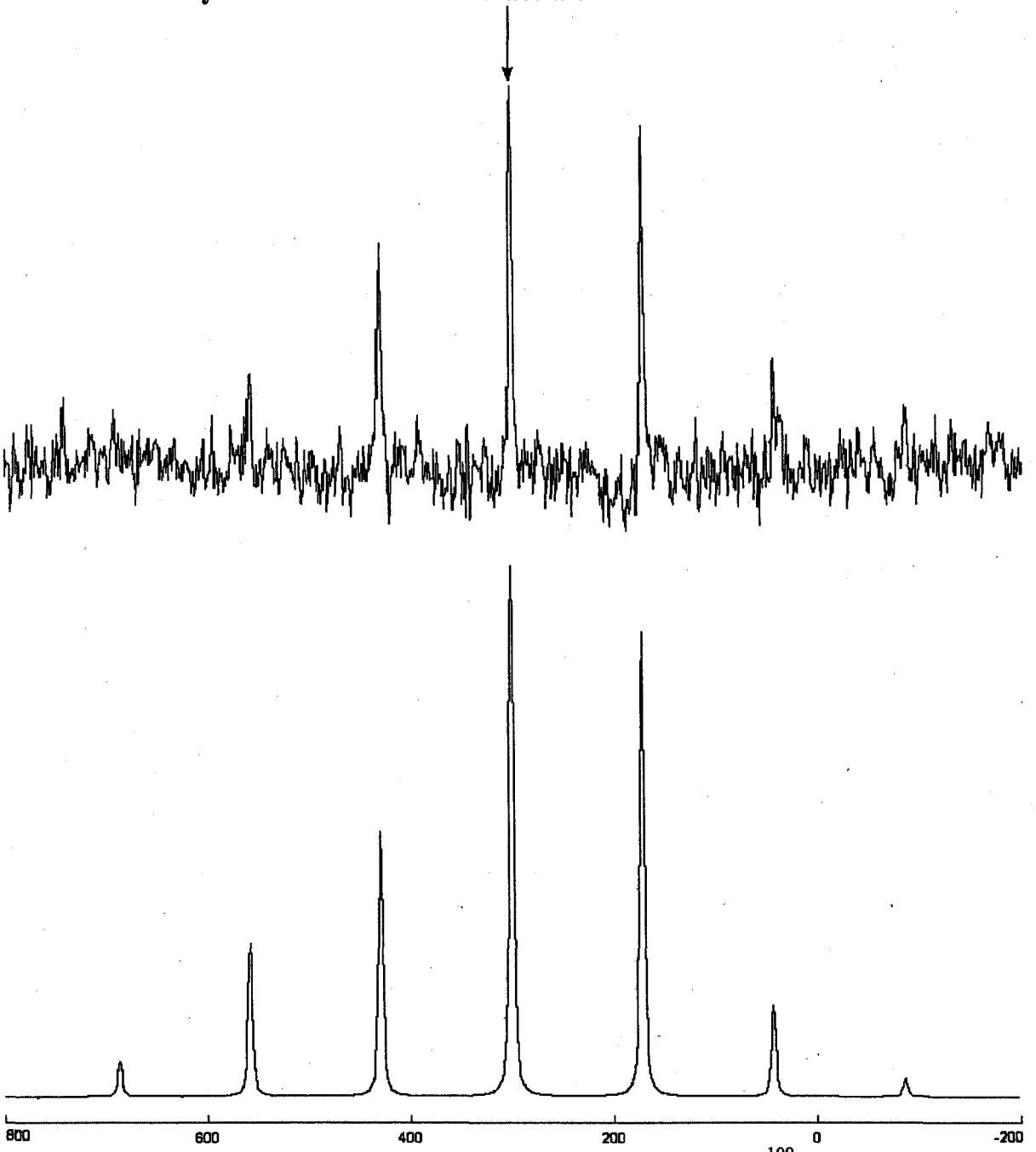

Figure 6.2.15 Experimental (top) and simulated (bottom) solid state ^{109}Ag CP/MAS NMR spectra of hexamethylbenzene silver trifluoroacetate, ν_R = 3 kHz, NS = 6660. The arrow indicates the isotropic chemical shift.

Table 6.2.9 Solid state ^{109}Ag NMR parameters of hexamethylbenzene silver trifluoroacetate obtained from the simulation of the experimental spectrum.

δ_{11}	δ_{22}	δ_{33}	δ_{iso}	Ω	κ
640 (18)	220 (14)	40 (12)	300 (4)	600 (28)	-0.40 (0.04)

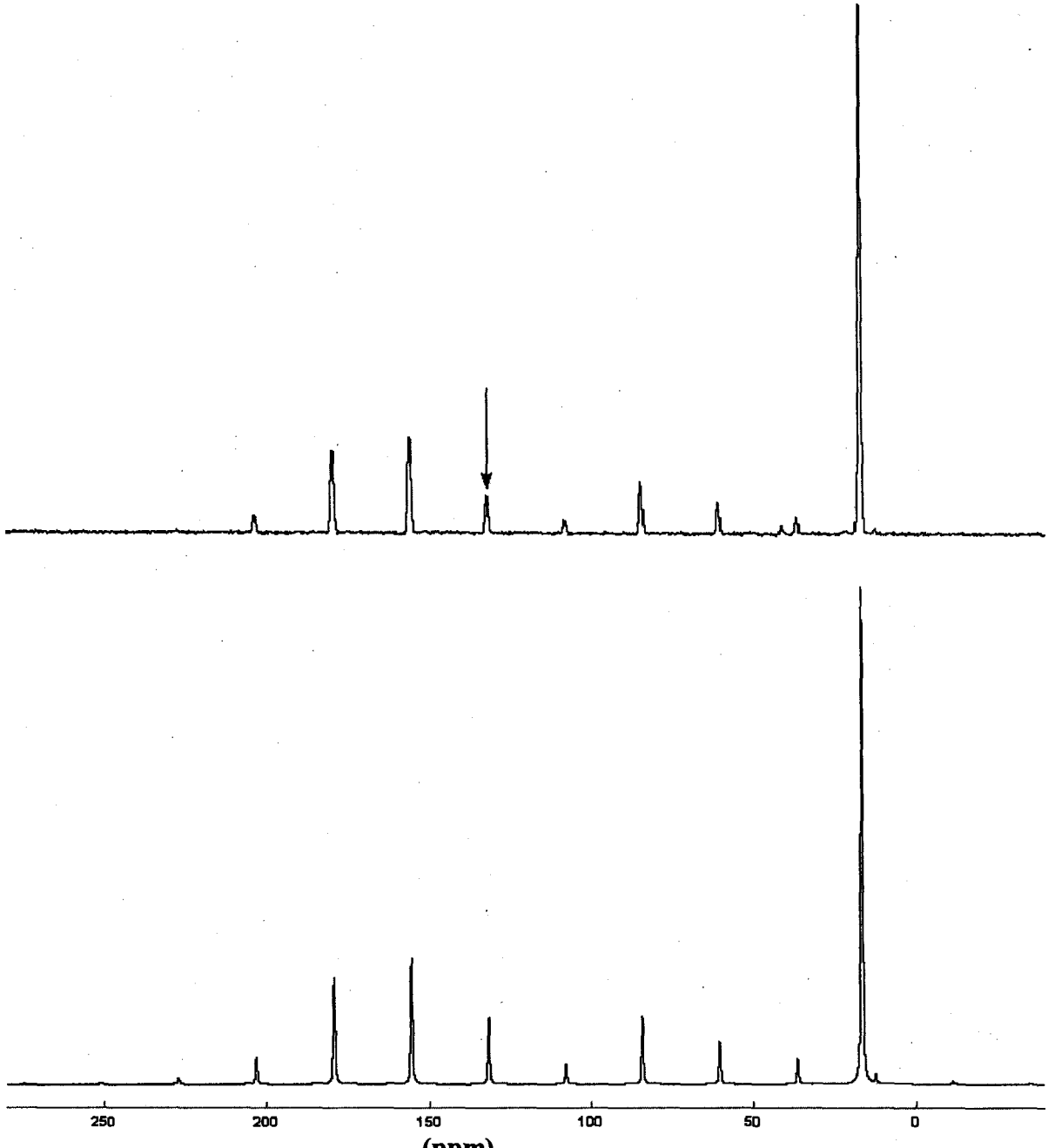

Figure 6.2.16 Experimental (top) and simulated (bottom) solid state ^{13}C CP/MAS NMR spectra of hexamethylbenzene silver trifluoroacetate, $\nu_R = 3$ kHz, NS = 128. The arrow indicates the isotropic chemical shift.

Table 6.2.10 Solid state ^{13}C NMR parameters of hexamethylbenzene silver trifluoroacetate obtained from the simulation of the experimental spectrum.

δ_{11}	δ_{22}	δ_{33}	δ_{iso}	Ω	κ
202 (8)	176 (6)	17 (8)	132 (1)	185 (12)	0.72 (0.06)

6.2.1.7 Hexamethylbenzene Silver Triflate

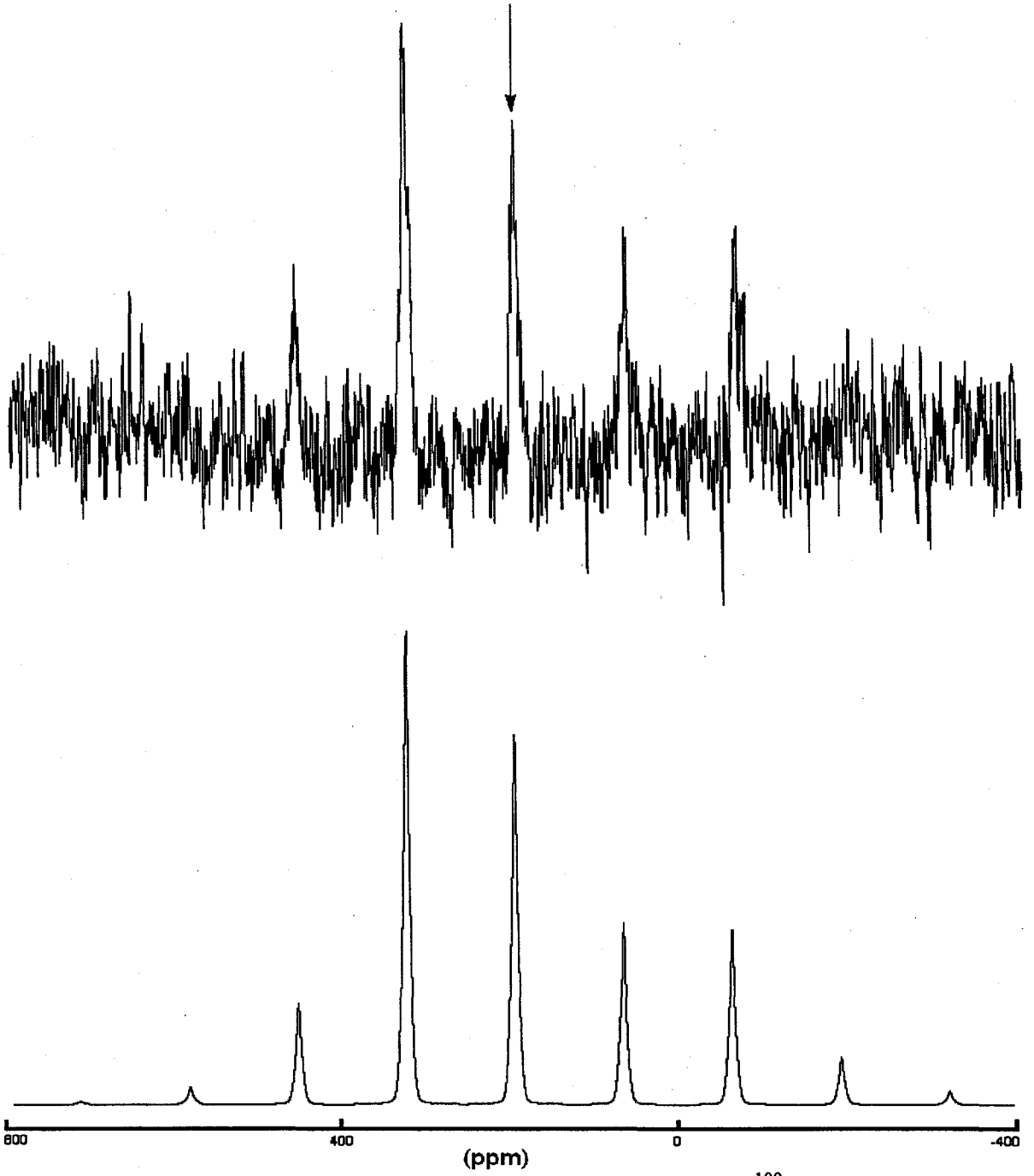

Figure 6.2.17 Experimental (top) and simulated (bottom) solid state ^{109}Ag NMR spectra of hexamethylbenzene silver triflate, ν_R = 3 kHz, NS = 8884. The arrow indicates the isotropic chemical shift.

Table 6.2.11 Solid state ^{109}Ag NMR parameters of Hexamethylbenzene silver triflate:

δ_{11}	δ_{22}	δ_{33}	δ_{iso}	Ω	κ
446 (20)	336 (20)	-200 (16)	194 (5)	646 (34)	0.64 (0.04)

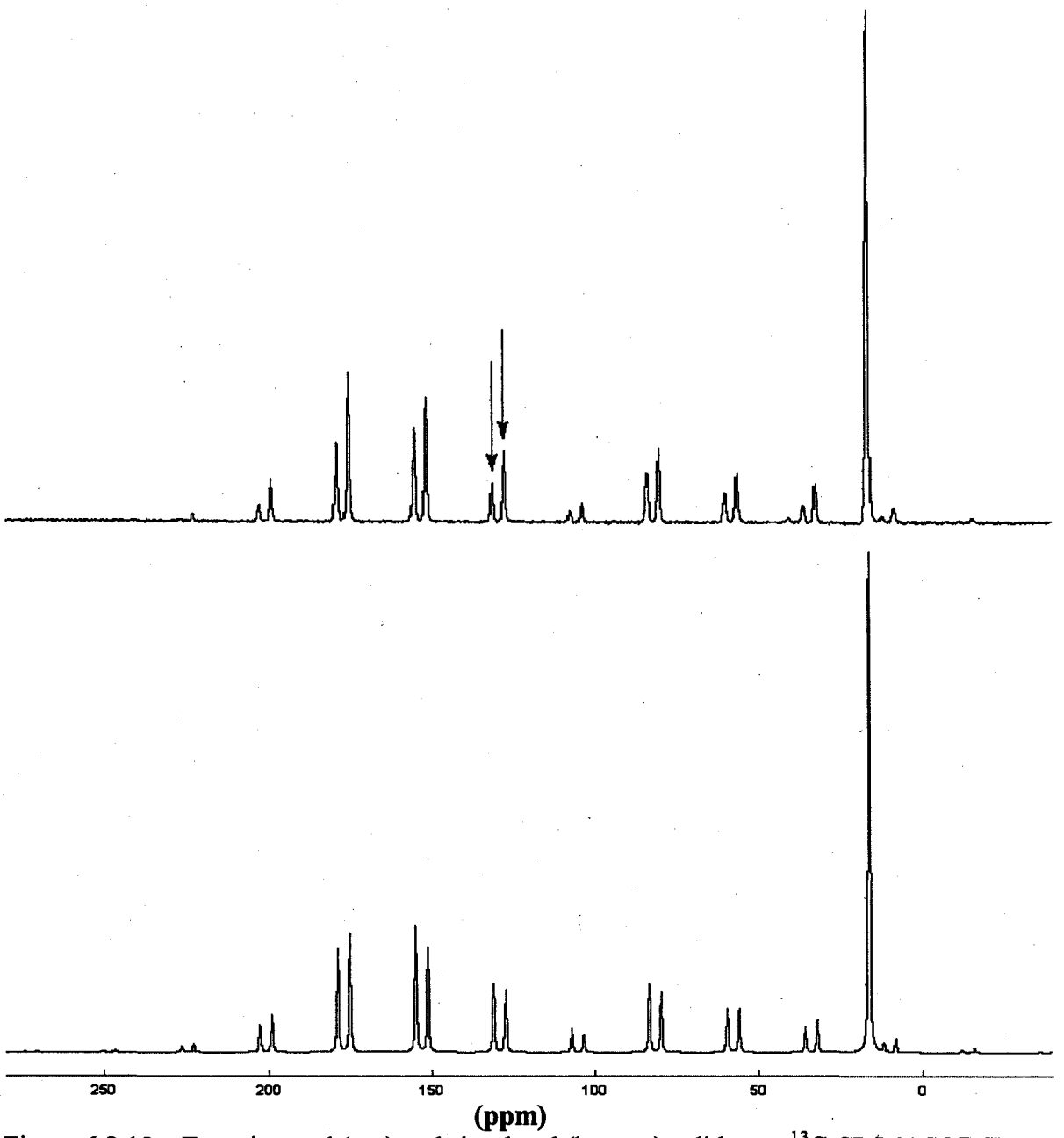

Figure 6.2.18 Experimental (top) and simulated (bottom) solid state ^{13}C CP/MAS NMR spectra of hexamethylbenzene silver triflate. ν_R = 3 kHz, NS = 400 and the intensity ratio is close to 1:1. The arrows indicate the isotropic chemical shifts.

Table 6.2.12 Solid state ^{13}C NMR parameters of hexamethylbenzene silver triflate obtained from the simulation of the experimental spectrum.

	δ_{11}	δ_{22}	δ_{33}	δ_{iso}	Ω	κ
S1	203 (8)	172 (6)	18 (8)	131 (1)	185 (12)	0.66 (0.06)
S2	202 (8)	178 (6)	2 (8)	127 (1)	200 (12)	0.70 (0.06)

S1 is the pattern of ^{13}C spinning sidebands of benzene ring of pure $C_6(CH_3)_6$, S2 is the pattern of ^{13}C spinning sidebands of benzene ring in $C_6(CH_3)_6$-$AgSO_3CF_3$.

6. 2. 2 Discussion of Solid State ^{13}C NMR Spectra of Some Silver-arene Complexes

The gross geometric aspects of this interaction were predicted early in the 1950's by Mulliken [13] and by Dewar [14] before any structural results were known. Excluding a ferrocene-like structure, which has never been observed, two different positions of the metal with respect to the arene can be envisaged. First, if the metal behaves as an electron acceptor (Figure 6.2.19, case A), then regardless of what metal orbital or hybrid orbital is an acceptor, the metal may be expected to position itself directly above one carbon of the aromatic ring where the electron density is the highest (Figure 6.2.19, case A) [15]. However, with filled *d* orbitals as in the case of silver, the metal might back-donate into a π^* orbital of the arene (Figure 6.2.19, case B). In this case, the best overlap would occur with the metal positioned midway between two carbons of the aromatic ring.

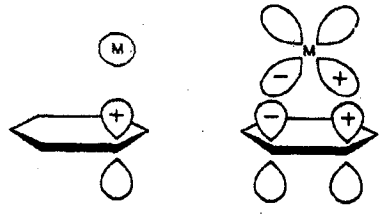

A B

Figure 6.2.19 Bonding modes for a metal atom with a benzene ring: (A) metal acting as a σ electron acceptor; (B) metal back-donation in a π^* orbital of the ring.

In general, neither pure case is seen. Amma and co-workers have done extensive structural studies on a wide range of silver-arene complexes [16]. They found that silver nearly always coordinates to aromatic molecules in an unsymmetrical fashion, somewhere

between case A and case B. But a common feature of all of these structures is a closest Ag-C distance of 2.45-2.49 Å; the next-nearest Ag-C contact varies from 2.6-2.9 Å. This suggests that it is more important for the arene to act as a σ donor of electron density than as a π acceptor. Supporting evidence comes from complexes of substituented arene where the silver is often, but not always, situated closest to the carbon with the highest electron density. The degree of back-donation and the distance to the next-nearest carbon apparently varies to accommodate crystal packing forces and the nature of the anions or other ligands to silver [17].

Table 6.2.13 lists the known molecular structure parameters of some benzene silver complexes, the terminal planar benzene ligand in these three benzene silver complexes is asymmetrically η^2-coordinated to Ag.

Table 6.2.13 Structural parameters of silver benzene complexes.

Compound	Lattice point group	Space group	Symmetry elements
$C_6H_6 \cdot AgClO_4$ [5]	Orthorhombic (Z = 4)	Cmcm	2-fold screw axis, 2-fold rotation axis, inversion center, glide plane, mirror plane, centering vector
$C_6H_6 \cdot AgCF_3SO_3$ [8, 9]	Monoclinic (Z = 8)	C2/c	2-fold screw axis, 2-fold rotation axis, inversion center, glide plane, centering vector
$C_6H_6 \cdot AgCF_3CO_2$ [2]	Monoclinic (Z = 8)	A2/m (C2/m)	2-fold screw axis, 2-fold rotation axis, inversion center, glide plane, mirror plane, centering vector

Table 6.2.14 summarizes the solid state ^{13}C chemical shift paramaters of the benzene ring in three benzene silver complexes.

Table 6.2.14 Solid state ^{13}C chemical shift parameters of benzene in three benzene silver complexes.

Compound	δ_{11}	δ_{22}	δ_{33}	δ_{iso}	Ω	κ
Benzene (20 K) [18]	234	146	9	129.7	225	0.22
Benzene (223 K) [19]	192	192	12	132	180	1.00
$C_6H_6 \cdot AgClO_4$	196 (6)	184 (4)	3 (6)	128 (1)	193 (10)	0.87 (0.04)
$C_6H_6 \cdot AgCF_3CO_2$	202 (6)	180 (4)	0 (6)	127 (1)	202 (10)	0.78 (0.04)
	199 (6)	166 (4)	4 (6)	123 (1)	195 (10)	0.66 (0.04)
$C_6H_6 \cdot AgCF_3SO_3$	193 (6)	180 (4)	8 (6)	127 (1)	185 (10)	0.86 (0.04)

The isotropic chemical shift δ_{iso} of pure liquid benzene at ambient temperature is 128 ppm.

When compared with the tensor components δ_{11} and δ_{22} of the frozen benzene at 20 K, it can be seen that these two tensor components of benzene in three complexes are nearly averaged because of the fast rotation of the benzene ring. The small difference between δ_{11} and δ_{22} is likely caused by the crystal asymmetry. The tensor component δ_{33} is nearly the same for all of the ring carbons shown in Table 6.2.14 (6 ± 6 ppm). Comparing the tensor components δ_{11}, δ_{22}, and δ_{33} of three complexes with those components of benzene at 223 K, one can see that the numbers do not change much, which indicates that the interaction between silver and benzene is weak. The isotropic chemical shifts δ_{iso} of three complexes are almost the same as that of pure liquid benzene, which also implies that the interaction between silver and benzene is weak.

Table 6.2.15 shows the solid state ^{13}C chemical shift parameters of benzene ring in hexamethylbenzene and two hexamethylbenzene silver complexes.

Table 6.2.15 Solid state ^{13}C chemical shift paramaters of benzene ring in hexamethylbenzene and two hexamethylbenzene silver complexes.

Benzene ring	δ_{11}	δ_{22}	δ_{33}	δ_{iso}	Ω	κ
$C_6(CH_3)_6$ (87 K) [20]	227	154	19	133	208	0.30
$C_6(CH_3)_6$ (Room Temperature)	203 (8)	172 (6)	18 (8)	131 (1)	185 (12)	0.66 (0.06)
$C_6(CH_3)_6$ - $AgCF_3SO_3$	202 (8)	178 (6)	2 (8)	127 (1)	200 (12)	0.70 (0.06)
$C_6(CH_3)_6$ - $AgCF_3CO_2$	202 (8)	176 (6)	17 (8)	132 (1)	185 (12)	0.72 (0.06)

All spectra were obtained at room temperature except reference one.

Through the comparison with the tensor components δ_{11} and δ_{22} of the frozen hexamethylbenzene at 87 K, the tensor components δ_{11} and δ_{22} of these two hexamethylbenzene silver complexes and hexamethylbenzene at room temperature are averaged by the fast benzene ring rotation. The tensor components δ_{33} of all chemicals in Table 6.2.14 do not change by much. The tensor components δ_{11}, δ_{22} and δ_{33} of the two hexamethylbenzene silver complexes are not changing much from those of hexamethylbenzene at room temperature, which means that the interaction between silver and hexamethylbenzene is weak. The similar isotropic chemical shifts δ_{iso} in table 6.2.15 also indicate that that the interaction between silver and hexamethylbenzene is weak.

6.2.3 Discussion of Solid State ^{109}Ag NMR Spectra of Some Silver-Arene Complexes

Table 6.2.16 summarizes the solid state ^{109}Ag chemical shift parameters of this work.

Table 6.2.16 The summary of solid state ^{109}Ag chemical shift parameters of our synthesized arene-silver complexes.

Compound	δ_{11}	δ_{22}	δ_{33}	δ_{iso}	Ω	κ
$C_6H_6 \cdot AgClO_4$	418 (8)	292 (8)	-292 (6)	139 (2)	710 (12)	0.64 (0.02)
$C_6H_6 \cdot AgCF_3CO_2$	630 (16)	596 (14)	-32 (11)	398 (3)	662 (22)	0.89 (0.03)
	440 (16)	250 (14)	-130 (11)	187 (3)	570 (22)	0.33 (0.03)
$C_6H_6 \cdot AgCF_3SO_3$	210 (18)	106 (12)	-190 (8)	42 (3)	400 (24)	0.48 (0.04)
	150 (18)	-70 (12)	-250 (8)	-57 (3)	400 (24)	-0.10 (0.04)
paraxylene-$AgClO_4$	552 (14)	376 (12)	-178 (8)	250 (2)	730 (24)	0.51 (0.04)
	468 (14)	354 (12)	32 (8)	285 (2)	436 (24)	0.47 (0.04)
Mesitylene-$AgCF_3SO_3$	374 (18)	374 (18)	-3 (12)	248 (4)	378 (28)	0.95 (0.04)
$C_6(CH_3)_6$ - $AgCF_3CO_2$	640 (18)	220 (14)	40 (12)	300 (6)	600 (28)	-0.40 (0.04)
$C_6(CH_3)_6$ - $AgCF_3SO_3$	446 (20)	336 (20)	-200 (16)	194 (6)	646 (34)	0.64 (0.04)

$C_6H_6 \cdot AgClO_4$ crystallizes in the monoclinic space group Cmcm with Z = 4 [5]. The crystal lattice of $C_6H_6 \cdot AgClO_4$ consists of chains of $[(C_6H_6)Ag]$ units as shown in Figure 6.2.1. Each pair of benzene molecules is bridged by an Ag atom. The Ag atoms are related by centers of inversion and are therefore chemically and magnetically equivalent to yield one ^{109}Ag resonance. The fast rotating benzenes are also related by centers of inversion, and thus they are chemically and magnetically equivalent to yield one ^{13}C resonance. This is in accordance with the ^{109}Ag and ^{13}C CP/MAS spectra, both of which consist of one type of silver and carbon.

Solid $C_6H_6 \cdot AgCF_3CO_2$ exists in the space group C2/c (Z = 8) with two chemically inequivalent Ag atoms in the crystallographic asymmetric units (ratio is 1:1) [2]. One Ag atom is bound to benzene and three oxygen atoms. The other Ag atom is bound only three

oxygen atoms. This structure implies that one should see two signals in the ^{109}Ag CP/MAS spectrum. The two patterns of ^{109}Ag and ^{13}C CP/MAS spectra and the intensity ratio of two patterns of spinning sidebands is 1:1 are in good agreement with the crystal structure.

Solid $C_6H_6 \cdot AgCF_3SO_3$ in space group A2/m with Z = 8 [9] with chemically equivalent Ag atoms in the crystallographic unit. The crystal structure indicates that each Ag atom is bound to benzene and four oxygen atoms. The ^{109}Ag CP/MAS spectrum clearly shows two patterns of spinning sidebands and the intensity ratio of two patterns of spinning sidebands is 1:1, which is not consistent with the crystal structure. The ^{13}C CP/MAS spectrum clearly shows one pattern of spinning sidebands, which is consistent with the crystal structure. The possible explanation of why only one pattern of ^{13}C spinning sidebands is observed is that ^{13}C is much less sensitive to very small changes in crystal structure.

It is also possible that there is an impurity which happens to give a spectrum with a 1:1 intensity ratio with respect to that for $C_6H_6 \cdot AgCF_3SO_3$.

No crystal structures are available for paraxylene-$AgClO_4$, Mesitylene-$AgCF_3SO_3$, $C_6(CH_3)_6 \cdot AgCF_3CO_2$ and $C_6(CH_3)_6 \cdot AgCF_3SO_3$. However some structural information can be obtained from the ^{109}Ag and ^{13}C CP/MAS spectra.

The solid state ^{109}Ag CP/MAS spectrum of paraxylene-$AgClO_4$ has two patterns of spinning sidebands, which indicates that there are two chemically inequivalent Ag atoms in the crystal units. The solid state ^{13}C CP/MAS spectrum of paraxylene-$AgClO_4$ is complex and the spinning sidebands are not analyzed. Therefore it is hard to predict the type of silver-carbon coordination. The interaction between silver and paraxylene could be η^2 or an Ag-C bond could be formed.

The solid state ^{109}Ag CP/MAS spectrum of mesitylene- $AgCF_3SO_3$ has a single pattern of spinning sidebands, which means that Ag atoms in the crystallographic unit cell are chemically equivalent. The solid state ^{13}C CP/MAS spectrum of mesitylene-$AgClO_4$ is complex and the spinning sidebands are not analyzed. Therefore the coordination between Ag and mesitylene is difficult to predict. The interaction between silver and mesitylene could be η^2 or an Ag-C bond could be formed. The ^{109}Ag chemical shift tensor shows a skew value near 1 (0.95 ± 0.04) which implies a silver site of nearly axial symmetry. This could occur if the Ag lies along a C_n axis, when $n \geq 3$.

The single pattern of the ^{109}Ag and ^{13}C CP/MAS spectra show that hexamethylbenzene ligands are η^2-coordinated to Ag atoms and the interaction between Ag and hexamethylbenzene is weak. Both $C_6(CH_3)_6 \cdot AgCF_3CO_2$ and $C_6(CH_3)_6 \cdot AgCF_3SO_3$ consist of one type of silver in crystal.

From table 6.2.16 one can conclude that the ^{109}Ag is very sensitive to the changes of crystal structure. Although the interactions between silver with benzene or hexamethylbenzene are weak, the tensor components of ^{109}Ag are still changing significantly. The above results show just how sensitive the ^{109}Ag chemical shift is when compared to ^{13}C.

6.2.4 Results of Solid State ^{109}Ag NMR Spectra of $AgClO_4$, $AgSO_3CF_3$ and $AgCO_2CF_3$

6.2.4. 1 $AgClO_4$

The solid state ^{109}Ag MAS NMR spectrum is shown in Figure 6.2.20. The crystalline structure of $AgClO_4$ is tetragonal with space group I42m and Z = 2 [21]. The crystal structure shows that the ClO_4^- tetrahedra are slightly stretched in the direction parallel to the *c* axis, with a Cl-O distance of 1.47 Å and that the two silver atoms are chemically equivalent. However the MAS NMR spectrum consists of two peaks with an intensity ratio of 1:2 at chemical shift of -222 ± 2 and -160 ± 2 ppm.

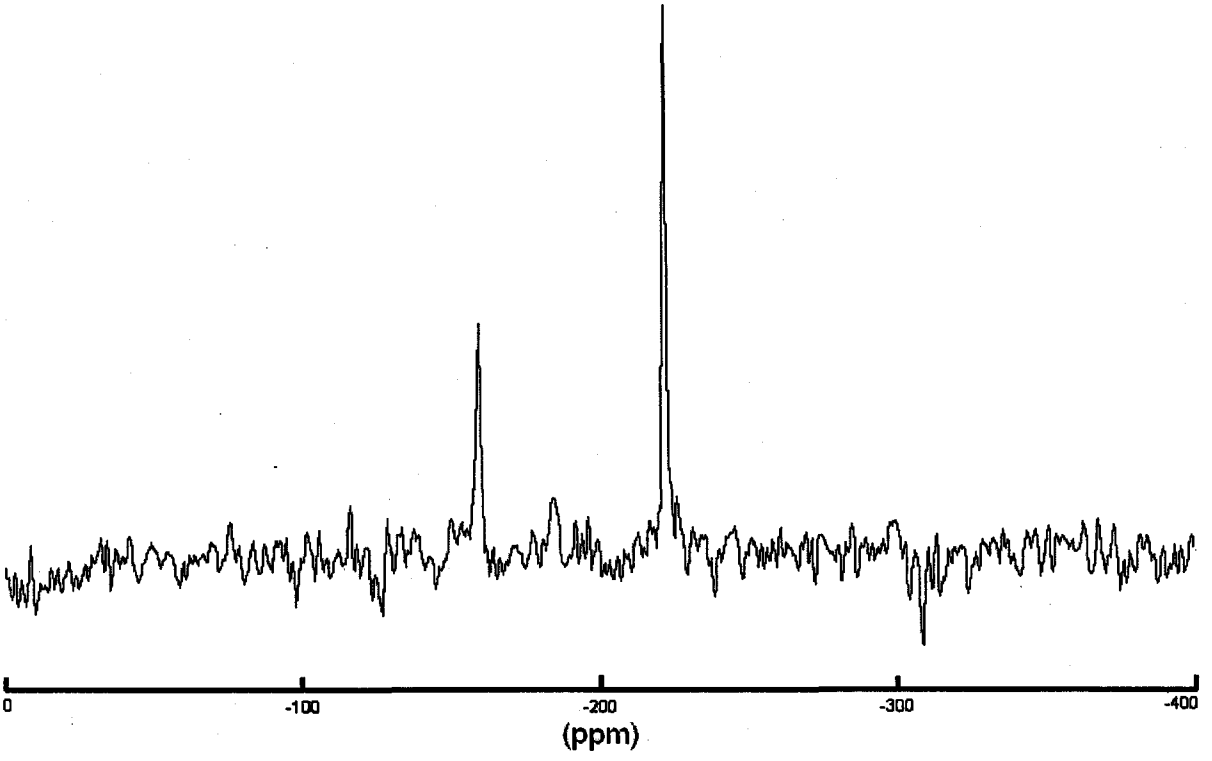

Figure 6.2.20 The ^{109}Ag MAS NMR spectrum of $AgClO_4$. ν_R = 3.5 kHz; D_1 = 24 hours; NS=1.

The ^{35}Cl NMR experiments have been run in order to compare with the observation from the solid state ^{109}Ag NMR spectrum. Figure 6.2.21 shows the solid state ^{35}Cl spectrum.

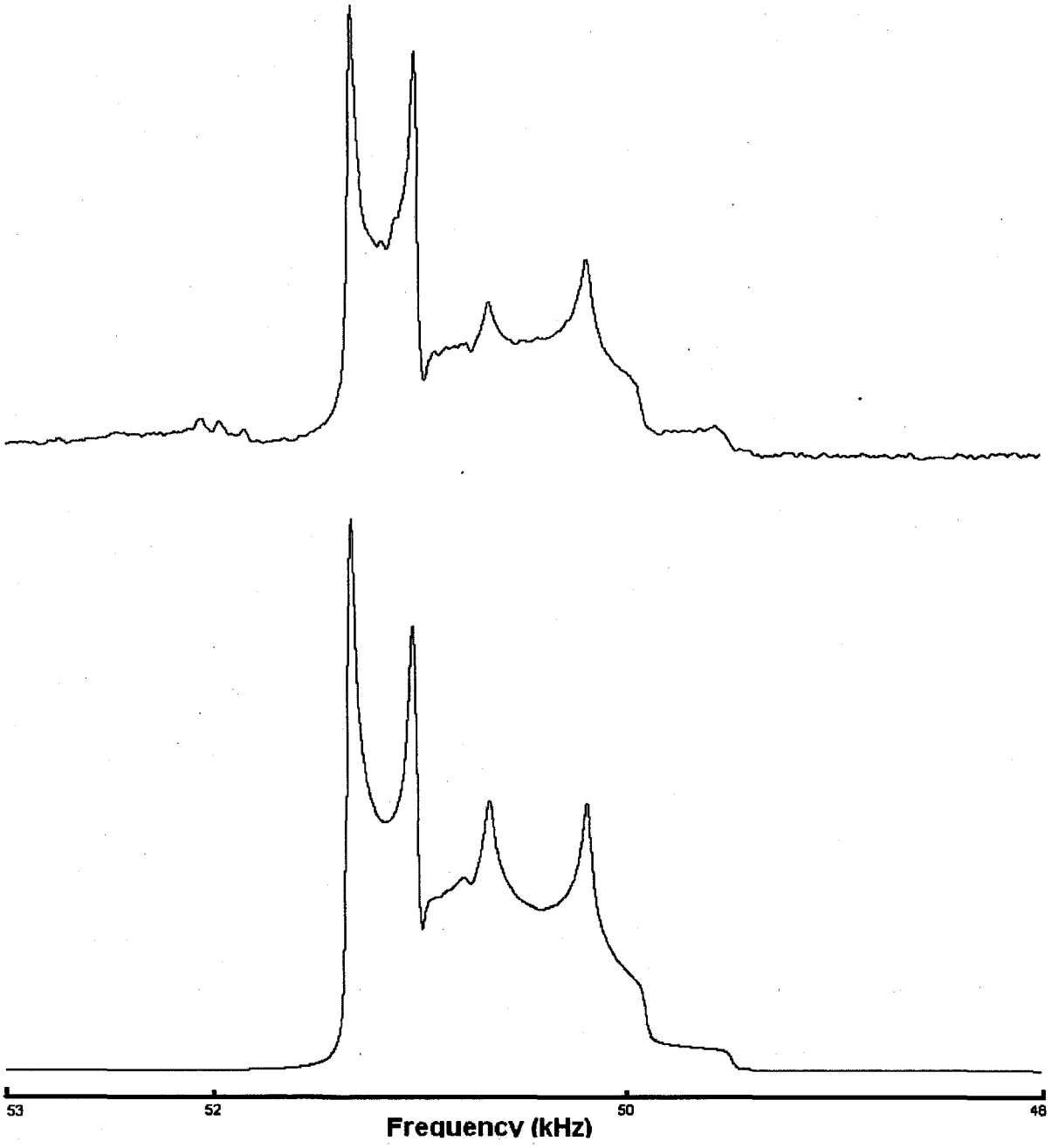

Figure 6.2.21 The ^{35}Cl MAS NMR spectrum of $AgClO_4$. ν_R = 10 kHz; D_1 = 1 second; NS = 8000. The intensity ratio of the two lineshapes is 2:3 (left:right). (B_0 = 11.75 T)

The ^{35}Cl NMR spectrum of $AgClO_4$ contains two types of resonance with an intensity ratio 2:3 (left peak: right peak). The left peak has a quadrupolar coupling constant of 0.73 ± 0.04 MHz, and an asymmetry parameter of 0.01 ± 0.01, and an isotropic shift of 1049.4 ± 2.0 ppm. The quadrupolar asymmetry parameter of zero means that there is a Cn ($n \geq 3$) symmetry at this Cl site.

The right peak has a quadrupolar coupling constant of 1.10 ± 0.05 MHz, and an asymmetry parameter of 0.36 ± 0.03, and an isotropic shift of 1042.4 ± 2.0 ppm. The nonzero quadrupolar asymmetry parameter means that there is a distorted tetrahedral symmetry at this Cl site. According to the solid state ^{109}Ag and ^{35}Cl MAS NMR spectrum, there are two kinds of Ag^+ and ClO_4^- ions in this sample.

The intensity ratios as obtained by ^{109}Ag and ^{35}Cl NMR spectroscopy are not in agreement. The ^{35}Cl chemical shifts tell us that there are two types of perchlorate anions in the sample. One possibility is that the crystal structure is wrong. Another is that there are two separate solid phases in the sample. A third possibility is that there is a mixture of anhydrous and hydrated $AgClO_4$, because commercial anhydrous $AgClO_4$ can easily absorb water in air to form $AgClO_4 \cdot H_2O$ and the ^{35}Cl NMR spectrum of $AgClO_4$ was obtained two months after the ^{109}Ag NMR spectrum.

6. 2. 4. 2 $AgSO_3CF_3$

A crystal structure for $AgSO_3CF_3$ is not available. The solid state ^{109}Ag MAS NMR spectrum of $AgSO_3CF_3$ is shown in Figure 6.2.22. This spectrum consists of one single narrow peak at a chemical shift 15.0 ppm. This indicates that there is one type of chemically equivalent silver atom in the crystallographic asymmetric unit. This compares to a value of 35.0 ppm for $AgSO_3CH_3$.

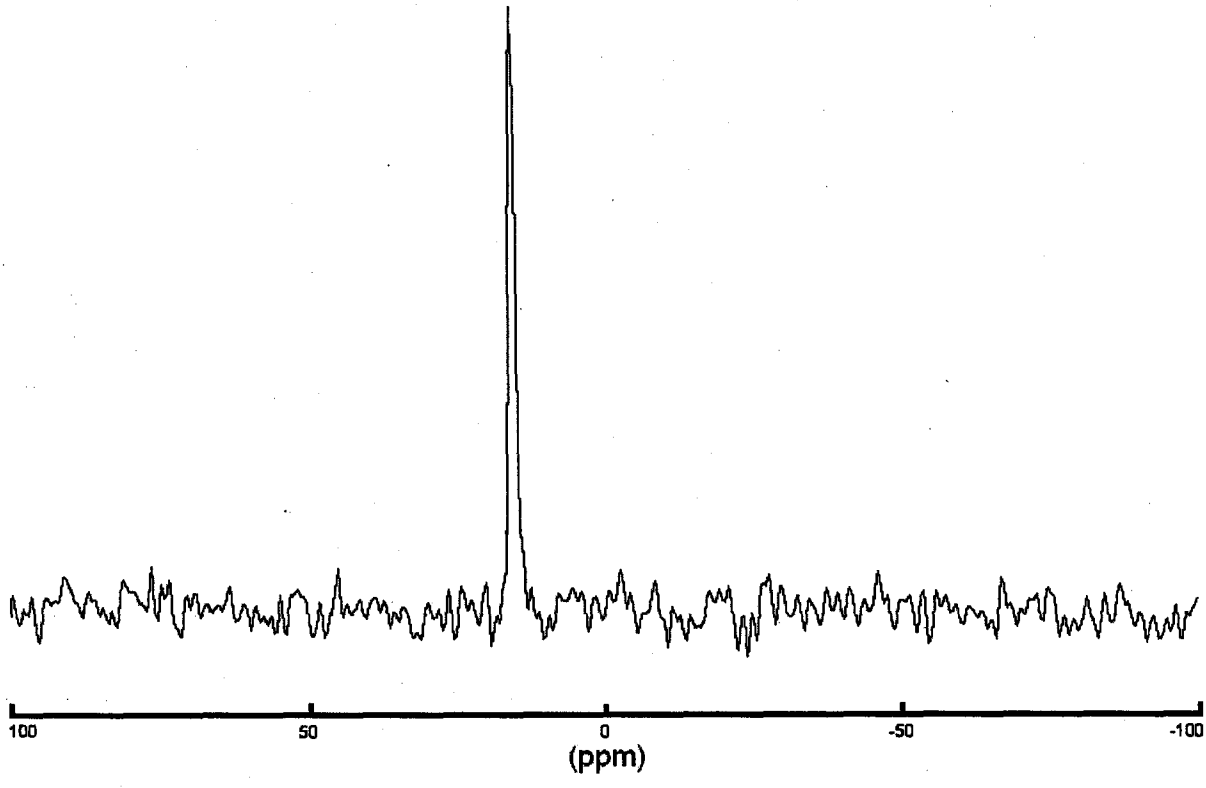

Figure 6.2.22 The ^{109}Ag MAS NMR spectrum of $AgSO_3CF_3$: $\nu_R = 3.5$ kHz; $D_1 = 1800$ s; NS = 8.

6. 2. 4. 3 $AgCO_2CF_3$

$AgCO_2CF_3$ crystallizes in a monoclinic space group with systematic absences conforming to the space groups Cc or C2/c with Z = 8 [22]. There is one independent $AgCO_2CF_3$ moiety in the asymmetric unit for C2/c and two for Cc. The NMR results (Figure 6.2.23) show two patterns of spinning sidebands. Although the spectrum is of poor quality it is consistent with the space group Cc in the asymmetric unit. This is an excellent example of how solid state NMR spectroscopy can be used to obtain crystallographic information.

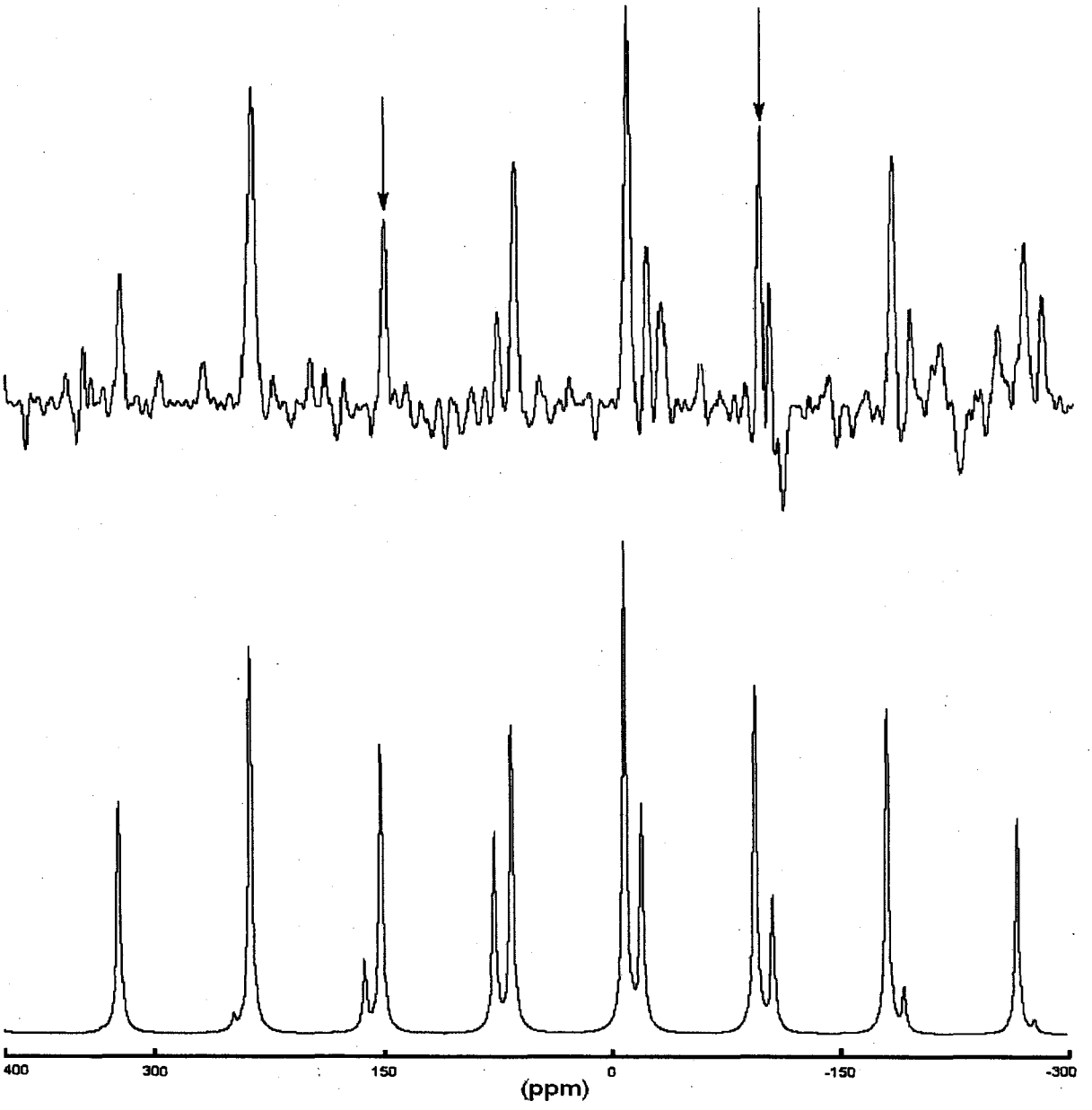

Figure 6.2.23 Experimental (top) and simulated (bottom) solid state ^{109}Ag NMR spectra of silver triflate, $\nu_R = 2$ kHz, $D_1 = 1800$ s, NS = 64, and an intensity ratio of 1:1. The arrows indicate the isotropic chemical shifts.

Table 6.2.17 The following Table shows the parameters used to simulate the ^{109}Ag spectrum of $AgCO_2CF_3$.

δ_{11}	δ_{22}	δ_{33}	δ_{iso}	Ω	κ
461 (53)	173 (46)	-179 (38)	152 (3)	640 (76)	0.10 (0.05)
157 (53)	-58(46)	-386 (38)	-96.2 (3)	540 (76)	0.20 (0.05)

Chapter 6-2: References

[1] H. W. Qinn, J. H. Tsai, *Adv. Inorg. Radiochem.*, 12 (1969) 217.

[2] G. W. Hunt, T. C. Lee, E. L. Amma, *Inorg. Nucl. Chem. Lett.*, 10 (1974) 909.

[3] R. E. Rundle, J. H. Goring, *J. Am. Chem. Soc.*, 72 (1950) 5337.

[4] H. G. Smith, R. E. Rundle, *J. Am. Chem. Soc.*, 80 (1958) 5075.

[5] R. K. McMullan, T. F. Koetzle, C. J. Fritchie Jr., *Acta Cryst.*, B53 (1997) 645.

[6] R. W. Turner, E. L. Amma, *J. Am. Chem. Soc.*, 88 (1966) 3243.

[7] M. J. Begley, D. B. Sowerby, R. D. Verma, A. Vig, *J. Organomet. Chem.*, 481 (1994) 243.

[8] M. B. Dines, *J. Organomet. Chem.*, 67 (1974) C55.

[9] H. Wadepohl, H. Pritzkow, *Acta Cryst.*, C57 (2001) 383.

[10] S. V. Ivanov, A. J. Lupinetti, S. M. Miller, O.P. Anderson, K. A. Solntsev, S. H. Strauss, *Inorg. Chem.*, 34 (1995) 6419.

[11] S. V. Ivanov, J. J. Rockwell, S. M. Miller, O. P. Anderson, K. A. Solntsev, S. H. Strauss, *Inorg. Chem.*, 35 (1996) 7882.

[12] A. S. Batsanov, S. P. Crabtree, J. A. K. Howard, C. W. Lehmann, M. Kilner, *J. Organomet. Chem.*, 550 (1998) 59.

[13] R. S. Mulliken, *J. Am. Chem. Soc.*, 74 (1952) 811.

[14] M. J. S. Dewar, *Bull. Soc. Chim. Fr.*, 18 (1951) C79.

[15] M. M. Francl, R. F. Hout, Jr, and W. J. Hehre, *J. Am. Chem. Soc.*, 106 (1984) 563.

[16] E. A. H. Griffith, E. L. Amma, *J. Am. Chem. Soc.*, 96 (1974) 743.

[17] K. Shelly, D. C. Finster, Y. J. Lee, W. R. Scheidt, and C. A. Reed, *J. Am. Chem. Soc.*, 107 (1985) 5955.

[18] H. Strub, A. J. Beeler, D. M. Grant, J. Michl, P. W. Cutts, and K. W. Zilm, *J. Am. Chem. Soc.*, 105 (1983) 3333.

[19] A. Pines, M. G. Gibby, and J. S. Waugh, *Chem. Phys. Lett.*, 15 (1972) 373.

[20] A. Pausak, J. Tegenfeldt, and J. S. Waugh, *J. Chem. Phys.*, 61 (1974) 1338.

[21] H. J. Berthold, J. M. Molepo, R. Wartchow. *Zeitschrift fuer Kistallographie*, 144 (1976) 116.

[22] R. G. Griffin, J. D. Ellett Jr., M. Mehring, J. G. Bullitt, and J. S. Waugh, *J. Chem. Phys.*, 57 (1972) 2147.

6.3 Theoretical Calculation of ^{109}Ag Chemical Shieldings with All-Electron Basis Set

NMR spectroscopy of transition metal nuclei is a very attractive tool for the elucidation of the structures of complexes of transition metals. Most transition metal nuclei span a very wide chemical shift range, and the dependence of this on the multiple coordination and binding modes of these metals is not easily predicted. Solid state NMR spectroscopy of silver nuclei is a good example, in that the chemical shift range is 1000 ppm [1]. Therefore, it is highly desirable to be able to predict the major features of these NMR spectra, and also relate the spectral parameters to electronic and molecular structure.

The quantum chemical calculation of nuclear shieldings provides an attractive method for structure elucidation, since it should yield an independent estimate of the chemical shift which can then be used to predict the spectral region in which an NMR signal can be found, and ultimately serve for spectral assignment through the comparison with experimental values. Quantum chemical methods have proved to be very effective in predicting the nuclear shielding of many nuclei [2], including transition metals [3-7]. Much emphasis has been placed on obtaining a near -1 slope in such correlations, which implies a correct prediction of the absolute magnitude of the nuclear shielding.

Few all-electron Gaussian basis sets are available for Ag. In this study the DGDZVP basis set was employed [8, 9, 10].

Calculated chemical shieldings for a set of molecules are shown in Table 6.3.1. These molecules were chosen because they are small (relatively few electrons), they have simple structures (easy geometry optimizations) and the experimental structures should not be solvent dependent (no ligand exchange).

6. 3. 1 Theoretical Chemical Shieldings Calculated using DGDZVP Basis Set at HF, B3LYP and MP2 Levels of Theory Compared with Previously Measured Chemical Shifts.

Calculated data are presented in the following Table and Figures. All calculated results were performed using the DGDZVP basis sets at the HF, B3LYP and MP2 levels of theory. These calculated values are compared with solution chemical shifts [11, 12].

Table 6.3.1 lists the calculated isotropic chemical shieldings using the DGDZVP basis set and experimental isotropic chemical shifts.

Table 6.3.1 GIAO isotropic chemical shieldings using DGDZVP basis and experimental isotropic chemical shifts.

Compound	HF	B3LYP	MP2	Expt. [11,12]
$Ag(CF_2H)CN$	3791.7	3411.3	3696.6	579.1
$Ag(CN)_2$	3786.4	3393.3	3676.5	584.3
$Ag(CF_3)CN$	3813.7	3434.6	3724.6	566
$Ag(CF_3)_2$	3841.8	3477.6	3661.0	565.5
$Ag(NH_3)_2$	4128.5	3735.1	4024.8	505
cis-$Ag(CF_2H)_2(CF_3)_2$	1977.3	2115.5	1893.3	2089.7
trans-$Ag(CF_2H)_2(CF_3)_2$	1879.7	2110.7	1837.2	2098
$Ag(CF_2H)_3(CF_3)$	1960.1	2147.5	1914.9	2136.5
trans-$Ag(CF_2H)_2(CN)_2$	1853.8	2036.1	1807.2	2110.8
$Ag(CF_3)_3(CN)$	1704.0	1935.3	1631.3	2250.4
cis-$Ag(CF_3)_2(CN)_2$	1668.7	1882	1570.7	2301.6
trans-$Ag(CF_3)_2(CN)_2$	1639.2	1894.3	1563.0	2292.5
$Ag(CF_3)(CN)_3$	1584.6	1824.2	1478.5	2343.7
$Ag(CF_3)_3Cl$	1764.1	2072.9	1699.3	2187.8
$Ag(CF_3)_3Br$	1865.5	2157.6	1826.9	2135.2
$Ag(CF_3)_3I$	2007.4	2262.1	2000.5	2003
$Ag(CF_2H)_4$	1983.9	2136.2	1935.6	2041.9

The double line separates the two ligand coordinated silver complexes from the four ligand coordinated silver complexes. Figures 6.3.1, 6.3.2, and 6.3.3 show the correlation between ^{109}Ag experimental chemical shifts and calculated chemical shieldings using the

DGDZVP basis set at HF, B3LYP and MP2 levels. The data are from Table 6.3.1. The two ligand coordinated silver complexes are shown in the upper cluster of points and the four ligand coordinated silver complexes are in the lower cluster in Figures 6.3.1, 6.3.2, and 6.3.3.

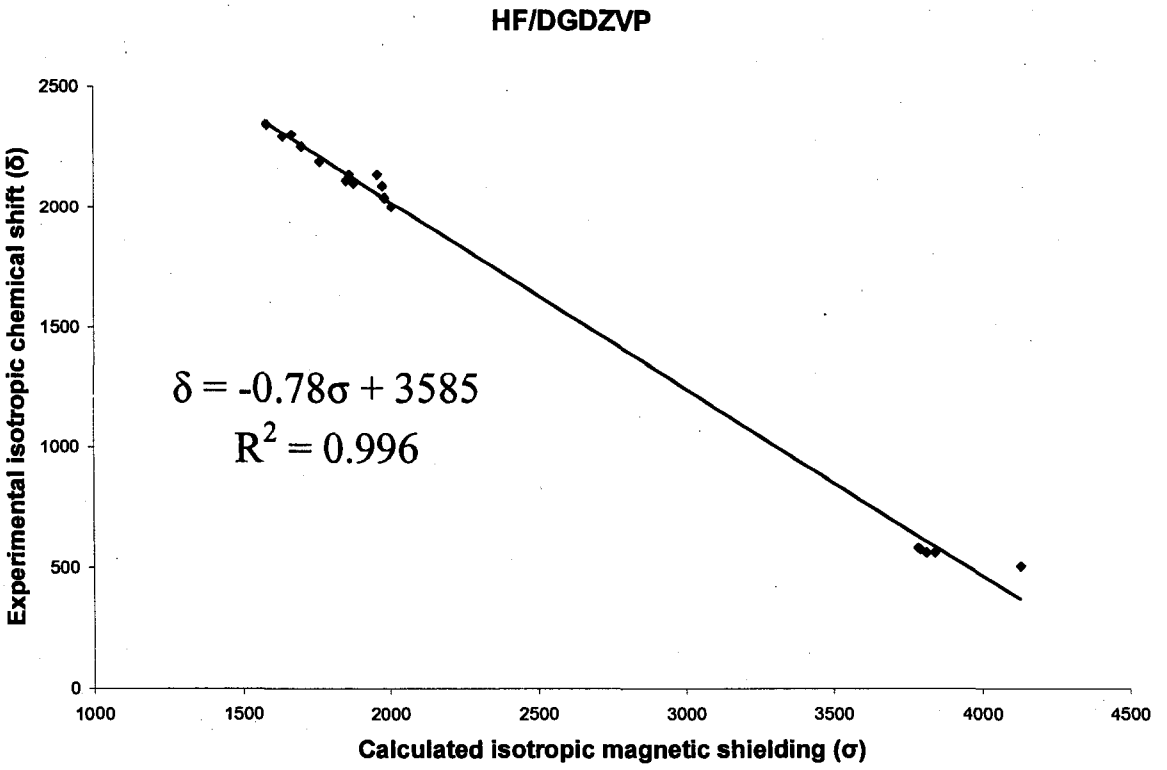

Figure 6.3.1 Correlation between ^{109}Ag experimental chemical shifts and calculated chemical shieldings at HF/DGDZVP level.

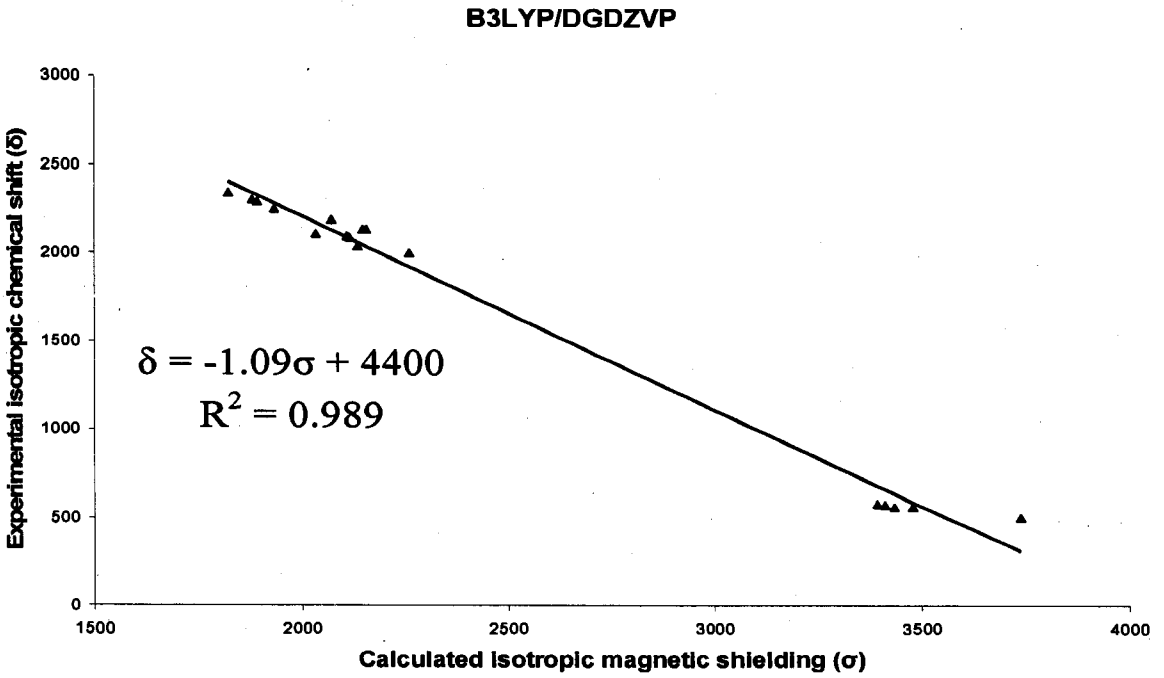

Figure 6.3.2 Correlation between ^{109}Ag experimental chemical shifts and calculated chemical shieldings at B3LYP/DGDZVP level.

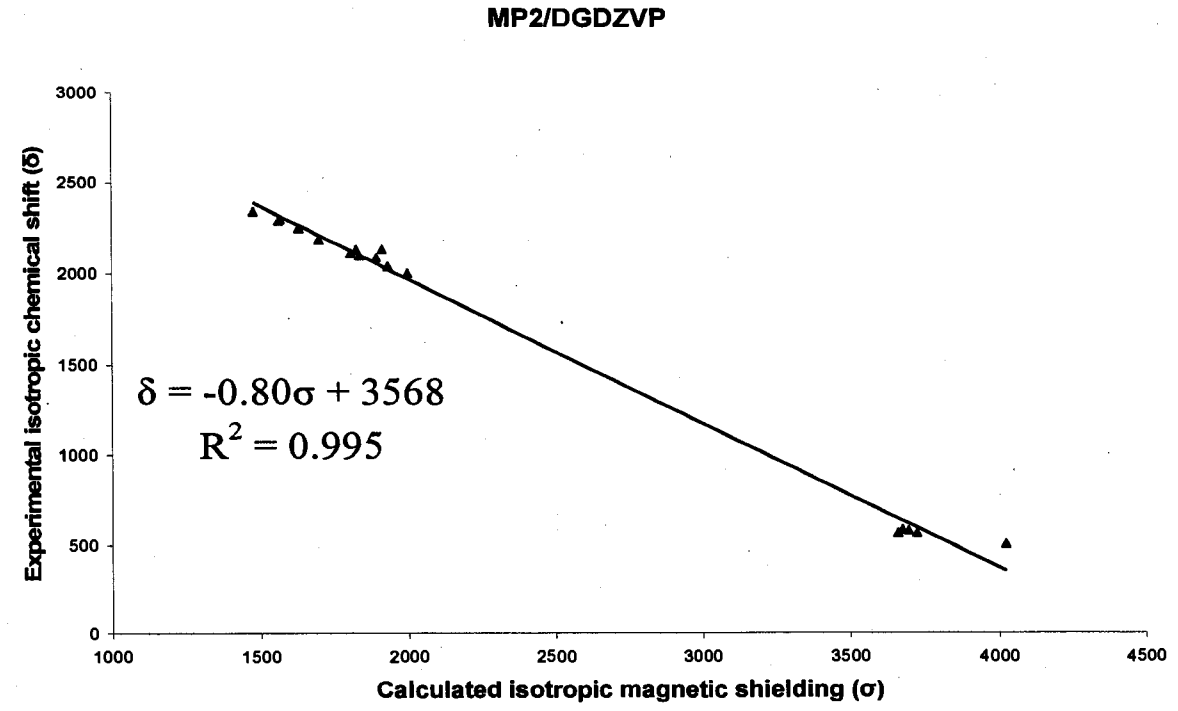

Figure 6.3.3 Correlation between ^{109}Ag experimental chemical shifts and calculated chemical shieldings at MP2/DGDZVP level.

The order of magnitude of calculated shieldings is correct, as shown by the correlation parameters, with slopes (-0.78, -1.09, -0.80) which are close to the expected value of -1. All three methods are sufficient to be used to predict chemical shifts.

The MP2 results do not appear to be very different from those obtained from HF calculations. This implies that electron correlation does not play a significant role in silver magnetic shielding calculations. Therefore, compared with the other methods, B3LYP/DGDZVP method is the best method to be used to predict silver magnetic shieldings. The DGDZVP basis set does not include relativistic effects, but it still can yield reasonably good results because the relativistic effects have been included in the intercept value. Therefore basis sets which do not include relativistic effects, such as DGDZVP, may be used to calculate magnetic shieldings.

Density functional calculations using ADF program should be performed on these molecules in the future, which have basis sets including relativistic effects. The calculated results include relativistic effects can be used to compare with results using DGDZVP basis set.

6.3.2 Comparison of Calculated and Experimental Chemical Shift Tensors for Selected Silver Complexes.

Since metal shielding tensor calculations at nonrelativistic levels are sensible for the 3d and 4d series metals [6], we calculated the NMR tensor components at the HF/DGDZVP and B3LYP/DGDZVP levels. For the compounds studied here X-ray crystal structure geometries were used.

The following Tables and Figures show the correlation between calculated magnetic shielding tensor components and experimental chemical shift tensors.

Table 6.3.2 GIAO anisotropic chemical shield tensors at B3LYP/DGDZVP level and experimental chemical shift tensors.

Compound		σ_{11}	σ_{22}	σ_{33}	σ_{iso}	Ω	κ
$[AgN_2CO C(CH_3)_3]_2$	Cal. (σ)	2983.2	2989.8	4309.0	3427.3	1325.8	0.990
	Expt. (δ)	1088	1088	-254	640.7	1340	1.000
IPr-AgCl	Cal. (σ)	2578.6	2654.8	4544.0	3259.1	1965.4	0.922
	Expt. (δ)	1210	1188	-612	595.3	1822	0.976
SIPr-AgCl	Cal. (σ)	2627.3	2704.1	4549.7	3293.7	1922.4	0.920
	Expt. (δ)	1210	1188	-612	595.3	1822	0.976

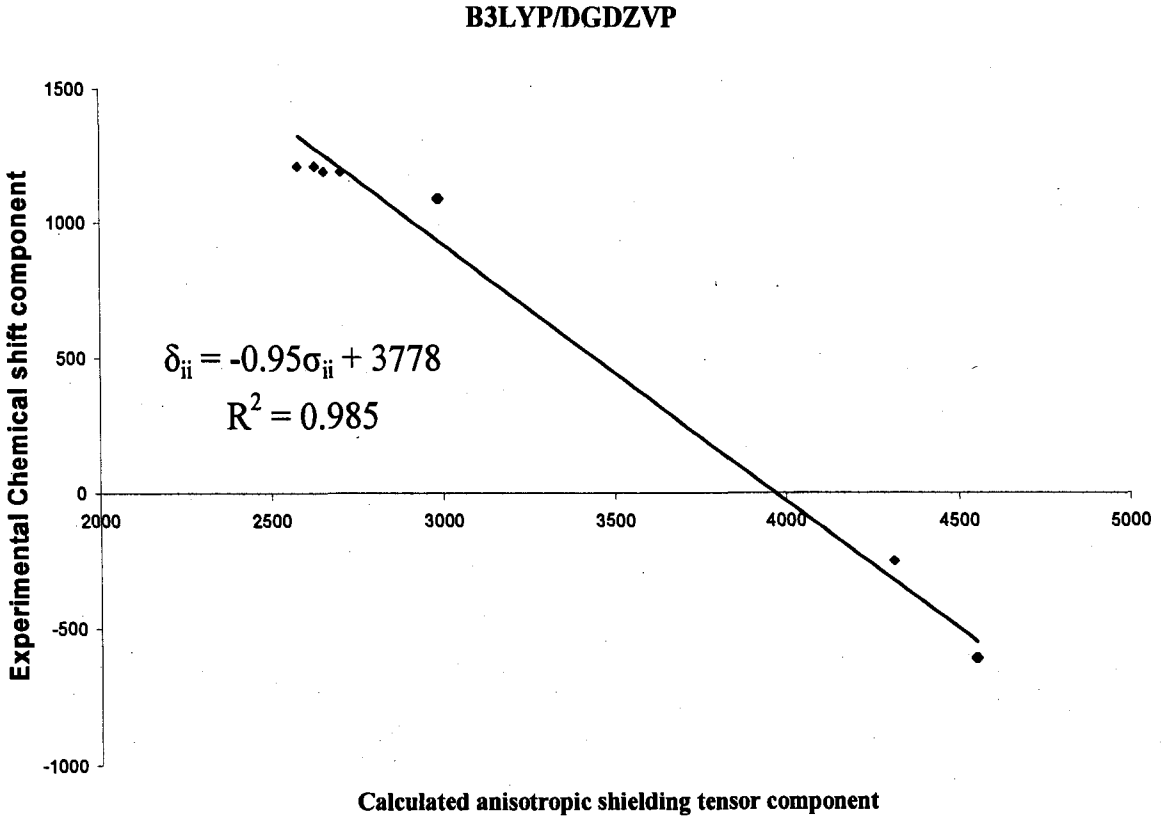

Figure 6.3.4 Correlation between ^{109}Ag experimental chemical shift tensors and calculated chemical shielding tensors at B3LYP/DGDZVP level.

Table 6.3.3 GIAO anisotropic chemical shield tensors at HF/DGDZVP level and experimental chemical shift tensors.

Compound		σ_{11}	σ_{22}	σ_{33}	σ_{iso}	Ω	κ
$[AgN_2CO C(CH_3)_3]_2$	Cal. (σ)	3335.4	3377.6	4511.7	3741.6	1176.3	0.928
	Expt. (δ)	1088	1088	-254	640.7	1340	1.000
IPr-AgCl	Cal. (σ)	3040.1	3047.2	4627.3	3571.5	1587.2	0.991
	Expt. (δ)	1210	1188	-612	595.3	1822	0.976
SIPr-AgCl	Cal. (σ)	3079.4	3103.5	4631.5	3604.8	1552.1	0.969
	Expt. (δ)	1210	1188	-612	595.3	1822	0.976

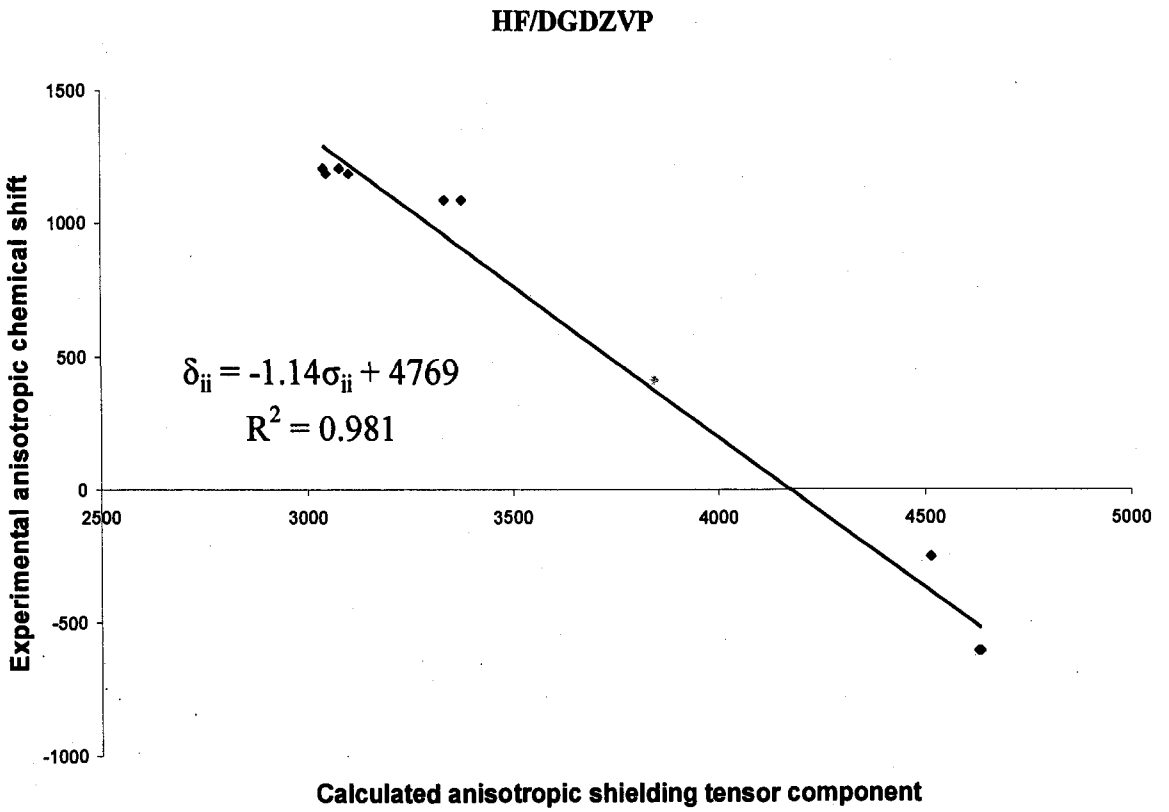

Figure 6.3.5 Correlation between ^{109}Ag experimental chemical shift tensors and calculated chemical shielding tensors at HF/DGDZVP level.

Since the slope obtained from the B3LYP/DGDZVP method is closer to the expected value of -1 than that for the HF/DGDZVP method. It is reasonable to conclude that B3LYP/DGDZVP is the better method.

6.3.3 Density Functional Calculations (LDA-PW91) of NMR Chemical Shielding Tensors with the Inclusion of Spin-orbit Relativistic Effects in Silver Compounds.

All DFT calculations in this section were carried out using the Amsterdam Density Functional program (ADF trial version) [13]. The functionals employed included the local density approximation of Vosko, Wilk, and Nusair (LDA VWN) [14] augmented with the nonlocal gradient correction PW91 from Perdew and Wang [15-17]. Relativistic corrections were added using the ZORA (zero order regular approximation) spin-orbit Hamiltonian [18-22].

ZORA calculations employed a double-ζ slater type basis set. Silver NMR shieldings were calculated by the NMR program of Wolff et al. [23, 24] using the orbitals generated by the single-point run.

Table 6.3.4 lists the calculated shielding tensors (σ) compared with experimental chemical shift tensors (δ).

Table 6.3.4 LDA-PW91 shielding tensors (σ) compared with experimental chemical shift tensors (δ).

Compound		σ_{11}	σ_{22}	σ_{33}	σ_{iso}	Ω	κ
$[AgN_2CO C(CH_3)_3]_2$	Cal.Rel.(σ)	2813.6	2898.6	4376.2	3362.8	1562.6	0.890
	Cal.non.(σ)	2502.5	2585.8	4008.3	3032.2	1505.8	0.889
	Expt.(δ)	1088	1088	-254	640.7	1340	1.000
IPr-AgCl	Cal.Rel.(σ)	2781.6	2892.8	4852.7	3509.0	2071.2	0.893
	Cal.non.(σ)	2471.5	2556.4	4422.7	3150.2	1951.2	0.913
	Expt.(δ)	1210	1188	-612	595.3	1822	0.976
SIPr-AgCl	Cal.Rel.(σ)	2841.9	2952.0	4842.4	3545.5	2000.5	0.890
	Cal.non.(σ)	2526.7	2615.6	4418.7	3187.0	1892.0	0.906
	Expt.(δ)	1230	1136	-600	588.7	1830	0.897

All experimental chemical shift tensors are solid state NMR results.

Figures 6.3.6 and 6.3.7 show the correlation between ^{109}Ag calculated chemical shielding tensors without and with relativistic effects included and experimental chemical shift tensors.

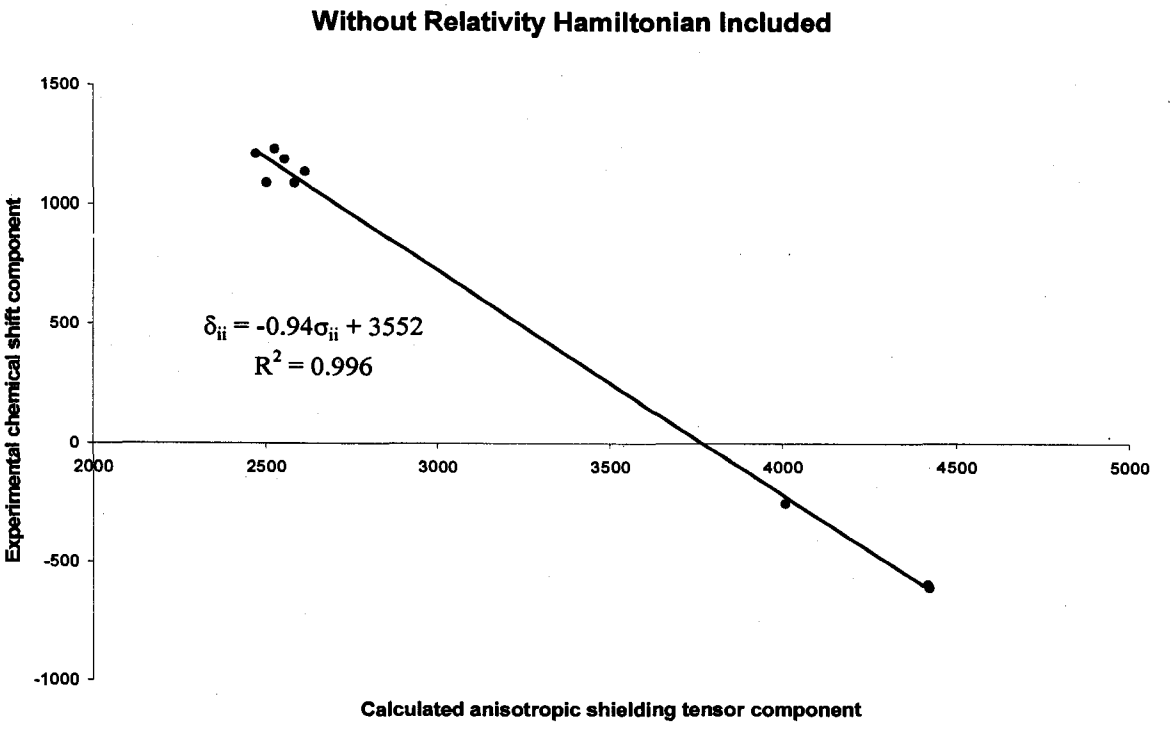

Figure 6.3.6 Correlation between ^{109}Ag calculated chemical shielding tensors without relativity Hamiltonian included and experimental chemical shift tensors.

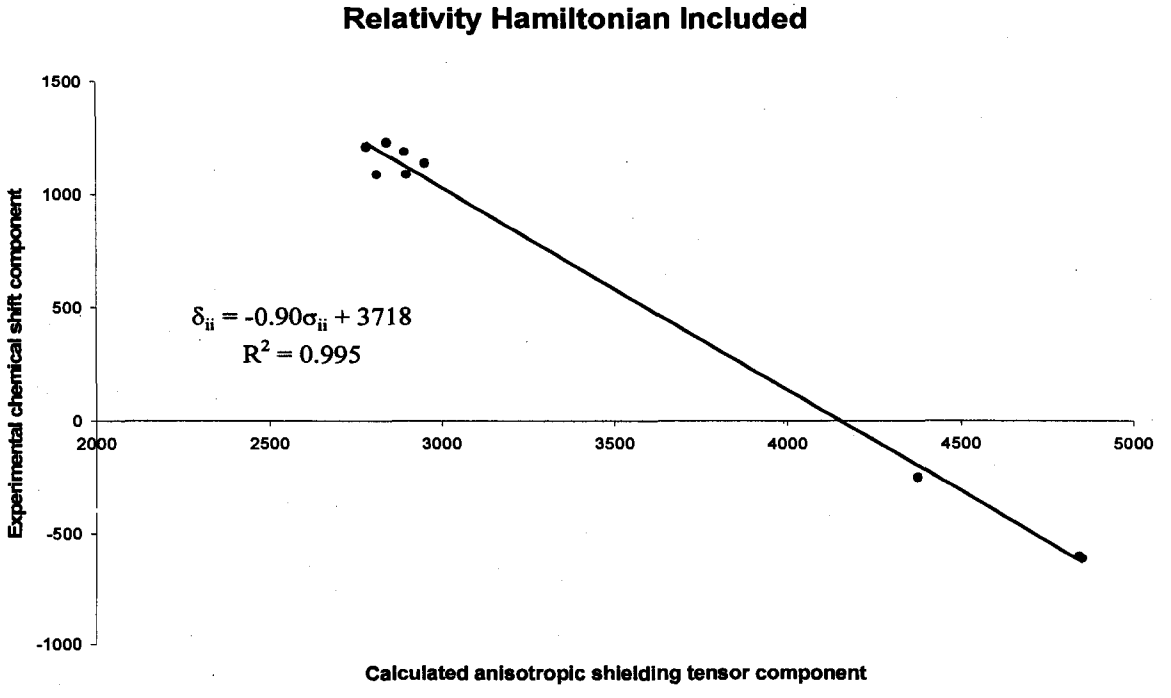

Figure 6.3.7 Correlation between ^{109}Ag relativistic calculated chemical shielding tensors and experimental chemical shift tensors.

The intercept changes from 3552 to 3718 ppm upon inclusion of relativistic effects. There is no significant change in the R^2 value. Therefore this set of calculations indicates that inclusion of relativistic effects should not, on average, improve the calculation shieldings of silver.

Comparing nonrelativistic calculations, inclusion of relativistic effects in the calculation of ^{109}Ag chemical shift tensors for the selected compounds changes the slope from -0.94 to -0.90, which is a deviation away from the expected value of -1.0.

Summary of Solid State NMR and Quantum Chemical Studies of Silver Containing Compounds:

The ^{109}Ag chemical shift tensor components of NHC complexes including SiPr-AgCl, IPr-AgCl, SiMes-AgCl, IMes-Ag-IMes, Iet-AgCl, Ity and SIPrFL have been obtained and a comparison of the spectra to what is expected from known crystal structures was performed.

The ^{109}Ag CP/MAS NMR spectra are in accordance with the crystal structure of SiPr-AgCl, SiMes-AgCl and IMes-Ag-IMes. The single pattern of spinning sidebands of solid state ^{109}Ag CP/MAS NMR spectra of Iet-AgCl, Ity and SIPrFL implies that only one type of Ag atom exists in each of these three complexes.

The ^{109}Ag and ^{13}C chemical shift tensor components of some silver-arene complexes including $C_6H_6 \cdot AgClO_4$, $C_6H_6 \cdot AgCF_3SO_3$, $C_6H_6 \cdot AgCF_3CO_2$, paraxylene$\cdot AgClO_4$, Mesitylene$\cdot AgCF_3SO_3$, $C_6(CH_3)_6 \cdot AgCF_3CO_2$, and $C_6(CH_3)_6 \cdot AgCF_3SO_3$ have been obtained;

The ^{109}Ag and ^{13}C CP/MAS spectra of $C_6H_6 \cdot AgClO_4$ and $C_6H_6 \cdot AgCF_3CO_2$ are consistent with the crystal structures of $C_6H_6 \cdot AgClO_4$ and $C_6H_6 \cdot AgCF_3CO_2$, respectively.

The ^{109}Ag CP/MAS spectrum of $C_6H_6 \cdot AgCF_3SO_3$ is not consistent with the crystal structure of $C_6H_6 \cdot AgCF_3SO_3$, but the ^{13}C CP/MAS spectrum $C_6H_6 \cdot AgCF_3SO_3$ clearly shows one pattern of spinning sidebands and is consistent with the crystal structure of $C_6H_6 \cdot AgCF_3SO_3$. The possible explanation is that the interaction between Ag and benzene in $C_6H_6 \cdot AgCF_3SO_3$ is weak.

When compared with the tensor components δ_{11} and δ_{22} of the frozen benzene at 20 K and the hexamethylbenzene at 87 K, it can be seen that these two tensor components in complexes are nearly averaged because of the fast rotation of the benzene ring.

Comparing the ^{13}C tensor components δ_{11}, δ_{22}, and δ_{33} of three complexes with those components of benzene at 223 K, one can see that the numbers do not change much, which indicates that the interaction between silver and benzene is weak.

The ^{13}C tensor components δ_{11}, δ_{22} and δ_{33} of the two hexamethylbenzene silver complexes are not changing much from those of hexamethylbenzene at room temperature, which means that the interaction between silver and hexamethylbenzene is weak.

The solid state ^{109}Ag and ^{35}Cl NMR spectra and parameters of $AgClO_4$ have been obtained. According to the solid state ^{109}Ag and ^{35}Cl MAS NMR spectrum, there are two kinds of Ag^+ and ClO_4^- ions in this sample. The intensity ratios as obtained by ^{109}Ag and ^{35}Cl NMR spectroscopy are not in agreement. The most likely possibility is that there is a mixture of anhydrous and hydrated $AgClO_4$.

The solid state ^{109}Ag MAS NMR spectrum of $AgSO_3CF_3$ shows one single narrow peak which indicates that there is one type of chemically equivalent silver atom in the crystallographic asymmetric unit.

$AgCO_2CF_3$ crystallizes in a monoclinic space group with systematic absences conforming to the space groups Cc or C2/c with Z = 8. There is one independent $AgCO_2CF_3$ moiety in the asymmetric unit for C2/c and two for Cc. The NMR results show two patterns of spinning sidebands. Although the spectrum is of poor quality it is consistent with the space group Cc in the asymmetric unit.

All calculated results performed using the DGDZVP basis sets at the HF, B3LYP and MP2 levels of theory give a good linear relationship with the known experimental chemical shifts. B3LYP/DGDZVP method is the best.

Chapter 6-3: References

[1] C. F. Shaw III, *The chemistry of organic derivatives of gold and silver*, John Wiley & Sons Ltd., Chapter 4, (1999).

[2] T. Helgaker, M. Jaszunski, and K. Ruud, *Chem. Rev.*, 99 (1999) 293.

[3] M. Bühl, O. L. Malkina, V. G. Malkin, *Helv. Chim. Acta*, 79 (1996) 742.

[4] M. Kaupp, V. G. Malkin, O. L. Malkina, D. R. Salahub, *Chem. Eur. J.*, 2 (1996) 24.

[5] O. L. Malkina,B. Schimmelpfennig, M. Kaupp, B. A. Hess, P. Chandra, U. Wahlgren, and V. G. Malkin, *Chem. Phys. Lett.*, 296 (1998) 93.

[6] N. Godbout, E. Oldfield, *J. Am. Chem. Soc.*, 119 (1997) 8065.

[7] P. J. Wilson, R. D. Amos, N. C. Handy, *Phys. Chem. Chem. Phys.*, 2 (2000) 187.

[8] N. Godbout, D. R. Salahub, J. Andzelm, and E. Wilmmer, *Can. J. Chem.*, 70 (1992) 560.

[9] C. Sosa, J. Andzelm, B. C. Elkin, E. Wimmer, K. D. Dobbs, and D. A. Dixon, *J. Phys. Chem.*, 96 (1992) 6630.

[10] M. Bühl, S. Gaemers, C. J. Elsever, *Chem. Eur. J.*, 6 (2000) 3272.

[11] R. Eujen, B. Hoge, and D. J. Brauer, *Inorg. Chem.*, 36 (1997) 3160.

[12] R. Eujen, B. Hoge, and D. J. Brauer, *Inorg. Chem.*, 36 (1997) 1464.

[13] Amsterdam Density Functional program (ADF trial version 2006.01); Division of Theoretical Chemistry, Vrije University, De Boelelaan 1083, 1081 HV Amsterdam, The Netherlands; http://www.scm.com.

[14] S. H. Vosko, L. Wilk, M. Nusair, *Can. J. Phys.*, 58 (1980) 1200.

[15] K. Burke, J. P. Perdew, and Y. Wang, in *Electronic Density Functional Theory: Recent Progress and New Directions*, Ed. J. F. Dobson, G. Vignale, and M. P. Das (Lenum, 1998).

[16] J. P. Perdew, in *Electronic Structure of Solids*, Ed. P. Ziesche and H. Eschrig (Akademie Verlag, Berlin, (1991) 11.

[17] J. P. Perdew, J. A. Chevary, S. H. Vosko, K. A. Jackson, M. R. Pederson, D. J. Singh, C. Fiolhais, *Phys. Rev.* B, 46 (1992) 6671.

[18] E. van Lenthe, E. J. Baerends, and J. G. Snijders, *J. Chem. Phys.*, 99 (1993) 4597.

[19] E. van Lenthe, E. J. Baerends, and J. G. Snijders, *J. Chem. Phys.*, 101 (1994) 9783.

[20] E. van Lenthe, J. G. Snijders, and E. J. Baerends, *J. Chem. Phys.*, 105 (1996) 6505.

[21] E. van Lenthe, R. van Leeuwen, E. J. Baerends, and J. G. Snijders, *Int. J. Quantum Chem.*, 57 (1996) 281.

[22] E. van Lenthe, A. E. Ehlers, and E. J. Baerends, *J. Chem. Phys.*, 110 (1999) 8943.

[23] S. K. Wolff, T. Ziegler, *Int. J. Quantum Chem.*, 61 (1997) 899 and references therein.

[24] S. K. Wolff, T. Ziegler, *J. Chem. Phys.*, 103 (1998) 895.

Chapter VII

Deuterium Lineshape and T_1 Studies of Deuterated-Benzene Silver Perchlorate Complexes

One way to gain further insight into the Ag-benzene interaction and its strength, is by investigating the rotational dynamics of the phenyl ring in complexes of benzene and silver salts. This can be done through the use variable temperature of deuterium lineshape and relaxation times.

7.1 ^{2}H Relaxation Time Study of $Ag(C_6D_6)ClO_4$

All of the displayed temperatures, calibrated temperatures, spin lattice relaxation times and $\ln T_1$ are shown in Table 7.1.

Table 7.1 The T_1 ^{2}H NMR experiment values of $Ag(C_6D_6)ClO_4$ at different temperatures

Displayed Temperature (K)	Calibrated temperature (K)	1000/T(calibrated temperature) (K^{-1})	T_1 (ms)	$ln T_1$
205 ± 1	200.8 ± 2.0	4.98 ± 0.5	70.1 ± 1.2	-2.66 ± 0.02
215 ± 1	211.3 ± 2.0	4.73 ± 0.5	38.3 ± 1.2	-3.26 ± 0.03
225 ± 1	221.8 ± 2.0	4.51 ± 0.4	20.1 ± 1.2	-3.91 ± 0.03
235 ± 1	232.4 ± 2.0	4.30 ± 0.4	11.4 ± 1.2	-4.47 ± 0.03
245 ± 1	242.9 ± 2.0	4.12 ± 0.4	7.4 ± 1.2	-4.91 ± 0.03
255 ± 1	253.4 ± 2.0	3.95 ± 0.4	5.8 ± 1.2	-5.15 ± 0.04
260 ± 1	258.7 ± 2.0	3.87 ± 0.4	5.6 ± 1.2	-5.18 ± 0.04
265 ± 1	264.0 ± 2.0	3.79 ± 0.3	5.4 ± 1.2	-5.22 ± 0.04
275 ± 1	274.5 ± 2.0	3.64 ± 0.3	6.0 ± 1.2	-5.12 ± 0.04
285 ± 1	285.0 ± 2.0	3.51 ± 0.3	7.4 ± 1.2	-4.90 ± 0.03
295 ± 1	295.5 ± 2.0	3.38 ± 0.3	9.8 ± 1.2	-4.62 ± 0.03
300 ± 1	300.8 ± 2.0	3.32 ± 0.3	11.7 ± 1.2	-4.45 ± 0.03
306 ± 1	307.1 ± 2.0	3.26 ± 0.3	235.6 ± 1.2	-1.45 ± 0.01
310 ± 1	311.4 ± 2.0	3.21 ± 0.2	257.8 ± 1.2	-1.36 ± 0.01
320 ± 1	321.9 ± 2.0	3.11 ± 0.2	307.1 ± 1.2	-1.18 ± 0.01
330 ± 1	332.4 ± 2.0	3.01 ± 0.2	332.2 ± 1.2	-1.10 ± 0.01
340 ± 1	342.9 ± 2.0	2.92 ± 0.2	398.3 ± 1.2	-0.92 ± 0.01
350 ± 1	353.5 ± 2.0	2.83 ± 0.2	418.1 ± 1.2	-0.87 ± 0.01

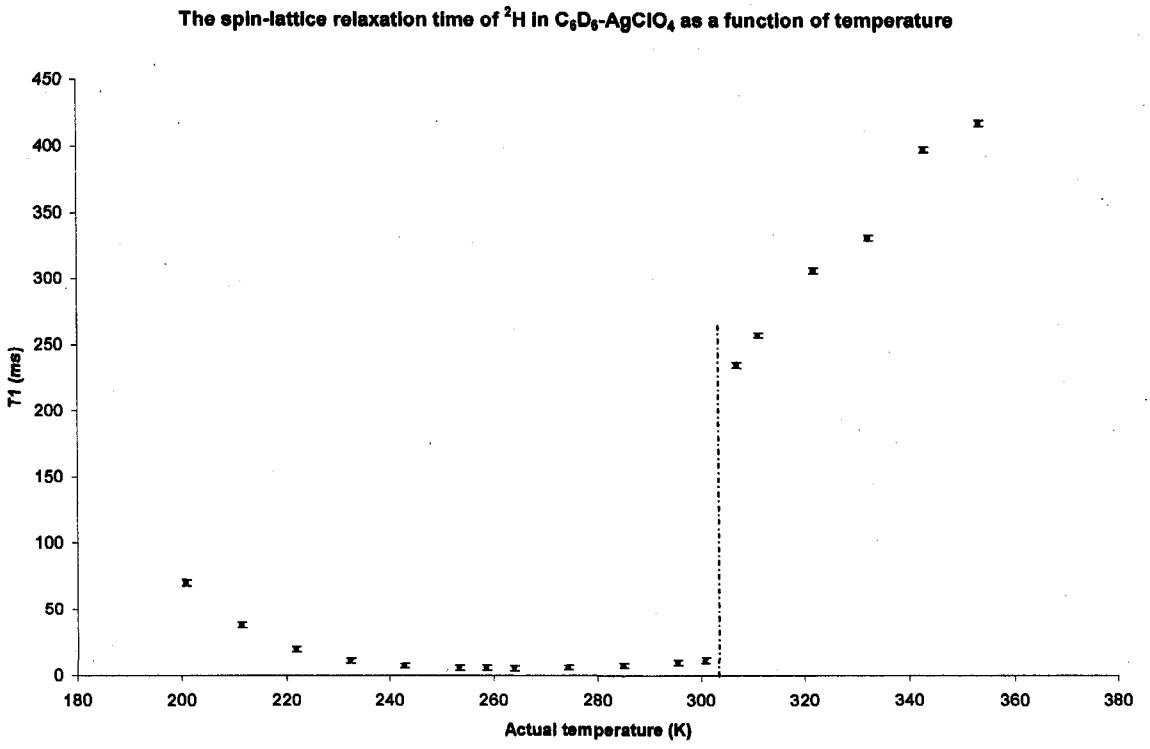

Figure 7.1 The T_1 data of ^2H in $C_6D_6 \cdot AgClO_4$ versus calibrated temperatures.

The ^2H T_1 values for solid $Ag(C_6D_6)ClO_4$ change abruptly at 303 ± 3 K. This is consistent with a solid-solid phase transition. The available crystal structure for $Ag(C_6D_6)ClO_4$ was obtained at room temperature.

The motional rates are much greater than the ^2H quadrupolar coupling constant in the high temperature phase (T > 300 K), therefore the lineshape does not change with temperature in this phase. ^2H relaxation time measurements can be used to obtain a description of the molecular motion. Figure 7.2 shows a plot of $\ln T_1$ versus the inverse temperature. The slope (slope = $-E_a/R$) of this graph provides the activation energy for jumps of the benzene ring about its C_6 axis in the high temperature phase (T > 300 K). The activation energy for this motion was found to be 11.3 ± 1.1 kJ/mol.

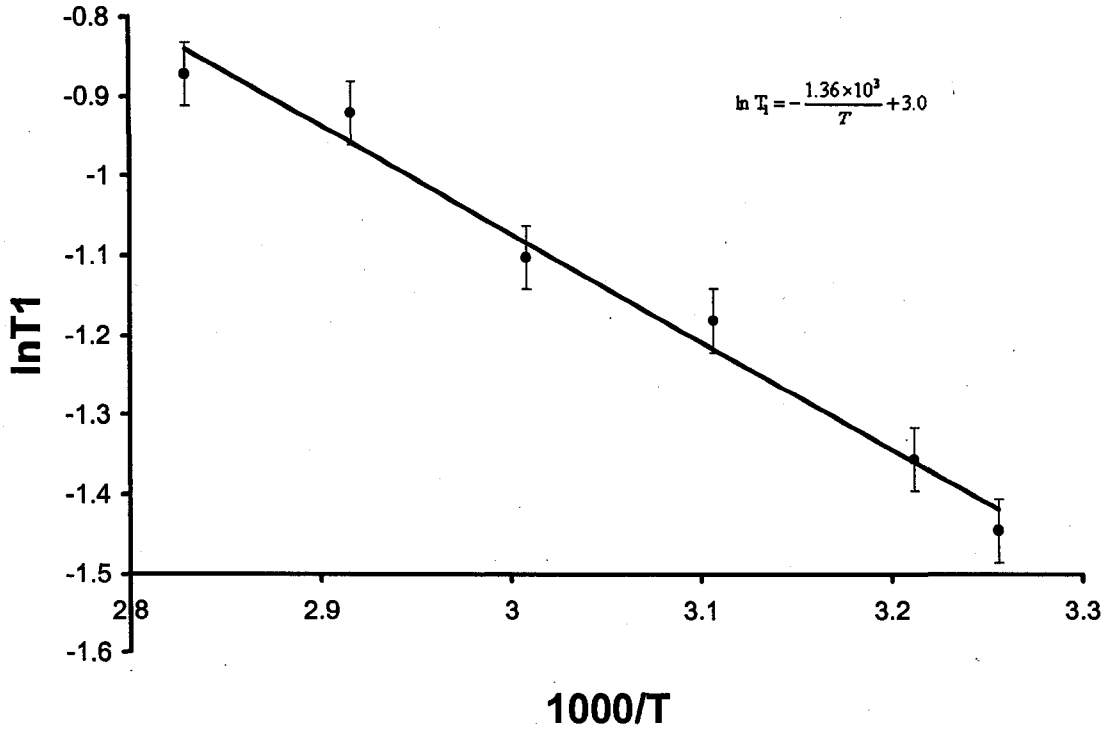

Figure 7.2: ^2H spin lattice relaxation times, as a function of temperature (307 K-353 K), at the high temperature phase of $Ag(C_6D_6)ClO_4$.

In the temperature range of 200 K to 300 K the motional rates are still much greater than the ^2H quadrupolar coupling constant, so ^2H relaxation time measurements were used to obtain a description of the molecular motion. In the low temperature phase the ln T_1 vs. 1/T curve passes through a minimum at about 265 K. Therefore it should be possible to fit this curve in order to obtain the dynamic parameters for the benzene reorientation. The plot in Figure 7.3 was fit using the Bloembergen, Purcell and Pound (BPP) theory [1] (see Equation 3.6 in section 3.4.2). E_a (activation energy), τ_∞ (correlation time at infinity temperature) and K (constant) were obtained as 23.9 ± 0.3 kJ/mol, 2.5 ± 0.5 x 10^{-14} s, 5.0 ± 0.5 x 10^{10} s^{-1}, respectively.

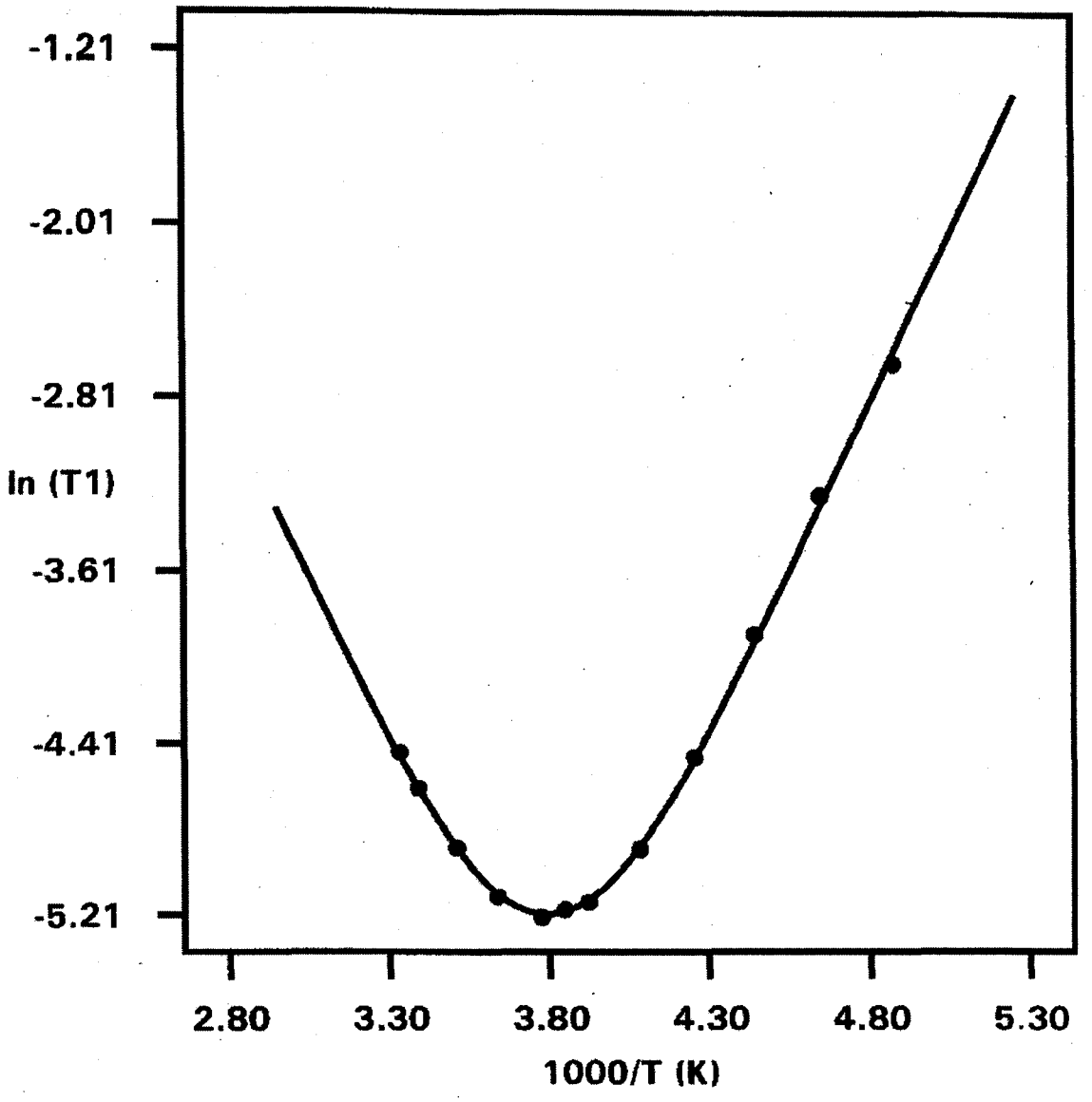

Figure 7.3: ^2H spin lattice relaxation times as a function of temperature (201 K - 306 K), for the low temperature phase of $Ag(C_6D_6)ClO_4$. This curve was fit using the BPP program.

E_a is the activation energy for the motion influencing T_1, and K depends on the strength of the dominant nuclear spin interaction (in this case the quadrupolar interaction) and the exact nature of the reorientational motion. For jumps of the C-D bond among three or more equivalent positions oriented at an angle θ about the rotational axis (in this case $\theta = 90°$), K is given by [2]

$$K = \frac{9\pi^2\chi^2}{40}(1-\frac{\eta_Q}{3})^2 \qquad (7.1)$$

where η_Q is the asymmetric parameter and χ is the quadrupolar coupling constant. Substitution of values for $K = 5.0 \pm 0.5 \times 10^{10}$ and $\eta_Q = 0$ the value of χ is calculated as 150 ± 8 kHz.

Deuterium spin echo spectroscopy is a particularly attractive technique for the characterization and measurement of the rates of anisotropic molecular motion in organic solids. If one assumes a $\eta_Q = 0$ and rapid rotation of the benzene ring around its 6-fold axis it can be shown [2] that:

$$\Delta\nu_{eff} = \frac{3}{8}\chi \qquad (7.2)$$

The powder splitting $\Delta\nu_{eff}$ has the value 67.6 ± 0.5 kHz. Substitution of this value Equation 7.3 yields value for χ of 180.3 ± 1.3 kHz. This value obtained for the quadrupole coupling constant was independent of temperature in the interval 201-300 K. Barnes and Bloom [3] had obtained the value $\chi = 180.7 \pm 1.5$ kHz from the powder spectrum at 77 K for pure deuterated benzene. A value $\chi = 177.0 \pm 2.4$ kHz of pure deuterated benzene was provided from Boden and his co-works in the temperature interval 150-250 K [2]. In this work the χ value is agreement with these two χ values. However the χ value obtained by analysis of the T_1 curve (see above) is smaller than these values. It is well known that χ values obtained from fitting temperature dependent T_1 curves are less reliable than those obtained from lineshape analysis [4]. This being the case, one can see that coordination of the benzene ring to silver has a negligible effect on the deuterium quadrupolar coupling onstant.

7.2 Lineshape Analysis of $Ag(C_6D_6)ClO_4$

The motional rate of the benzene ring in the temperature range of 153 K to 206 K is of the same order of magnitude as χ, therefore the ^2H NMR lineshape becomes very sensitive to the exchange rate. Simulations for these lineshapes give the rate constants which, when plotted against the inverse temperature, yields Arrhenius activation energies, E_a, for the rotation of benzene ring in the crystalline complexes.

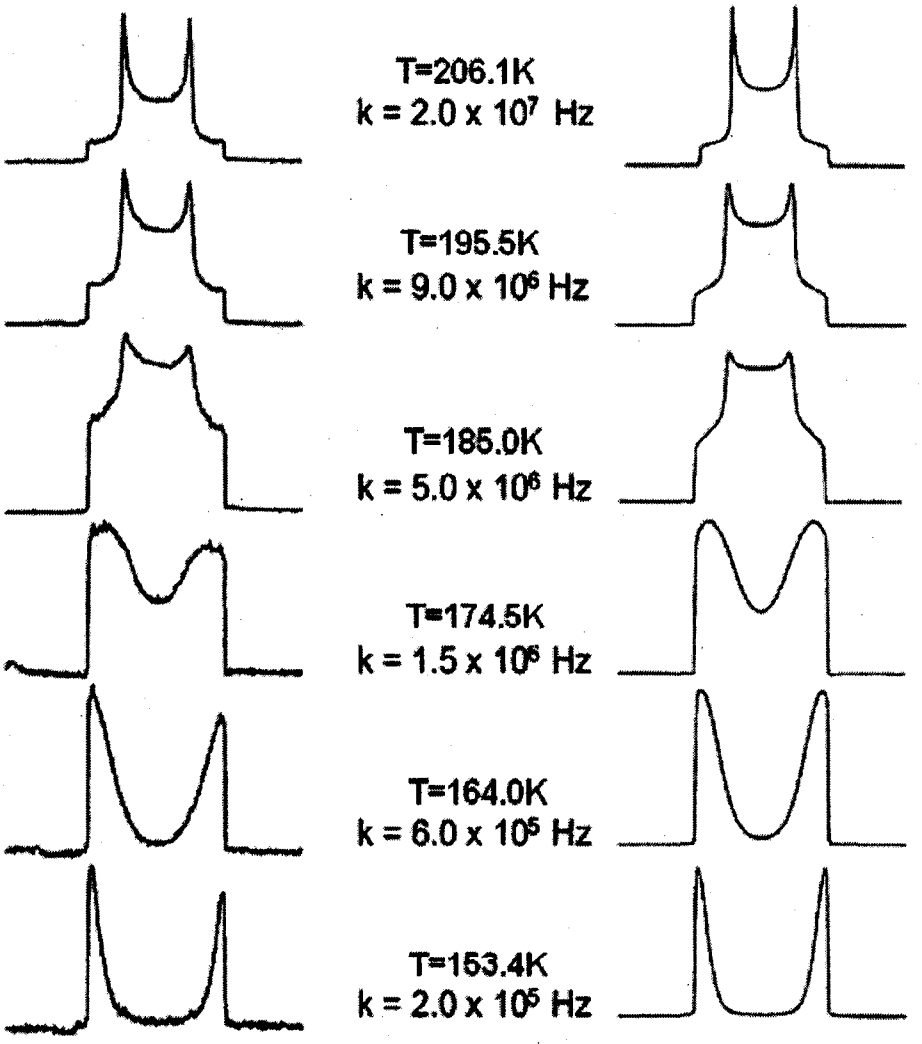

Figure 7.4: ^2H NMR spectra for $Ag(C_6D_6)ClO_4$ at various temperatures (153 K-206 K), along with best fit simulated lineshapes.

All spectra were simulated with quadrupole coupling constant $\chi = 180 \pm 3$ kHz and an asymmetry parameter $\eta_Q = 0$. One possible explanation for the discrepancy between the quadrupole coupling constant determined from spectra in the temperature range of 201-300 K and the ^2H lineshape analysis in the temperature interval 153-206 K is that the quadrupole coupling constant might not be strictly independent of temperature, leading to the difference as a result of the different temperature ranges. The quadrupole coupling constant determined from the spectra is essentially constant over their temperature range from 201 K to 300 K.

The intensity distributions in all recorded spectra are not symmetric. Experimental sources that can contribute to the asymmetry of ^2H NMR powder patterns have been discussed [5]. Changes in the ^2H NMR line shape with temperature in Figure 7.4 demonstrate clearly that the ^2H nuclei are mobile at these temperatures. The spectral simulation (constructed using the 6 sites jump model with jump frequency k) which best fits the experimental spectrum at each temperature is shown in Figure 7.5.

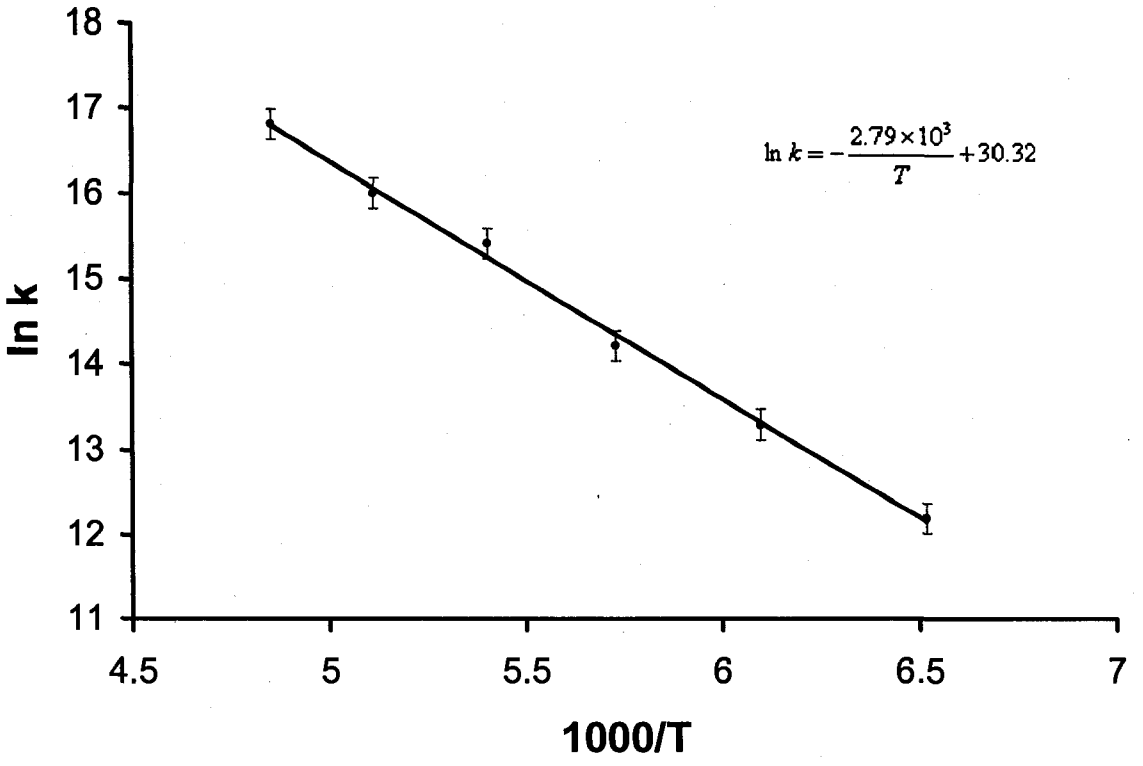

Figure 7.5: six-site exchange rates from ^2H lineshapes, as a function of temperature (from153 K to 206 K), for the low temperature phase of $Ag(C_6D_6)ClO_4$.

An Arrehnius plot of the jump rates as a function of temperature provides the activation energy for the jumps of the benzene ring about its C_6 axis. The activation energy is 23.2 ± 1.0 kJ/mol.

The two activation energies obtained for the low temperature phase in this work are in good agreement. From the above results, we know that the activation energy barriers to intermolecular exchange of the deuterium is very low, and the benzene ring still rotates very fast even at very low temperature. Again, this is consistent with weak interaction between the silver cation and the π-system of the benzene ring.

The in-plane reorientations of benzene in the pure solid and in numerous complexes and inclusion compound have been studied by several techniques and are summarized in Table 7.2.

Table 7.2 Comparison of activation parameters for in-plane rotation of benzene in its pure crystalline phase and in other environments.

system	Temp. range (K)	E_a (kJ/mol^{-1})	technique	ref.
C_6D_6	133-277	19.0	^{2}H NMR (T_1)	[6]
C_6D_6	87-140	16.5	^{2}H NMR (LSA)	[7]
$Ag(C_6D_6)ClO_4$	307-353	11.3 ±1.1	^{2}H NMR (T_1)	this work
$Ag(C_6D_6)ClO_4$	201-300	23.9 ±0.5	^{2}H NMR (T_1)	this work
$Ag(C_6D_6)ClO_4$	153-206	23.2 ±1.0	^{2}H NMR (LSA)	this work
$(\eta^6\text{-}C_6D_6)Cr(CO)_3$	119-163	19.6	^{2}H NMR (LSA)	[8]
$(\eta^6\text{-}C_6D_6)Cr(CO)_3$	119-398	17.7	^{2}H NMR (T_1)	[8]
$(\eta^6\text{-}C_6H_6)Cr(CO)_3$	115-170	17.6	^{1}H NMR (T_1)	[9]
$(\eta^6\text{-}C_6H_6)Cr(CO)_3$	10	27.5	IQNS	[10]
$(\eta^6\text{-}C_6H_6)Cr(CO)_3$	262-325	15.5	IQNS	[11]
$(\eta^6\text{-}C_6H_6)Cr(CO)_3$	120	25.9	Raman	[12]
$(\eta^6\text{-}C_6H_6)Cr(CO)_3$	300	19.7	Raman	[12]
$(\eta^6\text{-}C_6H_6)Cr(CO)_3$	293	19.7	PEC	[13]
$(\eta^6\text{-}C_6H_6)Cr(CO)_3$	78	31.8	PEC	[13]
C_6D_6/1,3-cyclohexanedione	124-191	24.9	^{2}H NMR (LSA)	[7]
$2C_6D_6{\cdot}Cd(NH_3)_2{\cdot}Ni(CN)_4$	97-163	15.0	^{2}H NMR (LSA)	[14]
$2C_6D_6{\cdot}Cd(NH_3)_2{\cdot}Ni(CN)_4$	133-305	16.4	^{2}H NMR (T_1)	[14]
$2C_6D_6{\cdot}Cd$-(ethylenediamine)-$Ni(CN)_4$	163-305	16.4	^{2}H NMR (T_1)	[14]
$1/2C_6D_6{\cdot}Cd$-$(dimethylamine)_2$-$Ni(CN)_4$	77-303	7.2	^{2}H NMR (T_1)	[14]

Abbreviations: LSA= line shape analysis, PEC = potential energy calculations. IQNS= Incoherent quasielastic neutrons cattering.

The activation energy for this 6 sites jump motion has been determined as 23.9 ± 0.5 kJ/mol from ^{2}H NMR T_1 measurements (201 K - 300 K) and 23.2 ± 1.0 kJ/mol from ^{2}H NMR line shape analysis (153 K - 206 K) at low temperature phase. Both of these values are

in the high end of the range (15.5 - 25.9 kJ/mol) spanned by the values reported previously, from the application of other techniques, for the temperature region from 87 K to 305 K. The activation energy determined as 11.3 ± 1.1 kJ/mol from ^{2}H NMR T_1 measurements in the high temperature phase (307 K - 353 K) is near the low end of the reported range of E_a values.

7.3 The Solid State ^{109}Ag and ^{13}C NMR Studies of $Ag(C_6H_6)ClO_4$ at High Temperature (T = 320 K)

Since it is obvious that $Ag(C_6H_6)ClO_4$ exist in two different phases, with very different activation energies for benzene ring rotation, it would be interesting to record the ^{109}Ag and ^{13}C CP/MAS spectra in the high temperature phase and compare these to the low temperature phase spectra reported in section 6.2.1.1.

The simulated and experimental ^{13}C and ^{109}Ag solid state NMR spectra of $Ag(C_6H_6)ClO_4$ at 320 K are shown in Figure 7.6 and Figure 7.7 respectively.

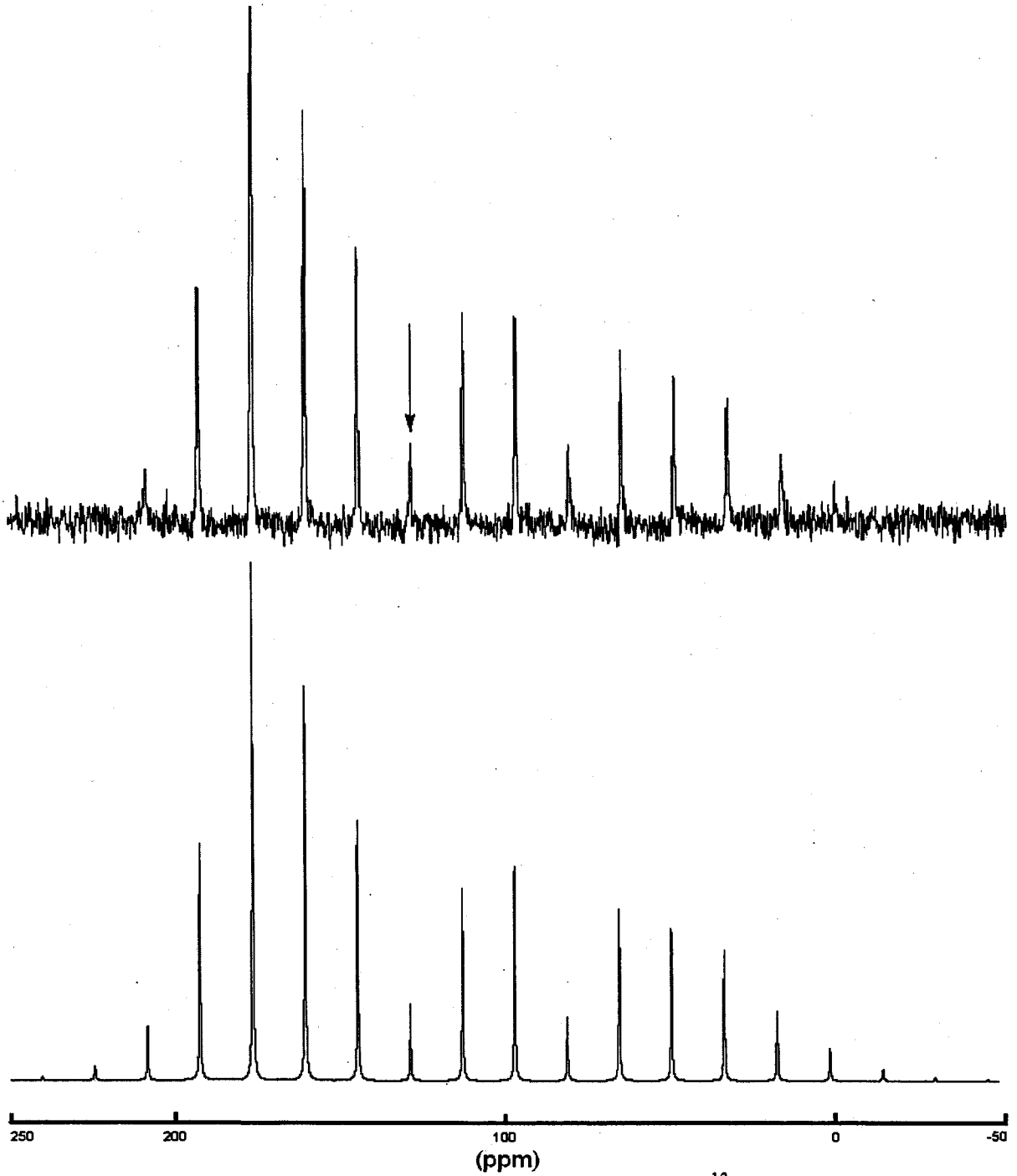

Figure 7.6 Experimental (top) and simulated (bottom) solid state ^{13}C CP/MAS NMR spectra of $Ag(C_6H_6)ClO_4$ at 320 K: $\nu_R = 2$ kHz, NS = 256. The arrow indicates the isotropic chemical shift.

Table 7.3 Solid state ^{13}C NMR parameters of $Ag(C_6H_6)ClO_4$ obtained from the simulation of the experimental spectrum.

δ_{11}	δ_{22}	δ_{33}	δ_{iso}	Ω	κ
197 (6)	185 (4)	4 (6)	129 (1)	193 (10)	0.88 (0.04)

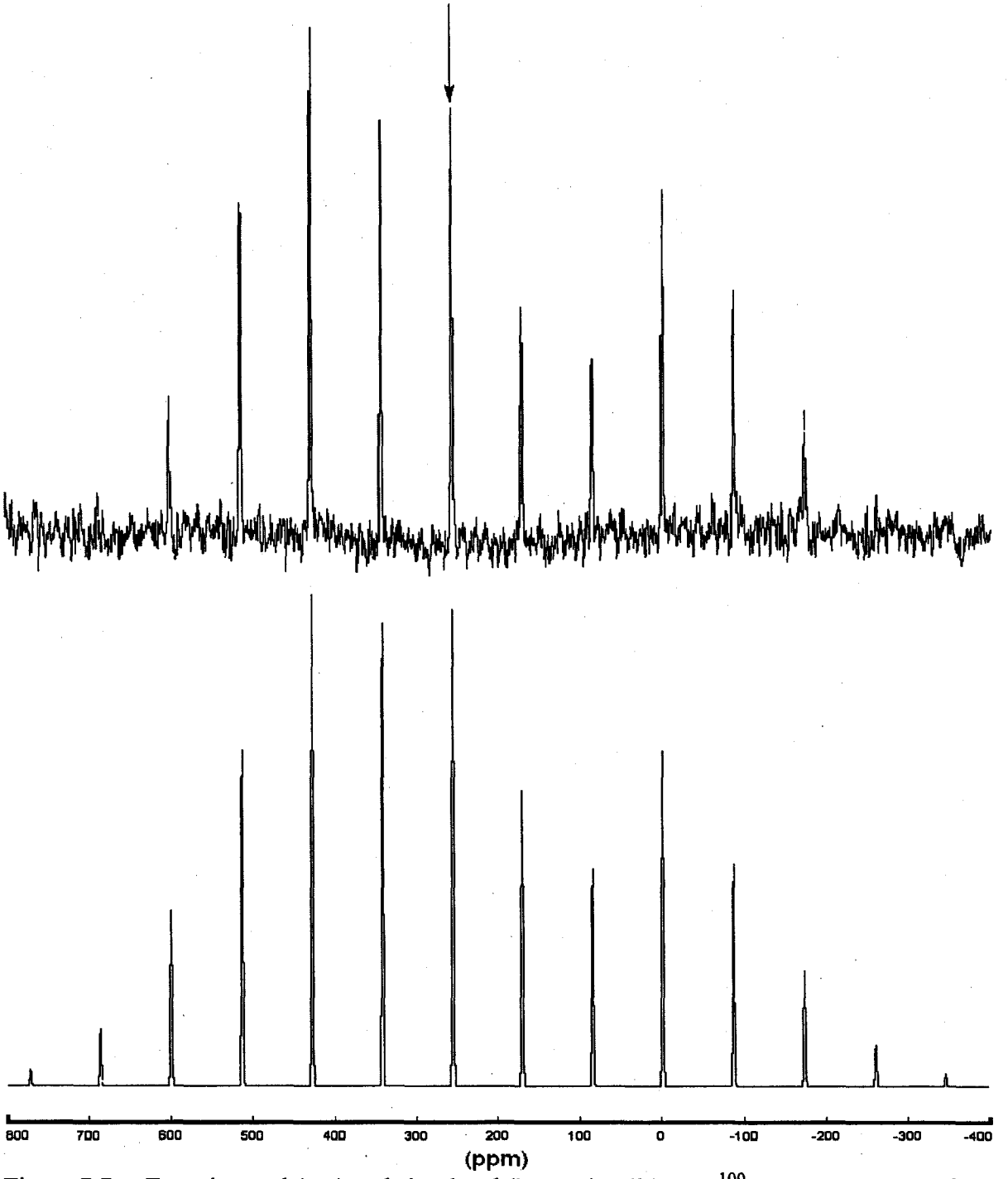

Figure 7.7 Experimental (top) and simulated (bottom) solid state ^{109}Ag NMR spectra of $Ag(C_6H_6)ClO_4$. $\nu_R = 2$ kHz, NS = 400. The arrow indicates the isotropic chemical shift.

Table 7.4 Solid state ^{109}Ag NMR parameters of $Ag(C_6H_6)ClO_4$ obtained from the simulation of the experimental spectrum.

δ_{11}	δ_{22}	δ_{33}	δ_{iso}	Ω	κ
656(8)	335 (8)	-224 (6)	255.7 (2)	880 (12)	0.27 (0.02)

The solid state ^{13}C and ^{109}Ag NMR parameters at both high temperature and low temperature are listed in Table 7.5. A solid state ^{13}C NMR spectrum was obtained at 280 K, this spectrum is nearly the same as the one obtained at room temperature and reported in section 6.2.1.1. The ^{109}Ag and ^{13}C CP/MAS spectra are consist with single Ag and C sites.

Table 7.5 Solid state ^{13}C and ^{109}Ag NMR parameters of $Ag(C_6H_6)ClO_4$ at 320 K and room temperature.

Nucleus/Temp.	δ_{11}	δ_{22}	δ_{33}	δ_{iso}	Ω	κ
^{109}Ag / 320 K	656(8)	335 (8)	-224 (6)	256 (2)	880 (12)	0.27 (0.02)
^{109}Ag/ 297 K	418 (8)	292 (8)	-292 (6)	139 (2)	710 (12)	0.64 (0.02)
^{13}C/320 K	197 (6)	185.6 (4)	4.2 (6)	129 (1)	193 (10)	0.88 (0.04)
^{13}C/297 K	196 (6)	184 (4)	3 (6)	128 (1)	193 (10)	0.87 (0.04)

The fact that the ^{13}C chemical shift tensor components and isotropic shift are not changing much from one phase to another indicates that the interaction between benzene and silver is weak and the phase change does not change the silver-benzene coordination by much. On the other hand all of the ^{109}Ag chemical shift tensor components differ significantly between the two phases. For example the isotropic shift changes by 117 ppm. This would suggest a significant change in the crystal structure for solid $Ag(C_6H_6)ClO_4$ in going from the low to high temperature phases. This would also explain the large difference in the E_a value for benzene ring reorientation between the two phases. Even though we do not know the crystal structure for the high temperature phase we do know that the benzene ring is much less tightly held in that phase and that the local electronic structure around the Ag^+ is significantly different from the room temperature phase.

Summary of Deuterium lineshape and T_1 Studies of Deuterated-Benzene Silver Perchlorate Complexes

The temperature dependent ^2H T_1 values show a large change at 303 ± 3 K. This is indication of a solid-solid phase change. The rate and activation energies for C_6D_6 ring rotation are very different in the two phases. The Ea in the low temperature phase is 23. 9 ± 0.5 kJ/mol from T_1 studies and 23.2 ± 1.0 kJ/mol from the temperature dependent lineshapes. The temperature dependent T_1 value in the high temperature phase yield an Ea of 11.3 ± 1.1 kJ/mol.

The phase transition is confined by obtaining a ^{109}Ag CP/MAS spectrum for the two phases indicate a significant change in silver environment at the phase transition. By contrast, the ^{13}C spectra for the two phases are nearly the same.

Chapter 7: References

[1] N. Bloembergen, E. M. Purcell and R. V. Pound, *Phys. Rev.*, 73 (1948) 679.

[2] N. Boden, L. D. Clark, S. M. Hanlon, and M. Mortimer, *Faraday Symp. Chem. Soc.*, 13 (1978) 109.

[3] R. G. Barnes, and J. W. Bloom, *J. Chem. Phys.*, 57 (1972) 3082.

[4] A. E. Aliev, K. D. M. Harris, and F. Guillaume, *J. Phys. Chem.*, 99 (1995) 1156.

[5] R. G. Griffin, *Methods Enzymeol.*, 72 (1981) 108.

[6] N. Boden, L. D. Clark, S. M. Hanlon, M. Mortimer, *Faraday Symp. Chem. Soc.*, 13 (1978) 109.

[7] J. H. Ok, R. R. Vold, R. L. Vold, *J. Phys. Chem.*, 93 (1989) 7618.

[8] A. E. Aliev, K. D. Harris, *J. Phys. Chem.*, 99 (1995) 1156.

[9] P. Delise, G. Allegra, E. R. Mognashi, A. Chierico, *J. Chem. Soc.*, Faraday Trans. 71 (1975) 207.

[10] J. Howard, K. Robson, T. C. Waddington, *J. Chem. Soc.*, Dalton Trans. (1982), 967.

[11] G. Lucazeau, K. Chhor, C. Sourisseau, A. Dianoux, *J. Chem. Phys.*, 76 (1983) 307.

[12] K. Chhor, G. Lucazeau, *J. Raman Spectrosc.*, 13 (1982) 235.

[13] D. Braga, F. Grepioni, *Polyhedron*, 9 (1990) 53.

[14] E. Meirovitch, I. Belsky, *J. Phys. Chem.*, 88 (1984) 6407.

Chapter VIII

High-field ^{75}As, ^{13}C and ^{127}I NMR Studies of Solid $(CH_3)_4AsI$

8.1 Solid State NMR Study of Arsenic Compounds

The suitability of a quadrupolar nucleus for solid state NMR studies depend on i) receptivity and ii) the existence of a relatively symmetric local environment.

The extremely large ^{75}As quadrupolar couplings reported to date [1-3] make arsenic NMR a traditionally unattractive approach. On the other hand, ^{75}As has a natural abundance of 100% and a fairly high receptivity. There have been several ^{75}As nuclear quadrupole resonance (NQR) studies of minerals [4-7], but NQR does not give the quadrupolar asymmetry parameter or chemical shielding, both of which are important structural probes. Because very broad peaks lead to poor sensitivity, most ^{75}As NMR studies of solids have focused on synthetic semiconductor materials and crystalline compounds of relatively high symmetry [8-12]. However, Hari and co-workers have reported ^{75}As NMR data for chalcogenide glasses (As_2Se_3 and As_2S_3) and arsenite oxide (As_2O_3), some of which have quadrupolar couplings greater than 50 MHz (as determined by NQR) [3]. Hari et. al implemented a stepped-field echo approach to collect histograms of the ^{75}As powder patterns [13]. Such an approach can partly circumvent the sensitivity and instrumentation difficulties associated with acquiring NMR resonances from these materials.

R. J. Kirkpatrick and co-workers were the first to use spin echo and quadrupolar Carr-Purcell-Meiboom-Gill (QCPMG) approaches to examine arsenate and arsenite compounds [14].

Table 8.1 lists the properties of the quadrupolar nuclei which were the focus of this work.

Table 8.1 NMR properties of quadrupolar nuclei in this section

Isotope	Spin	Natural abundance(%)	Magnetogyric ratio $\gamma/10^7$ rad T^{-1} s^{-1}	Quadrupole moment 10^{28} $Q{\cdot}m^{-2}$	NMR frequency (MHz) relative to ^1H with 500MHz
^{75}As	3/2	100	4.595	0.314	85.900
^{127}I	5/2	100	5.3817	-0.710	100.585

8.2 Results and Discussion

8.2.1 Solid State ^2H NMR Study of Me_4AsI-d_3

The crystal structure of α-$As(CH_3)_4I$ at room temperature is cubic with space group $Pa\bar{3}$ [15]. Differential thermal analysis showed three phase transitions at 103, 175 and 215°C. The crystal structure of the high temperature phases are: β-$As(CH_3)_4I$ (tetragonal); γ-$As(CH_3)_4I$ (hexagonal) and δ-$As(CH_3)_4I$ (hexagonal). Figure 8.1 shows the structure of the $(CH_3)_4As^+$ cation in the room temperature crystal structure of α-$(CH_3)_4AsI$.

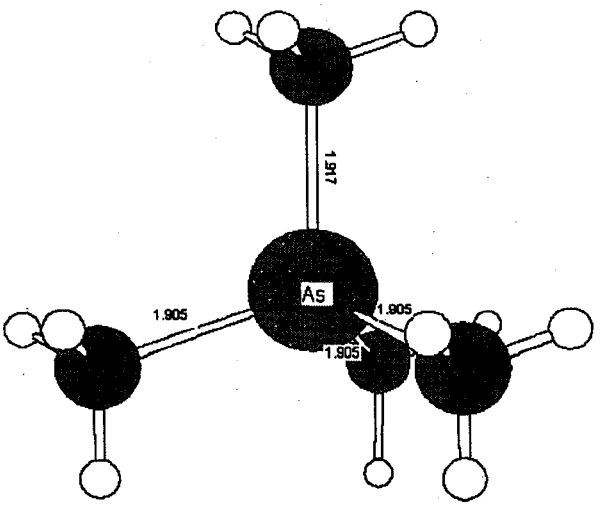

Figure 8.1 The molecular structure of the $(CH_3)_4As^+$ cation in crystalline α-$(CH_3)_4AsI$ [15].

Figures 8.2 and 8.3 show the ^2H spectra of $Me_4AsI\text{-}d_3$ at room temperature and 353 K respectively.

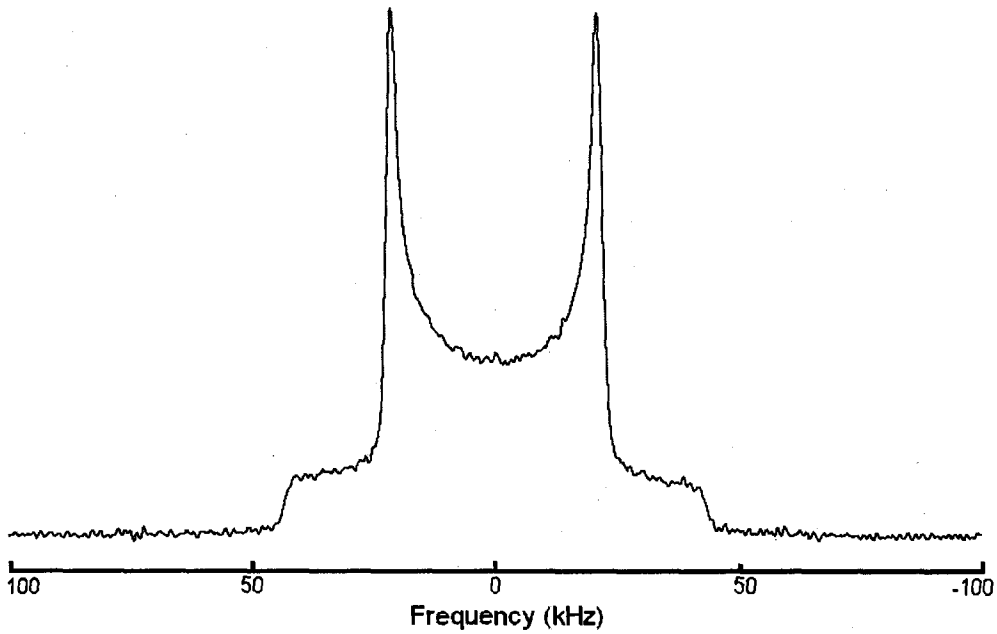

Figure 8.2 The ^2H spectrum of $Me_4AsI\text{-}d_3$ at room temperature.

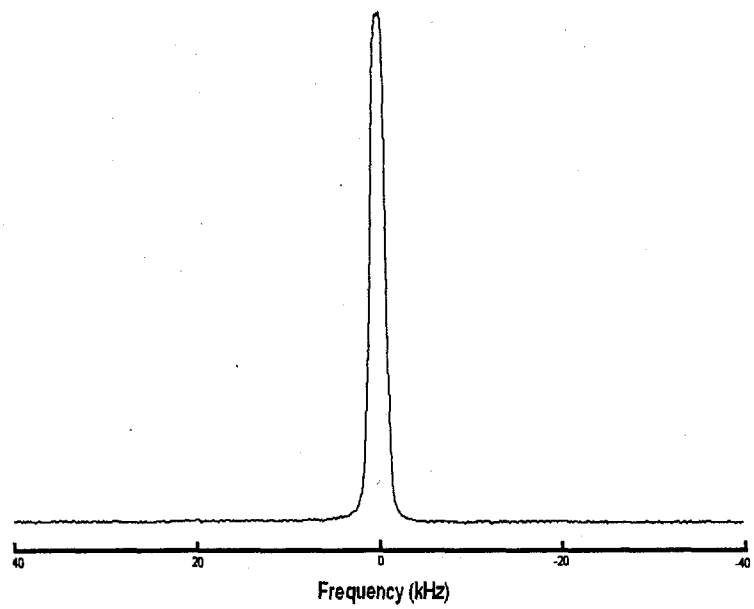

Figure 8.3 The ^2H spectrum of $Me_4AsI\text{-}d_3$ at a temperature of 353 K.

At room temperature, the spectrum is typical of fast methyl rotation and slow exchange between the methyl groups. At 353 K, the spectrum is as expected for the rapid rotation of methyl and the rapid interchanging of the four methyl groups. This indicates that the Me_4As^+ cation is undergoing rapid tetrahedral jumps in the high temperature phase.

8.2.2 The Solid State ^{75}As NMR Study of Me_4AsI at Room Temperature

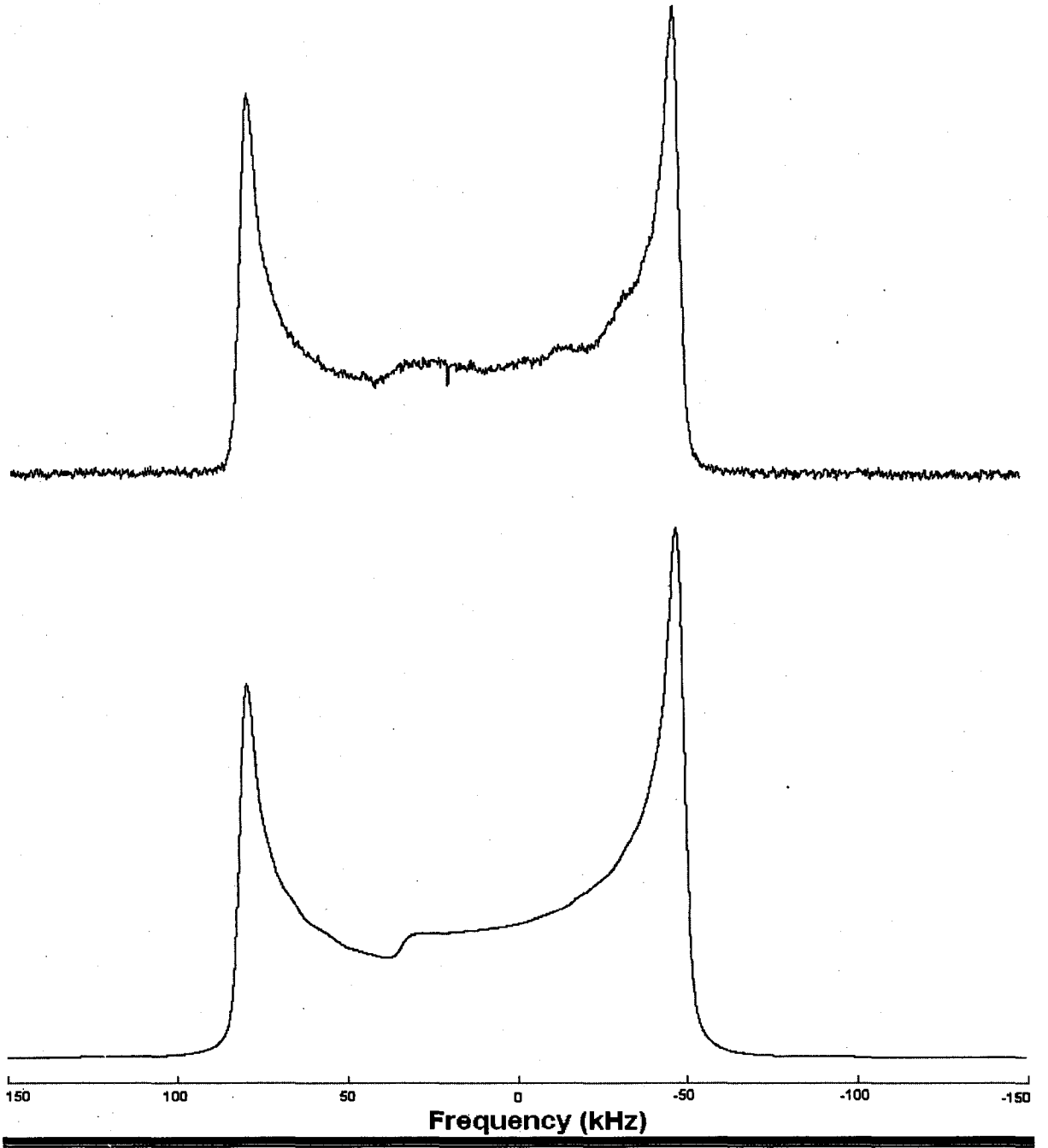

Figure 8.4 Experimental (top) and simulated (bottom) ^{75}As static spectra of Me_4AsI at room temperature. ($B_0 = 21.15$ T)

Figure 8.4 is the solid state ^{75}As NMR spectrum of Me_4AsI at room temperature. The ^{75}As NMR spectrum of α-$As(CH_3)_4I$ contains a single resonance with a relatively large quadrupolar coupling constant of 12.38 ± 0.30 MHz, and an asymmetry parameter of 0.01 ± 0.01, and an isotropic shift of 222 ± 6 ppm. The quadrupolar asymmetry parameter of zero agrees with the C_3 symmetry at the arsenic site [15]. It is obvious from the large ^{75}As QCC that the ^{75}As nucleus is not at a site of perfect tetrahedral symmetry. This is in agreement with the crystal structure, which shows that the local symmetry at Arsenic is C_3, not T_d. The consequence of this can be seen in the structure of the Me_4As^+ ion which shows one As-C bond length 1.917 (along the C_3 axis) while the other three have a length of 1.905 .

8.2.3 The Solid state ^{75}As NMR Study of Me_4AsI at 350 K

Figure 8.5 shows the ^{75}As spectrum at 353 K. The ^{75}As NMR spectrum of β-As $(CH_3)_4I$ contains a single resonance with a relatively small quadrupolar coupling constant of 3.6 ± 0.2 MHz, and an asymmetry parameter of 0.01 ± 0.01, and an isotropic shift of 202 ± 6 ppm.

There are two factors which should change the ^{75}As QCC in going from the α phase to the β phase. First, the crystal structure itself has changed which will change the relative position of the atomic changes that determine the efg at the ^{75}As nucleus. In addition the efg at the ^{75}As due to the difference between the As-C bond lengths will be averaged to zero by rapid rotation of the $(CH_3)_4As^+$ cation.

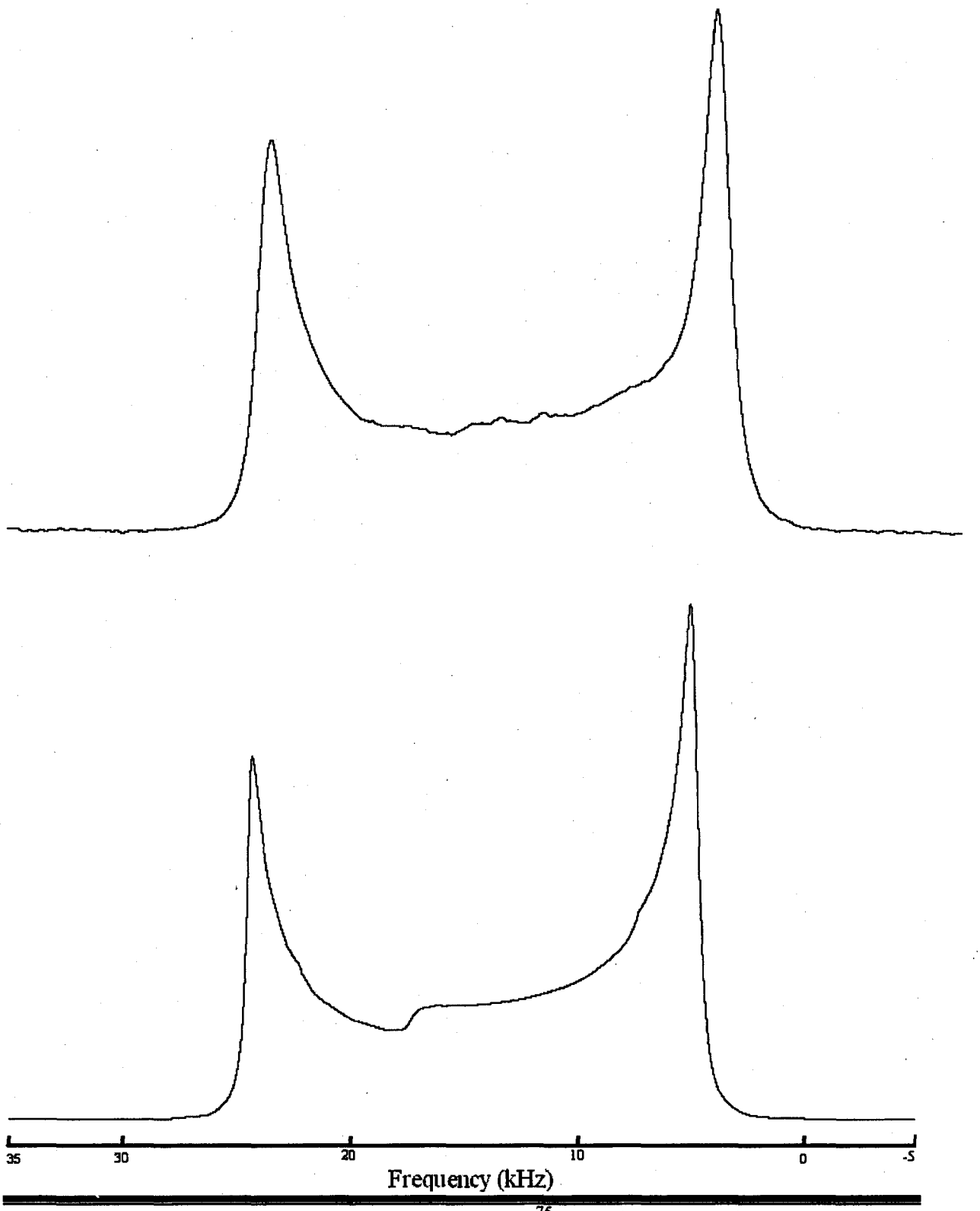

Figure 8.5 Experimental (top) and simulated (bottom) ^{75}As static spectra of Me_4AsI at 350 K ($B_0 = 11.75$ T).

8.2.4 The Solid State NMR ^{13}C Study of Me_4AsI

The direct dipolar nuclear spin-spin coupling interaction is analogous to the classical magnetic interaction between two bar magnets and depends intimately on the motionally averaged inverse cube of the internuclear distance of the two coupled nuclei, $\langle r_{IS}^{-3} \rangle$. This interaction is quantified by the direct dipolar coupling constant, R_{DD}:

$$R_{DD} = \frac{\mu_0}{4\pi} \frac{\gamma_I \gamma_S \hbar}{2\pi r_{IS}^{-3}} \tag{8.1}$$

Here, γ_I and γ_S are the magnetogyric ratios of the coupled nuclei.

The J coupling interaction may be described as the sum of isotropic, J_{iso}, and anisotropic, ΔJ, parts. The isotropic coupling constant is well known from solution NMR spectroscopy, where it manifests itself as a field-independent splitting. The Hamiltonian describing the anisotropic part of the J coupling tensor is identical in form to the Hamiltonian describing the direct dipolar interaction [16], and as a result, the two interactions cannot be separated. This phenomenon is represented by the following equation:

$$R_{eff} = R_{DD} - \frac{\Delta J}{3} \tag{8.2}$$

where the effective dipolar coupling constant, R_{eff}, is the quantity which is measured experimentally.

The failure of MAS in averaging the ^{13}C-^{75}As dipolar interaction to zero arises from the fact that that the ^{75}As nucleus is not solely quantized by the applied external magnetic field, but also by the orientation-dependent nuclear quadrupolar interaction. As a consequence, each peak in the ^{13}C MAS spectrum associated with one of the allowed eigenstates m of the ^{75}As nucleus exhibits in principle a powder pattern, resulting in broadening or splitting of the

isotropic peak. The shift, ν_m, relative to the unperturbed ^{13}C isotropic resonance frequency produced by the m eigenstates of the quadrupolar nucleus I, ν_{iso}, are determined by

$$\nu_m = \nu_{iso} - mJ_{iso} + \frac{I(I+1)-3m^2}{I(2I-1)}d \qquad (8.3)$$

where I is the nuclear spin of the quadrupolar nucleus; m = I, I-1,..., I, J_{iso} is the isotropic indirect spin-spin coupling and d is the residual dipolar coupling, which is defined as

$$d = \left(\frac{3\chi R_{eff}}{20\nu_I}\right)\left[\left(3\cos^2\beta^D - 1\right) + \eta_Q \sin^2\beta^D \cos 2\alpha^D\right] \qquad (8.4)$$

Here, ν_I is the Larmor frequency of the quadrupolar nucleus, and α^D and β^D are angles defining the orientation of the dipolar vector with respect to the EFG tensor frame. In this case, the EFG tensor is axially symmetric ($\eta_Q = 0$) and that the intranuclear vector is parallel to the largest component of the EFG tensor $\beta^D = 0$.

Simulations of the ^{13}C MAS spectra of Me_4AsI obtained at three different magnetic fields were performed employing the following parameters. The C-As bond lengths are 1.917Å and 1.905Å respectively from the known crystal structure [15]. Thus dipolar coupling constants of R_{DD} (^{13}C-^{75}As) are 750.4 Hz and 736.4 Hz accordingly. The quadrupolar coupling constant was found to be 12.24 MHz, and this value was used for the simulation of the ^{13}C MAS NMR spectrum of Me_4AsI. If ΔJ is assumed to be negligible, this leaves only two parameters to be varied, ^1J (^{75}As,^{13}C) and the linebroadening. For all these experiments the ^{13}C CP/MAS spectra can be adequately simulated with ^1J (^{75}As,^{13}C) = ±20 Hz.

The calculated ^1J (^{75}As,^{13}C) values are close to +12.4 Hz using the B3LYP/6-311G method. With the increasing of basis sets the calculated J values using B3LYP method are

getting a little bit smaller, but the sign still is positive. Therefore the sign of ^{1}J (^{75}As,^{13}C) value is probably positive and ^{1}J (^{75}As,^{13}C) is 20 ± 2 Hz.

The frequency differences between the two carbons were 181.0 Hz at B_0 = 4.7 T, 452.6 Hz at 11.75 T and 814.7 Hz at 21.15 T. The deviation of the observed spectrum from that simulated at 4.7 T is due to the possibility of an exchange rate between the methyl groups that is approaching 181 Hz, the frequency difference at 4.7 T.

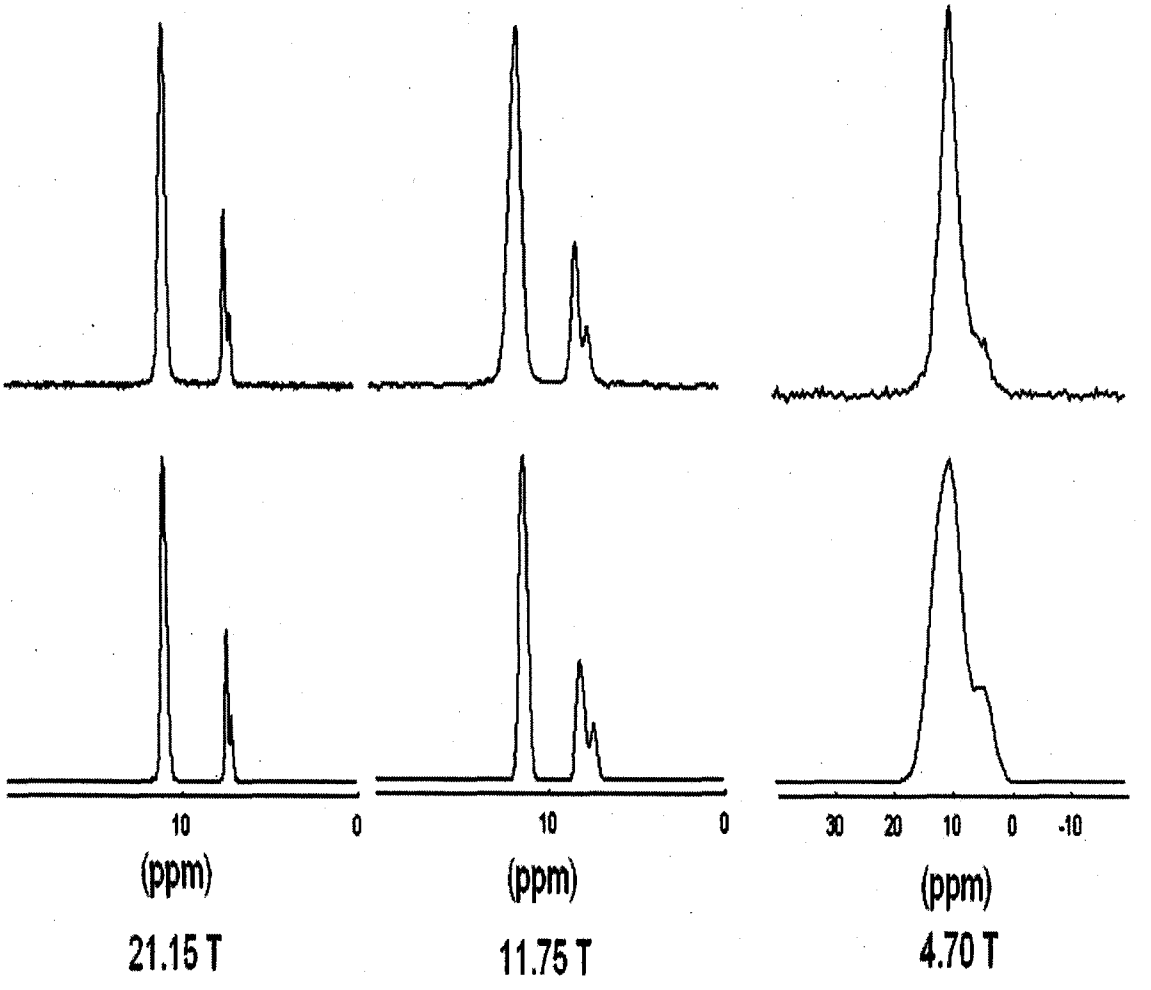

Figure 8.6 Experimental (top) and simulated (bottom) ^{13}C static spectra of Me_4AsI at different magnetic field.

This is the first experimental determination of J-coupling between ^{75}As and ^{13}C. Solution ^{13}C NMR studies of molecules containing As-C bonds usually show no ^{75}As-^{13}C coupling due to the fact that the relaxation of ^{75}As is so fast that it is essentially self-decoupled from ^{13}C [17]. The intensity ratio of the carbon signals in the spectrum acquired at 21.13 T is 3:1, which agrees with the ratio of the two types of chemically and magnetically inequivalent methyl groups in the unit cell of Me_4AsI.

8.2.5 The Solid State ^{127}I Study of Me_4AsI

^{127}I has a large NMR receptivity, but its applicability as a useful NMR nucleus is limited because of its large nuclear electronic quadrupole moment and resultant linewidth factor. Solid state ^{127}I NMR studies of diamagnetic solids are to date, limited to periodate (IO_4^-) salts and cubic alkali metal iodides [18]. Bryce and Sward have written a thorough review of ^{127}I solid state NMR data [18].

Me_4AsI crystallizes in the space group $Pa\bar{3}$ and there is a single iodide in the asymmetric unit [15]. The iodide anions are at the apexes of a tetragon. Figure 8.7 shows the tetragon formed by the iodine anions. The simulated and experimental solid state ^{127}I NMR spectra of Me_4AsI are shown in Figure 8.8.

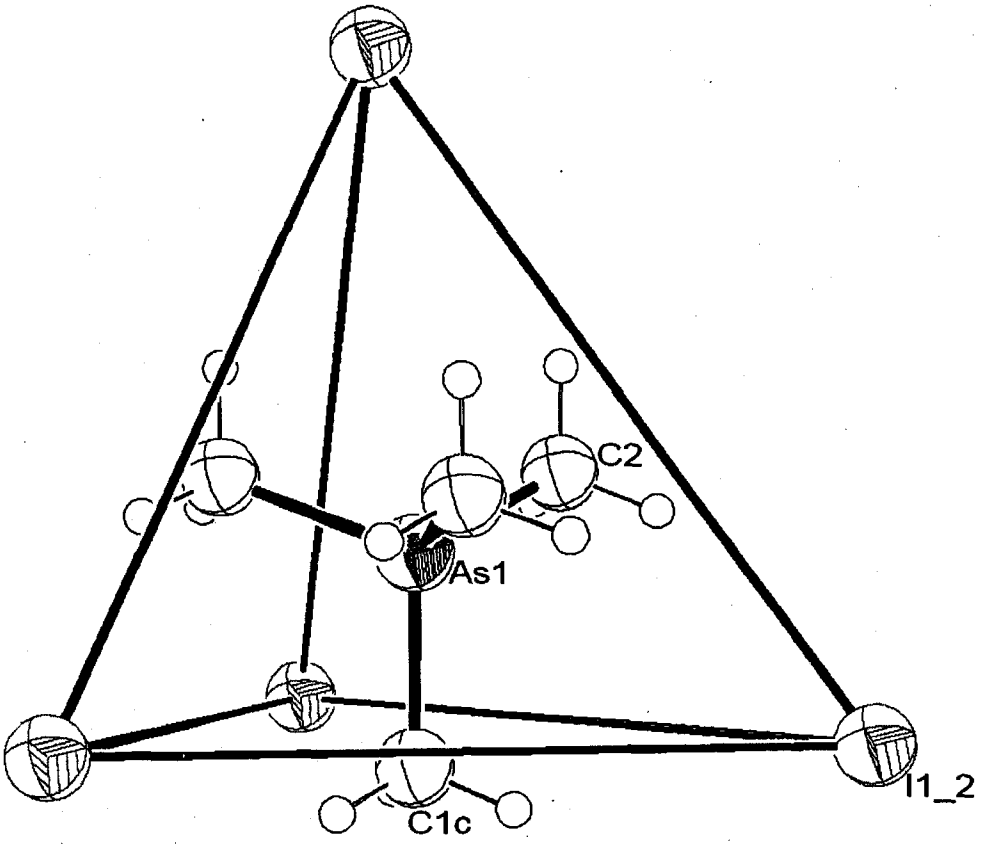

Figure 8.7 The crystal structure of Me_4AsI. [15]

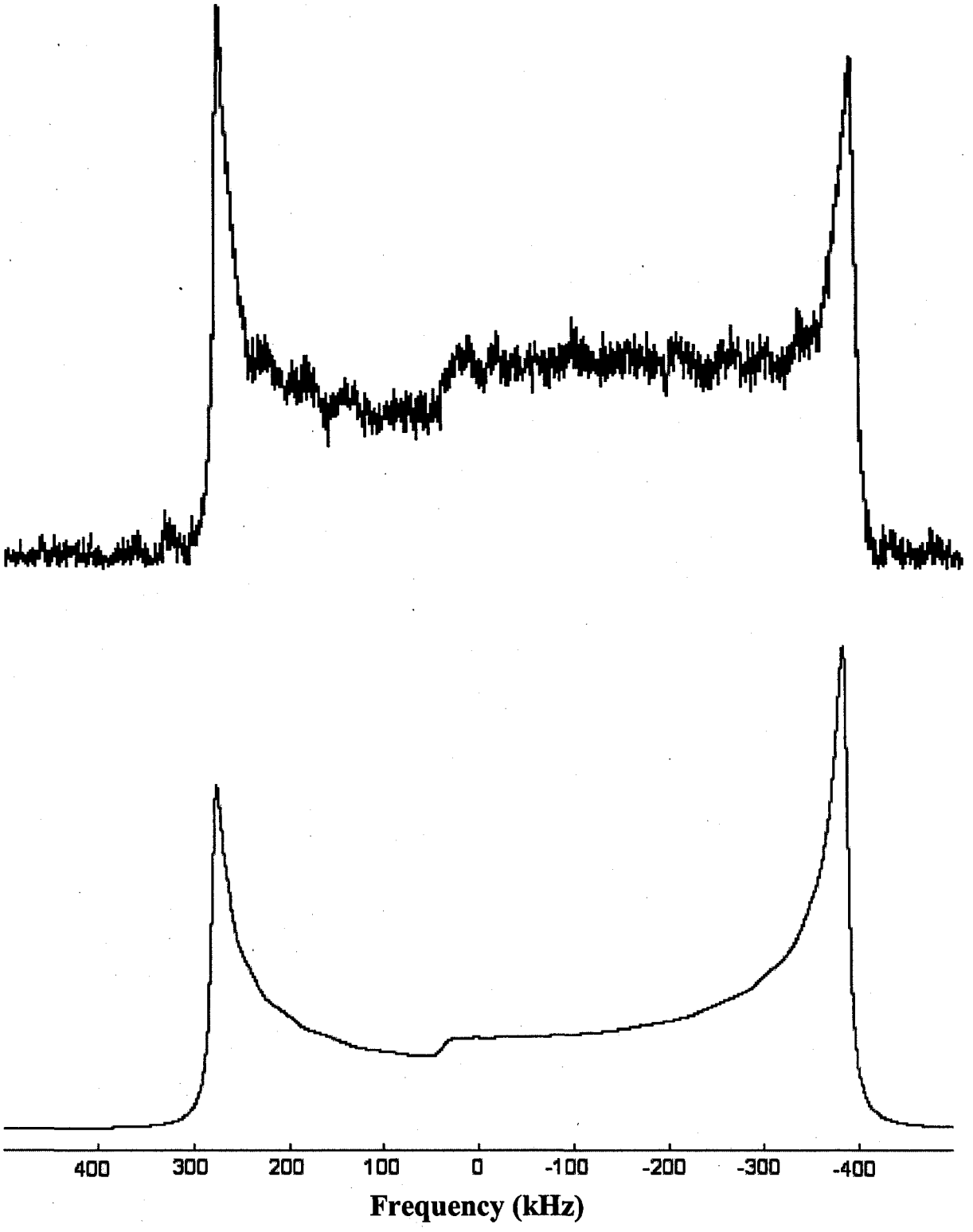

Figure 8.8 Experimental (top) and simulated (bottom) ^{127}I static spectra of Me_4AsI ($B_0 = 21.15$ T).

Me_4AsI crystallizes in the cubic space group $Pa\bar{3}$ with Z = 8[15]. The iodine atoms are related by an inversion centers and therefore are chemically and magnetically equivalent yielding one ^{127}I resonance. This is consistent with the observed ^{127}I spectrum. The ^{127}I NMR spectrum of Me_4AsI contains a single resonance with a relatively large quadrupolar coupling constant of 62.0 ± 0.5 MHz, an asymmetry parameter of 0.01 ± 0.01, and an isotropic shift of 220 ± 6 ppm. The observation of an axially symmetric electronic field gradient (EFG) at the ^{127}I nucleus in this compound is expected based on the fact that each I atom lies along a C_3 axis.

8.2.6 Theoretical Calculation of ^{75}As and ^{127}I QCCs in Me_4AsI

Calculation of the molecular electronic field gradient allows for theoretical prediction of the quadrupolar coupling constant, the QCC being proportional to the EFG. In order to assess the accuracy of these calculations, the results were compared to QCC tensor components measured from the solid state ^{75}As NMR spectra obtained in this work (QCC = 12.38 ± 0.30 MHz).

The calculated QCCs listed in Table 8.2 were used the following equation:

$$\chi = \frac{e^2 q_{zz} Q}{h} = -235 \cdot eq_{zz} \cdot Q \qquad (8.5)$$

where Q is in millibarn (10^{-31} m^2), eq_{zz} in atomic units (10^{-3} s^{-1} m^{-2}), and χ in kHz. The Q values of ^{75}As and ^{127}I are 314 and -710 millibarn respectively.

The calculated QCCs listed in Table 8.2 were those used to assess the quality of the basis sets. Calculations of the EFGs were performed on the structure of Me_4As^+ (shown in

Figure 8.1) using three levels of theory: Hartree-Fock (HF) theory, second-order Møller-Plesset perturbation (MP2) theory and density functional theory (DFT). The references of the three theories are listed in Chapter III.

Table 8.2 Calculated ^{75}As quadrupolar coupling constants of Me_4As^+.

	6-311G (d,p)	6-311G (2d,2p)	6-311+G (2d,2p)	6-311+G (2df,p)	6-311+G (2df,pd)	6-311++G (2d,2p)
B3LYP	3.52	3.60	3.61	3.58	3.58	3.61
HF	3.42	3.36	3.37	3.32	3.32	3.37
MP2	3.32	3.26	3.27	3.21	3.22	3.26

Experimental ^{75}As QCC of Me_4As^+ is 12.38 ± 0.30 MHz and the units of calculated results are MHz

The QCCs calculated with the three levels of theory and five basis sets are shown in Table 8.2. The calculated value is almost a quarter of the experimental value. With all of the methods, increasing the number of polarization and diffusion functions did not change the QCCs. Therefore in order to improve the calculated ^{75}As QCC, intermolecular effects such as the I^- anion positions and crystal symmetry (i.e. intermolecular interaction) must be taken into account. The basis sets that can be used for iodine are limited. Table 8.3 lists the calculated QCC values for ^{75}As and ^{127}I at the B3LYP level with 6-311++G (2d, 2p) basis set for Arsenic and Lanl2DZ [19-21] or DGDZVP [22-24] basis sets for iodine using the crystal structure (shown in Figure 8.7).

Table 8.3 Calculated ^{75}As and ^{127}I quadrupolar coupling constants of Me_4AsI at the B3LYP level with the 6-311++G(2d, 2p) basis set for As and Lanl2DZ or DGDZVP basis set for I

Basis set of Iodine / Nucleus	Lanl2DZ (MHz)	DGDZVP (MHz)	Expt. (MHz)
^{75}As	79.06	-1.47	12.38 ± 0.30
^{127}I	-27.3	10.1	62.0 ± 0.5

The calculated QCC values for ^{75}As do not match with the experimental results, as the calculated values presented in Table 8.3 demonstrate that more reliable basis sets for iodine are required.

8.2.7 The Solid State ^{127}I Study of Me_4NI

It is of interest to compare the ^{127}I NMR parameter for Me_4AsI to the related system Me_4PI and Me_4NI. Me_4PI is not commercially available and there is no crystal structure available, but Me_4NI is commercially available and the crystal structure is also available.

The iodide atoms in solid Me_4NI site on the corners of cubes formed by a network of I^- ions. Me_4N^+ cations are located at the centers of each cube [25]. The symmetry characteristic of I^- in the crystal unit of Me_4NI is shown in Figure 8.9. The simulated and experimental solid state ^{127}I NMR spectra are shown in Figure 8.10.

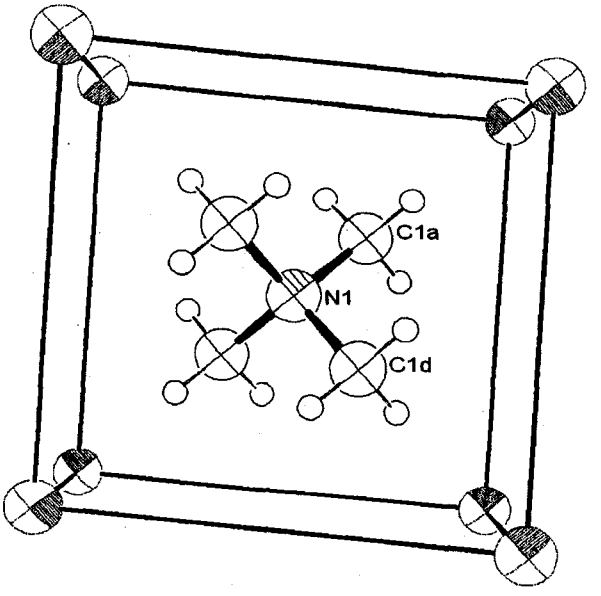

Figure 8.9 Crystal structure of Me_4NI.

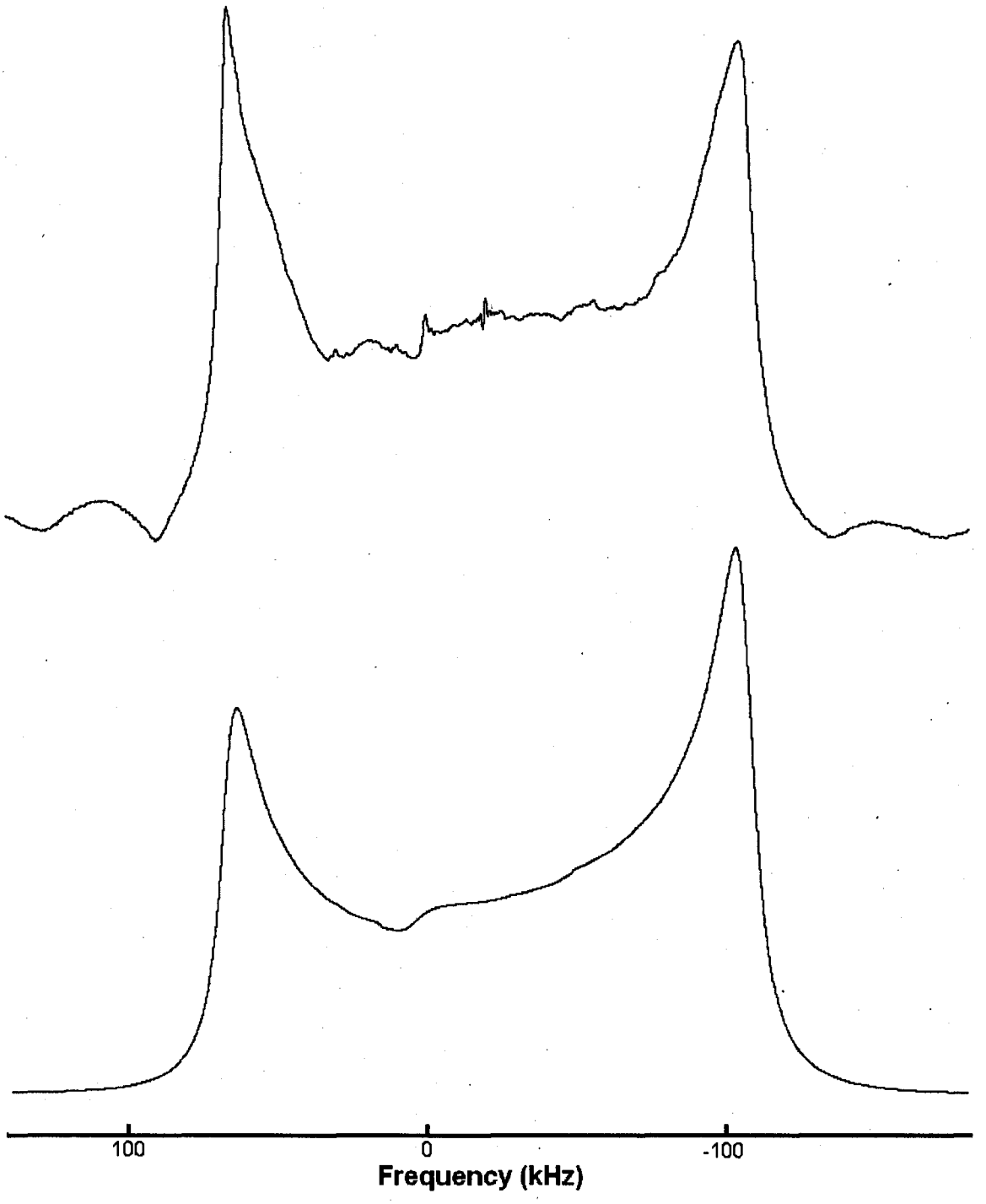

Figure 8.10 Experimental (top) and simulated (bottom) ^{127}I static spectra of Me_4NI (B_0 = 11.75 T).

The space group of Me_4NI is P4/nmm with Z = 2. The iodine atoms are related by an inversion center and therefore are chemically and magnetically equivalent yielding a single

resonance. This is consistent with the observed ^{127}I spectrum. The ^{127}I NMR spectrum of Me_4NI contains a single resonance with a quadrupolar coupling constant of 23.6 ± 0.2 MHz, an asymmetry parameter of 0.01 ± 0.01, and an isotropic shift of 50 ± 4 ppm. The observation of an axially symmetric electronic field gradient (EFG) at the ^{127}I nucleus in this compound is in agreement with the crystallographic symmetry present at the I^- site.

The experimental ^{127}I NMR parameters for solid Me_4AsI and Me_4NI are given in Table 8.4. together with crystal structure information. The big different I-I internuclear distances cause the different electronic field gradients at I sites, therefore the QCC values differ significantly between the two.

Unfortunately, as shown in section 8.2.5, basis sets that would provide reasonable calculated δ and QCC values into the electronic structure of these compounds, are not available.

Table 8.4 Solid State ^{127}I NMR parameters

Compound	Space group	I - I internuclear distance	δ_{iso} (ppm) [a]	e^2qQ/h [b] (MHz)	η_Q
Me_4NI	P4/nmm(Z =2)[17]	3.978	50 (4)	23.6 (0.2)	0.01 (0.01)
Me_4AsI	$Pa\bar{3}$ (Z = 8) [15]	7.357	220 (6)	62.0 (0.5)	0.01 (0.01)

Summary

i) Summary of the Solid State ^{13}C NMR Study of Me_4AsI

Two peaks in a 3:1 ratio are observed as expected, and $(CH_3)_4As^+$ cation is reorientating slower than the ^{13}C chemical shift timescale at $B_0 = 21.15$ T and 11.75 T ($k < 450\ s^{-1}$). At 4.7 T the effects of exchange between the methyl carbons can be seen ($k \approx 180\ s^{-1}$).

From an analysis of the lineshapes ^1J (^{75}As,^{13}C) was obtained as 20 ± 2 Hz. This is the first reported of indirect spin-spin coupling value between ^{75}As and ^{13}C.

ii) Summary of Solid State ^{75}As and ^{127}I NMR Studies of Me_4AsI

The iodine and arsenic atoms in Me_4AsI crystals are related by inversion centers and therefore are chemically and magnetically equivalent. Single ^{127}I and ^{75}As resonance are consistent with the crystal structure.

The quadrupolar asymmetry parameter of zero agrees with the high symmetry at the arsenic and iodine sites. In α-Me_4AsI phase, both the arsenic and iodine sites are on C_3 axes.

The symmetry of β-Me_4AsI is higher than α-Me_4AsI, so the QCC of arsenic in β-Me_4AsI is smaller than that in α-Me_4AsI as expected.

Chapter 8: References

[1] P. Hari, S. Guzel, T. Su, P. C. Taylor, P. L. Kuhns, W. G. Moulton, and N. S. Sullivan, *J. Non-Cryst. Solid.*, 326 (2003) 199.

[2] P. Hari, T. Su, P. C. Taylor, P. L. Kuhns, W. G. Moulton, and N. S. Sullivan, *J. Non-Cryst. Solid.*, 266 (2000) 929.

[3] P. C. Taylor, P. Hari, A. Kleinhammes, P. L. Kuhns, W. G. Moulton, and N. S. Sullivan, *J. Non-Cryst. Solid.*, 230 (1998) 770.

[4] P. C. Taylor, T. Su, P. Hari, E. Ahn, A. Kleinhammes, P. L. Kuhns, W. G. Moulton, and N. S. Sullivan, *J. Non-crystal. Solid.*, 326 (2003) 193.

[5] D. J. Treacy nad P. C. Taylor, *Solid State Commun.*, 40 (1981) 135.

[6] I. N. Pen'kov and I. A. Safin, *Doklady Akademii Nauk SSSR*, 156 (1964) 139.

[7] I. N. Pen'kov, *Geokhimiya*, (1971) 731.

[8] M. Suemitsu and N. Nakajo, *J. Appl. Phys.*, 66 (1989) 3178.

[9] L. D. Potter and Y. Wu, *J. Magn. Reson.* A, 116 (1995) 107.

[10] L. D. Potter, A. A. Guzelain, A. P. Alivisatos, and Y. Wu, *J. Chem. Phys.*, 103 (1995) 4834.

[11] J. Takeuchi, H. Nakamura, H. Yamada, E. Kita, A. Tasaki, and T. Erata, *Solid State Nucl. Magn. Reson.*, 8 (1997) 123.

[12] R. W. Schurko, S. Wi, and L. Frydman, *J. Phys. Chem.*, A, 106 (2002) 51.

[13] P. Hari, P. C. Taylor, A. Kleinhammes, P. L. Kuhns, W. G. Moulton, and N. S. Sullivan, *Solid State Commun.*, 104 (1997) 669.

[14] G. M. Bowers and R. J. Kirkpatrick, *J. Magn. Reson.*, accepted.

[15] W. Assenmacher, M. Jansen, *Z. Anorg. Allg. Chem.*, 621 (1995) 143.

[16] W. P. Power, R. E. Wasylishen, *Annu. Rep. Nucl. Magn. Reson. Spectrosc.*, 23 (1991) 1.

[17] G. E. Maciel, "*Topics in ^{13}C NMR Spectroscopy*", Vol1, chapter 2, Wiley, New York, (1974).

[18] D. L. Bryce, and G. D. Sward, *Magn. Reson. Chem.*, 44 (2006) 409.

[19] P. J. Hay, and W. R. Wadt, *J. Chem. Phys.*, 82 (1985) 270.

[20] W. R. Wadt, and P. J. Hay, *J. Chem. Phys.*, 82 (1985) 284.

[21] P. J. Hay, and W. R. Wadt, *J. Chem. Phys.*, 82 (1985) 299.

[22] N. Godbout, D. R. Salahub, J. Andzelm, and E. Wilmmer, *Can. J. Chem.*, 70 (1992) 560.

[23] C. Sosa, J. Andzelm, B. C. Elkin, E. Wimmer, K. D. Dobbs, and D. A. Dixon, *J. Phys. Chem.*, 96 (1992) 6630.

[24] M. Bühl, S. Gaemers, C. J. Elsever, *Chem. Eur. J.*, 6 (2000) 3272.

[25] H. Jacobs, H. Barlage, and M. Friedriszik, *Z. Anorg. Allg. Chem.*, 630 (2004) 645.

FUTURE WORK

In order to extend our knowledge of the aforementioned organosilver compounds, such that unambiguous correlations can be established between their crystal structures and NMR parameters, it is essential to perform the following experiments:

1. Determination of crystal structures for Iet-AgCl, Ity and SIPrFL.

This will confirm the relationship between the ^{109}Ag chemical shift tensors and silver coordination in the crystal unit cell. These structures can be obtained by X-ray diffraction analysis. A better ^{109}Ag spectrum of SIMes-AgCl should be obtained.

2. Determination of crystal structures for paraxylene-$AgClO_4$, Mesitylene-$AgCF_3SO_3$, $C_6(CH_3)_6 \cdot AgCF_3CO_2$, and $C_6(CH_3)_6 \cdot AgCF_3SO_3$.

The crystal structures of paraxylene-$AgClO_4$ and mesitylene- $AgCF_3SO_3$ can clearly show the coordination between paraxylene/mesitylene and Ag, which can aid in explaining the carbon spectra were so complex. The crystal structures can also be used to confirm the relationship between the ^{109}Ag chemical shift tensors and silver coordination in the crystal unit cell.

3. Determination of crystal structure for $C_6H_6 \cdot AgClO_4$ in the high temperature phase.

This structure can be used to compare with the structure at low temperature phase. This structure can also be used to confirm the relationship between the ^{109}Ag chemical shift tensors and silver coordination in the crystal unit cell. This structures can be obtained by X-ray diffraction analysis.

4. A 2D ^{13}C exchange experiment on α-Me_4AsI should be performed in order to obtain the exchange rate between methyl groups. This technique can probe slower exchange rates.